Shapes, Kinematics, and Formation Histories of Galaxies in Cosmological Simulations

Lucas Valenzuela

Munich 2021

Galaktische Formen, Kinematik und Entstehungsgeschichten in kosmologischen Simulationen

Lucas Valenzuela

München 2021

Shapes, Kinematics, and Formation Histories of Galaxies in Cosmological Simulations

Lucas Valenzuela

Master's Thesis

at the University Observatory Munich

Ludwig Maximilian University

Submitted by

Lucas Valenzuela

born in Böblingen

Supervised by

Dr. Rhea-Silvia Remus

Dr. Klaus Dolag

Munich, September 14, 2021

Contents

1 Introduction

Few things have fascinated humanity as much and as consistently as the night sky. As the window to the outside of our own planet, many civilizations have put a lot of effort into observing and trying to understand those peculiar bright objects – some of them moving, some of them seemingly not. And yet, until not even a hundred years ago, the concept of our Universe was still entirely limited to our own Galaxy, the Milky Way. In 1925, Hubble (1925) put this idea into question when he showed that the distance to the Andromeda Galaxy would actually place it beyond the reaches of the Milky Way. Since then, a huge number of galaxies have been observed as the imaging has been able to go increasingly deep. The Hubble Ultra-Deep Field (Beckwith et al., 2006) is the deepest optical and near-infrared image of our Universe to date, based on which Conselice et al. (2016) estimated the total observable number of galaxies to be over 2×10^{11} at that depth. On the theoretical side, the field of cosmology has advanced our understanding of the evolution of our Universe and the structure formation within. In 1916, Einstein (1916) revolutionized the understanding of gravity, space, and time, and laid the groundwork for the cosmological model described by the Friedmann-Lemaître-Robertson-Walker metric, which was independently developed by four scientists (Friedmann, 1922, 1924; Lemaître, 1927; Robertson, 1935, 1936a,b; Walker, 1937). According to this description, the Universe can be open, flat, or closed, and may expand or contract. Based on this model and the observations made over the years, the Universe is believed to have begun in a "Big Bang" and has expanded ever since. In this time of expansion, structures began forming, finally giving rise to the Universe as we see and know it today.

1.1 Structure Formation

Given such a large number of galaxies far out in our Universe, the intrinsic curiosity of humanity wants to understand where they come from and how they were formed. Naturally, we would expect that the properties of today's galaxies are a result of their formation history. It turns out that to understand their origin, it is necessary to start at very early times of the Universe.

1.1.1 Early Universe

In 1964, an accidental discovery by Penzias & Wilson using a Dicke radiometer revealed that there is an isotropic microwave radiation across the entire sky, which they measured as an

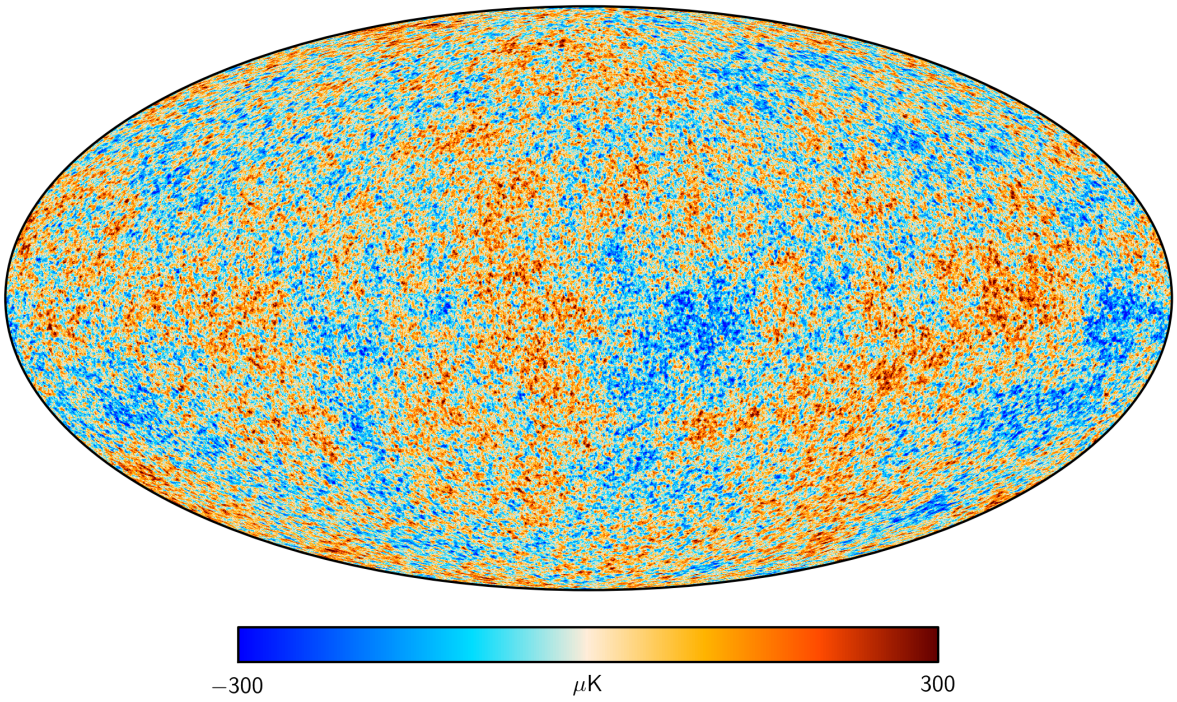

Figure 1.1: High-resolution image of fig. 9 from Planck Collaboration (2016): Temperature fluctuations of the CMB by ESA and the Planck Collaboration.

excess temperature of 3.5 K (Penzias & Wilson, 1965). Later missions, such as COBE (e.g. Smoot et al., 1992), WMAP (e.g. Komatsu et al., 2011), or Planck (e.g. Planck Collaboration, 2020), showed that this *cosmic microwave background* (CMB) radiation corresponds to a black body temperature of 2.725 K that has small temperature fluctuations on the order of 10^{-5} on small scales (Figure 1.1). In the cosmological context, this is understood to be the radiation emitted at the so-called *recombination*, where matter decoupled from radiation at early times (around 370 000 years after the Big Bang, which is estimated to have taken place around 13.8 Gyr ago), resulting in an optically transparent Universe. The anisotropy of the CMB is an imprint of the baryonic density fluctuations in the early Universe, which originated from dark matter (DM), a type of matter that does not interact electromagnetically, forming potential wells: baryonic matter streamed into these by gravitational force and was compressed, leading to a rise of radiation pressure that induced oscillations of the baryons within the DM potentials. The scales of these oscillations have been measured by the missions that explored the CMB in temperature power spectra (Figure 1.2), where the peaks indicate the oscillation scales. The power spectrum is used to constrain cosmological parameters that determine the evolution of our Universe. This understanding of the early Universe is part of the most widely accepted cosmological model: the ΛCDM model.

1.1.2 Galaxy Formation

In the ΛCDM model, small structures merge and form larger structures in a hierarchical manner. In this way, DM structure continuously grows more massive and gains angular momentum through tidal torques. Simultaneously, it accretes gas, which is capable of

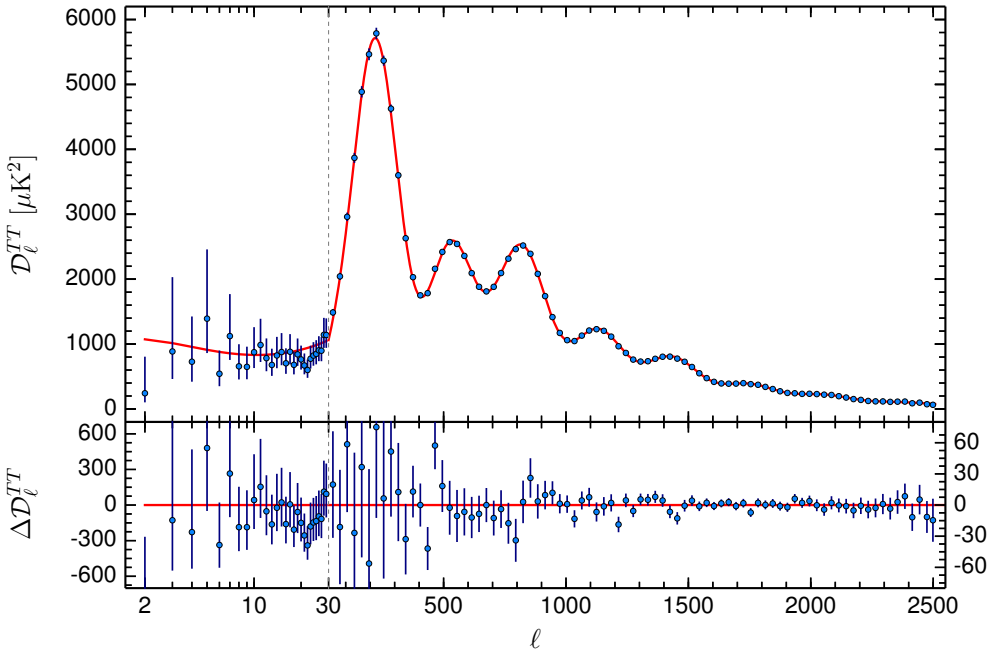

Figure 1.2: Fig. 11 from Planck Collaboration (2016): Temperature power spectrum (top) and residuals of the best fitting ΛCDM model (bottom) of the CMB by ESA and the Planck Collaboration. The red line indicates the best fitting model and the error bars the 1σ uncertainties of the measurements at a given multipole ℓ.

bringing in angular momentum to the central regions. In contrast to DM, gas interacts electromagnetically and can radiate away energy, thus cooling and redistributing its angular momentum. This enables the gas to condense in dense structures at the center of the DM structures. Here, in the DM structures, called DM *halos*, the first stars were born. The formation details of these *Population III* stars is still unclear and they have not yet been observed. The feedback from these first stars led to the enrichment of the gas with heavier metals, from which the second generation of stars were formed, the so-called *Population II* stars.

Star formation generally occurs in cold and dense gas. It has been found that the cosmic star formation rate (SFR) peaked at a redshift of $z = 2$ (around 10.5 Gyr ago), after which it decreased again (Figure 1.3, Madau & Dickinson, 2014), leading to an increase in the number of *quiescent* galaxies, which are gas-poor galaxies with little to no ongoing star formation (Brammer et al., 2011). Cosmological simulations revealed two phases of galaxy formation, where *in-situ* stars are first formed within the galaxies themselves through infalling cold gas and gas-rich mergers at $z \gtrsim 2$ and later *ex-situ* stars are accreted mostly through gas-poor mergers at $z \lesssim 3$ (Oser et al., 2010). The switch from the first to the second phase is a result of two contending mechanisms that take place: streams of cold gas funnelling into the galaxies feed the star formation (Dekel & Birnboim, 2006; Dekel et al., 2009), while feedback mechanisms (e.g. stellar winds, supernovae, or AGN) in the growing galaxies increasingly deplete the gas (e.g. Hopkins et al., 2012). The fraction of in-situ stars in galaxies has been studied in simulations and observations and has been shown to be highest in small, low-mass

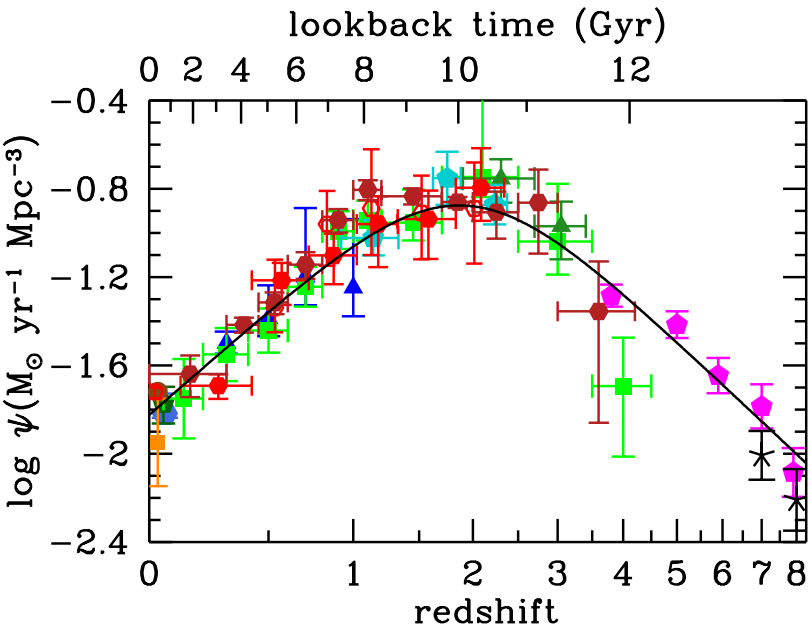

Figure 1.3: Left panel of fig. 9a from Madau & Dickinson (2014): Evolution of the cosmic star formation rate density, ψ, from far-UV (blue, green, magenta, and black points) and infrared (orange and red points) measurements. The black solid line is a fit to the SFR density data points.

galaxies, and is generally strongly correlated with the merger history of the galaxies (Remus & Forbes, 2021).

Observations have shown that the morphology of galaxies changes over time. Historically, it was assumed that elliptically shaped, almost featureless galaxies were first formed, such that these *elliptical galaxies* are commonly called *early-type galaxies* (ETGs). These were first believed to evolve into *spiral galaxies* that have a rotating disk and a *bulge* at the center, which are referred to as *late-type galaxies* (LTGs). However, the opposite appears to be true: in galaxy merger simulations, it was discovered that the elliptical galaxies are more likely formed through the mergers of disk galaxies (e.g. Gerhard, 1981; Burkert & Naab, 2003). Disk galaxies, in turn, form through the infalling gas in a halo, which cools and redistributes its angular momentum because of not being collisionless. As a result, it is able to settle in a disk perpendicular to its angular momentum and form stars there.

It has been found that not only the morphology, but also the relation between the stellar masses and sizes of galaxies, the *mass-size relation*, changes with time: the effective radius, the radius within which half the light of a galaxy is emitted, is larger at later times at constant mass or luminosity (e.g. Oesch et al., 2010; van der Wel et al., 2014; Shibuya et al., 2015; Allen et al., 2017). Interestingly, the size of ETGs, which are generally formed at later times than LTGs, increase much faster at a given mass than LTGs (Figure 1.4). For LTGs, the trend of smaller sizes at earlier times even continues to larger redshifts (Figure 1.5, for the evolution of the LTG size distribution). The overall evolution of the mass-size relation is believed to be driven by *dry* minor mergers, i.e., gas-poor and thus collisionless minor mergers (e.g. Naab et al., 2009; Hilz et al., 2013; Karademir et al., 2019). Finally, a type of rare objects that occur at high redshifts, but not in the present day, are very bright and compact galaxies

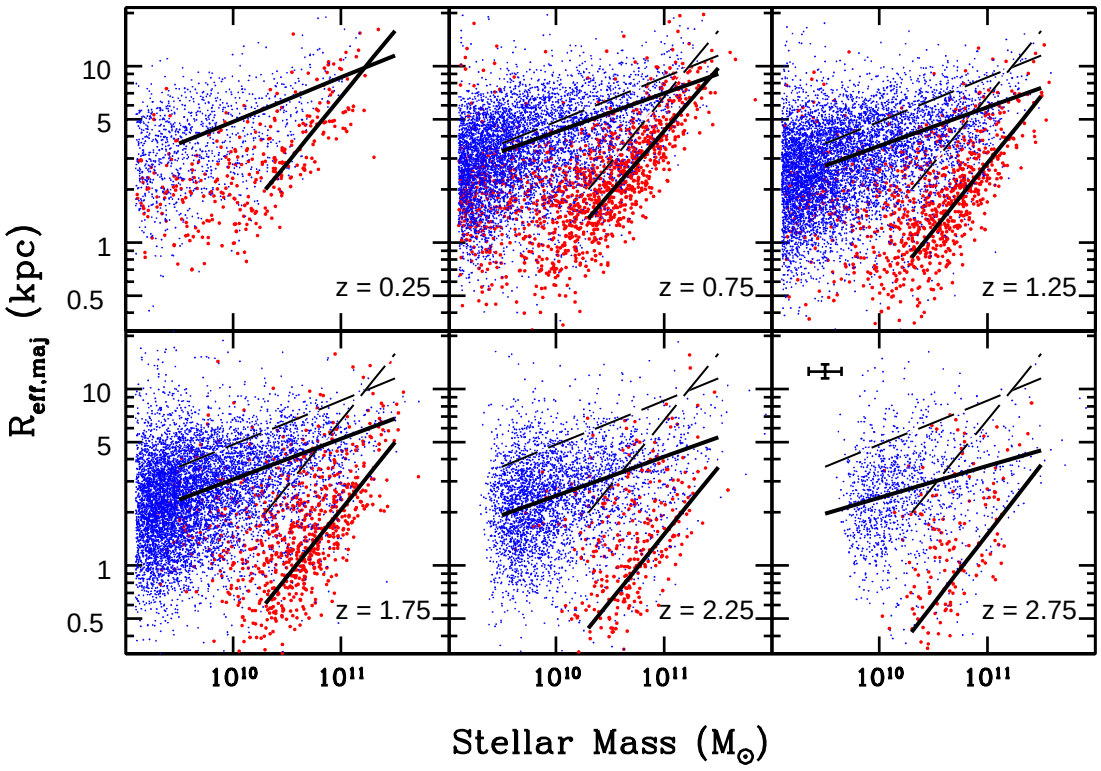

Figure 1.4: Fig. 5 from van der Wel et al. (2014): Evolution of the mass-size relation of LTGs (blue) and ETGs (red) in redshift bins within the range of z = 0–3. The solid lines indicate fits to the LTG and ETG data points and the dashed lines correspond to the fit at $0 < z < 0.5$ for comparison in the other redshift bins.

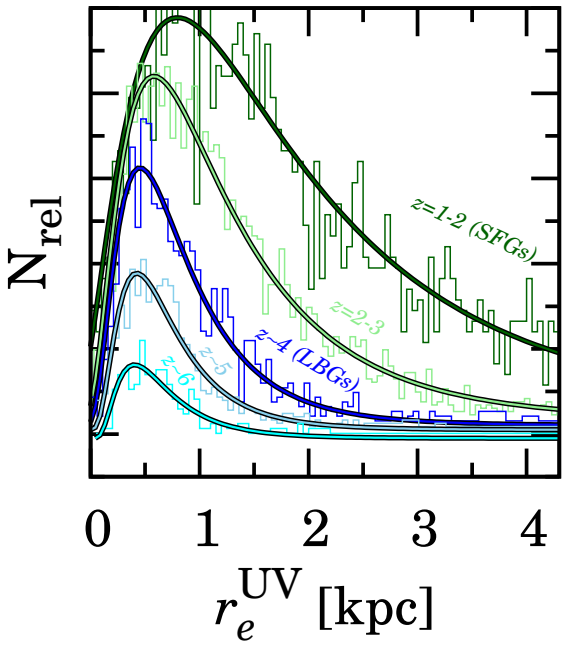

Figure 1.5: Fig. 6 from Shibuya et al. (2015): Distribution of the effective radii in UV for star forming galaxies (SFGs) at lower redshifts (z = 1–2 and z = 2–3) and Lyman break galaxies (LBGs) at higher redshifts ($z \sim$ 4, 5, and 6), obtained from Hubble Space Telescope data. The solid curves show the best-fit log-normal functions to the respective redshift bins.

(Fernández Lorenzo et al., 2011), which are also believed to have increased in size at almost constant mass.

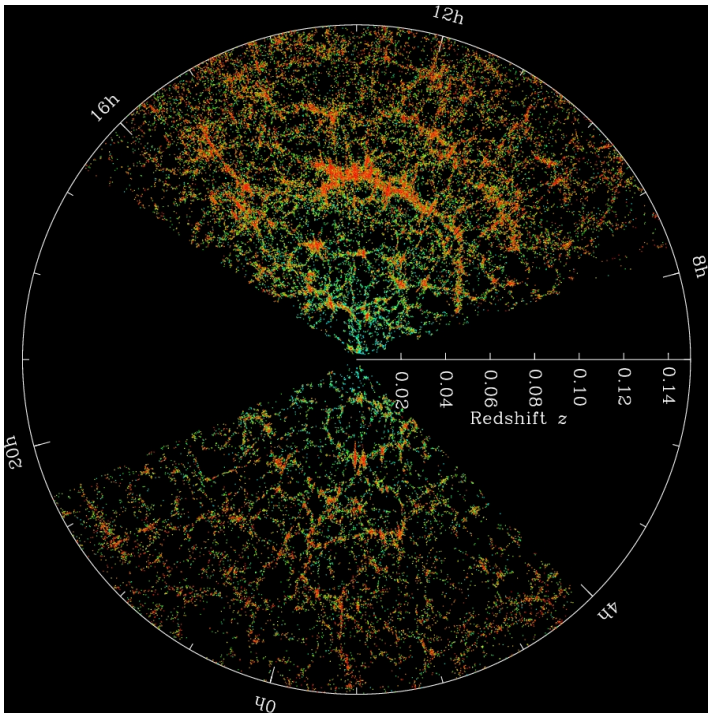

Figure 1.6: Cosmic web map from the galaxies observed by the Sloan Digital Sky Survey (SDSS) up to redshift $z \approx 0.15$. Each dot is a galaxy and is colored by the local density, with red indicating the denser environments. The wedges with observations in them are perpendicular to the Milky Way's disk. *Image credit*: M. Blanton and SDSS (www.sdss.org).

1.1.3 Cosmic Environment

Observations have shown that galaxies are not entirely uniformly distributed in space on small scales, but are found in large filamentary structures that connect clusters of galaxies, i.e., the especially dense node regions (Figure 1.6). In this *cosmic web*, the largest gravitationally bound structures are very massive DM halos containing thousands of galaxies, called *galaxy clusters*. The larger filamentary structures are typically subdivided in elongated *filaments* and even larger flattened *walls*. Such a wall can be seen in the upper wedge of Figure 1.6 at around $z \approx 0.07$, called the Sloan Great Wall (Gott et al., 2005). Finally, the low-density regions between these structures are referred to as *voids*. Large DM-only and baryonic cosmological simulations, such as the Millenium simulation (Springel et al., 2005b), the EAGLE simulations (Schaye et al., 2015), the Illustris Project (Vogelsberger et al., 2014), and the Magneticum Pathfinder simulations[1], have shown how the cosmic web structures form and evolve by matter collapsing as filaments and then being accreted onto the cluster nodes along the filaments.

Galaxies forming in the different environments are naturally subjected to different processes, which in fact affect their evolution. Considering that the formation history of a galaxy is the key to its present-day properties, the cosmic environment of a galaxy can be expected to be a relevant factor for understanding the properties of galaxies that we see today. In a galaxy cluster environment, the encounters between galaxies in the cluster potential feature such high velocities that they are generally unable to merge. Still, in such encounters, called

[1] www.magneticum.org

galaxy harassment, the galaxies lose orbital energy, which is redistributed to their internal energy, i.e., the galaxies are kinematically heated and increase in size (e.g. Moore et al., 1996). This facilitates the stripping of matter in their outer regions. In this way, it seems likely that disk galaxies could be stripped of their disks in a cluster environment and become elliptical galaxies. A second process in dense environments is caused by the hot gas in the halo of the cluster, which exerts pressure on the gas of a galaxy in the cluster potential. This leads to the hot and then the cold gas being stripped from the cluster member galaxy (which we will refer to as satellite galaxies henceforth, and also includes Milky Way-like and even more massive galaxies), which is called *ram-pressure stripping* (e.g. Gunn & Gott, 1972; Abadi et al., 1999). Finally, *strangulation* of satellite galaxies in a cluster is caused by the inability of a satellite to accrete more gas, such that star formation and stripping remove all the available gas irretrievably (e.g. Fujita, 2004). This causes blue disk galaxies to turn red and finally lose their spiral structures to become spheroidal. These processes all lead to gas-poor galaxies that typically have an elliptical morphology in cluster environments, which is actually what is also observed (e.g. Goto et al., 2003, for galaxies from SDSS). They also likely contribute to the *Butcher-Oemler effect*, which is that the fraction of blue galaxies, i.e., gas-rich and star-forming, in galaxy clusters has been observed to increase with redshift (Butcher & Oemler, 1978, 1984).

At the centers of galaxy clusters there are the brightest cluster galaxies (BCGs), which are the most massive galaxies of the clusters and are generally ellipticals. In contrast to the satellite galaxies, a BCG continuously accretes matter: in particular the more massive satellites quickly fall to the center of the cluster's potential because of dynamical friction, leading to BCGs typically having had several large mergers. In this way, a BCG "consumes" its satellite galaxies over time and increases in size and mass, which is called *galactic cannibalism* (e.g. Ostriker & Hausman, 1977).

In contrast, in the low-density regions of the cosmic web, the voids, there are no such massive clusters, but only a comparably small number of galaxies. These mostly are gas-rich LTGs and can form loosely bound galaxy groups (Szomoru et al., 1996). Such void galaxies have been observed to be accreting gas, indicating that they are still in the process of assembling (Kreckel et al., 2012). Void galaxies typically are small and have been found to have a slightly larger SFR than field galaxies of similar masses (Beygu et al., 2016).

1.2 Properties of Galaxies

Classifying objects or entities is not only fun, but also contributes an important part towards the discovery and advancement of knowledge (Kwasnik, 1999). Any classification is based on qualitative or quantitative properties of the objects or entities in question, which here of course are galaxies. With this in mind, a number of different morphological and kinematic parameters and properties are presented in the following. Additionally, the relevant background for the analysis of galaxy shapes in this work is presented.

1.2.1 Morphology

Hubble Sequence

In 1926, a first morphological classification scheme of galaxies was proposed by Edwin Hubble (Hubble, 1926), which laid the foundation for the *Hubble sequence* (Hubble, 1936), whose depiction is commonly called the "Hubble tuning fork" . Most galaxies were discovered to belong to one of three general classes: *elliptical* galaxies (E), which have smooth and featureless elliptical shapes, *spiral* galaxies (S), which feature a flat disk of stars, gas, and dust, with spiral arms extending out from the central bulge, and *lenticular* galaxies (S0), which were later introduced by Sandage (1961) and are an intermediate class between elliptical and spiral galaxies, having a disk, but no spiral structures. The *tuning fork* of the Hubble-Sandage classification is shown in Figure 1.7. These classes were also extended by *irregular* galaxies (I), which cannot be assigned to any of the other types and include galaxies like the Magellanic clouds. Elliptical galaxies, or ETGs as previously introduced, are classified by their apparent ellipticity, given by the semi-major and semi-minor axes, a and b, of the 2D projected galaxy:

$$\epsilon = 1 - \frac{b}{a}. \tag{1.1}$$

The galaxies are then labeled by EN, where N is the integer closest to 10ϵ, which ranges from E0 to E7 in practice. However, it was later put into question whether especially elongated ellipticals of types E6 and E7 actually have large-scale disks that are inclined and should rather be classified as S0 instead (Liller, 1966). Ellipticals usually have very old stellar populations and are gas-poor, resulting in a red appearance.

Spiral galaxies, or LTGs as previously introduced, are labeled as SB if they have a bar-like structure in the center, whereas normal spirals without bars are only labeled as S. Galaxies with tightly wound spiral arms additionally are labeled by the letter a, while more loosely wound spiral arms are labeled as b and c. Examples of six differently classified spiral galaxies can be seen in Figure 1.7. Most spiral galaxies feature a large bright stellar component in the center, called the bulge. The bulge is typically largest for galaxies with the most tightly wound spiral arms and the smallest for Sc and SBc galaxies. While the disk component oftentimes features active star formation and young stellar populations in its spiral arms, therefore appearing blue, the bulge is more similar to elliptical galaxies because of its featureless appearance and old stars.

Note that even though elliptical galaxies tend to show little star formation and are therefore usually *quiescent*, the terms "elliptical" and "quiescent" are not equivalent. The same is true for "spiral" galaxies and "star forming" galaxies, where spiral galaxies often feature active star formation in their spiral arms. All types of galaxies can experience so-called *starbursts* with very high rates of star formation, which typically occur in the process of a merger with a gas-rich galaxy (e.g. Hau et al., 1999). There is also an interesting class of red disk galaxies, which have been found to have stellar population properties similar to elliptical galaxies (e.g.

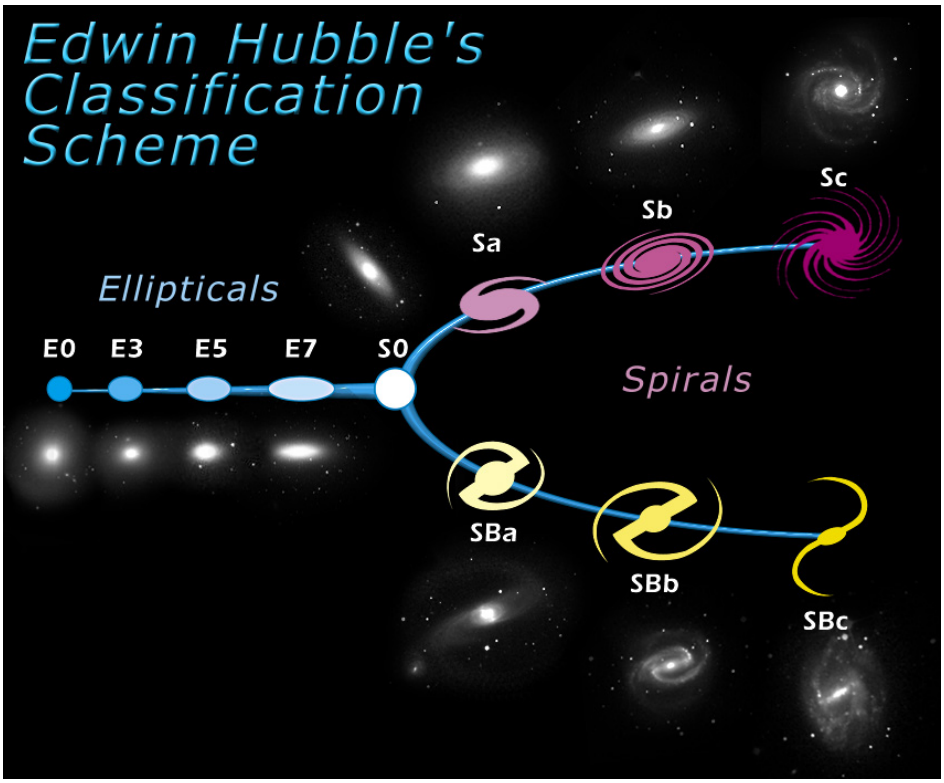

Figure 1.7: Hubble sequence of galaxies: Elliptical galaxies (E) are classified by their apparent ellipticity, while spiral galaxies (S) are classified by the existence of a bar feature at the center and by how tightly the spiral arms are wound. The sequences are connected by the class of lenticular galaxies, S0. *Image credit*: NASA & ESA (`www.esahubble.org`).

van den Bergh, 1976; Robaina et al., 2012). Clearly, the morphology and the star formation of galaxies are closely linked, but need to be considered separately when discussing galaxies.

There have been a number of other proposed morphological classification schemes. For example, the *de Vaucouleurs* system (de Vaucouleurs, 1959) adds a further feature of spiral galaxies to the classification system, in which the bars, spiral arms, and the existence of ring-like structures are considered. Because of the ellipticity of elliptical galaxies mainly just correlating with the inclination of a galaxy, Kormendy & Bender (1996) introduced a revised classification of ellipticals by the shape of their isophotes, which can be disky or boxy. The reason for this choice was that the shape of the isophotes can be used as an indicator to the kinematics, where disky ellipticals show faster rotation than boxy ellipticals.

The classification of galaxies according to their morphology was crucial to gaining a better understanding of galaxies and their formation, as stated at the beginning of this chapter. Despite being imperfect due to the huge variety of galaxies, even only the simple distinction between elliptical and spiral galaxies advanced the physical concepts of how galaxies form and evolve. Overall, the morphology is found to be closely linked to the formation history of a galaxy and is therefore an important fundamental property of galaxies.

b-Value

With the modern-day possibilities of measuring the kinematics of galaxies in the outer regions using kinematic tracers, such as planetary nebulae (PNe) or globular clusters (GCs),

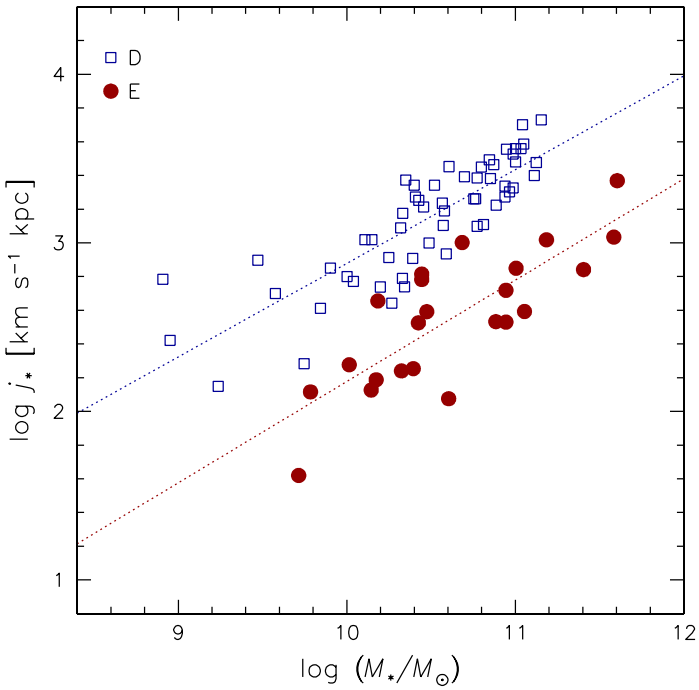

Figure 1.8: Fig. 2 from Fall & Romanowsky (2013): Relation between the specific stellar angular momentum and the total stellar mass for the disks of LTGs (squares) and for ETGs (circles) for a sample of 95 observed galaxies. The dotted lines represent the relation in Equation 1.3 with $\alpha = 0.6$.

it is possible to determine the total stellar angular momentum, $\boldsymbol{J}_*$. It was found that the specific stellar angular momentum, $\boldsymbol{j}_*$, where the specific angular momentum is defined by the total angular momentum divided by the total mass,

$$\boldsymbol{j} = \frac{\boldsymbol{J}}{M}, \tag{1.2}$$

shows different relations with the total stellar mass, M_*, for ETGs and LTGs (Fall, 1983; Romanowsky & Fall, 2012; Fall & Romanowsky, 2013). In fact, they found that both morphological types followed the same exponential law, only with different proportionality factors (Figure 1.8):

$$j_* \propto M_*^{\alpha}, \tag{1.3}$$

with $j_* = |\boldsymbol{j}_*|$ and $\alpha = 0.6 \pm 0.1$. The difference between ETGs and LTGs is that at a given mass, LTGs have a higher specific angular momentum, which is what one would expect given the intrinsic rotational property of disks. The relations are also in agreement with other observations (e.g. Cortese et al., 2016) and simulations (e.g. Teklu et al., 2015; Lagos et al., 2017).

The proportionality factor of Equation 1.3 was used by Teklu et al. (2015) to describe the morphological position of an individual galaxy in the j_*-M_*-plane, which corresponds to the y-intercept of the line with slope α on which the galaxy lies in logarithmic space. They defined the "b-value" using $\alpha = 2/3$:

$$b = \log\left(\frac{j_*}{\mathrm{kpc\,km\,s^{-1}}}\right) - \frac{2}{3}\log\left(\frac{M_*}{\mathrm{M}_\odot}\right). \tag{1.4}$$

The b-value therefore combines three important aspects of galaxy formation: angular momentum, mass, and morphology. It has proven to be a good indicator for morphology and has recently started to be used to classify galaxies morphologically. A big advantage of using the b-value for galaxies in simulations is that it can be computed directly from the particle properties and does not require a manual inspection of every galaxy. In this work, we follow the classification for galaxies at $z = 0$ used by Schulze et al. (2020), who used the same cosmological simulation as in this work, and by Emami et al. (2021):

(i) LTGs: $-4.35 < b$

(ii) Intermediates: $-4.73 < b < -4.35$

(iii) ETGs: $b < -4.73$

In this work, the b-value is calculated from the stellar particles within three stellar half-mass radii of the galaxy's center.

1.2.2 Kinematics

With the advances of observational instruments and telescopes, it has become possible to access the kinematics of galaxies along the line of sight. Major findings have been made possible through this. For example, the analysis of the radial velocity profiles of disk galaxies revealed much too high velocities at large distances from the center, which provided evidence for the existence of DM and advanced the research on DM halo density profiles. At the same time, the kinematics of individual galaxies contain important information for the respective galaxy: just like the morphology, the kinematics are a direct result of a galaxy's formation history, such that analyzing and modeling kinematics has evolved to be a central topic in galaxy physics.

IFU Spectroscopy

Integral field unit (IFU) spectroscopy has enabled observers to obtain two-dimensional spectroscopic data through IFU instruments, usually consisting of an array of lenses or fibers, that yields spatially resolved maps of spectra. From these spectra, it is possible to obtain the line-of-sight velocity distributions (LOSVDs). The first survey to map the galaxy kinematics in two dimensions was SAURON (Bacon et al., 2001; de Zeeuw et al., 2002), in which around 50 nearby galaxies were observed and mapped. Later, the ATLAS^{3D} Project extended this to a sample of 260 ETGs within a distance of 42 Mpc with the goal of kinematically characterizing the ETGs in a statistically significant way (Cappellari et al., 2011). A number of other IFU studies have taken place in recent years, including DiskMass for face-on intermediate-to-late-type disk galaxies (Bershady et al., 2010), SAMI for a large sample of galaxies (currently over 3000) across multiple environments (Croom et al., 2012, 2021), CALIFA for almost 700 galaxies as a wide-field IFU survey (Sánchez et al., 2012), MaNGA as the IFU program of SDSS for around 10 000 nearby galaxies (Bundy et al., 2015), SINS/zC-SINF for 35 galaxies at redshift $z = 2$ (Förster Schreiber et al., 2018), and MAGPI for galaxies at redshifts of $0.25 < z < 0.35$ in different environments (Foster et al., 2021).

Kinematic Maps

Different properties of the LOSVDs obtained from IFU spectroscopy for each pixel can be mapped as two-dimensional images. By simply fitting a normal distribution or directly computing the statistical mean and standard deviation for a LOSVD, the pixel velocities, $\langle V \rangle_i$, and velocity dispersions, σ_i, are determined for each pixel i. While it would be possible to simply create a map directly from these values, it is generally preferred to bin the pixels to improve the signal-to-noise ratio (particularly relevant for the regions with low surface density). A commonly used method is an adaptive spatial binning technique using centroidal Voronoi tessellations (Cappellari & Copin, 2003; Cappellari, 2009), which ensures roughly circular bins of pixels, an approximately constant signal-to-noise ratio across all bins, and a proper spatial resolution. The kinematic maps are then created according to the average velocity or velocity dispersion in each bin.

A velocity map can reveal some of the most important kinematic features of a galaxy, including if and how fast it rotates, along which (two-dimensional) axis it rotates, and if there are differences between the inner and outer line-of-sight velocity maps. For obvious reasons, disks have been found to have strongly ordered rotation around the minor axis (note that face-on disks will generally not reveal their rotational motion in velocity maps, however), while the bulge component was found to have more disordered motion. Similar to the bulges, ETGs usually also show less ordered rotation. The velocity dispersion offers a quantification of the disorder of motion, which should always be considered alongside the magnitude of the velocities themselves (just like the standard deviation is meaningless without knowing how large the mean is). The velocity dispersion is generally highest in ETGs, where younger ETGs have been found to often have lower central velocity dispersions (Forbes & Ponman, 1999), revealing a connection between velocity dispersion and formation history: mergers will generally bring in material from different directions, such that the overall rotation of the central galaxy will become more disordered and its shape more spherical. The details of the merger orbits and masses of the accreted structures will then determine how the kinematics of the central galaxy change, therefore strongly linking the merger history and the kinematics. The velocity and velocity dispersion maps of an example disk galaxy observed in the SAMI survey are shown in the two left panels of Figure 1.9 (not binned with the Voronoi tesselation method, however). The velocity map shows a clear sign of ordered rotation, while the velocity dispersion map shows the different kinematic behavior in the bulge and disk: the velocity dispersion is larger in the central bulge region.

Of course, the LOSVDs are not perfect normal distributions, but deviate from a Gaussian curve. Most parametrizations of these deviations involve the Gauss-Hermite moments, h_3 and h_4. These higher-order moments describe the asymmetric deviations (h_3) and symmetric deviations (h_4) from a Gaussian curve. Both quantities have been studied in observations, where for example one of the first studies by Bender et al. (1994) found that the deviations are generally small, with the asymmetric deviations being larger than the symmetric ones. In the SAURON survey, it was found that there is an anticorrelation of h_3 with the rotational

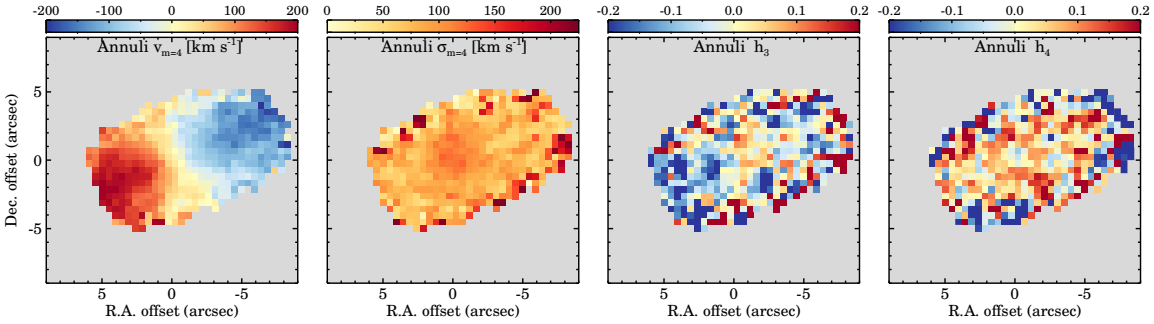

Figure 1.9: Four left panels of the middle row of fig. 24 from van de Sande et al. (2017b): Kinematic maps of a SAMI disk galaxy of the stellar kinematic parameters velocity, V, velocity dispersion, σ, and the two higher-order moments, h_3 and h_4, from left to right. *Annuli* refers to the template method used to obtain the stellar kinematic parameters.

support, quantified by V/σ (e.g. Bender et al., 1994; Krajnović et al., 2006). Because of the difficulty in interpreting the higher-order moments in observations, simulations have been employed to investigate the drivers of the behavior of the LOSVDs (e.g. Bendo & Barnes, 2000; Jesseit et al., 2007; Schulze et al., in preparation). The two right panels of Figure 1.9 show the higher-order moment kinematic maps of the example SAMI galaxy. Compared to the velocity and velocity dispersion maps, it is a lot more difficult to determine what patterns exist in these maps.

Kinematic Groups

As part of the ATLAS^{3D} project, Krajnović et al. (2011) studied the kinematic maps of 260 ETGs and determined five kinematic groups of their galaxies: regular rotators, non-rotators, galaxies with complex velocity maps, but no specific features, galaxies with kinematically distinct cores, and galaxies with double peaks in the velocity dispersion maps. The diversity of kinematic features is especially remarkable in light of the morphologically featureless ETGs compared to LTGs. The by far largest group of classified ETGs are the regular rotators, with about 80% of the galaxies. Interestingly, these galaxies were found to have velocity maps more similar to those of disk galaxies than to remnants of equal-mass mergers, giving insights into what the most common formation histories may look like. ETGs appear to often be disk-like galaxies that have a near-axisymmetric shape, where two important formation processes are likely minor mergers and gas accretion. The other four groups were determined to typically be located in dense regions, which is consistent with the idea that accretion from random directions in dense environments leads to a disordering of galaxies' rotation. Krajnović et al. (2011) suggested that major mergers could be an important factor of their formation histories.

For the cosmological simulation considered in this work, Schulze et al. (2018) classified the galaxies by using the velocity maps from an edge-on perspective, since this allows a more consistent classification of galaxies that is not dependent on an observer from a random direction. Moreover, rotation generally occurs along the minor or major axis of a galaxy, such that an edge-on perspective ensures that these types of rotation will be found in the velocity

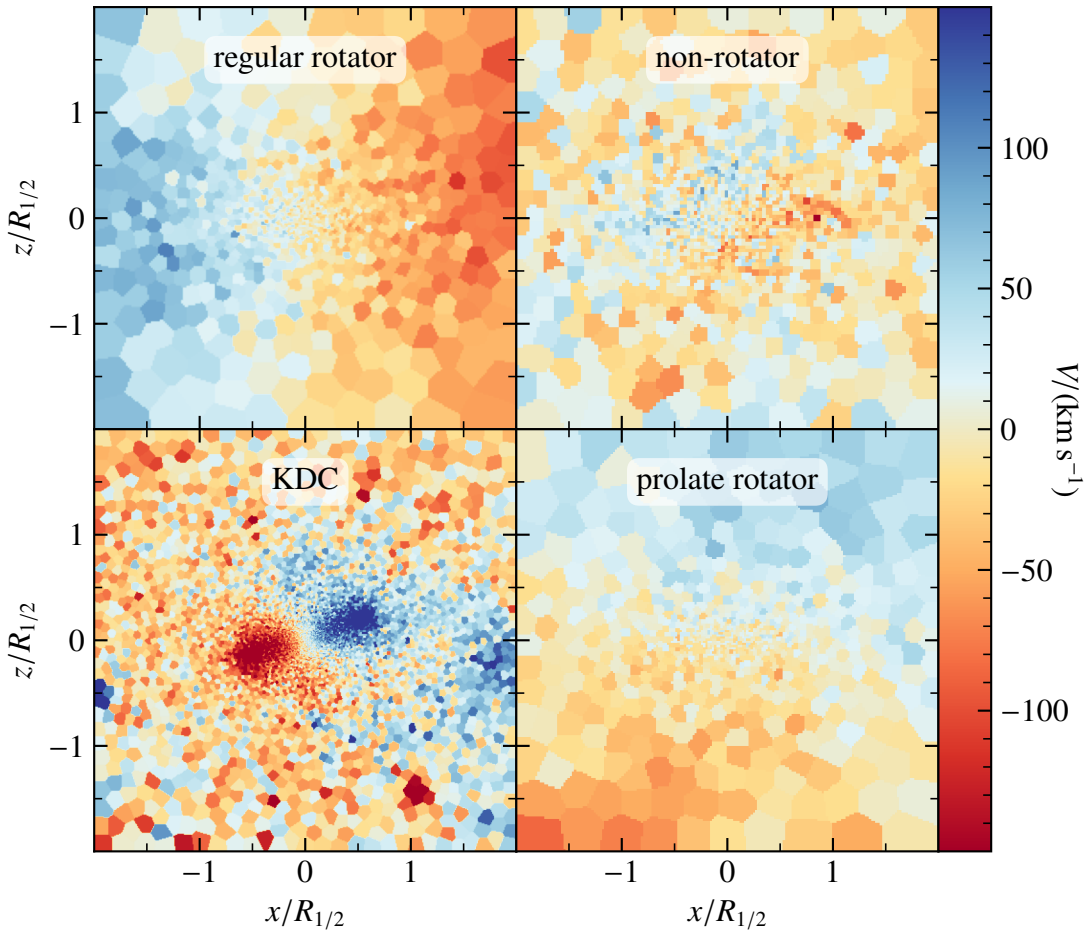

Figure 1.10: Example velocity maps of the four kinematic groups used in this work: regular rotators, non-rotators, KDCs, and prolate rotators. The inner two half-mass radii of the galaxies are viewed from an edge-on perspective. The velocity maps were created using the Voronoi tesselation method for the bins, where each bin contains around 100 stellar particles from the simulation. The four galaxies are from Box4 (uhr) of the Magneticum Pathfinder simulation suite (see Section 2.1 for further details).

maps. Schulze et al. (2018) divided the galaxies into five kinematic groups, which are based on those of Krajnović et al. (2011):

(i) Regular rotators: The galaxy has an ordered rotation around the minor axis.

(ii) Non-rotators: The velocity map shows low velocities with no distinct features.

(iii) Distinct cores (DCs): There is a central rotating core that is surrounded by a non-rotating component.

(iv) Kinematically distinct cores (KDCs): There is a central rotating core that is surrounded by a rotating component around a different axis.

(v) Prolate rotators: The galaxy has an ordered rotation around the major axis.

In this work, the classifications determined by Schulze et al. (2018) are used, but count both the DCs and KDCs to the group of KDCs because of the very small number of KDCs, thus considering only four kinematic groups. Four example velocity maps of these kinematic groups are shown in Figure 1.10, where all galaxies are shown from an edge-on perspective. Note that in all of the discussed classifications, there is a further "group" of unclassifiable galaxies due to poor resolution or unclear kinematic features.

Especially the two rarest groups, the KDCs (including the DCs) and prolate rotators, are intriguing with respect to their formation history. KDCs have been observed and investigated in multiple studies, ranging back from one-dimensional slit spectroscopic data (e.g. Efstathiou et al., 1982; Bender, 1988) to modern IFU surveys (e.g. ATLAS^{3D}: Cappellari et al., 2011; MaNGA: Bundy et al., 2015) and simulations (e.g. Tsatsi et al., 2015; Schulze et al., 2017; Ebrová et al., 2021). The term "KDC" has not been defined consistently in the literature, where different minimum misalignment thresholds of the core's rotational axis compared to the outer rotational axis were required (e.g. 20° for SAURON and 30° for ATLAS^{3D}), or where certain types of kinematic features are distinguished from KDCs. These include counter-rotating cores (a feature used in the ATLAS^{3D} survey), galaxies with two velocity dispersion peaks (which often also have KDCs), distinct cores (as seen above, from Schulze et al., 2018). Others, such as Ebrová et al. (2021), include galaxies with any of those features in the group of KDCs. While a number of studies suggest that young KDCs are likely formed through retrograde mergers (e.g. Balcells & Quinn, 1990; Bois et al., 2011), there have also been findings of old KDCs originating from originally prograde orbits, where reactive forces because of mass loss led to a significant change in the orbital spin (Tsatsi et al., 2015). In a study by Schulze et al. (2017), a binary spiral galaxy major merger simulation formed an ETG with a kinematically distinct core. In fact, Ebrová et al. (2021) found that most KDCs in the Illustris cosmological simulation were formed through mergers, most of them major mergers, and others were formed through fly-bys or through precession of a rapidly rotating core component. Schulze et al. (2020) found both old and young KDCs in the cosmological simulation studied in this work, which may have two different typical formation histories: mergers with plenty, but not too much gas for younger cores (Hoffman et al., 2010), and the remnant of an old disk at the center.

Prolate rotators, the rarest among the four kinematic groups, were theoretically predicted through a class of orbits around the major axis called long axis tubes (de Zeeuw, 1985). This kinematic behavior has been observed in the bulges of early-to-intermediate type disk galaxies (e.g. Bertola et al., 1999) and in massive ETGs (e.g. Tsatsi et al., 2017; Krajnović et al., 2018), where it was found that prolate rotation occurs more often in the most massive galaxies. Prolate rotators and their formation histories have also been studied in simulations (e.g. Ebrová & Łokas, 2015; Tsatsi et al., 2017; Ebrová & Łokas, 2017). One possible formation mechanism that has been suggested is a dry major polar merger of disk galaxies, where the disks are originally oriented perpendicular to each other, which appears to lead to a correlation between the line-of-sight velocity and the higher-order moment h_3 (Tsatsi et al., 2017). Ebrová & Łokas (2017) found that prolate rotators in the Illustris simulation are strongly linked to the last major merger of the galaxy, where the actual formation of the prolate rotation appears to depend on the details of the initial conditions in a non-trivial way. They determined several different formation channels of prolate rotation, including dry and wet mergers, but also found systems without significant mergers to show such a kinematic feature.

Circularity Parameter

A kinematic parameter that quantifies the rotational properties around the minor axis is the *circularity*, ϵ_{circ}. Introduced by Abadi et al. (2003), it can be computed for each particle in a simulation (such that the 3D data of the particles and of the potential are available) and describes how close the angular momentum around the minor axis is to that of a particle on a Keplerian circular orbit:

$$\epsilon_{\mathrm{circ}} = \frac{j_z}{j_{\mathrm{circ}}} = \frac{j_z}{rV_{\mathrm{circ}}}, \tag{1.5}$$

where j_z is the angular momentum component of a particle along the minor axis of the galaxy, r is the distance from the galaxy's center, and

$$V_{\mathrm{circ}} = \sqrt{\frac{GM(r)}{r}} \tag{1.6}$$

is the Keplerian circular velocity with the total enclosed mass, $M(r)$, within r. The distribution of the circularity for the stellar particles is expected to peak at around $\epsilon_{\mathrm{circ}} \sim 1$ for a disk component, whereas a peak at $\epsilon_{\mathrm{circ}} \sim 0$ indicates a component dominated by velocity dispersion. For this reason, the circularity distribution has been used to decompose the stars into disk and spheroid components (e.g. Scannapieco et al., 2008) and the mean circularity even as an indicator for the morphology (Teklu et al., 2015). For this reason, there is a strong correlation between the mean circularity and the b-value.

Rotational Support – V/σ

As already stated, the absolute value of the velocity dispersion is meaningless without putting it in relation with the velocity itself. For this reason, the quantity V/σ has been used in the past to measure the amount of rotation as the ratio of ordered to random motion (Illingworth, 1977), where V has been defined as the maximum velocity and σ as the mean central dispersion, or V as the mass-weighted root mean square of the velocities and σ as the mass-weighted mean velocity dispersion. It was found that larger values of V/σ tend to correspond to larger ellipticities, ϵ, i.e., flatter galaxies, but also that most flat ETGs are not flattened by rotation, in part having data consistent with no rotation at all (e.g. Illingworth, 1977; Binney, 1978). This flattening of *slow rotators* was generally assumed to carry information about the formation history of ETGs, and has been interpreted as the result of the remnant anisotropy of the velocity distribution.

Rotational Support – λ_R-Parameter

The usage of V/σ was revisited with the advent of IFU surveys, since the small number of slits used in earlier spectrographs, which usually only covered small regions of galaxies, limited the available kinematic data of a galaxy and because the value of V/σ fails to distinguish small-scale from large-scale rotation. Based on a theoretical study by Binney (2005), Emsellem et al. (2007) introduced a new parameter within the SAURON project that

aimed to obtain the same general nature of V/σ: to describe the ordered versus the random motion. This new parameter, λ_R, acts as a proxy of the specific angular momentum in relation to the random motion and is defined as

$$\lambda_R = \frac{\langle R|V|\rangle}{\left\langle R\sqrt{V^2+\sigma^2}\right\rangle}, \tag{1.7}$$

where R is the distance to the galaxy's center, V and σ are again the line-of-sight velocity and velocity dispersion, and the brackets $\langle\cdot\rangle$ correspond to the luminosity-weighted average. The term $\langle R|V|\rangle$ enables the distinction between small-scale and large-scale motion by resembling a kind of mean projected angular momentum. Large-scale rotation will therefore lead to large values of $\langle R|V|\rangle$, while small-scale rotation will have small values of the term.

Assuming a constant mass-to-light ratio, Equation 1.7 is implemented for simulations as (following e.g. Jesseit et al., 2009; Naab et al., 2014; Schulze et al., 2018)

$$\lambda_R = \frac{\sum_i M_i R_i |V_i|}{\sum_i M_i R_i \sqrt{V_i^2+\sigma_i^2}}, \tag{1.8}$$

where the sums run over the 2D bins (in this work the previously introduced Voronoi tesselation binning method is used), and the quantities M_i, R_i, V_i, and σ_i are the total mass, distance from the galaxy's center, mean velocity, and mean velocity dispersion of the ith bin, respectively. The sum is performed over the Voronoi bins instead of over a pixel-based grid to avoid issues with limited mass and spatial resolution in the simulation, which can cause statistical errors (following the approach taken by Schulze et al., 2018; a thorough study on resolution in simulations is performed by Bois et al., 2010). This approach leads to a lower limit of λ_R in simulations, since the statistical noises in the bins add up because of the cumulative definition of λ_R (Bois et al., 2010; Naab et al., 2014; Schulze et al., 2018), corresponding to around 0.07 for the simulation considered in this work.

When viewed from an edge-on perspective, galaxies dominated by rotation have values of $\lambda_R \sim 1$, whereas dispersion-dominated galaxies have values of $\lambda_R \sim 0$. This motivated Emsellem et al. (2007) to use λ_{R_e} (where R_e is the effective radius, within which half the light of the galaxy is found) to classify ETGs as *slow rotators* ($\lambda_{R_e} < 0.1$) and *fast rotators* ($\lambda_{R_e} > 0.1$). The larger galaxy sample of the ATLAS^{3D} survey allowed Emsellem et al. (2011) to redefine the threshold criterion based on both the λ_R-parameter and the ellipticity, ϵ, within one effective radius:

(i) slow rotator: $\lambda_{R_e} < 0.31 \cdot \sqrt{\epsilon_{R_e}}$

(ii) fast rotator: $\lambda_{R_e} > 0.31 \cdot \sqrt{\epsilon_{R_e}}$

This separates galaxies into the two groups depending on their position in the λ_R-ϵ plane, which also corresponds to the refined version of the previously considered relation between V/σ and ϵ. Emsellem et al. (2011) found that 66% of the elliptical galaxies are fast rotators, suggesting that the majority of ETGs are consistent with disk-like systems, while only a comparably small percentage shows more spherical properties.

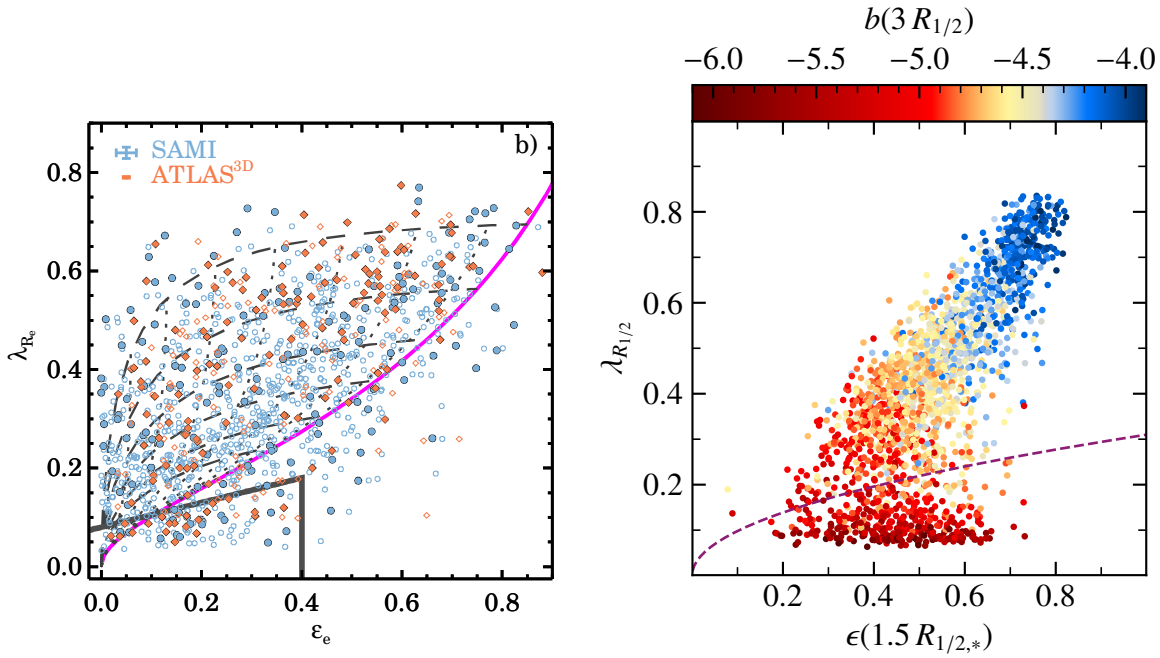

Figure 1.11: *Left*: Right panel of fig. 9 from van de Sande et al. (2017a): The λ_{R_e}-ϵ plane for galaxies in the SAMI and ATLAS^{3D} galaxy surveys. The filled symbols indicate aperture-corrected measurements, whereas the small open symbols correspond to data without aperture corrections. The dashed lines indicate where galaxies of different intrinsic ellipticities would be located, while the dotted lines correspond to different viewing inclinations, starting from edge-on (solid magenta line), for galaxies with an anisotropy of $\delta = 0.7 \cdot \epsilon$. The enclosed region by the solid gray line indicates the location of slow rotators according to the classification by Cappellari (2016). *Right*: The $\lambda_{R_{1/2}}$-ϵ plane for the edge-on sample of galaxies used in this work, colored by the b-value. The dashed line indicates the threshold between fast and slow rotators, lying above and below the line, respectively.

Figure 1.11 shows this plane for galaxies from the SAMI and ATLAS^{3D} surveys (left panel) and for the sample of galaxies considered in this work with the threshold line separating slow and fast rotators (right panel), where the values of λ_R and ϵ are computed from the particles within one and one-and-a-half half-mass radii, respectively, following Schulze et al. (2018). The parameters are computed from the edge-on perspective of the galaxies to ensure that rotation is maximally captured. Note the strong correlation of the morphology with the λ_R-parameter, where more disk-like objects generally are more rotationally supported. As discussed for the V/σ quantity, rotationally supported galaxies tend to be flatter, but there is also the interesting class of flat slow rotators, which are flattened by their larger anisotropies in the velocity distribution (e.g. Illingworth, 1977; Binney, 1978, 2005).

Clearly, the λ_R-parameter presents an important measure of the rotational support of galaxies that can easily be compared between simulations and observations. Its correlation with the b-value, with the projected shape of galaxies, and with the anisotropy make it a very effective property of galaxies which has already helped better understand the kinematics and formation histories of ETGs.

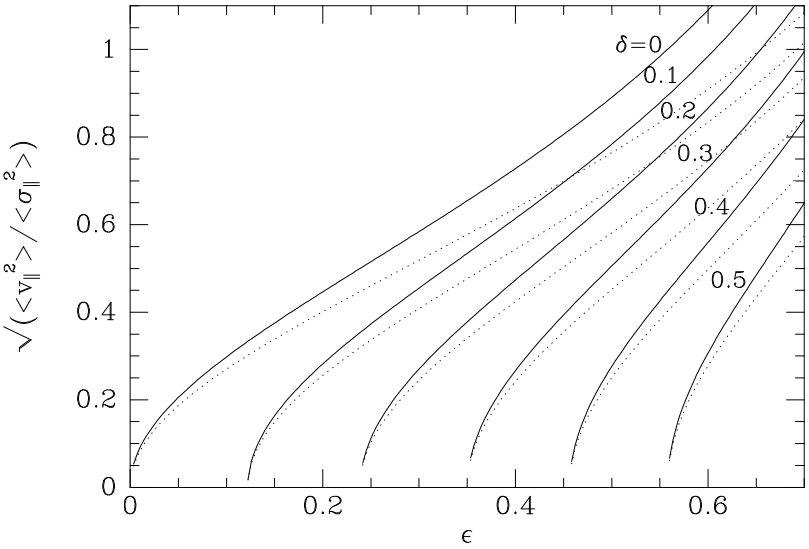

Figure 1.12: Fig. 2 from Binney (2005): Constant anisotropy parameter curves in the V/σ-ϵ plane. The solid lines correspond to the rotational behavior of a solid body, whereas the dotted lines indicate the constant anisotropy curves of galaxies with some shear of the stellar flow.

Anisotropy Parameter

In the theoretical study by Binney (2005), the tensor virial theorem was used to derive a relation between the rotation (V/σ), shape (ϵ), and velocity anisotropy of galaxies. Here, the quantity V/σ was used as the ratio of root mean squares of the line-of-sight velocity and velocity dispersion. It was shown that the anisotropy depends on the location of a galaxy in the V/σ-ϵ plane and introduced the global anisotropy parameter:

$$\delta = 1 - \frac{\Pi_{zz}}{\Pi_{xx}} = 1 - \frac{\sum_i M_i \sigma_{z,i}^2}{\sum_i M_i \sigma_{x,i}^2}, \tag{1.9}$$

where Π_{xx} and Π_{zz} are measures for the random motion in the x and z directions by the mass-weighted mean square velocity dispersion along the respective axis. The anisotropy parameter takes on values of $\delta = 0$–1. The curves of constant anisotropy in the V/σ-ϵ plane are shown in Figure 1.12.

Based on the tight relationship between V/σ and λ_R (Emsellem et al., 2011), Schulze et al. (2018) found that the anisotropy parameter is also accurately predicted by the position of a galaxy in the λ_R-ϵ plane. It also becomes apparent that the flattened slow rotators (galaxies with low values of λ_R, but high ellipticity in Figure 1.11) have large values of the global anisotropy parameter, confirming early attempts of determining the driver of the peculiar non-rotating flattened systems (Illingworth, 1977).

Radial λ_R-Profiles

Schulze et al. (2020) investigated the radial profiles of λ_R out to five half-mass radii for a subsample of the galaxies considered in this work. They computed the values of λ_R from the edge-on projection of the galaxies in a differential manner to avoid missing any

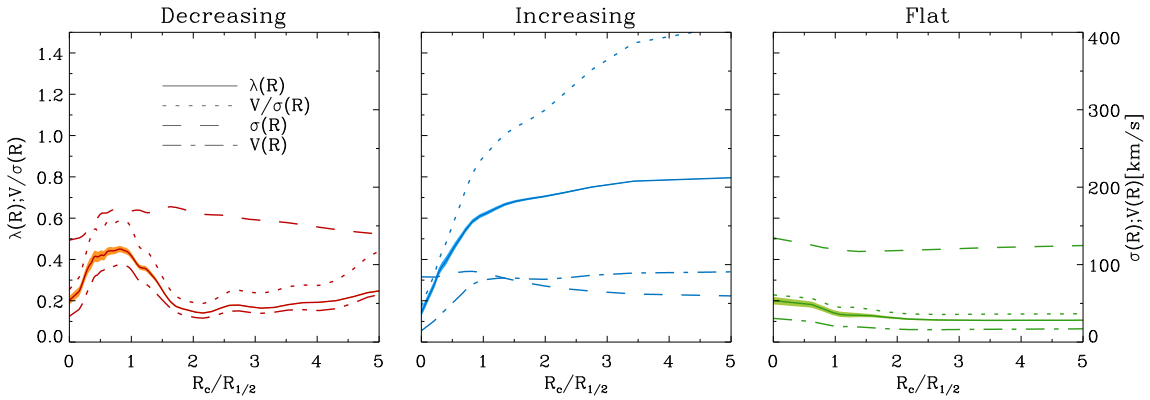

Figure 1.13: Fig. 5 from Schulze et al. (2020): Example λ_R-profiles of selected galaxies for each of the three profile types: decreasers, increasers, and flats. The plots include the profiles for the velocity, V, the velocity dispersion, σ, and the quantity V/σ. The three galaxies are from Box4 (uhr) of the Magneticum Pathfinder simulation suite (see Section 2.1 for further details).

kinematic transition features of the profiles. From the shapes of the profiles, they found three characteristic radial profile types:

(i) Increasing profile (increasers): The λ_R-profile increases linearly with radius and potentially plateaus at larger radii.

(ii) Decreasing profile (decreasers): The λ_R-profile has a central peak between 0.5 $R_{1/2,*}$ and 2 $R_{1/2,*}$, after which it decreases towards the outer regions.

(iii) Flat profile (flats): The λ_R-profile stays approximately constant within the full radial range up to 5 $R_{1/2,*}$.

An example profile for each of the three types can be seen in Figure 1.13. Almost half of the galaxies were classified as increasers, while decreasers and flats each make up almost 20% of the galaxies. As for the kinematic groups, some galaxies remain unclassified, often due to large fluctuations in the profiles because of ongoing mergers or tidal interaction. Both increasers and flats are comprised of slow and fast rotators, where they are found to equal parts among the increasers and where 70% of the flats are slow rotators. The increasers tend to have the largest b-values, i.e., they are the most disk-like, and while the flats cover a similar range of b-values, they overall have smaller b-values than the increasers. The decreasers were found to mostly be fast rotators, which is consistent with observations from the SLUGGS survey (Arnold et al., 2014) and the SAMI survey (Foster et al., 2018) of such galaxies having inner stellar rotation within a non-rotating halo.

For the formation histories of the different λ_R-profile types, Schulze et al. (2020) found that the largest difference between the classes was the fraction of mass accreted through major mergers. Only 13% of a decreaser's mass is accreted through major mergers, while the fraction is 22% and 32% for flats and increasers, respectively. Overall, the decreasers tend to accrete the least amount of mass through mergers and only around a third of them have experienced a major merger, most of which occurred more than 5 Gyr ago, such that the kinematics of decreasers is generally driven by minor and mini mergers. This finding can explain the low values of λ_R in the outskirts, where the accreted material leads to a large

velocity dispersion, whereas the central in-situ stellar component continues with an ordered disk-like rotation, as the centers are never disturbed by the small mergers (Karademir et al., 2019, for a study of how matter is deposited through mergers of different orbits and mass ratios). Thus, for decreasers, the transition radius from the rotationally supported central component to the outer dispersion dominated component marks the transition from the old in-situ to the ex-situ stars. Increasers accrete the largest amount of gas, where the difference to the other profile types is especially driven through major mergers. They propose that there is an evolution channel from increasers over flats to decreasers, which mainly depends on the stellar mass accreted and on the major mergers since $z = 2$.

Schulze et al. (2020) suggested that decreasers could evolve to flats, such that decreasers and flats may have similar merger histories, where flats are formed through a merger event that removes the rotational peak of λ_R. Interestingly, only a small fraction of decreasers are KDCs, which is likely a result of the kinematic groups having been determined only within one half-mass radius, suggesting a complex relation between the kinematics in the centers and halos of galaxies.

1.2.3 Angular Momentum

Unlike observations, simulations are not limited to a 2D projected view of galaxies. This allows for 3D analyses of the galaxies, such as the kinematics. Two such parameters have already been introduced in Section 1.2.2, which were necessary for defining the b-value (Equation 1.4): the angular momentum, $\boldsymbol{J}$, and the specific angular momentum, $\boldsymbol{j} = \boldsymbol{J}/M$, where the total angular momentum of a set of particles is known from classical mechanics and is defined by

$$\boldsymbol{J} = \sum_i m_i \boldsymbol{r}_i \times \boldsymbol{v}_i, \tag{1.10}$$

where the sum runs over all particles and m_i, $\boldsymbol{r}_i$, and $\boldsymbol{v}_i$ are the mass, position, and velocity of the ith particle, respectively. In comparison to V/σ and λ_R, these 3D vectors are not dependent on the line-of-sight, but are intrinsic properties of an object.

The statistics of angular momenta in simulations was first primarily studied in DM halos, since the first cosmological simulations only contained DM. Bullock et al. (2001) discovered a universal angular momentum profile for DM halos, where the mass having at most a certain specific angular momentum can be described by a two-parameter function, given by

$$M(< j) = M_{\text{halo}} \frac{\mu j}{j_0 + j}, \tag{1.11}$$

where μ and j_0 are the two free parameters. With the introduction of increasingly accurate hydrodynamic simulations, the three-dimensional nature of the angular momentum was exploited to compare the rotation of the stellar, gas, and DM components (e.g. van den Bosch et al., 2002; Sharma & Steinmetz, 2005; Sharma et al., 2012; Teklu et al., 2015). It was found that the angular momenta of baryonic matter and DM have median misalignments of between 20° and 50°. For the Magneticum simulation used in this work, Teklu et al. (2015)

determined that the stellar and gas angular momenta are well aligned in disk galaxies, but approximately randomly oriented in elliptical galaxies, where the misalignment gets worse over time. At low redshifts, the alignment of the angular momenta between the stellar and DM components is better than that between the stars and the gas. They also investigated the alignment of the angular momentum in the central regions of a galaxy with that in the halo and found a median misalignment of 47°, consistent with the findings of Hahn et al. (2010). The misalignment is less for disk galaxies, however. In the context of galaxy formation and evolution, note that angular momentum can only be changed by infalling or escaping matter, which for example can be caused by mergers, fly-bys, or feedback. Also, gas can redistribute its angular momentum, as discussed in Section 1.1.2, which is not possible for the solely gravitationally interacting DM.

Global Spin Parameter λ

Based on his work in 1969 (Peebles, 1969), Peebles (1971) introduced a dimensionless *spin parameter*, λ, to express the residual angular momentum, $\boldsymbol{J}$, of a proto-galaxy:

$$\lambda = \frac{J|E|^{1/2}}{GM^{5/2}}, \tag{1.12}$$

where E is the total energy of the galaxy and M its total mass. Mo et al. (1998) adopted this parameter in their study of the formation of galactic disks and Bullock et al. (2001) defined a modified component-wise spin parameter to measure the spin of the stellar, gas, and DM separately. This was later expressed in terms of the specific angular momentum by van den Bosch et al. (2002), which additionally is directly obtainable from the particle data in simulations:

$$\lambda_k(R) = \frac{j_k}{\sqrt{2}RV_{\rm circ}}, \tag{1.13}$$

where k denotes the component (i.e., stars, gas, or DM), and $V_{\rm circ}$ is the Keplerian circular velocity at the radial distance, R, defined by Equation 1.6. In this work, the spin parameter will be referred to as "spin parameter" or "global spin parameter", since here it is used as a measure of the spin within the virial radius. The λ_R-parameter (which is sometimes referred to as the *spin* of a galaxy in other literature), will always be referred to as "λ_R" or the "λ_R-parameter".

The distribution of the global spin parameter is well fitted by a log-normal distribution (van den Bosch et al., 2002), where the gas component has the largest values, followed by the DM and finally, with the smallest values of λ, the stars (Danovich et al., 2015; Teklu et al., 2015). The large gas spin is a result of the gas component continuously transporting angular momentum from the outer parts to the inner parts through cooling, leading to an increasing spin of the gas. This effect is not possible for stars and DM, which approximately retain their angular momenta. The stellar spin is the smallest because of its concentration in the central regions, whereas the DM spin is concentrated in the outer halo region.

The global spin parameter at the virial radius of the galaxies enables a robust comparison between the total large-scale spin properties of different galaxies and their components. For instance, Teklu et al. (2015) found that the spins of disk galaxies tend to be slightly larger than the those of elliptical galaxies and suggested that the formation history of the DM halo is an important factor for the morphology of galaxies by cross-matching halos between a DM-only and an equivalent full hydrodynamical simulation. The angular momentum and spin of a galaxy therefore represent important properties of galaxies and give indications of their formation history.

1.2.4 Shapes

The first morphological classification schemes all were based on the 2D projections of galaxies. While the apparent ellipticity of ETGs was found to mostly just be correlated with the inclination and is not an intrinsic property of galaxies (since it depends on the line of sight), a three-dimensional characterization of galaxy shapes offers a physical description and is independent of an observer. As one of the most fundamental properties, the spatial distribution of matter is a key component for modeling galaxies and their dynamics; a good understanding of the 3D shapes of galaxies is therefore necessary. Models based on the Schwarzschild orbit-superposition method (Schwarzschild, 1979, 1982) require assumptions to be made about the shape of a galaxy, where axisymmetric spheroids (e.g. Krajnović et al., 2005, for a galaxy from the SAURON survey) or the more general triaxial ellipsoids (e.g. Zhu et al., 2018, for spiral galaxies from the CALIFA survey) have been used, which are then fitted to the observations of the projected galaxy.

Ellipsoids

In contrast to observations, simulations of galaxies have the 3D positional data of the particles readily available. While the well-known density profiles are based on spherically symmetric descriptions of the particle distributions, such as the Hernquist profile (Hernquist, 1990) or the NFW-profile (Navarro et al., 1997), the shapes have generally been described by ellipsoids (e.g. Gerhard, 1983; Katz, 1991; Springel et al., 2004; Allgood et al., 2006; Bett, 2012; Pulsoni et al., 2021). These are typically used to approximate the iso-density surfaces of the particle distribution. The surface of an ellipsoid that has its three axes aligned with the coordinate axes is defined by

$$\frac{x^2}{a^2} + \frac{y^2}{b^2} + \frac{z^2}{c^2} = 1, \tag{1.14}$$

where a, b, and c are the semi-axis lengths of the ellipsoid. Ellipsoids with two axes of the same length are called *spheroids*, where the spheroid is *oblate* if the two longer axes have the same length and *prolate* if the two shorter axes have the same length. An ellipsoid with three axes of different lengths is called *triaxial* and an ellipsoid becomes a sphere when $a = b = c$.

Axis Ratios

When comparing the shapes between different galaxies, for example with respect to being flat or prolate, the absolute values of the axis lengths are not of interest, but their ratios. Assuming $a > b > c$ without loss of generality, the axis ratios are defined as

$$q = b/a, \tag{1.15}$$

$$s = c/a, \tag{1.16}$$

$$p = c/b, \tag{1.17}$$

where in this work, q is referred to as the *major axis ratio* and s as the *minor axis ratio*. The axis ratio p is not used as commonly in the literature. Note, however, that some authors define $p = b/a$ and $q = c/a$ instead (e.g. Pulsoni et al., 2020, 2021). The minor axis ratio is also known as the *sphericity* (e.g. Bett, 2012), since a value of $s \sim 1$ means that the ellipsoid is approximately a sphere. It also describes how flat an object is, as lower values of s indicate flatter objects. From the definitions of oblate and prolate ellipsoids, it follows that $q = 1$ indicates an oblate shape and $q = s$ indicates a prolate shape.

Triaxiality

To quantify whether an ellipsoid is closest to being oblate, prolate, or triaxial, the *triaxiality* parameter is used (Franx et al., 1991), which is defined as

$$T = \frac{a^2 - b^2}{a^2 - c^2} = \frac{1 - q^2}{1 - s^2}. \tag{1.18}$$

Ellipsoids with $T = 0$ are perfectly oblate, while $T = 1$ indicates a perfectly prolate shape. While different definitions are used for the exact intervals, a commonly used classification of shapes using the triaxiality is the following, which is also used in this work:

(i) oblate: $0 \leq T < 1/3$

(ii) triaxial: $1/3 \leq T < 2/3$

(iii) prolate: $2/3 \leq T \leq 1$

A visualization of the values of the triaxiality depending on the axis ratios is shown in Figure 1.14, together with the regions of the oblate, triaxial, and prolate shapes in the q-s plane.

This Thesis

In this thesis, the galaxy shapes, their properties, and their relations with other galaxy properties are investigated to provide insights for numerous fields. This is the case for the dynamical modeling of galaxies, which requires assumptions with respect to a galaxy's shape. It is also relevant to the information that observers can extract from combining morphological and other properties, and to the connection between formation histories and the resulting galaxies' shapes.

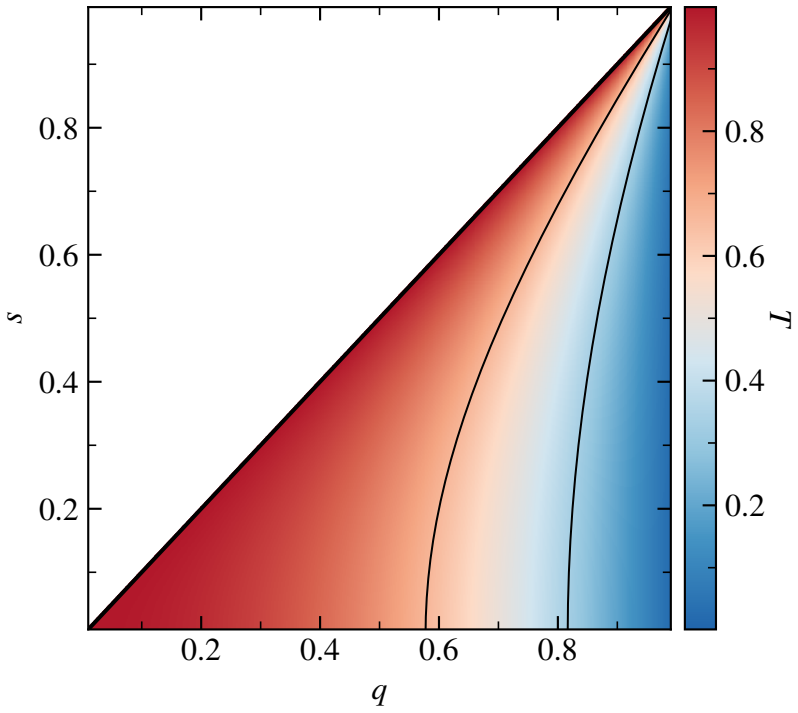

Figure 1.14: Visualization of the triaxiality, T, in the plane spanned by the major and minor axis ratios, q and s. The solid lines indicate the borders between prolate, triaxial, and oblate shapes, from left to right, respectively. The two dividing curves are given by $T = 1/3$ and $T = 2/3$.

In Chapter 2, the cosmological simulation and the galaxy sample used in this work are presented. Chapter 3 presents the methodology used in this work, with a special focus on the theoretical background of shapes and the analysis of the different shape determination methods, which were performed as a part of this work. The shapes of the galaxies in the sample, their statistics, and the differences between stellar and DM shapes are presented in Chapter 4. The following chapters show the results of the relations between shapes and other galaxy properties: global properties (Chapter 5), kinematic classifications and the overall radial shape and alignment profiles (Chapter 6), large scale properties (Chapter 7), and symmetry properties (Chapter 8). Finally, the results of this work are summarized and concluded in Chapter 9.

2 Simulation

Because of the non-linear growth of structure and the complex behavior of baryonic matter with gas, stars, and feedback, cosmological hydrodynamical simulations present a wonderful site for studying galaxy formation self-consistently. However, the need for large volumes, which are necessary for statistically relevant studies and for obtaining larger galaxy clusters, and for high resolution makes the simulations computationally expensive. By now there are five big suites of fully cosmological hydrodynamical simulations: Magneticum Pathfinder[1] (Dolag et al., in preparation), from which the cosmological box used in this work is taken, Illustris (Vogelsberger et al., 2014), IllustrisTNG (e.g. Pillepich et al., 2018), EAGLE (Schaye et al., 2015), and HorizonAGN (Dubois et al., 2014).

2.1 Magneticum Pathfinder Simulations

The galaxies studied in this work are extracted from the *Magneticum Pathfinder* project, a suite of cosmological hydrodynamical simulations of different volumes (see the website for more information on the available boxes: `www.magneticum.org`), performed with the Tree/SPH code `GADGET-3`, which is an extended version of `GADGET-2` (Springel et al., 2001b; Springel, 2005). The improvements include the treatment of viscosity and the used kernels (Dolag et al., 2005; Beck et al., 2016). The implemented baryonic physics include gas cooling (Wiersma et al., 2009), star formation based on the subresolution model by Springel & Hernquist (2003), black hole growth and feedback from active galactic nuclei (AGNs) (Springel et al., 2005a; Di Matteo et al., 2005; Fabjan et al., 2010; Hirschmann et al., 2014; Steinborn et al., 2015), and stellar evolution and metal enrichment (Tornatore et al., 2007).

The simulations adopt a standard ΛCDM cosmology with parameters according to the seven year results of WMAP (Komatsu et al., 2011), which are shown with their values in Table 2.1. For this work, the galaxies were selected from the medium-sized cosmological Box4, which has a side length of 48 Mpc h^{-1}, at ultra high resolution (uhr). The DM particle mass is $m_{\mathrm{DM}} = 3.6 \times 10^7\,\mathrm{M}_\odot\,h^{-1}$ and the initial gas particle mass is $m_{\mathrm{gas}} = 7.3 \times 10^6\,\mathrm{M}_\odot\,h^{-1}$, with softening lengths of $\epsilon_{\mathrm{soft,DM/gas}} = 1.4\,\mathrm{kpc}\,h^{-1}$ for DM and gas particles and $\epsilon_{\mathrm{soft},*} = 0.7\,\mathrm{kpc}\,h^{-1}$ for stellar particles, which correspond to around $\epsilon_{\mathrm{soft,DM/gas}} \approx 2\,\mathrm{kpc}$ and $\epsilon_{\mathrm{soft},*} \approx 1\,\mathrm{kpc}$. Gas particles lose mass by forming up to four stellar particles in their lifetime, where the stellar particles also vary in mass through stellar winds and have an average mass of around $m_* = 1.4 \times 10^6\,\mathrm{M}_\odot\,h^{-1}$. Initially, there are 576^3 DM particles and 576^3 gas particles.

[1] `www.magneticum.org`

Table 2.1: ΛCDM cosmological parameters used in the Magneticum Pathfinder simulations.

Hubble parameter	h	0.704
dark energy density parameter	Ω_Λ	0.728
matter density parameter	Ω_M	0.272
baryonic density parameter	Ω_b	0.0451
normalization of the fluctuation amplitude at 8 Mpc	σ_8	0.809

This simulation has a size that is large enough to ensure a sufficient galaxy sample while providing the resolution necessary to adequately analyze the kinematic and morphological properties of the galaxies.

Galaxies in a given snapshot are identified with the subhalo finder `SUBFIND` (Springel et al., 2001a), modified to treat baryonic matter in addition to the DM component (Dolag et al., 2009). The algorithm uses the friends-of-friends (FOF) method (Davis et al., 1985) to identify the parent halos (which are not substructures of other galaxies). The parent halos found through the FOF method have overdensities that are characteristic for virialized objects predicted by the spherical collapse model (Eke et al., 1996). For this reason, the virial radius of a parent halo can be determined by the density contrast based on the top-hat model. In a second step, a global density threshold is lowered step by step to find locally overdense regions. In each of these overdense regions the gravitationally bound particles are kept, which finally constitute the substructures, called *subhalos*. In this work, the majority of galaxy properties are determined from the particles assigned to a given subhalo, i.e., main galaxies without their identified substructures, and satellite galaxies. Figure 2.1 shows an example main galaxy including the substructure (left pane) and without the substructure (right pane). `SUBFIND` often does not identify the full substructure, such that their outer regions remain in the main halo when removing the identified substructures. This can be seen in the right pane, where denser regions hint at the existence of substructures. Other features in the outskirts of galaxies include shells, streams, and other tidal stripping remnants, which would often still be considered part of the satellite galaxies in observations. For this reason, the galaxies obtained from `SUBFIND` should be treated with caution at larger radii.

2.2 Galaxy Sample

The galaxy sample studied in this work consists of galaxies in the latest snapshot of Magneticum Pathfinder Box4 (uhr) at $z \approx 0.066$ that fulfill the following criteria:

(i) To ensure a sufficient number of stellar particles for a kinematic and morphological analysis, only galaxies with stellar masses of $M_* \geq 10^{10}\,\mathrm{M}_\odot$ are considered, which corresponds to approximately 5000 stellar particles.

(ii) Some satellite galaxies are identified by `SUBFIND` with very few DM particles. To exclude these galaxies, a mass cut for the DM mass is also applied: $M_{\mathrm{DM}} \geq 10^{10}\,\mathrm{M}_\odot$. This corresponds to approximately 200 DM particles, which is still a very low number

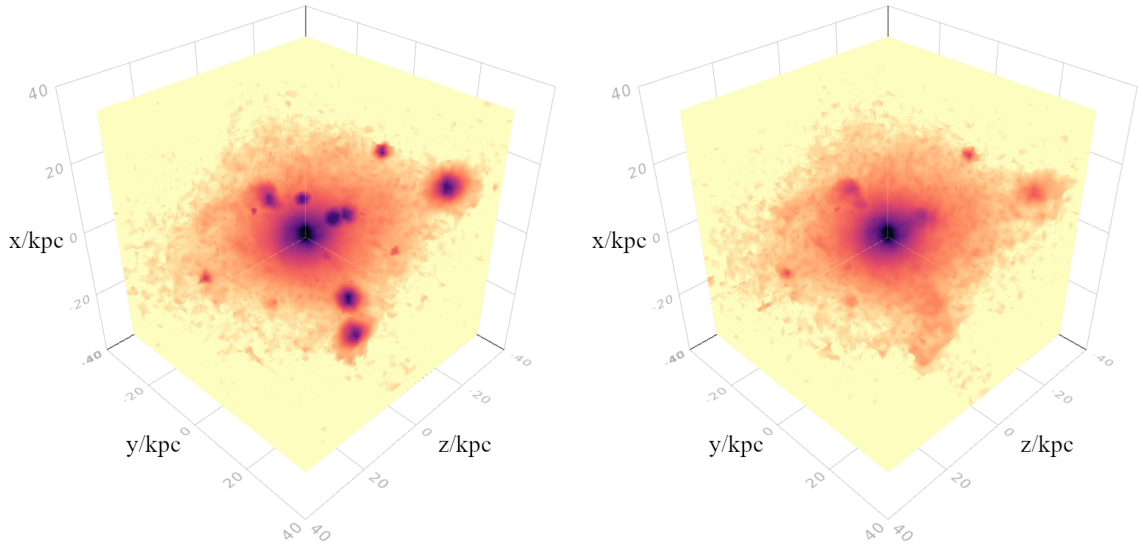

Figure 2.1: Example main galaxy from Magneticum Pathfinder Box4 (uhr) at $z = 0$ shown with all the substructure (left) and without (right). The excluded satellites in the right pane are the ones identified by `SUBFIND`.

of particles, but this threshold was found to be sufficient to filter out the problematic galaxies.

(iii) To prevent the central regions of the galaxies from being insufficiently resolved, the stellar half-mass radius is required to satisfy $R_{1/2,*} \geq 2\,\mathrm{kpc}$, which corresponds to the DM and gas softening length, or to twice the stellar softening length. This follows the approach taken by Schulze et al. (2018) and Schulze et al. (2020) for the same cosmological simulation.

The resulting galaxy sample consists of a total of 1995 galaxies, of which 1260 are main galaxies and 735 are satellites.

Some of the galaxy properties studied in this work are only available for a subset of the full galaxy sample:

(i) The mean stellar ages within one stellar half-mass radius (Section 5.4) and the radial λ_R-profile groups (Section 6.2) were obtained from Felix Schulze (Schulze et al., 2020) for the galaxies with stellar masses of $M_* \geq 3 \times 10^{10}\,\mathrm{M}_\odot$, which is the case for 743 of the galaxies (469 main galaxies and 274 satellites).

(ii) The in-situ fractions within $1\,R_{1/2,*}$ (Section 5.4) were obtained by Felix Schulze (Schulze et al., in preparation) based on the work of Remus & Forbes (2021) for 510 main galaxies; this only consists of the galaxies for which the stellar particles could be properly tracked back through time.

(iii) The global spin parameters (Section 7.1) and the local density (Section 7.2) were only computed for the 1260 main galaxies, consistent with the choice of galaxies by Teklu et al. (2015) for the same cosmological simulation as used in this work.

(iv) Finally, an additional requirement for a galaxy's gas mass was applied for the spin parameters of the gas component to ensure a sufficient number of gas particles: $M_\mathrm{gas} \geq 10^{10}\,\mathrm{M}_\odot$. This is the case for 968 of the 1260 main galaxies.

3 Methodology

For the computation and analysis of galaxy shapes and their relations to other properties, it is important to have a robust understanding of their theoretical background and methodology. In this chapter, the necessary steps of preprocessing the particles of a given galaxy and the theoretical foundation for galaxy shapes are first presented, after which a number of shape determination methods are introduced and thoroughly tested, with the objective of finding the best method to be used in the following chapters. This analysis of the methodology was performed as part of this work.

3.1 Center of Particles

When determining any property of a galaxy at some radial distance, it is vital to have a meaningful point at the origin. As the most basic example, the origin in the case of a sphere should be its center since radial properties are the most meaningful for spherical symmetry. Also, the shape determination methods discussed in Section 3.3 require a predefined origin around which an ellipsoid is determined to describe the particle distribution. For the DM component, the position outputted for the given subhalo by `SUBFIND` can be used, which indicates the position of the most-bound DM particle. This is reasonable because the DM distribution dominates a galaxy's potential. However, the stellar and gas components can be shifted with respect to the subhalo's position, indicating the need for a method of finding the actual "center" of a given set of particles.

To determine such a center, a modified version of the iterative shrinking sphere method described by Power et al. (2003) is used in this work: the radius of a sphere is repeatedly shrunk by 2.5% until the number of particles within the sphere reaches 1000 particles or 1% of the particles within the initial sphere, whichever is smaller. At each step, the center of the new sphere is placed at the barycenter of the particles within the previous sphere. The barycenter of the particles within the final sphere is the wanted center of particles. Note that none of the galaxies dealt with in this work have so few stellar particles that the particle number within the sphere becomes unreasonably low. The method is only applied to the stellar component for all the shape and global properties (Chapters 4 to 6 and 8), but not for the large scale properties (Chapter 7), to be consistent with the approach taken by Teklu et al. (2015). The shrinking sphere method is found to be stable even for different initial parameters, under the condition that the initial sphere is large enough (Power et al., 2003). In general, the method finds the densest region within the most massive subcomponent (if

multiple components exist). For this reason, this method is only applied to the subhalo's particles according to SUBFIND to prevent the method from finding the center of a more massive structure nearby.

For this work, the procedure is modified by adding a further criterion for the shrinking to stop, which is when the radius of the shrinking sphere reaches half of a preliminarily computed half-mass radius of the stellar particles. The stellar half-mass radius is estimated using the subhalo's center obtained from SUBFIND and is determined from all stellar particles within 10% of the virial radius or in the entire subhalo for satellite galaxies. Since one application of the computed center is to determine radial properties out until a few half-mass radii, the center point should not be too dependent on the very inner particle distribution, but should approximate the center on the order of the half-mass radius. For this, an inner limit of half of the half-mass radius is found to be a good and stable approximation of the center point. To ensure that the center of the stellar component lies within the initial sphere, the initial radius is set to three preliminary stellar half-mass radii. Only in a second step, after having found the center of particles, is the final stellar half-mass radius calculated from the obtained center point.

3.2 Center of Velocity

Just like for the central position of a galaxy, the velocity of the stellar component can differ from the velocity given by SUBFIND for the subhalo. Because of this, it is necessary to find a method for obtaining the center of velocity of a galaxy. A reasonable approach would be to simply use the mass-weighted mean velocity of the stellar particles within a certain radius of the center of the galaxy. To avoid individual particles or particles in substructures (those not identified by SUBFIND) with especially high velocities from influencing the mean velocity too strongly, the particles with the largest absolute velocities are excluded from the computation of the mass-weighted mean velocity. These absolute velocities are determined relative to the median velocity of the stellar particles. In this work, the particles within $4\,R_{1/2,*}$ are considered for the center of velocity, and the particles with the 10% highest absolute velocities are excluded for the mass-weighted mean velocity. As for the center of particles, this is only applied to the stellar component, where the velocities are shifted according to the center of velocity.

For the global spin parameters (Section 7.1), the approach for finding the center of velocity used by Teklu et al. (2015) is applied. In this approach, the center of velocity is computed as the mass-weighted mean velocity of all DM, gas, and stellar particles within $0.1\,R_{\rm vir}$ of the subhalo's position given by SUBFIND.

3.3 Shape Determination

To better understand the mathematical and physical meaning of the shape parameters analyzed in this work, a fundamental understanding of their origin and determination methods is necessary. The tests of the different methods of determining shapes were performed as a part of this work. In general, the shape ellipsoid is determined from the eigenvectors and eigenvalues of a tensor describing the mass distribution, for which a variety of different methods have been used in the literature.

3.3.1 Theoretical Background

Shape Tensor

For the introduction of the shape tensor, we follow the derivation by Zemp et al. (2011). In classical mechanics, the moment of inertia tensor, $\mathbf{I}$, describes the linear relation between the angular momentum, $\boldsymbol{L}$, and the angular velocity, $\boldsymbol{\omega}$:

$$\boldsymbol{L} = \mathbf{I}\boldsymbol{\omega}. \tag{3.1}$$

The elements of the moment of inertia tensor are given by

$$I_{ij} = \int_V d^3\boldsymbol{r}\, \rho(\boldsymbol{r})\left(r^2\delta_{ij} - r_i r_j\right), \tag{3.2}$$

where $i, j \in \{x, y, z\}$, ρ is the mass density at a given point, δ is the Kronecker delta, and the integral is over the volume of the body with the position vector, $\boldsymbol{r}$, based at the body's center. Note that in our notation r_i is the i-component of the vector $\boldsymbol{r}$ and $r = |\boldsymbol{r}|$. We can identify the subtrahend term with the second moment of the mass distribution, $\mathbf{M}$:

$$M_{ij} = \int_V d^3\boldsymbol{r}\, \rho(\boldsymbol{r}) r_i r_j, \tag{3.3}$$

with which Equation 3.2 can be expressed by

$$I_{ij} = \sum_i M_{ii}\delta_{ij} - M_{ij} = \mathrm{tr}(\mathbf{M})\delta_{ij} - M_{ij}. \tag{3.4}$$

The tensor $\mathbf{M}$ is therefore the part of the moment of inertia tensor that describes the actual matter distribution. Finally, Zemp et al. (2011) introduce the shape tensor as

$$\mathbf{S} = \frac{\mathbf{M}}{M_{\mathrm{tot}}}, \tag{3.5}$$

where M_{tot} is the total mass within the considered volume.

From the Shape Tensor to the Ellipsoid

The tensors $\mathbf{M}$ and $\mathbf{S}$ trivially have the same eigenvectors. Plugging Equation 3.4 into the eigenequation of $\mathbf{I}$ with an eigenvector, $\boldsymbol{v}$, and its eigenvalue, λ, gives us:

$$\begin{aligned} & \mathbf{I}\boldsymbol{v} = \lambda\boldsymbol{v} \\ \Rightarrow \quad & \mathrm{tr}(\mathbf{M})\boldsymbol{v} - \mathbf{M}\boldsymbol{v} = \lambda\boldsymbol{v} \\ \Rightarrow \quad & \mathbf{M}\boldsymbol{v} = \big(\mathrm{tr}(\mathbf{M}) - \lambda\big)\boldsymbol{v}. \end{aligned} \tag{3.6}$$

The eigenvectors of $\mathbf{M}$ and $\mathbf{S}$ are therefore also the same as those of $\mathbf{I}$, i.e., they point along the principal axes, and the eigenvalues of $\mathbf{M}$ are given by $\mathrm{tr}(\mathbf{M}) - \lambda$ for any eigenvalue λ of $\mathbf{I}$, which are the principal moments of inertia. The eigenvalues of $\mathbf{S}$ are proportional to those of $\mathbf{M}$, being smaller by a factor of M_{tot}.

To understand the mathematical meaning of the eigenvectors and eigenvalues of the tensors $\mathbf{M}$ and $\mathbf{S}$, we consider the covariance matrix of a vector of three random variables, X_i, with $i \in \{1, 2, 3\}$:

$$\mathrm{cov}(X_i, X_j) = \Big\langle \big(X_i - \langle X_i \rangle\big)\big(X_j - \langle X_j \rangle\big) \Big\rangle, \tag{3.7}$$

with $i, j \in \{1, 2, 3\}$ and where $\langle\cdot\rangle$ is the expected value of the respective argument. According to the law of the unconscious statistician (LOTUS), the expected value of a function $g(X)$ is given by

$$\langle g(X) \rangle = \int_{-\infty}^{\infty} dx\, f(x) g(x), \tag{3.8}$$

where the random variable, X, has the probability density function $f(x)$. Using this and comparing the covariance defined in Equation 3.7 with $\mathbf{M}$ given in Equation 3.3, it is found that $\rho(\boldsymbol{r})$ can be identified with $f(x)$ and r_i with $(X_i - \langle X_i \rangle)$ (analogously for the index j). This shows that the second moment of the mass distribution, $\mathbf{M}$, is the three-dimensional covariance matrix of the mass distribution, as long as the center of mass is at the origin of the coordinate system. The same is true for $\mathbf{S}$ by instead identifying $\rho(\boldsymbol{r})/M_{\mathrm{tot}}$ with $f(x)$, for which we obtain the covariance matrix of a normalized mass distribution.

By identifying $\mathbf{S}$ with a covariance matrix, it follows that its eigenvalues are the variances of the normalized mass distribution along the axes of the corresponding eigenvectors, i.e., along the principal axes. This means that the standard deviation along the principal axes is given by the square root of the respective eigenvalues. The ratios between these standard deviations are finally used as the axis ratios of the ellipsoid used to describe the shape of a galaxy's particle distribution. Given the three eigenvalues $\lambda_1 > \lambda_2 > \lambda_3$, we obtain the axis ratios $q = \sqrt{\lambda_2/\lambda_1}$, $s = \sqrt{\lambda_3/\lambda_1}$, and $p = \sqrt{\lambda_3/\lambda_2}$, with $q > s$.

3.3.2 Discretization

While the most general approach was taken in the previous section by assuming a continuous mass distribution, the output of simulations only contains discrete particle information. Even if it would theoretically be possible to treat these particles as individual spherically symmetric mass distributions, testing this would be cumbersome and computationally expensive while hardly differing from treating them as point particles, as long as there is a sufficient number of particles analyzed.

For N point particles, the density is described by

$$\rho(\boldsymbol{r}) = \sum_{k=1}^{N} m_k \delta(\boldsymbol{r} - \boldsymbol{r}_k), \tag{3.9}$$

where m_k is the mass and $\boldsymbol{r}_k$ the position of particle k, and δ is the Dirac delta function. Plugging this into Equation 3.3 and Equation 3.5, we obtain, again following Zemp et al. (2011):

$$S_{ij} = \frac{\sum_k m_k \boldsymbol{r}_{k,i} \boldsymbol{r}_{k,j}}{\sum_k m_k}, \tag{3.10}$$

where the sum notation over all particles is abbreviated and $\boldsymbol{r}_{k,i}$ is the i-component of the position of particle k.

3.3.3 Practical Issues

Choice of Origin

Despite having a clear understanding of the meaning of the ellipsoid found through the eigendecomposition of the shape tensor, there are a number of issues with this method in practice, depending on the objectives. The first issue is related to Section 3.1, in which the need of determining a center of particles was discussed: galaxies generally have a core, both in the DM and stellar components (even if not always located at the same place), that has a higher density than found in the rest of the galaxy. Especially when determining the radial profiles of the shapes, it is sensible to place the origin at the center of such a core, whereas the center of mass is much more impacted by asymmetries in the galaxy and by the exact particles used to compute it, additionally making it less stable than the shrinking sphere method.

Substructure

Another issue is that many galaxies have satellites that one would intuitively ignore when approximating the shape manually. Such structures will dominate the summation for the shape tensor and thus bias the determined ellipsoids. While `SUBFIND` identifies the larger substructures as subhalos, it oftentimes only cuts out their central part, assigning the outer region of the satellites to the parent halo, and entirely misses the smaller substructures. Of course, the strong non-ellipsoidal nature of extreme cases puts the meaningfulness of an ellipsoid that was determined for them into question, showing how any shape determination

method with ellipsoids will necessarily have its limits. However, it is still reasonable to only compute the shapes from the particles assigned to the particular halo by the halo finder. Some of the variations of the shape tensor discussed in the following chapter try to address some of the issues introduced by substructure.

3.3.4 Methods

In the literature a variety of shape determination methods are used with different versions of the shape tensor. For this, the shape tensor can be generalized following Zemp et al. (2011) by including a weight function $w(\boldsymbol{r})$ and replacing the particle mass, m_k, with a generalized mass weight, $\tilde{m}_k$:

$$S_{ij} = \frac{\sum_k \tilde{m}_k w(\boldsymbol{r}_k) \boldsymbol{r}_{k,i} \boldsymbol{r}_{k,j}}{\sum_k \tilde{m}_k}. \tag{3.11}$$

Mass Weight

To recover Equation 3.10, one simply uses $w(\boldsymbol{r}) = 1$ and $\tilde{m}_k = m_k$. In particular for DM-only simulations one has used $\tilde{m}_k = 1$ because all particles have the same mass (e.g. Allgood et al., 2006). Since the simulation analyzed in this work includes baryonic matter and forms star particles with different masses, we decided against using this approach, especially because a single additional multiplication per particle is negligible with respect to computational time. A third approach to the mass weight was employed by Warnick et al. (2008) with $\tilde{m}_k = 1/\rho_k$, where ρ_k is the local density of particle k. This prevents particles in denser regions from dominating the summation, which is especially a problem in the presence of substructures as discussed in the previous section. As a non-standard approach to the shape tensor, their method is not further considered in this work.

Iteration

Since the objective is to determine the shapes of extended objects at different radii, the most basic approach would be to compute the shape tensor from all the particles within the given radius to obtain the axis ratios of the ellipsoid. However, this in fact only determines the standard deviation ratios along the principal axes for the particle distribution within a sphere, which will always be biased towards spherical shapes, most noticeable for very elongated galaxies. A way to circumvent this issue is by iteratively selecting only the particles within the previously determined ellipsoid for the following computation of the shape tensor until the axis ratios converge. In this way, the sphere is continuously deformed, such that the spherical bias is reduced in each iteration step until convergence is reached. There are two commonly used sizes of the bounding ellipsoid: either its major axis length is held constant or its volume. These are kept at the initial sphere's radius or volume, respectively. In the former case, the volume of the final ellipsoid will be smaller than that of the initial sphere, and in the latter case, the largest axis length will be larger than the initial radius.

Shells

An alternative to considering all particles within an enclosed ellipsoid is to only compute the shape tensor from the particles within a homoeoid (an ellipsoidal shell) to obtain the local shape at a given distance. In the non-iterative case, the shape tensor is only determined from the particles in a spherical shell, while it is deformed into a non-spherical homoeoid in the iterative case. While Zemp et al. (2011) recommended using the homoeoid approach for the most accurate description of the local shape in well resolved halos, they advised only using this approach if at least a few thousand particles per radial bin can be ensured. The galaxies analyzed in this work ($M_* \geq 10^{10}\,\mathrm{M}_\odot$) have stellar particle numbers ranging from under 6000 to 1.7×10^6 and can have far fewer DM particles, whereas Zemp et al. (2011) set up their halos with 10^7 to 10^8 particles and analyzed galaxies in a hydrodynamical simulation with more than 10^6 particles. To treat the galaxies in a consistent way across different galaxy sizes, the homoeoid method is not used in this work.

Weight Function

The weight function $w(\boldsymbol{r})$ is found to be either 1, r^{-2}, or r_{ell}^{-2} in the literature, where $r = |\boldsymbol{r}|$ is the Euclidean distance of the respective particle from the origin, and r_{ell} is the ellipsoidal distance, defined as

$$r_{\mathrm{ell}} = \sqrt{x_{\mathrm{ell}}^2 + \frac{y_{\mathrm{ell}}^2}{q^2} + \frac{z_{\mathrm{ell}}^2}{s^2}}, \tag{3.12}$$

where x_{ell}, y_{ell}, and z_{ell} are the particle coordinates in the eigenvector coordinate system of the shape tensor and q and s are the ellipsoid axis ratios defined in Section 3.3.1. The coordinates are along the major, middle, and minor axis of the ellipsoid, respectively. These versions of the shape tensor are oftentimes called *unweighted* for $w(\boldsymbol{r}) = 1$ and *reduced* for $w(\boldsymbol{r}) = r_{(\mathrm{ell})}^{-2}$ (e.g. Allgood et al., 2006; Pereira et al., 2008). In this work, we will differentiate between the *reduced* (r^{-2}) and *reduced ellipsoidal* method (r_{ell}^{-2}). Note that the reduced ellipsoidal method can only be used iteratively because of the dependence on the axis ratios. For the initial sphere in the first step, the axis ratios are therefore set to 1 and are subsequently altered until convergence is reached.

The reduced and reduced ellipsoidal weightings were introduced to prevent substructures in the outer regions from dominating the shape, which is caused by the unweighted shape tensor being proportional to r^2 (Equation 3.10). This, however, comes at a cost, as is shown in Section 3.3.5.

Naming Conventions

Note that both the second moment of the mass distribution defined in Equation 3.3 as well as the shape tensor in Equation 3.5 and Equation 3.10 are often incorrectly referred to as the "moment of inertia tensor" or just "inertia tensor", as pointed out by Zemp et al. (2011).

Table 3.1: Shape tensor methods tested. All methods use the normal mass weight of $\tilde{m}_k = m_k$ and consider all particles within an enclosed ellipsoid (instead of a homoeoid). The terms in parentheses indicate the respective quantity held constant in the iterative procedures.

	not iterative	iterative (major axis)	iterative (volume)
unweighted	✓	✓	✓
reduced	✓	✓	✓
reduced ellipsoidal		✓	✓

Unfortunately, this has remained largely unchanged even in the more recent literature (e.g. Emami et al., 2021; Pulsoni et al., 2021).

3.3.5 Testing the Shape Methods

Implementation

In the following, eight different methods for determining shapes of some example galaxies from the Magneticum Pathfinder Box4 (uhr) simulation are tested (Table 3.1). The tensor computations are implemented as

$$M_{ij} = \sum_k m_k w(\boldsymbol{r}_k) \boldsymbol{r}_{k,i} \boldsymbol{r}_{k,j}, \tag{3.13}$$

since the second moment of the mass distribution, $\mathbf{M}$, has the same eigenvectors and eigenvalue ratios as those of the shape tensor. When keeping the major axis constant in the iterative methods, particles within the ellipsoid are selected by the criterion

$$r_{\mathrm{ell},k} \leq r, \tag{3.14}$$

where $r_{\mathrm{ell},k}$ is the ellipsoidal distance of particle k from the origin. When keeping the volume constant, particles are selected by

$$r_{\mathrm{ell},k} \leq \frac{r}{(qs)^{1/3}}. \tag{3.15}$$

This is derived from two properties of an ellipsoid: its volume is $V_{\mathrm{ell}} = \frac{4}{3}\pi abc$, with the semi-axis lengths a, b, and c. It is held constant at the spherical volume, such that $abc = r^3$ or $qsa^3 = r^3$ is required. Secondly, an ellipsoid aligned with the coordinate system is given by all particles satisfying

$$\begin{aligned} & \frac{x^2}{a^2} + \frac{y^2}{b^2} + \frac{z^2}{c^2} \leq 1 \\ \Rightarrow \quad & x^2 + \frac{y^2}{q^2} + \frac{z^2}{s^2} \leq a^2 \\ \Rightarrow \quad & r_{\mathrm{ell}}^2 \leq a^2 \end{aligned}$$

$$\Rightarrow \qquad r_{\mathrm{ell}} \leq \frac{r}{(qs)^{1/3}}, \tag{3.16}$$

which recovers Equation 3.15. For the iterative methods, the convergence criterion is implemented by requiring q and s to vary by less than 10^{-4} in relative terms from one step to the next. The method is also quit after 50 steps, which prevents the axis ratios from jumping back and forth by a relative step larger than 10^{-4} indefinitely.

First Insights: Iterative Methods

Figure 3.1 shows a simple visual test to get first insights into what the determined ellipsoids look like when their contours are overplotted onto the surface density map of a galaxy. The selected galaxy is deliberately picked to be rather flat in the edge-on view to address the concerns with respect to a bias towards more spherical shapes. This bias can indeed be seen for the non-iterative unweighted and all reduced methods, since their contour ellipses clearly have eccentricities that are too small compared to what one would expect from the surface density maps. The reason for this, in the case of the non-iterative methods, has already been discussed in Section 3.3.4. This supports the decision of Zemp et al. (2011), who only briefly mention the possibility of non-iterative methods, but do not see any physical meaning in their outcomes.

Reduced Methods

In addition to the non-iterative methods leading to biased shapes, there also appears to be an issue with the reduced methods in general, independent of computing the ellipsoid iteratively or not. Considering only the non-iterative reduced method, the eccentricity is even smaller than that of the non-iterative unweighted method. The source of this bias is found in the definition of the reduced method, given by the weight function $w(\boldsymbol{r}) = r^{-2}$. This weight function is used by some to prevent substructures in the outer region of the ellipsoid from dominating the summation for the shape tensor by only taking the unit position vector into account. The problem with this approach is that all particles are essentially projected onto a unit sphere, irrespective of the actual shape. In Figure 3.2, this is visualized for a two dimensional particle distribution (upper subfigure) projected onto a circle (middle subfigure). Note that the reduced shape tensor of the upper subfigure is equal to the unweighted shape tensor of the middle subfigure. Since the projected particles all lie on a sphere, the only thing making the shape more ellipsoidal is the varying particle density on the sphere's surface. Still, by entirely removing the distance component from the origin, it ignores how a shape also depends on the distances of the particles. Compared to the bottom subfigure, which shows how the reduced ellipsoidal method projects the particles onto an ellipse in two dimensions, it becomes more clear why the reduced method has a bias towards more spherical shapes, whereas the reduced ellipsoidal one does not. For this reason, the reduced methods are not further considered for the shape determination.

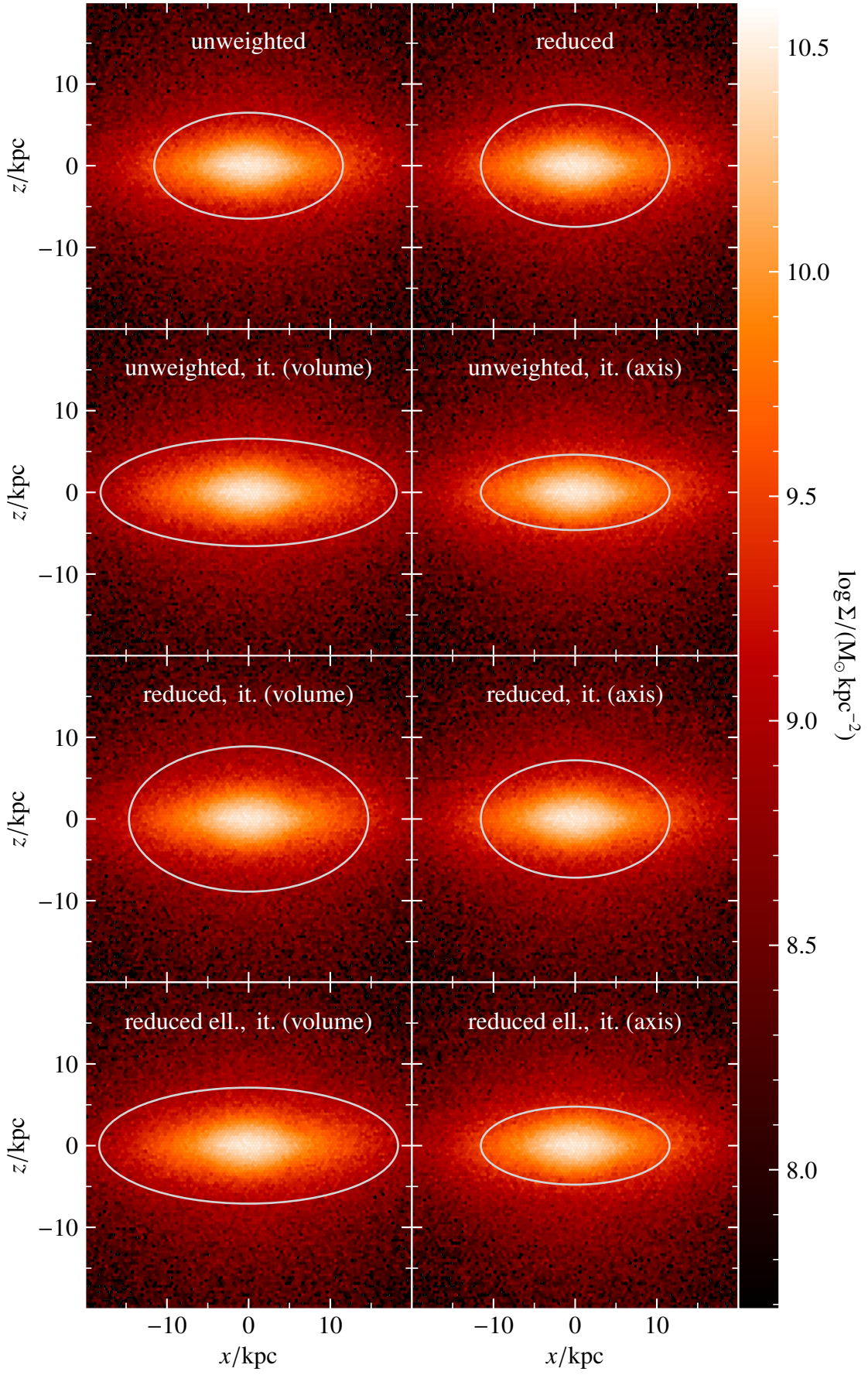

Figure 3.1: Surface density map of an example galaxy with the overplotted ellipsoid contour at 1 $R_{1/2,*}$ for the considered shape determination methods. The galaxy is viewed edge-on in the eigenvector coordinate system of the respective shape tensors. The iterative methods are denoted by "it.".

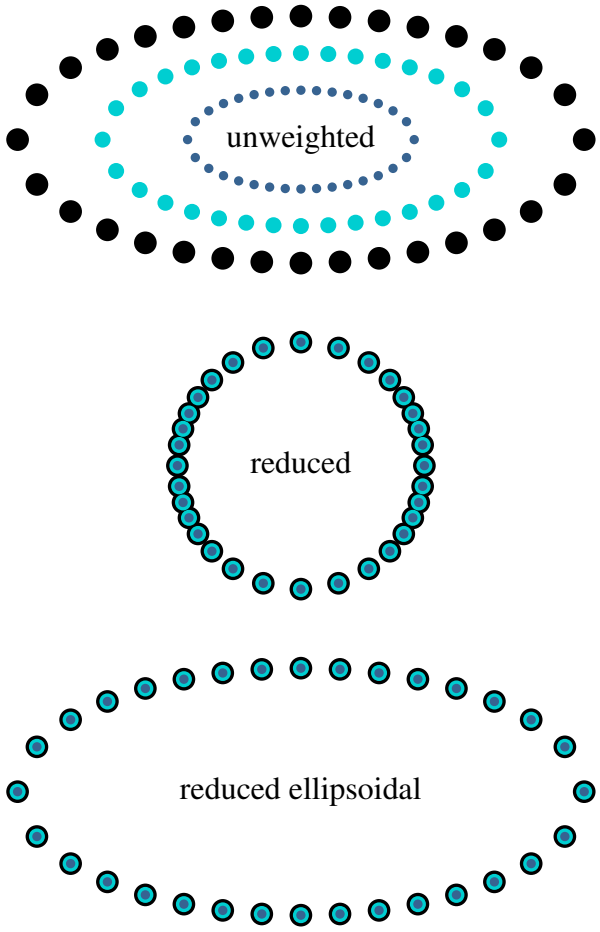

Figure 3.2: Visualization in two dimensions of how the unweighted, the reduced, and the reduced ellipsoidal weight functions project the particle distribution onto itself, onto a sphere (circle in 2D), and onto an ellipsoid (ellipse in 2D) in the summation for the shape tensor. The colors and sizes of the particles only are different to emphasize that the reduced and reduced ellipsoidal weightings project their positions onto the same circle and ellipsoid, respectively.

Unweighted and Reduced Ellipsoidal Methods

This leaves us with the iterative unweighted and reduced ellipsoidal methods. The bottom panel of Figure 3.2 nicely shows how the projection of the particles onto an ellipse (or ellipsoid in three dimensions) weights particles at all distances in the same direction equally. In contrast, the unweighted shape tensor depends more strongly on the particles that are the furthest out because of the proportionality with r^2. For these reasons, the unweighted method is more useful for a local description of the shape at a certain distance, while the reduced ellipsoidal method can be applied globally to find an average shape for the entire galaxy. When only used locally, the reduced ellipsoidal radial shape profile is smoothed out compared to what one obtains for the unweighted method, as found by Zemp et al. (2011). In fact, they also concluded that the iterative unweighted method (their S1) is the best at reproducing the shape of the isodensity surfaces out of the methods that consider all particles within an ellipsoid (as opposed to in homoeoids).

The different behavior of the unweighted and reduced ellipsoidal methods can be clearly seen for galaxies with morphological twists. Such a galaxy is shown in Figure 3.3 with the overplotted ellipses as before, except the shape tensors are calculated at three half-mass radii to also include particles further out. While the unweighted methods largely ignore the twisted core by determining an ellipsoid close to the actual isodensity surface at three half-mass radii, the reduced ellipsoidal method is dominated by the large amount of particles in the core, thus placing the galaxy in an edge-on view mostly according to the core shape. The meaning of the reduced ellipsoidal shape found at a certain distance therefore rather describes the average shape of the particles within. The iterative unweighted methods will therefore be used for any radial or local description of a galaxy's shape, while "globally averaged" shapes should be computed via the iterative reduced ellipsoidal method.

Constant Quantity in the Iteration

Finally, we are left with the question of whether it is better to keep the major axis or the volume of the deforming ellipsoid constant during the iterations. Running the two algorithms on a larger sample of galaxies, corresponding to the main halos and subhalos found by `SUBFIND` shows a major disadvantage of keeping the major axis constant: the ellipsoid is flattened completely for one galaxy at three half-mass radii, such that no stellar particles are found in the ellipsoid and the shape becomes undefined. Clearly, methods keeping the major axis constant are not entirely robust for all particle distributions. To understand why this happens, the edge-on density map of this galaxy is plotted for the iterative unweighted method with constant volume at three half-mass radii in Figure 3.4. A number of interesting things can be concluded from this galaxy: first of all, `SUBFIND` does not always manage to identify stellar substructures, as can be seen by the dense region about ~70 kpc to the left of the actual galaxy's center. Additionally, this example shows how the meaningfulness of a shape found for certain galaxies is questionable, since an ellipsoid is clearly not suitable for describing a particle distribution with two cores. Not even the reduced ellipsoidal method, which is

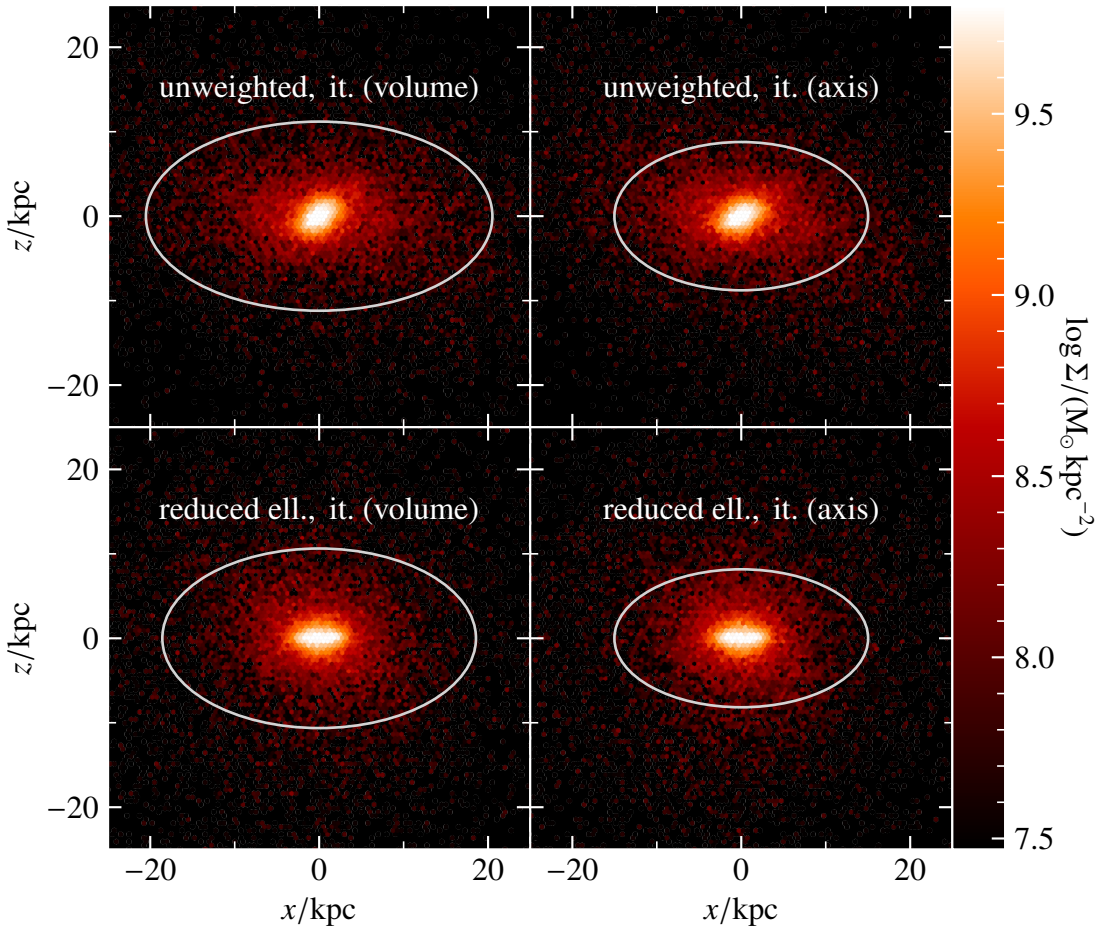

Figure 3.3: Surface density map of an example galaxy with the overplotted ellipsoid contour at three half-mass radii for the iterative unweighted and reduced ellipsoidal shape determination methods. The galaxy is viewed edge-on in the eigenvector coordinate system of the respective shape tensors. The differences in orientation are caused by the morphological twist of the galaxy, to which the shape determination methods react differently.

supposed to generally be less impacted by substructure, can properly determine the shape of the central part of the galaxy (Appendix A.1). Despite the unclear meaning of the determined shape, it becomes evident that the approach keeping the major axis constant is intrinsically more unstable against substructure than the one keeping the volume constant. While it may be possible to construct very specific particle distributions that lead to the constant volume approach being more unstable, this is never the case for any of the tested shape calculations. As a last point, the reason for the instability of the constant major axis approach is found to be linked to the very dense substructure outside the actual galaxy's center. Just barely within the three half-mass radii, it dominates the summation for the shape tensor, which leads to a very elongated ellipsoid with the substructure on the major axis. By keeping the major axis constant, this substructure continues to be right on the border of the enclosing ellipsoid. It therefore persistently dominates the shape, such that it becomes increasingly elongated, until it becomes completely flat. Because of this instability against substructure, the iterative unweighted method with constant ellipsoidal volume will be used in this work, unless noted

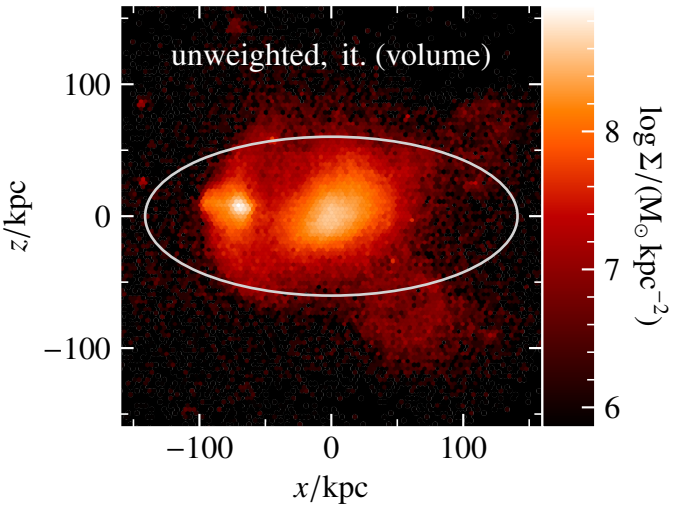

Figure 3.4: Surface density map of an example galaxy with the overplotted ellipsoid contour at three half-mass radii for the iterative unweighted shape determination method with constant volume. The galaxy is viewed edge-on in the eigenvector coordinate system of the shape tensor. Keeping the major axis constant instead of the volume of the ellipsoid leads to the ellipsoid being flattened completely.

otherwise. As a side note, when the reduced ellipsoidal method may be necessary, it is recommended to also apply the constant volume approach for reasons of consistency.

3.4 Shapes & Ellipticity

While the full three-dimensional data of the particles can be extracted from simulations, it is only possible to observe real galaxies as a two-dimensional projection, from which a three-dimensional shape can not be directly computed. As introduced in Section 1.2.1, the ellipticity is oftentimes used to describe the 2D shape of a galaxy's projection. There are also a variety of different methods used to determine the best fitting ellipse: for the SAURON (Bacon et al., 2001) and ATLAS^{3D} (Cappellari et al., 2011) projects, the ellipticity is computed as:

$$\epsilon = 1 - \sqrt{\frac{\sum_{n=1}^{N} F_n y_n^2}{\sum_{n=1}^{N} F_n x_n^2}}, \tag{3.17}$$

where the sums run over the bins of pixels, F_n is the flux contained within the nth bin, and x_n and y_n are its coordinates in the eigenvector coordinate system of the projection (Cappellari et al., 2007). Assuming a constant mass-to-light ratio, such that we can exchange the fluxes F_n by the masses M_n, this is actually the result of using the unweighted shape tensor in two dimensions. This is because the fraction consists of the diagonal elements of the 2D unweighted shape tensor, which in the eigenvector coordinate system correspond to the eigenvectors. The square root of their ratio is therefore simply the axis ratio of the ellipse, relating it to Equation 1.1. As has been shown for the three-dimensional shape tensor, the unweighted method has a bias towards large axis ratios. For this reason, that conclusion is

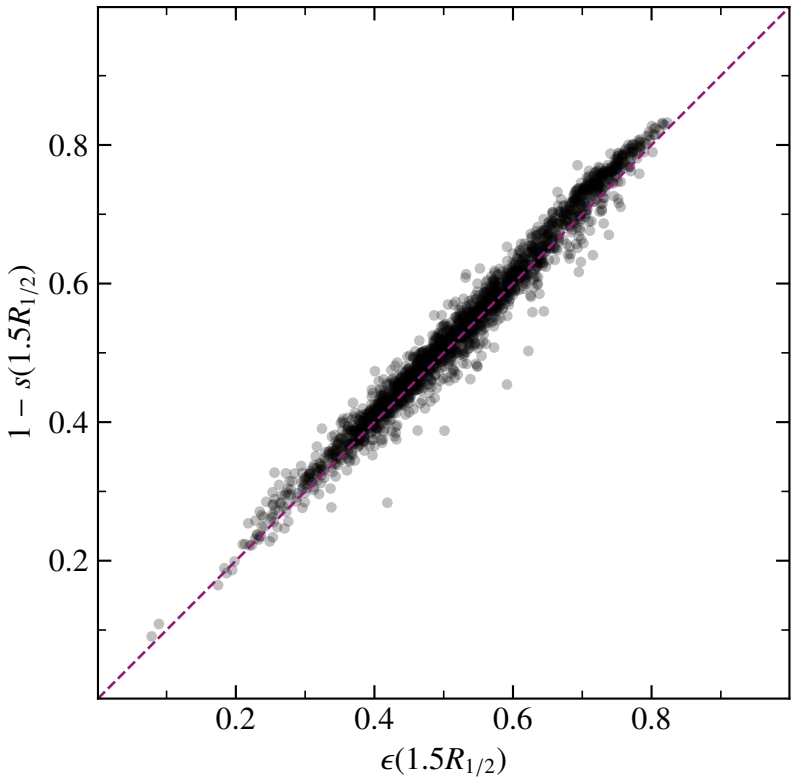

Figure 3.5: Edge-on ellipticity at 1.5 half-mass radii of the galaxy sample compared to the axis ratio s from the 3D ellipsoid. The edge-on view for the ellipticity was determined from the determined ellipsoid at 1.5 half-mass radii.

directly applied to the two-dimensional case in this work and the ellipticity is computed via the iterative unweighted method, keeping the area of the deforming ellipse constant.

It becomes apparent that the axis ratio of such an ellipse could match those of the 3D ellipsoid when viewed along one of the ellipsoid's axes. Comparing this for the galaxies in Magneticum Box4 (uhr) shows a close relation between the 2D determined edge-on ellipticity and the 3D axis ratio s at the same radial distance (Figure 3.5), where $\epsilon \approx 1 - s$. This demonstrates the direct relevance of the ellipsoid's 3D axis ratios for comparisons between simulations and observations. Of course, galaxies are observed in random orientations in practice, such that the values of the axis ratios q and s represent the upper and lower bounds of $1 - \epsilon$. It is interesting to note that there appears to be a trend of the ellipticities from the 3D shapes, $1 - s$, being a little larger than the 2D ellipticities. This may be caused by integrating over the line of sight in the projection for the 2D ellipse. In this work, the focus is on the intrinsic 3D shape properties rather than the randomly projected 2D properties, leaving a full analysis of the statistics and correlations of projected ellipticities from random orientations for future work. Here, the main point to keep in mind is that any references to q and s can also be understood as approximately one minus the ellipticity from a face-on and edge-on perspective, respectively.

3.5 Summary & Conclusion

As shown in this chapter, to ensure a meaningful description of the shapes, kinematics, and radial properties of a galaxy's stellar component, the particles have to be preprocessed by finding the particles' center and their center of velocity, and transforming them into that frame of reference. The galaxy shapes are described by ellipsoids aligned with the principal axes of the inertia tensor, where the lengths of the ellipsoid axes correspond to the positional standard deviations in the given directions.

A variety of shape determination methods are used in the literature, for which the tests performed in this chapter show that a local description of the shape is best done using the *mass-weighted, iterative, unweighted method*, while keeping the *volume* of the ellipsoid constant throughout the iterations. For a global description of a galaxy's shape, the best method is the *mass-weighted, iterative, reduced-ellipsoidal method*, where all particles of a galaxy are considered. Applying any of the other methods can lead to biased results through substructure, to biases towards spherical shapes, and to less robust algorithms that do not converge to a physical result. In this work, the local shapes at specific radial distances are analyzed in detail. Therefore, the mass-weighted, iterative, unweighted method, which keeps the ellipsoid's deforming volume constant, will be used throughout this thesis.

4 Shapes of the Magneticum Galaxies

Having decided on the most appropriate shape determination method to be used, the shapes of all galaxies in the sample are investigated in detail in this chapter. The statistics of the axis ratios and triaxialities for the stellar and DM components and their relation with the b-value, the morphological parameter, are important for the analysis of the relations between the shapes and other galaxy properties starting in Chapter 5, since they provide the foundation for the interpretations of the findings. From a qualitative perspective, and keeping the morphological classifications in mind (Section 1.2.1), the stellar shapes of LTGs would be expected to be flatter, i.e., have lower values of s compared to ETGs. LTGs should also be more oblate on average due to their disk-like shapes. Because DM cannot redistribute angular momentum, while gas is capable of settling in a disk, and because of stars preferably forming in the gas disk of LTGs, the DM shapes can be expected to be more spherical than those of the stars. Other authors have found most DM halos to be prolate in shape from DM-only simulations (e.g. Allgood et al., 2006), arguing that the prolate shapes are a consequence of merging along preferred directions (e.g. Knebe et al., 2004; Faltenbacher et al., 2005). This argument can also be made for the stellar component of ETGs. Lastly, a comparison between the inner and outer stellar and DM shapes is made to get an impression of how variable the determined shapes are radially and how similar the stellar and DM shapes are to each other.

4.1 Axis Ratios

Stellar Component

In a first step, we take a look at the distribution of the galaxy sample in the q-s axis ratio plane of the stellar component at one and three half-mass radii (left panel of Figure 4.1). A feature that is immediately apparent is that the galaxies' inner and outer regions occupy different places in the q-s-plane: at 1 $R_{1/2,*}$, q spans a large interval with most galaxies having $q \gtrsim 0.5$ and s being mostly between 0.2 and 0.6, while at 3 $R_{1/2,*}$, the generally high values of $q \gtrsim 0.75$ indicate more circular face-on shapes, with s moving to a higher range between 0.3 and 0.7. Clearly, more galaxies are identified as oblate when also considering their outer regions, while the inner regions often feature more triaxial and prolate shapes. While some of these could be interpreted as large bars (and others could simply be elongated ETGs), the spatial resolution of the inner parts of the less massive galaxies is unfortunately too close to the softening length. For this reason, the shape distribution may be affected by numerical

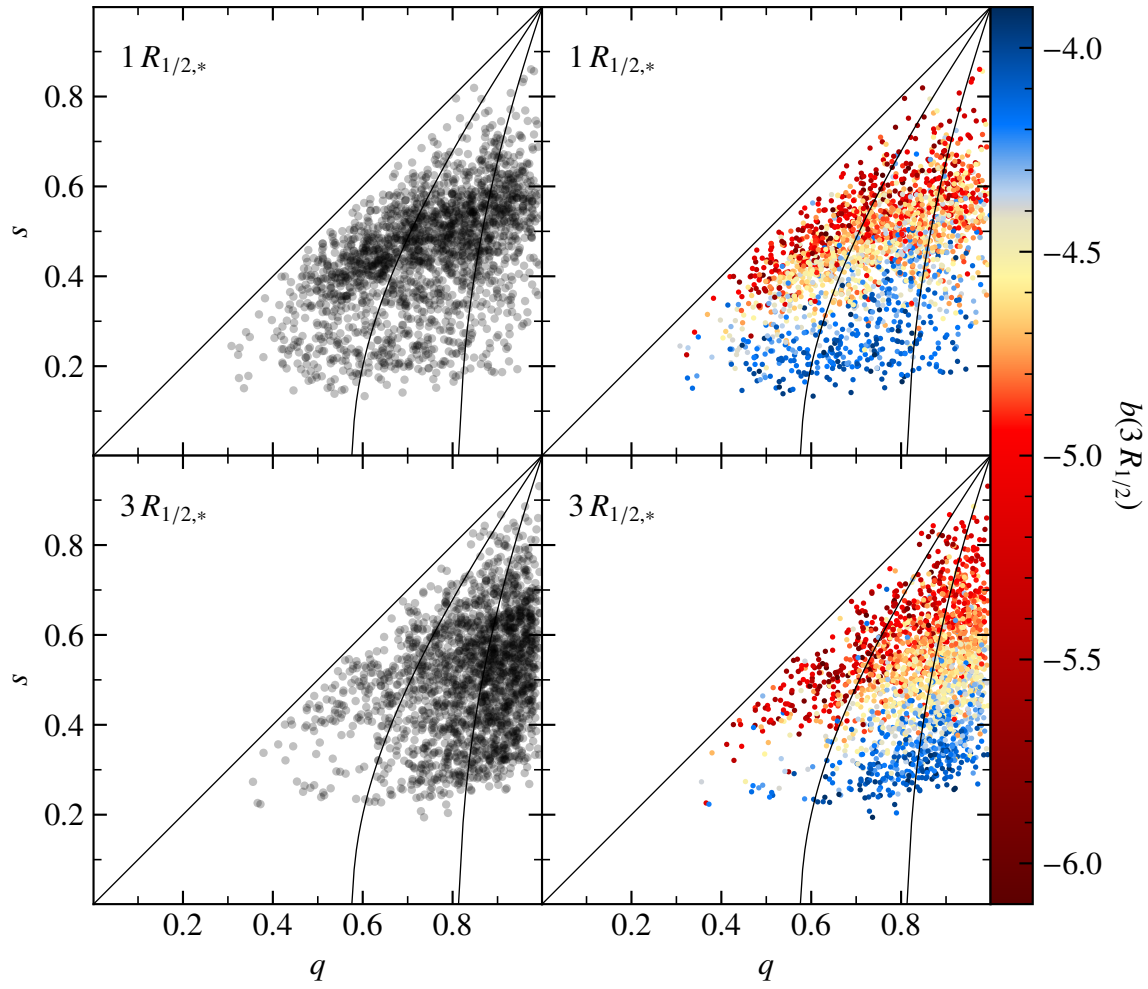

Figure 4.1: Axis ratios q and s of the stellar component of the galaxy sample at one and three stellar half-mass radii. On the left, the points are plotted semi-transparently to better show their distribution, while the same points are colored by b-value on the right. The solid lines indicate the borders between prolate, triaxial, and oblate shapes, from left to right, respectively.

resolution artifacts, which should be analyzed more closely in higher resolution simulations in the future.

Another point of interest is that more galaxies have spherical shapes (i.e., large values of s) at larger radii than in the core. This may also be due to numerical issues related to the higher number of particles being used to compute the outer shapes, but could also simply be the result of spherical stellar halos.

Next, we examine how the axis ratios relate to the morphologies of the galaxies. As introduced in Section 1.2.1, the best quantifier of a galaxy's morphology is its b-value, with LTGs having higher and ETGs lower values of b. On the right side of Figure 4.1, the same data is plotted as on the left, but now with the points colored by the b-value. A very clear trend emerges at both radii: LTGs have low values of s and are therefore flatter in the edge-on view, while ETGs have higher values of s. Interestingly, there is also a small trend with q, which is partly due to the constraint of $q > s$, but is also more pronounced at $3\,R_{1/2,*}$. The correlation with the b-value appears to be somewhat tighter in the intermediate (yellow

data points) galaxy regime at 3 $R_{1/2,*}$. This could be related to resolution issues in the inner regions of the less massive galaxies.

The visualization with the b-value now reveals that while LTGs can be prolate in the inner regions, most become oblate and some triaxial in the outer regions. This shows how disky structures usually only become apparent when considering a larger part of the galaxy. Additionally, LTGs are less flat further out, with the axis ratios s hardly dropping below 0.2. The cause of this is not directly clear, but the lower bound of $s_{\min} \approx 0.2$ is significantly higher than the lowest values found in the SDSS Galaxy Zoo project (Rodríguez & Padilla, 2013), in selected SAMI galaxies (Foster et al., 2017), and in ultra-flat galaxies (Kaisin et al., 2020) of $s < 0.1$. This indicates that the galaxies' disks are too thick in the simulation compared to observations. Pulsoni et al. (2020) determined the axis ratios at 8 $R_{1/2,*}$ of the ETGs in TNG50 and TNG100, finding a similar lower bound of $s_{\min} \sim 0.2$. However, it is not clear how this could differ for their LTGs. An attempt to explain the lower bound in a very rudimentary way is to take the mean half-mass radius of the galaxy sample as a disk radius, which is around 5 kpc (6 kpc for the LTGs), and relate it to the softening length of 1 kpc as a lower bound of the disk height: this leads exactly to the minimum axis ratio of $s_{\min} = 0.2$. Future higher resolution simulations will likely lead to thinner disks, which was also what Pillepich et al. (2019) observed for the higher resolution simulation of TNG50 compared to the lower resolved ones.

A further point to note is that of the near-spherical galaxies at 3 $R_{1/2,*}$, almost all of them are ETGs, as opposed to at one half-mass radius, where more intermediate galaxies are found to have close to spherical shapes. ETGs are also the most common to have prolate shapes in the outer regions, while there are a number of LTGs and intermediate galaxies with prolate inner regions, again raising the question if these elongated shapes in the LTGs could be bars or bar-like features. As mentioned earlier, this will have to be approached in the future with higher resolution simulations. Finally, there are also interesting outliers to these trends: some LTGs have prolate shapes, with individual LTGs even having higher minor axis ratios up to $s \sim 0.7$, indicating a spherical shape. Such objects may have very large bulge-like behavior and likely have interesting formation histories which should be studied in the future.

The axis ratio plots at three half-mass radii for the iterative reduced and reduced ellipsoidal methods are included in Appendix A.2. The distribution of shape parameters for the reduced method confirms the bias towards spherical shapes as discussed in Section 3.3.5. The distribution of shape parameters for the reduced ellipsoidal method appears to be a mix of those found for the unweighted method at 1 $R_{1/2,*}$ and 3 $R_{1/2,*}$, which is consistent with the reduced ellipsoidal method describing the average shape within the given radial distance.

Dark Matter Component

Having a better understanding of what the stellar shapes look like for the galaxies, we now turn to the DM shapes. One of the most obvious questions is how the distribution of the axis ratios of the DM compares to that of the stellar component. Because of the larger softening

length for DM particles (2 kpc compared to 1 kpc for stellar particles), only the axis ratios of the shape at $3\,R_{1/2,*}$ are explored (top row of Figure 4.2). It is immediately evident that the DM shapes are more spherical than the stellar shapes. Most galaxies have $s_{\mathrm{DM}} \gtrsim 0.5$ and $q_{\mathrm{DM}} \gtrsim 0.7$. There are also a lot more galaxies with both axis ratios above 0.8, whereas that is only the case for the stellar shapes of a small number of galaxies. There is also not a strong correlation with the b-value, in contrast to the stellar component. It appears that there are more LTGs found in the oblate region at low s_{DM} and high q_{DM}, whereas the prolate shapes are mostly found to be ETGs. It remains to be seen whether there is a correlation between the DM and stellar shapes at three stellar half-mass radii, which will be further investigated in the next section.

As the DM particles of a galaxy generally reach further out than the stellar particles, the dark matter half-mass radius is usually larger than three stellar half-mass radii, except for the smallest galaxies, where the DM half-mass radius can be as small as $1.5\,R_{1/2,*}$. The axis ratio distribution does actually change at $1\,R_{1/2,\mathrm{DM}}$ (middle row of Figure 4.2), where the shapes are increasingly spherical. There are also more elongated prolate DM shapes with lower values of q_{DM}. These galaxies have a wide range of stellar and DM half-mass radii, which means that the elongated DM shapes are not a result of low resolution. Finally, when considering all DM particles identified for the galaxies by `SUBFIND`, the DM shapes become less oblate and move towards triaxial and prolate shapes for the lower values of s_{DM} (bottom row of Figure 4.2). This leads to an even higher number of prolate DM halos with comparably low axis ratios of $q_{\mathrm{DM}} < 0.6$. The differences between the DM shapes at $1\,R_{1/2,\mathrm{DM}}$ and the full DM shapes could be related to the details of the respective cosmic environments. However, this is outside the scope of this work and is subject to future analysis. Unsurprisingly, no correlation with the b-value can be seen for the axis ratios at $1\,R_{1/2,\mathrm{DM}}$ or of all DM particles, just as at $3\,R_{1/2,*}$.

4.2 Inner & Outer Shapes

Having compared the axis ratio distributions in the q-s-plane at different radii for the stellar and DM components, the focus is now placed on how the shape parameters differ for the galaxies at different radii and between the two components (Figure 4.3). For this, we not only compare the axis ratios, q and s, but also include the triaxiality, T (Equation 1.18), as a commonly used quantification of shapes in the literature. In the top row, we observe a clear trend between the stellar minor axis ratios, s, at $1\,R_{1/2,*}$ and $3\,R_{1/2,*}$ (middle column): flat galaxies in the inner regions tend to also be flat in the outer regions. The observed correlation with the b-value from Figure 4.1 is again clearly visible. While not as strong, there is also a trend between the corresponding major axis ratios, q (left column): galaxies with low values of q in the inner regions tend to have small values of q in the outer regions as well. However, galaxies with $q \gtrsim 0.6$ at $1\,R_{1/2,*}$ tend to have larger values at $3\,R_{1/2,*}$, which means that they are more circular from a face-on perspective in the outer regions. The very slight correlation with the b-value can also be seen here, as expected from Figure 4.1.

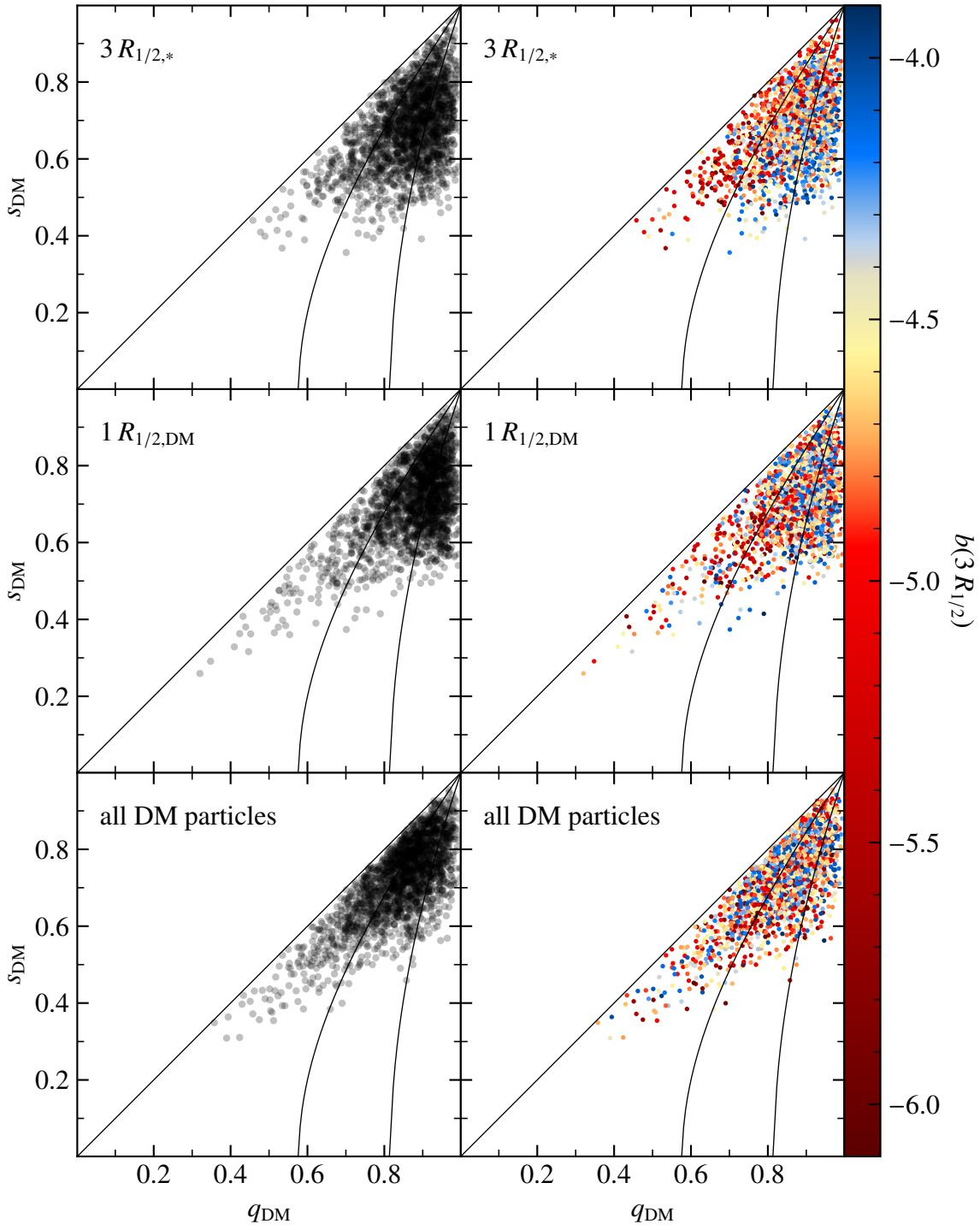

Figure 4.2: Axis ratios q and s of the DM component of the galaxy sample at different radii: three stellar half-mass radii, one DM half-mass radius, and computed for all DM particles identified for the given galaxy by `SUBFIND`. On the left, the points are plotted semi-transparently to better show their distribution, while the same points are colored by b-value on the right. The solid lines indicate the borders between prolate, triaxial, and oblate shapes, from left to right, respectively.

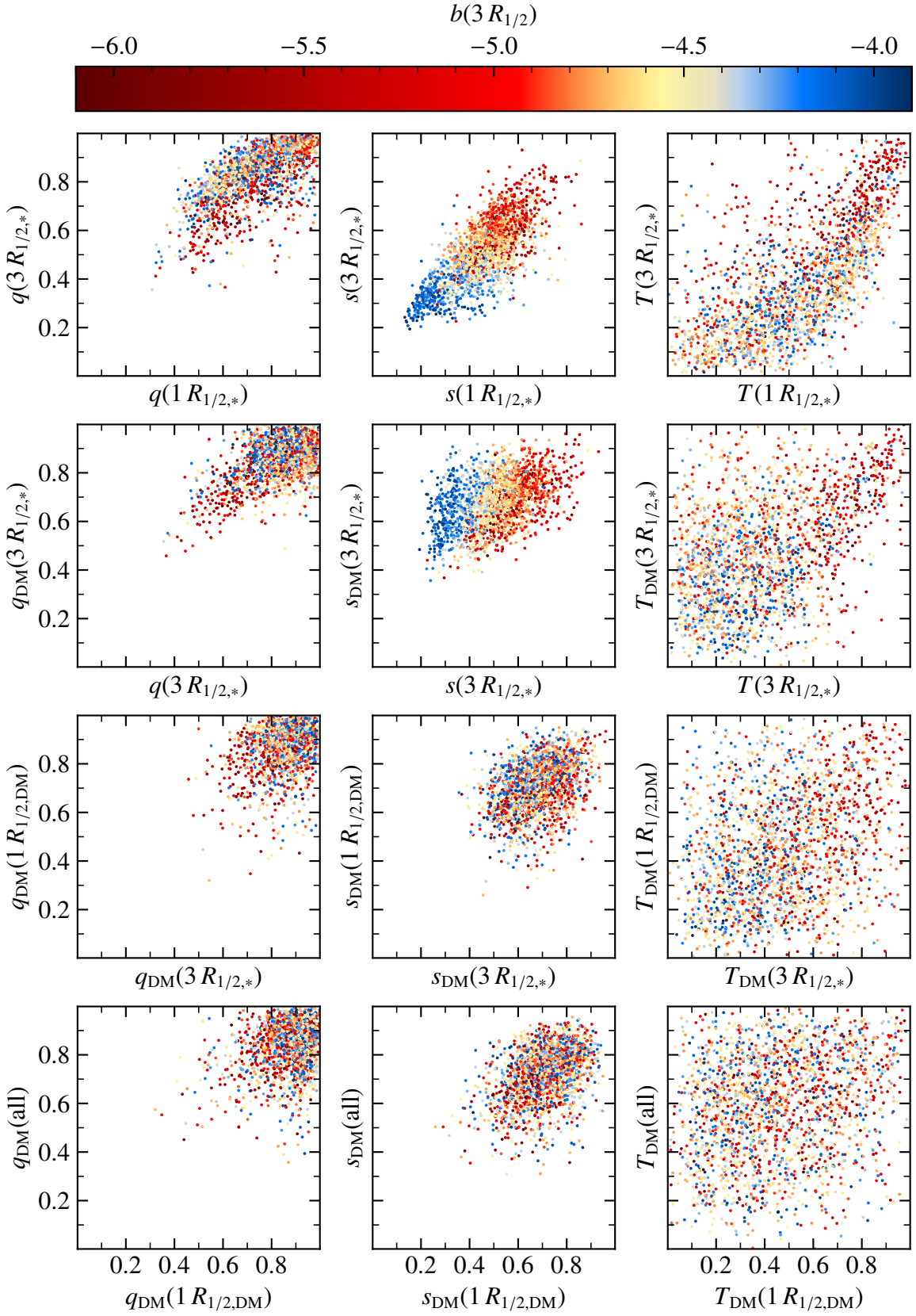

Figure 4.3: *Top row*: Stellar shape parameters at 1 $R_{1/2,*}$ and 3 $R_{1/2,*}$. *Second row*: Stellar and DM shape parameters at 3 $R_{1/2,*}$. *Third row*: DM shape parameters at 3 $R_{1/2,*}$ and 1 $R_{1/2,\rm DM}$. *Bottom row*: DM shape parameters at 1 $R_{1/2,\rm DM}$ and for all DM particles.

These radial behaviors of the axis ratios lead to an interesting trend seen for the triaxiality (right column): high triaxialities in the inner regions stay high in the outer regions, but lower ones tend to be even lower further out. This means that prolate galaxies in the inner regions become more triaxial in the outer regions, and triaxial galaxies become more oblate, which again is consistent with what is found in Figure 4.1. This first quantitative visualization of the triaxiality distributions also shows how ETGs tend towards being prolate and LTGs towards being oblate. The correlation is rather weak, however, which is a result of the very weak correlation of q with the b-value, since the triaxiality is a function of q and s. It is also found that the overall trend of the triaxiality between 1 $R_{1/2,*}$ and 3 $R_{1/2,*}$ is weaker than for the axis ratios, which can be attributed to the combined variances of q and s in Equation 1.18 for the triaxiality.

At three stellar half-mass radii, the DM major axis ratios generally follow those of the stellar component for $q \lesssim 0.7$ (second row of Figure 4.3), which mostly affects ETGs. For values of q close to 1, however, any stellar value of q above 0.7 can correspond to any value of q_{DM} above 0.7. For the minor axis ratios, the correlation between the stellar and DM components is weak: there seems to be a lower bound of s_{DM} for a given stellar minor axis ratio that increases with s; however, the upper bound is almost constant and is around $s_{\mathrm{DM,upper}} \sim 0.90$–$0.95$, such that the variance in s_{DM} is rather large. Interestingly, the lower bound of s_{DM} combined with the correlation between the stellar minor axis ratio and the b-value leads to a slight trend of s_{DM} with the b-value. This contributes to the behavior we have already seen in Figure 4.2, that galaxies with oblate DM shapes with low values of s_{DM} tend to be LTGs. Here it becomes apparent that there is a slight trend even for the intermediate galaxies and ETGs of larger stellar minor axis ratio corresponding to larger s_{DM}. The trends observed in q and s lead to a weak correlation in triaxiality: as seen before, ETGs dominate the prolate shapes of the stellar and DM components, and there is a large variance in the oblate to triaxial regime, which LTGs preferably occupy. There is an approximate lower bound for the DM triaxiality, meaning that prolate stellar shapes will almost always be accompanied by prolate DM shapes. This is likely a result of the lower bound seen for s. Also, oblate and triaxial stellar shapes tend to have oblate or triaxial DM shapes, although the scatter is larger than for prolate shapes. In general, this shows that DM and stars feature similar shapes at 3 $R_{1/2,*}$, confirming other studies suggesting that DM and its shapes are influenced by the baryonic potential (e.g. Chua et al., 2019; Cataldi et al., 2021; Emami et al., 2021).

When comparing the DM shapes at three stellar half-mass radii with the DM shapes at one DM half-mass radius (third row of Figure 4.3), a large scatter in both q and s is found, although the comparison of the triaxiality reveals a slight correlation between its values at the two radial distances, which appears to be more pronounced for ETGs than for LTGs. As discussed earlier, the DM half-mass radius is usually larger than 3 $R_{1/2,*}$, but can also be smaller for some galaxies and the ratio between $R_{1/2,\mathrm{DM}}$ and $R_{1/2,*}$ can strongly differ. This could contribute to the lack of a strong correlation found for the shapes between the two radial distances.

Finally, the correlation between DM shapes at 1 $R_{1/2,\mathrm{DM}}$ and the DM shapes accounting for all DM particles attributed to the galaxies by SUBFIND again is weak for q and s with large overall scatters, but is weaker when considering the triaxiality. There is the trend of galaxies having low values of q_{DM} at 1 $R_{1/2,\mathrm{DM}}$ to also have low q_{DM} for all DM particles. The same is also true for s_{DM}. For the triaxiality, the clearest trend is that prolate DM shapes at 1 $R_{1/2,\mathrm{DM}}$ tend to also be prolate for all DM particles. An important conclusion that can be drawn from these relations is that the full DM halo shapes are at most weakly affected by the details of the stellar shape in the inner halo region. Further analysis on how DM halo shapes are affected by the inclusion of baryonic matter in cosmological simulations, compared to DM-only simulations, is beyond the scope of this work and has been studied for some properties by Chua et al. (2019) in Illustris and by Cataldi et al. (2021) in Fenix and EAGLE.

4.3 Summary & Conclusion

The galaxies' shapes in Magneticum Pathfinder Box4 (uhr) are found to be overall consistent with the qualitative expectations: LTGs have flatter and more oblate stellar shapes, whereas ETGs tend to be more spherical and triaxial, which are likely linked to the merger histories of the galaxies. The shapes at 3 $R_{1/2,*}$ appear to fit these general trends more strongly than at 1 $R_{1/2,*}$, which suggests that there may be a connection with large bulges of disk-like galaxies that make LTGs and intermediate galaxies have more triaxial to prolate shapes in the inner regions, and more oblate in the outer regions. A question that remains open is why the shapes in the inner regions tend to be flatter than further out for LTGs. The generally more spherical stellar outer halos could be part of the answer, as well as elongated bars or bar-like features in the central region. Flatter disk galaxies may also be expected in future simulations with higher resolutions. An additional interesting trend with the b-value was found, which is that for a given minor axis ratio, s, the stellar major axis ratio, q, is larger for higher b-values, i.e., q is larger for LTGs.

The stellar shapes at 1 $R_{1/2,*}$ and 3 $R_{1/2,*}$ are correlated with each other, which is seen the strongest for the minor axis ratio. This indicates that most trends found for s at one radial distance will also apply at the other. The correlation is not as strong for q and T, which means that trends with these quantities may not be as clear as for the minor axis ratio.

The trends for the DM shapes were found to be consistent with the literature: the shapes of the full DM halos tend to be prolate in shape. DM shapes at all considered radii (3 $R_{1/2,*}$, 1 $R_{1/2,\mathrm{DM}}$, and for all DM particles) show a preference towards being more spherical and show little to no correlation with the b-value. There is a correlation between the stellar and DM shapes at the same radial distance of 3 $R_{1/2,*}$, which leads to a minor trend between the b-value and the DM shape with LTGs having preferably flat DM shapes and ETGs prolate and spherical shapes. Since there is no correlation between the inner and outer DM shapes, the DM shape trend with the b-value is lost at larger radii. This suggests that the inner regions

of a galaxy tend to be decoupled from the outer parts, which is likely a result of the accretion of substructure that only changes the morphology and kinematics in the outer regions.

5 Shapes & Global Galaxy Properties

Having a better understanding of the statistics of the galaxies' shapes and of the relation between the shapes and morphology, we now turn to investigating the relation of the shapes with a variety of global galaxy properties. As one of the most important observational kinematic properties, the λ_R-parameter of an edge-on galaxy, which quantifies the rotational support, has previously been shown to be correlated with the projected ellipticity and the anisotropy (e.g. Illingworth, 1977; Binney, 1978, 2005; Schulze et al., 2018). Since the edge-on ellipticity of a galaxy is closely related to the minor axis ratio via $\epsilon \approx 1 - s$, the same trends as seen in Figure 1.11 and Figure 1.12 for the λ_R-parameter and the anisotropy, respectively, are expected for the relations with s: galaxies are flattened through larger rotational support or through higher anisotropies in the velocity distribution.

Two further important properties of galaxies are the stellar mass and the half-mass radius, which together also describe the mass distribution of a galaxy when combined. Since more massive galaxies are generally ETGs, a reasonable assumption would be that the stellar shapes are more spherical for massive galaxies. Shapes are simply another way of describing the distribution of matter, such that a trend between the shapes and the mass together with the half-mass radius seems reasonable. For the total mass of galaxies, it has been found in previous cosmological simulations that more massive halos tend to be less spherical and more prolate (e.g. Allgood et al., 2006; Bett et al., 2007). A major difference between those simulations and the one studied in this work is that here a hydrodynamical instead of a DM-only simulation is used.

As all the present-day properties of galaxies are necessarily the result of their formation histories, it can be expected that there are relations between some properties describing aspects of the formation histories and the shapes. LTGs tend to have ongoing star formation, whereas ETGs mostly have little to no ongoing star formation. Because LTGs are generally flatter and ETGs more spherical, the minor axis ratio is likely smaller for galaxies with small specific star formation rates (star formation rate per mass). Similarly, galaxies with on average younger stars can be expected to be flatter than those with older stellar populations, assuming that ongoing star formation is correlated with younger stellar populations on average. Considering that there is observational evidence for quiescent red spiral galaxies (e.g. van den Bergh, 1976; Goto et al., 2003; Schawinski et al., 2014; Guo et al., 2020), a population of LTGs is expected that has old stellar populations, no ongoing star formation, but flat shapes. The in-situ fraction, which tends to be smaller for more massive galaxies (Remus & Forbes, 2021), may be related to the galaxy shapes through the accretion of smaller galaxies, leading to lower in-situ fractions and more spherical and triaxial shapes.

Finally, the kinematics of the stellar and DM components and their alignments are an interesting aspect that can currently only be studied within simulations. The angular momenta of the stellar and DM components have been found to overall be aligned (e.g. van den Bosch et al., 2002; Sharma et al., 2012; Teklu et al., 2015), where the alignment is stronger for LTGs than for ETGs. Because of this relation, flatter galaxies can be expected to have stronger alignments between the stellar and DM angular momenta. These assumptions will all be tested in the following.

5.1 Relations with the λ_R-Parameter

The first property we compare the shapes to is the λ_R-parameter at one stellar half-mass radius, which is denoted as $\lambda_{R_{1/2}}$, consistent with Schulze et al. (2018). For the shapes at $1\,R_{1/2,*}$ (top row of Figure 5.1), we find a strong correlation between the axis ratio s and $\lambda_{R_{1/2}}$, where rotationally supported galaxies with high values of $\lambda_{R_{1/2}}$ have low values of s, and dispersion dominated galaxies with low values of $\lambda_{R_{1/2}}$ have higher values of s. In the latter case, the scatter in s is higher, however. Recalling that the axis ratio s can be identified with one minus the edge-on ellipticity (Section 3.4), it becomes apparent that the s-$\lambda_{R_{1/2}}$ plot recovers the relation between ϵ and $\lambda_{R_{1/2}}$ presented in Figure 1.11. The same is true for the relation seen for s in the bottom row of Figure 5.1 for a radial distance of $3\,R_{1/2,*}$. In this case, the larger scatter of s shows that the minor axis ratio s at $3\,R_{1/2,*}$ does not correlate as well with the value of λ_R at $1\,R_{1/2,*}$ as s at $1\,R_{1/2,*}$, which is likely related to the different radial distances chosen. Comparing the values of λ_R at different radial distances with the corresponding shapes will be the aim of a future study. In particular, it will be interesting to investigate the radial behavior of the λ_R-ϵ plane in the light of the findings by Foster et al. (2018), Pulsoni et al. (2020), and Schulze et al. (2020), who showed that for some galaxies λ_R can drastically change with radius.

Curiously, the relation between $\lambda_{R_{1/2}}$ and q is tighter at $3\,R_{1/2,*}$ than at $1\,R_{1/2,*}$, which may result from the overall higher values of q for intermediate galaxies and LTGs further out, whereas they span a larger range of values at $1\,R_{1/2,*}$ almost uniformly, dropping down to $q_{\mathrm{min}} \approx 0.4$, as previously found in Figure 4.1. Because of the correlation between $\lambda_{R_{1/2}}$ and the b-value, this means that galaxies with $\lambda_{R_{1/2}} \gtrsim 0.3$ tend to have high values of $q \gtrsim 0.7$ at $3\,R_{1/2,*}$, while their values of q at $1\,R_{1/2,*}$ have a larger scatter with $q = 0.4$–1.0. For ETGs, of which many have low values of $\lambda_{R_{1/2}} \lesssim 0.3$ (mostly the slow rotators) and some even have larger values (most of the fast rotators), the range of the major axis ratio at both considered radial distances is $q = 0.4$–1.0, as well.

The correlations with $\lambda_{R_{1/2}}$ found for q and s lead to different relations with the triaxiality (right column of Figure 5.1): while the large scatter with q at $1\,R_{1/2,*}$ leads to an almost constant relation of the triaxiality for $\lambda_{R_{1/2}} \gtrsim 0.2$, the triaxiality declines further with $\lambda_{R_{1/2}}$ at $3\,R_{1/2,*}$, reaching a constant relation for $\lambda_{R_{1/2}} \gtrsim 0.6$, which mostly corresponds to LTGs. This behavior is clearly connected to the different relations between $\lambda_{R_{1/2}}$ and q, since LTGs only have especially high values of q at $3\,R_{1/2,*}$ that lead to oblate shapes. At both radial

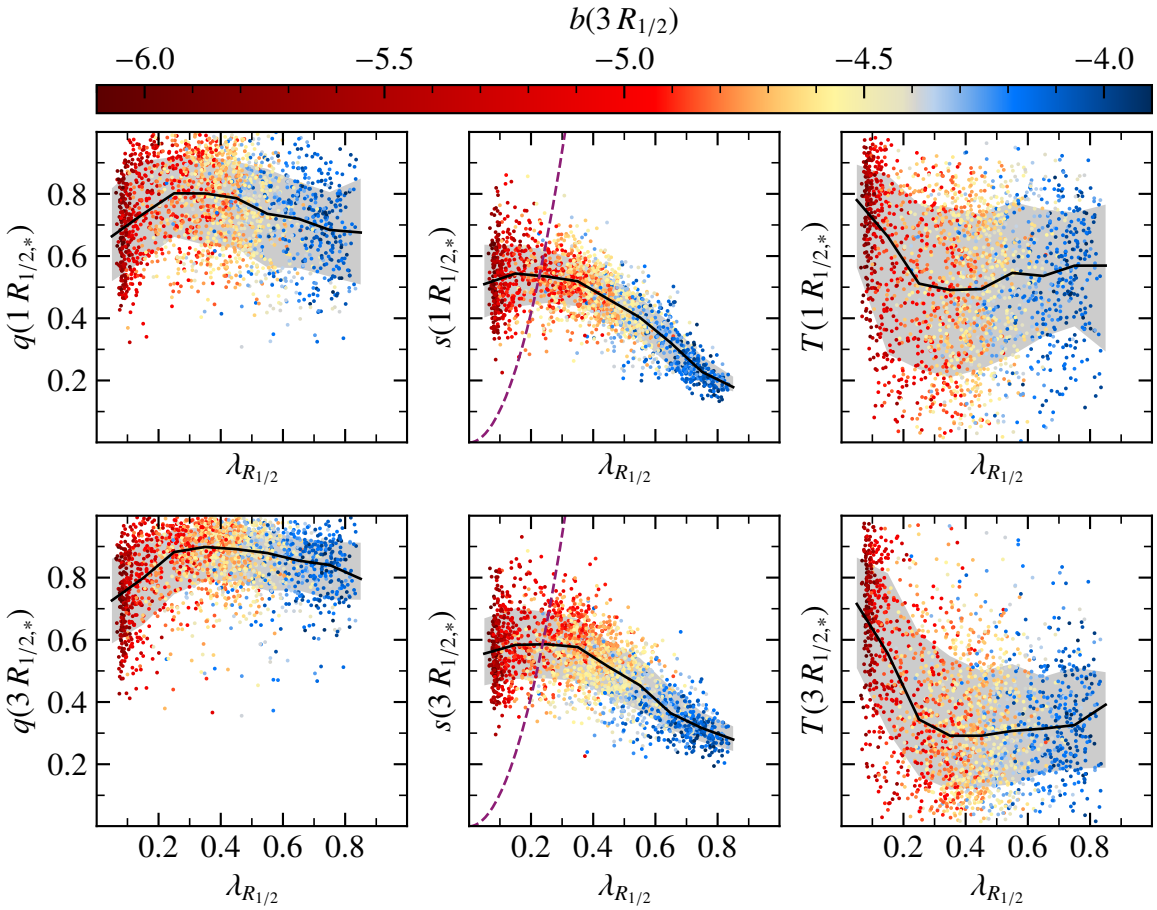

Figure 5.1: Relation between shape parameters at one (top row) and three (bottom row) stellar half-mass radii and $\lambda_{R_{1/2}}$, colored by the b-value. The dashed blackberry lines in the middle column indicate the threshold between slow and fast rotators, lying to the left and right of the line, respectively. The black lines indicate the median values in the respective $\lambda_{R_{1/2}}$ bins and the shaded regions the 1σ ranges (containing 68% of the galaxies above and below the median). The dashed part of the lines indicates where there may be effects caused by low number statistics.

distances, the ETGs with low values of $\lambda_{R_{1/2}}$ show a strong preference for prolate shapes. It is interesting how these effects lead to especially prolate shapes of dispersion dominated galaxies with low values of $\lambda_{R_{1/2}}$ at both radial distances, whereas the expected tendency towards oblate shapes for rotationally dominated galaxies is only found at larger radii. Future higher-resolution studies will be necessary to determine how strongly this behavior is affected by the limited resolution and whether stellar bulges and bars play a role or not.

5.2 Relations with the Anisotropy

As a parameter that can be determined from a galaxy's position in the $\lambda_{R_{1/2}}$-ϵ plane (Binney, 2005; Schulze et al., 2018), we next compare the shapes to the anisotropy at one stellar half-mass radius, $\delta_{R_{1/2}}$. Again identifying the minor axis ratio, s, with one minus the edge-on ellipticity and considering the correlation between $\lambda_{R_{1/2}}$ and the b-value, it is not surprising that we find a clear trend between $\delta_{R_{1/2}}$, s, and the b-value (middle column of Figure 5.2): the minor axis ratio decreases at constant b-value with higher anisotropy and as noted before,

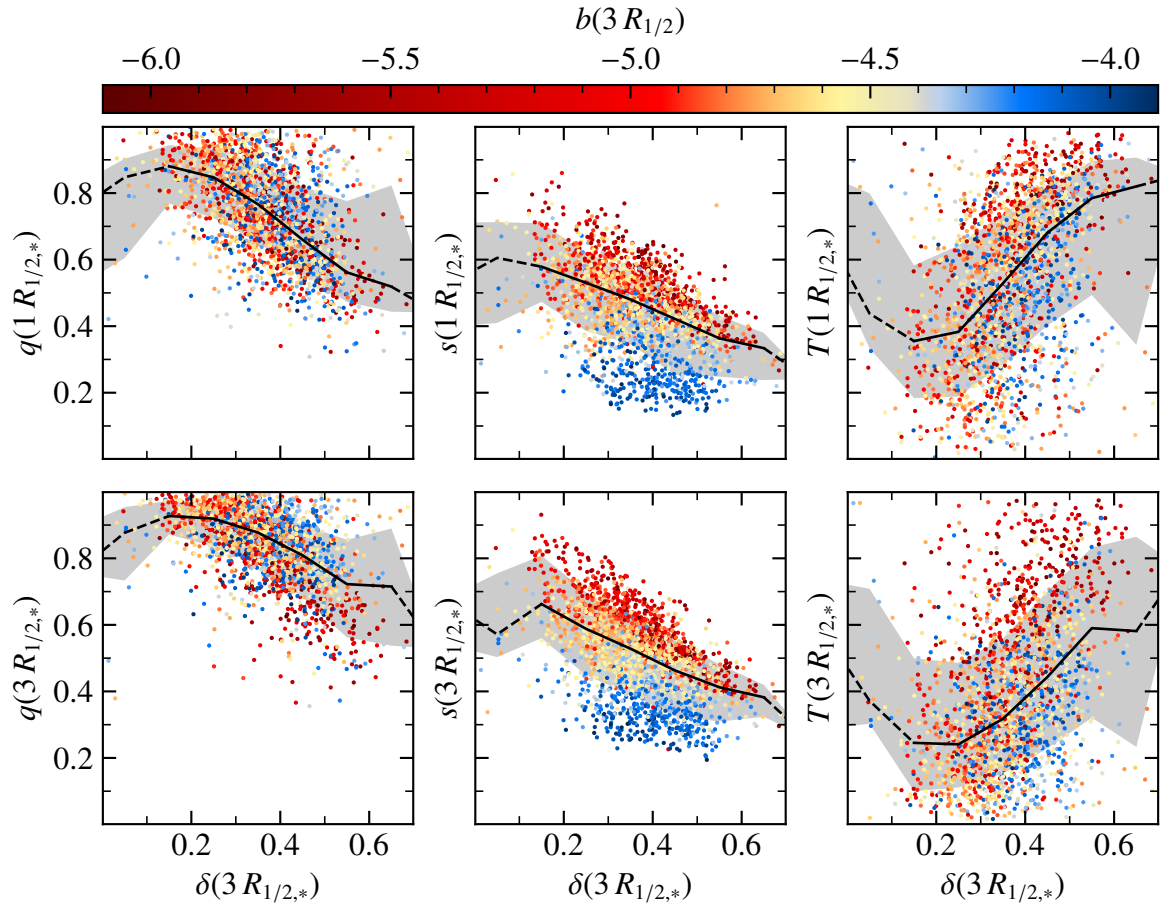

Figure 5.2: Relation between shape parameters at one (top row) and three (bottom row) stellar half-mass radii and the anisotropy at one half-mass radius, $\delta_{R_{1/2}}$, colored by the b-value. The black lines indicate the median values in the respective anisotropy bins and the shaded regions the 1σ ranges (containing 68% of the galaxies above and below the median). The dashed part of the lines indicates where there may be effects caused by low number statistics.

s increases with the b-value. This trend is the clearest at $1\,R_{1/2,*}$, which is likely related to the anisotropy being computed at that radial distance. Analyzing the radial behavior of the anisotropy and how it compares to the galaxies' shapes for a larger galaxy sample (in particular with more LTGs) will be the subject of future work.

Interestingly, there is a similar relation between q and $\delta_{R_{1/2}}$ that q decreases with increasing $\delta_{R_{1/2}}$, except that the relation with the b-value is largely lost. As for the minor axis ratio, the relation is tighter at $1\,R_{1/2,*}$, again likely related to the determination of $\delta_{R_{1/2}}$ within one half-mass radius. The fact that galaxies with a higher anisotropy are generally flatter in the face-on and edge-on views leads to more prolate shapes at the high anisotropy end, and high values of q for low anisotropies lead to more oblate shapes at the low anisotropy end. This trend is seen for the triaxiality at both radial distances (right column of Figure 5.2), although the variance is larger than for the axis ratios. As for the axis ratios, the trend is slightly tighter at $1\,R_{1/2,*}$. From this, we conclude that all three shape parameters considered correlate with the anisotropy, though only the minor axis ratio, i.e., the edge-on ellipticity, provides a tight relation together with the b-value for the determination of the anisotropy from a galaxy's

projection. Clearly, both the degree of order in the orbits and the morphology strongly drive the shapes of galaxies.

The relations of the shape parameters with both the anisotropy and the λ_R-parameter show that even though the triaxiality encodes the 3D shape information of a galaxy as a function of both axis ratios, an axis ratio can provide more meaningful information on certain galaxy properties. This means that even for randomly oriented galaxies that are observed, it should be possible to further constrain certain galaxy properties given the inclination and the projected view.

5.3 Relations with the Mass

Total Mass

We now turn to the relation between the global DM halo shapes of all DM particles attributed to a given galaxy and the total galaxy masses. Given that these properties are heavily influenced by the exact cut of `SUBFIND` for subhalos (see Section 2.1 for more details), only main galaxies are considered for these relations. For the minor axis ratio, s, we find smaller values of s with increasing mass (top left plot of Figure 5.3) and higher values for the triaxiality (bottom left plot). Note that the first and last mass bins have large uncertainties due to low number statistics, and the first mass bins are likely further biased by the lower half-mass radius threshold of the galaxy sample. The highest mass bins are also limited in number and mass due to the medium-sized volume of the cosmological box. In a future study, the shape statistics will be extended by including halos in the larger cosmological volumes.

The smaller minor axis ratio for more massive halos is consistent with early studies of DM halo shapes in DM-only simulations (e.g. Kasun & Evrard, 2005; Allgood et al., 2006; Bett et al., 2007). The tendency towards prolate shapes for the more massive galaxies was also pointed out by Bett et al. (2007) to be related to massive galaxies accreting matter from filaments for the Millenium simulation, leading to the more elongated shapes. In fact, we find consistent results in both median values and scatter for s and T with their results (right column of Figure 5.3). The minor axis ratios of the Magneticum halos reach higher values for lower masses, which may be a result of the higher resolution compared to the Millenium simulation ($m_{\mathrm{DM}} = 3.6 \times 10^7\,\mathrm{M}_\odot\,h^{-1}$ compared to $m_{\mathrm{DM}} = 8.6 \times 10^8\,\mathrm{M}_\odot\,h^{-1}$ for the DM particle mass). A further resolution analysis of how the shape statistics change with resolution is beyond the scope of this work. Similarly, the triaxiality of the lower-mass Magneticum halos is slightly smaller than in the Millenium simulation, again possibly linked to the resolution.

Stellar Mass

Having inspected the correlation of the total mass with the DM halo's shape, we now explore the relations between the stellar mass and the shape parameters at three half-mass radii (Figure 5.4). It is remarkable how the medians of both axis ratios stay nearly constant with stellar mass, showing only a very slight downward trend for q and upward for s. Still, these

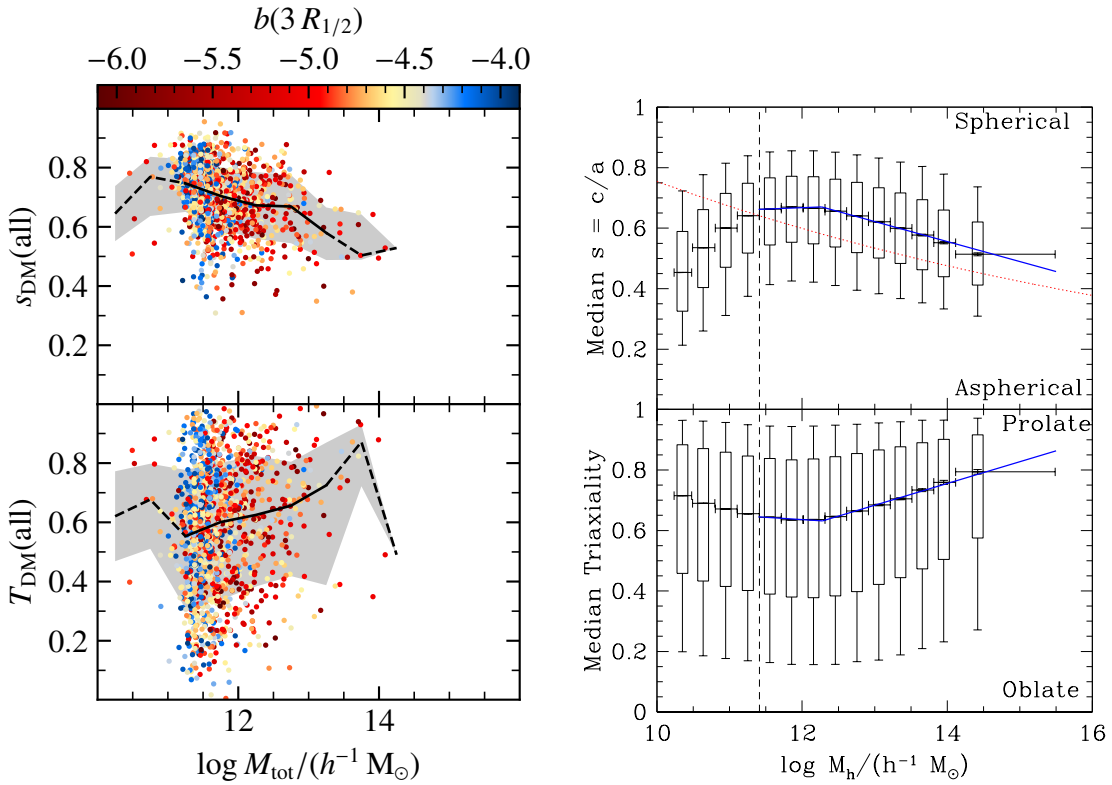

Figure 5.3: *Left*: Relation between the total mass and the full DM halo shape parameters, $s_{\rm DM}$ and $T_{\rm DM}$, for all main galaxies in the Magneticum sample, colored by the b-value. The solid black lines indicate the median values in the respective mass bins and the shaded regions the 1σ ranges (containing 68% of the galaxies above and below the median). *Right*: Figure 12 from Bett et al. (2007) with the DM halo masses and shapes from the Millenium simulation (Springel et al., 2005b). The short, horizontal black bars indicate the median values, the boxes the 1σ ranges, and the extended vertical lines the 2σ ranges. The solid blue line is a broken-line fit to the median values and the dotted red line is a fit from Allgood et al. (2006) (which corresponds to a different definition of a halo, however, as noted by Bett et al., 2007). The vertical dashed line marks the halo mass corresponding to 300 DM particles. The x- and y-axes have been set to be equal for proper comparison between the simulations.

slight trends result in a stronger upward relation for the triaxiality with stellar mass. As the LTGs generally have lower masses than the ETGs, this leads to an interesting relation seen for the minor axis ratio, where more massive galaxies have smaller values of s at constant b-value, leading to more triaxial to prolate shapes, which is consistent with the idea that such galaxies accrete matter from random directions. How these relations scale for lower and higher stellar masses by additionally considering galaxies in cosmological volumes at different resolutions will be the subject of future work. Further analysis will also include a more detailed inspection of the triaxiality trends with stellar mass at constant b-value. Overall, the impact of the stellar mass on the shapes appears to be minimal.

Mass-Size Relation

One of the most important relations to test in determining whether the matter distribution in simulated galaxies is realistic or not is the mass-size relation, which is shown for our galaxy

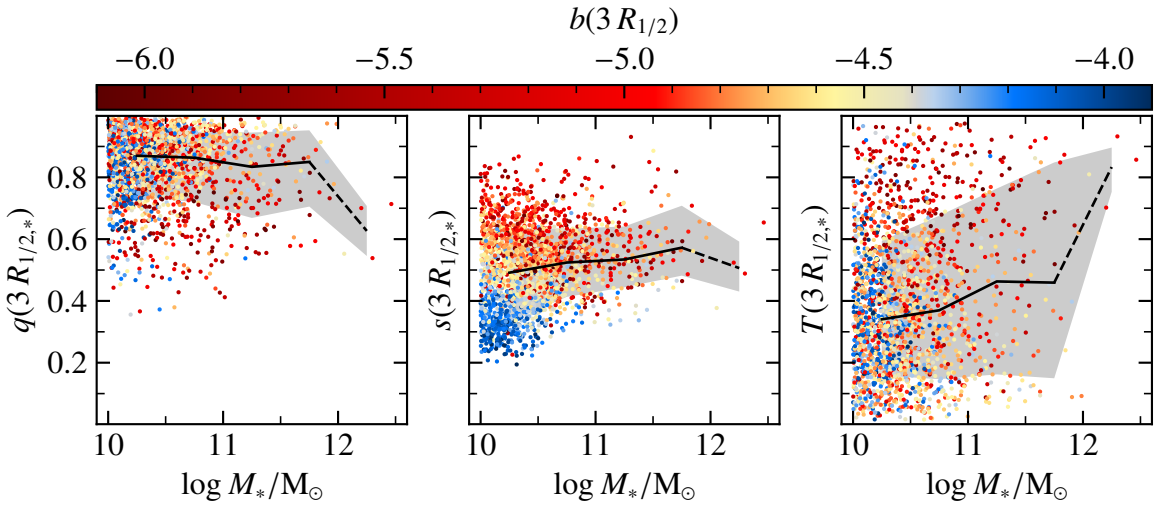

Figure 5.4: Relation between the stellar mass and the stellar shape parameters at three half-mass radii, q, s, and T, colored by the b-value. The black lines indicate the median values in the respective mass bins and the shaded regions the 1σ ranges (containing 68% of the galaxies above and below the median). The dashed part of the lines indicates where there may be effects caused by low number statistics.

sample in Figure 5.5. While the general trend of the stellar half-mass radius increasing with stellar mass is already visible when taking all galaxies in the sample into account (left plot of Figure 5.5), splitting up the sample into ETGs and LTGs (here the intermediate galaxies are left out) shows much tighter relations (center and right plots). This is especially the case for the ETGs, which is likely related to the larger mass range in which they are found, whereas the LTGs mostly have masses of $M_{*,\mathrm{LTGs}} \lesssim 10^{11}\,\mathrm{M}_\odot$. In particular, the ETG relation matches that of the GAMA ETGs (Lange et al., 2015) well, with the exception of a steeper slope of the GAMA ETGs. For the LTGs, the mass-size relation of the Magneticum sample has a comparably large scatter over a small mass range, such that it is more difficult to assess how well it matches the GAMA LTG relation, though they are overall in agreement. Note that our galaxy sample has a lower half-mass radius threshold value of 2 kpc, which prevents a direct comparison with the GAMA relation at low masses. Still, even for the LTGs, which have overall larger half-mass radii, the GAMA relation predicts slightly lower radii than we find for our sample. This may be related to the GAMA half-mass radii being computed from the 2D projection, whereas the half-mass radii of the simulated galaxies are computed taking all three dimensions into account (e.g. Genel et al., 2018).

When considering all galaxies, there is no apparent trend with triaxiality in the mass-size relation. We find that stellar shapes tend to be more prolate at high masses and large half-mass radii. By splitting the galaxy sample by morphology, the trend of LTGs having more oblate stellar shapes at $3\,R_{1/2,*}$ is recovered, whereas a large fraction of ETGs have prolate shapes. This is consistent with the more massive galaxies generally being ETGs and the trend of massive galaxies being more prolate. Interestingly, the strongest trend with triaxiality in the mass-size relation is seen for the ETGs, where galaxies with larger half-mass radii have the tendency to be more prolate. The origin of this is not entirely clear, but may be related to the

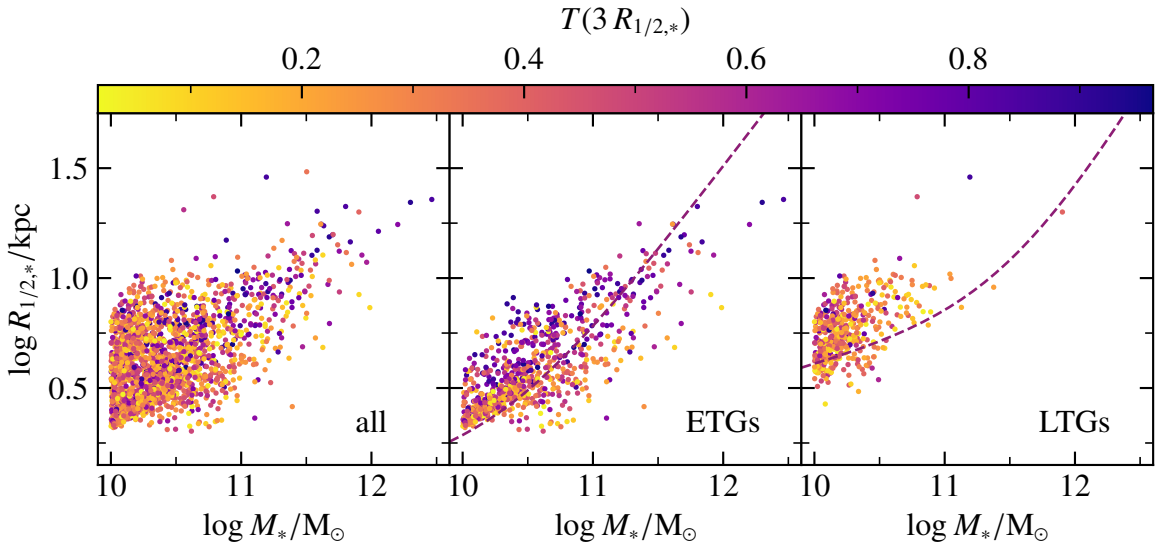

Figure 5.5: Mass-size relation of the Magneticum galaxy sample for all galaxies, only ETGs ($b \leq -4.73$), and only LTGs ($b \geq -4.35$), colored by triaxiality. The dashed lines indicate the two-component fits to the GAMA ETGs and LTGs by Lange et al. (2015) in the r-band for their morphology cut.

half-mass radius being computed by defining it as the radius of a sphere containing half of the mass. This leads to an elongated galaxy having a larger half-mass radius than if it were spherical in shape. For the LTGs, there is no clear trend with triaxiality. Note that the two LTGs with the largest half-mass radii are both undergoing mergers, such that their radii and shapes have little meaning. Clearly, splitting the mass-size relation between ETGs and LTGs is not only essential for the mass-size relation itself, but also for revealing the triaxiality trend in the mass-size relation for ETGs. On the whole, it is found that not the stellar mass itself, but the mass distribution through the mass-size relation is related to the stellar shape.

5.4 Relations with the Formation History

Specific Star Formation Rate

Moving towards parameters related to the formation histories of galaxies, we compare the specific star formation rate (sSFR) with the shape parameters (Figure 5.6). Note that the galaxies found here are mainly LTGs. We find a clear correlation of galaxies with higher sSFR having smaller minor axis ratios, s, with the relation being the tightest for LTGs. In contrast to the relation with the mean stellar ages, the trend with s is not so clear at constant b-value for intermediate galaxies or ETGs, however. The scatter towards larger values of s is especially higher for intermediate galaxies and ETGs. We find an approximately constant median of q and the triaxiality with the sSFR. There may be a slight downward trend of the major axis ratio with increasing sSFR, which is accompanied by an increasing downward scatter, such that the lowest values of q are only reached by galaxies with high sSFR. However, this could be due to low number statistics at the low sSFR end. In the future,

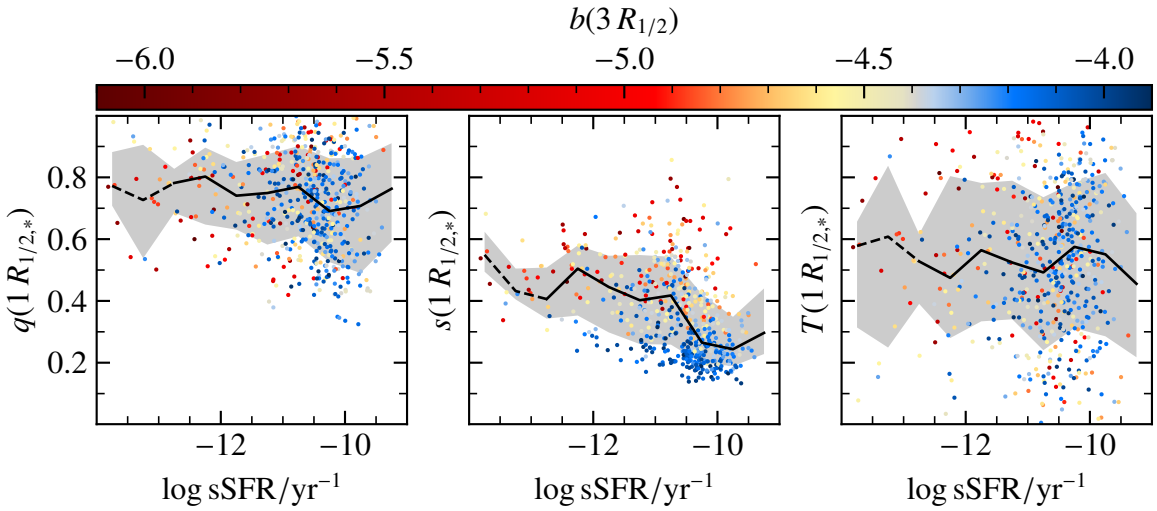

Figure 5.6: Relation between the specific star formation rate and the stellar shape parameters at $1\,R_{1/2,*}$, q, s, and T, colored by the b-value. The black lines indicate the median values in the respective sSFR bins and the shaded regions the 1σ ranges (containing 68% of the galaxies above and below the median). The dashed part of the lines indicates where there may be effects caused by low number statistics.

larger cosmological simulations with a larger sample of star forming intermediate galaxies and ETGs could better show if there is a relation found for the shapes of these types of galaxies with the sSFR. Finally, we find the trend of LTGs having a high sSFR and ETGs having a low sSFR, with many ETGs having no ongoing star formation at all, which is unsurprising. The few ETGs in which stars are being formed at $z = 0$ are likely experiencing starbursts, which could be triggered through a recent gas-rich merger.

Stellar Ages

A quantity that is related to the ongoing star formation is the mean stellar age. The stellar shape parameters are compared with the mean central stellar ages within one half-mass radius in Figure 5.7. Most galaxies have old central stellar ages of $\langle t_{\mathrm{age},*} \rangle \gtrsim 8\,\mathrm{Gyr}$, which is especially the case for the ETGs (note that the sample of galaxies for which mean stellar ages are available has masses $M_* > 3 \times 10^{10}\,\mathrm{M}_\odot$, which mainly consists of ETGs). Most of the galaxies with younger stellar ages are intermediate, though there are a few LTGs and ETGs that also have young stellar populations (top row). The majority of these galaxies have high specific star formation rates (bottom row), independent of their b-value (bottom row), whereas galaxies with older stellar populations generally have little or no ongoing star formation. First of all, we conclude from this that the mean stellar age within only one half-mass radius is an indicator for the total specific star formation rate of a galaxy. Combined with the finding that most ETGs do not have ongoing star formation, it also becomes apparent that wet mergers can occur in all types of galaxies and trigger starbursts.

The median values and scatters of q and the triaxiality are approximately constant for different central stellar ages, though the triaxiality may be minimally larger for older stellar populations. In contrast, we again find a clear trend for the minor axis ratio, with s tending

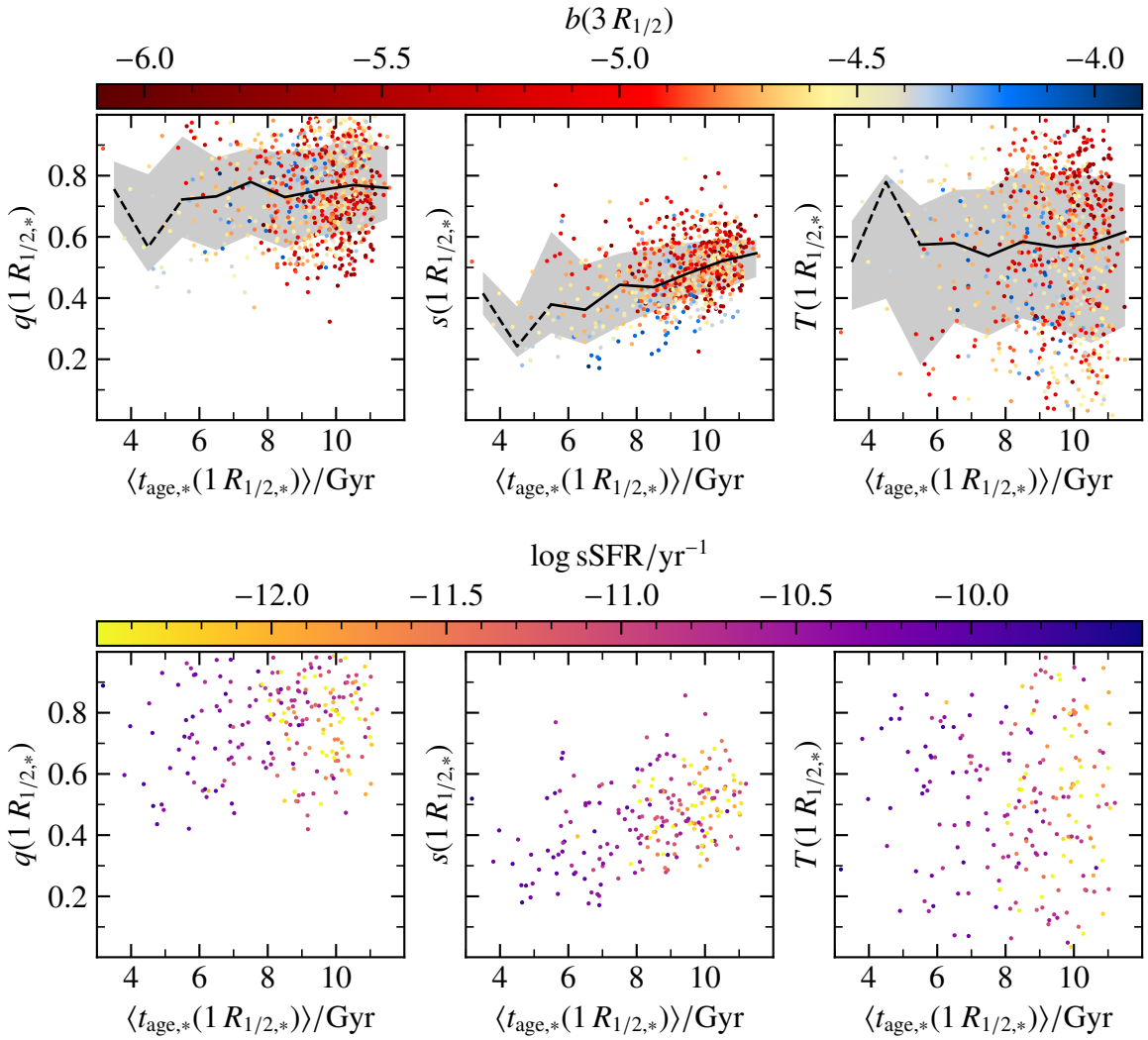

Figure 5.7: Relation between the mean stellar ages within 1 $R_{1/2,*}$ and the stellar shape parameters at 1 $R_{1/2,*}$, q, s, and T, colored by the b-value (top) and by the specific star formation rate (bottom). The black lines indicate the median values in the respective age bins and the shaded regions the 1σ ranges (containing 68% of the galaxies above and below the median). The dashed part of the lines indicates where there may be effects caused by low number statistics. In the bottom row, only the galaxies with a specific star formation rate larger than zero are displayed.

to be larger for older stellar populations, which means that younger stellar populations are usually flatter from an edge-on perspective. This trend is even true at constant b-value, which means that galaxies with an overall older stellar population tend to be less flat than galaxies at the same b-value with younger stellar populations. This may be due to an inflation of galaxies over time through dynamical scattering. In the future, further analysis of how the shapes of galaxies change over time depending on their mean stellar ages may reveal further insights into the relations between shapes, morphologies and star formation histories. Interestingly, the galaxies with younger stellar populations feature a larger variance of s compared to galaxies with older centers. This may be related to mergers occurring independently of morphology, such that starbursts leading to especially young stellar populations cover a wide range of flatness.

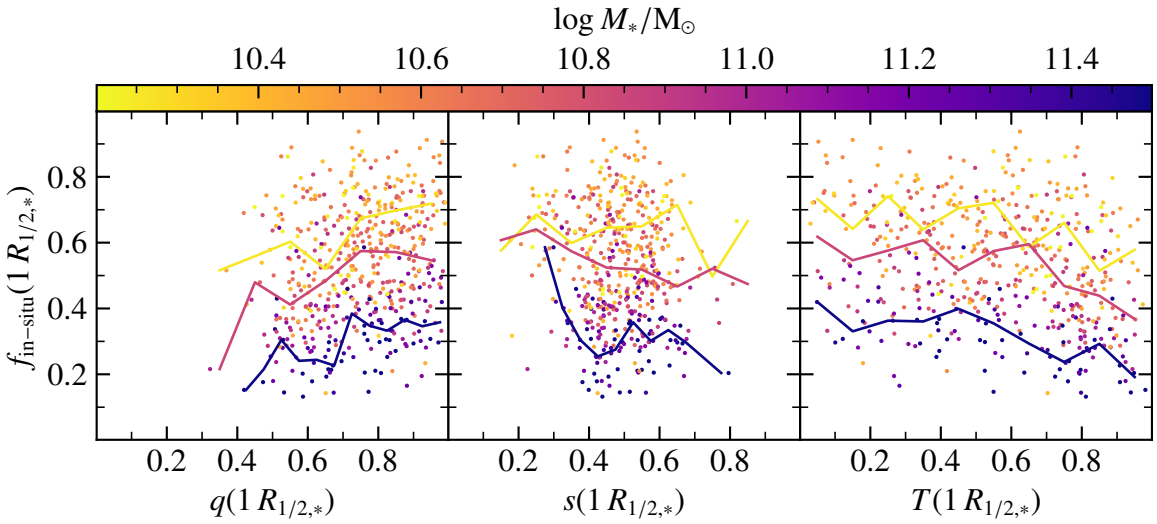

Figure 5.8: Relation between the in-situ star formation fraction within $1\,R_{1/2,*}$ and the stellar shape parameters at $1\,R_{1/2,*}$, q, s, and T, colored by the stellar mass. The solid lines indicate the median values in the respective in-situ fraction bins ($\log M_*/M_\odot < 10.5$, $10.5 \leq \log M_*/M_\odot < 11.2$, and $\log M_*/M_\odot \geq 11.2$).

In-Situ Fraction

The fraction of stars a galaxy made itself compared to the amount of stars that have been accreted is a crucial indicator of the violence in the formation pathway of a galaxy. Therefore, a correlation between the in-situ fraction and the shape of a galaxy should be expected if the formation history is the main driver of different shapes. Thus, we look at the in-situ fraction within one half-mass radius. While there are no trends to be seen at first glance, we find trends for all three shape parameters, q, s, and T, with the in-situ fraction at constant stellar mass (Figure 5.8): at constant M_*, the in-situ fraction increases with larger major axis ratio and decreases with larger minor axis ratio and triaxiality. This means that more circular galaxies from a face-on perspective and flatter galaxies from an edge-on perspective (and thus more oblate) tend to have larger in-situ fractions. While the in-situ fraction is strongly related to the stellar mass by being small for massive galaxies and large for less massive galaxies, all three shape parameters disentangle this relation even further. As a result, the knowledge of q, s, or T can be used together with the stellar mass to constrain the in-situ fraction even more than it would be possible using only the stellar mass. This is of particular relevance for observations, where the projected view of a galaxy and its inclination could be used to deduce one of the axis ratios from any orientation. In future work, the relation between the in-situ fraction and the ellipticity for random orientations of the galaxies will be further analyzed, which may further aid in constraining the in-situ fractions of observed galaxies, providing a much needed possibility for observers to obtain in-situ fractions, even if only indirectly.

Overall, it can be concluded that the formation history has an impact on the shape of a galaxy. To further understand how different merger and accretion histories influence the shapes, future work will involve tracking galaxies back through time using merger trees.

5.5 Relations with the Angular Momentum

Finally, we turn to a three-dimensional kinematic parameter: the angular momenta of the stellar and DM components, $\boldsymbol{j}_*$ and $\boldsymbol{j}_{\rm DM}$. Their absolute values clearly correlate with each other, where galaxies with a large stellar angular momentum also tend to have a large DM angular momentum (left plot of Figure 5.9). Around 75% of galaxies have a larger angular momentum in the stellar component than in DM. Interestingly, there are clear lower and upper bounds of $j_{\rm DM}$ for a given $j_* \gtrsim 10^2\,\mathrm{kpc\,km\,s^{-1}}$, which form an increasingly tight relation at higher angular momenta. The angular momentum vectors of the stellar and DM components are generally strongly aligned for high angular momenta, which is particularly the case for $j_*, j_{\rm DM} \gtrsim 10^2\,\mathrm{kpc\,km\,s^{-1}}$ and is the case for the majority of the galaxies. For galaxies with low angular momenta, however, the correlation breaks down and the angular momenta become largely independent of each other. These galaxies also feature the largest misalignment angles between $\boldsymbol{j}_*$ and $\boldsymbol{j}_{\rm DM}$. This suggests that the alignment is almost random for smaller angular momenta, although it should be further analyzed statistically in the future. It is also interesting that the median DM angular momentum is almost constant, only increasing with a small slope for low values of j_*. This means that galaxies with low stellar angular momenta mostly have decoupled DM components. Such systems are likely a result of their merger histories, in which the components are decoupled from each other. Additionally, the galaxies with high angular momenta, but large misalignments between them, could be inspected in more detail, which will likely reveal connections with the individual merger histories.

The alignment angle between $\boldsymbol{j}_*$ and $\boldsymbol{j}_{\rm DM}$ also has a trend with the b-value (right plot of Figure 5.9): LTGs tend to have aligned angular momenta, whereas intermediate galaxies and ETGs have increasingly larger values and scatters of $\theta(\boldsymbol{j}_*, \boldsymbol{j}_{\rm DM})$. However, even for the lowest b-values, the alignment between the stellar and DM angular momenta is not random, which would require a median of 90°. Counter-rotating DM compared to the stellar component appears to be rare for LTGs, but is found for both intermediate galaxies and ETGs. These findings are consistent with the left side of Figure 5.9, since we expect LTGs to generally have higher angular stellar momenta. There does not appear to be a direct relation between the stellar mass and the alignment, besides the LTGs usually having lower masses than ETGs.

We now consider the relation of the angular momenta alignment angle with the shape parameters at three stellar half-mass radii (Figure 5.10). Considering the trend of $\theta(\boldsymbol{j}_*, \boldsymbol{j}_{\rm DM})$ with the b-value seen in the right plot of Figure 5.9 and the previously discussed relation of the minor axis ratio, s, with the b-value, it is not surprising to find the alignment angle being correlated with s, too: galaxies with good alignment between the stellar and DM angular momenta tend to have flat edge-on shapes. This is also consistent with the result that well-aligned angular momenta tend to correspond to higher stellar angular momenta (as seen in the left plot of Figure 5.9) and with galaxies having flatter shapes for high values of λ_R (Figure 5.1), where it would be expected that there is a correlation between λ_R and j_* because of the relation between λ_R and the b-value (Schulze et al., 2018) and through the dependence of the b-value on j_*. For alignments of $\theta(\boldsymbol{j}_*, \boldsymbol{j}_{\rm DM}) \gtrsim 45°$, the median minor axis ratio and

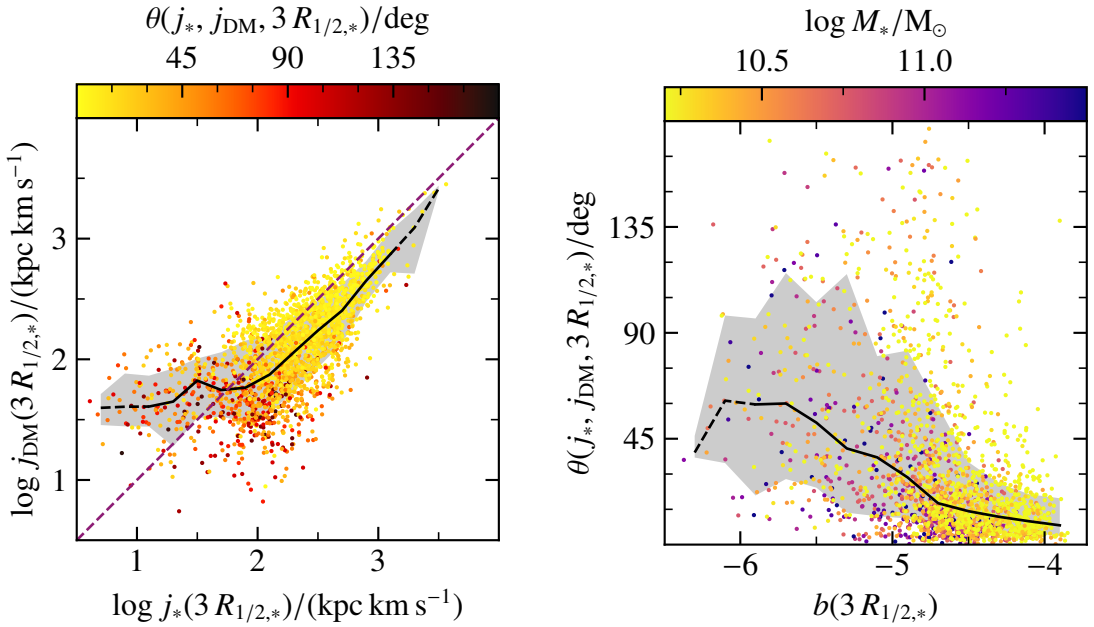

Figure 5.9: *Left*: Relation between the absolute values of the stellar and DM angular momenta, colored by the angle between their vectors, $\theta(\boldsymbol{j}_*, \boldsymbol{j}_{\rm DM})$, all for within three half-mass radii. The dashed blackberry line denotes where the absolute angular momenta are equal to each other. *Right*: Relation between the b-value and $\theta(\boldsymbol{j}_*, \boldsymbol{j}_{\rm DM})$ within $3\,R_{1/2,*}$, colored by the stellar mass. The black lines indicate the median values in the respective mass bins and the shaded regions the 1σ ranges (containing 68% of the galaxies above and below the median). The dashed part of the lines indicates where there may be effects caused by low number statistics.

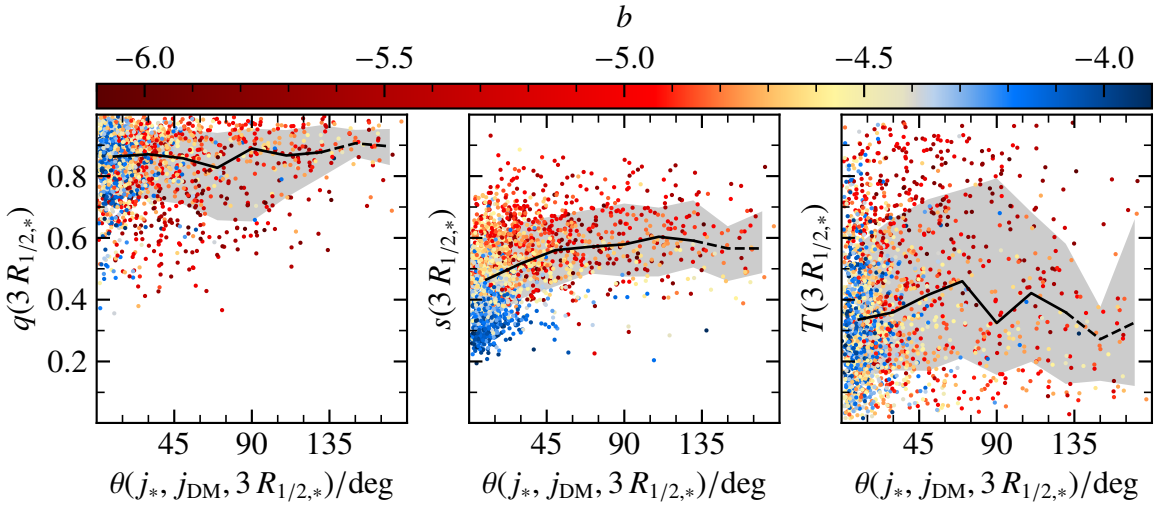

Figure 5.10: Relation between the alignment angle of the stellar and DM angular momenta within $3\,R_{1/2,*}$ and the corresponding shape parameters, q, s, and T, colored by the b-value. The solid black lines indicate the median values in the respective angle bins and the shaded regions the 1σ ranges (containing 68% of the galaxies above and below the median).

its scatter stay approximately constant. For both the major axis ratio and the triaxiality, there are no clear trends with the alignment angle. A curious feature, however, is the large upward scatter of the triaxiality at $\theta(\boldsymbol{j}_*, \boldsymbol{j}_{\rm DM}) \approx 90°$, which decreases towards smaller and larger angles. In the future, larger samples of galaxies may help resolve if this has a physical origin or if it is due to low number statistics. It should be highlighted that large misalignments of the angular momenta do not preferably correspond to triaxial or prolate shapes, but cover a similar range of triaxialities as galaxies with strong alignment with mostly oblate to triaxial shapes. In future work, the behavior of stellar and dark matter shapes with respect to the absolute angular momenta will be inspected and an analysis of their radial correlation will be performed.

5.6 Summary & Conclusion

The relations between the shapes and other galaxy properties are found to feature a multitude of trends: as expected, the relations of the minor axis ratio with the λ_R-parameter and the anisotropy are consistent with those found in the literature (e.g. Binney, 2005; Schulze et al., 2018), where galaxies with higher rotational support or with higher anisotropy tend to be flatter. This supports the idea that on the one hand, rotational support generally flattens galaxies, and on the other hand, even slow rotators can be flattened – not through rotation, but through the anisotropy of the velocity distribution that is understood to be a remnant of the formation history of ETGs (Illingworth, 1977). The relation between the minor axis ratio and the anisotropy within $3\,R_{1/2,*}$ even reveals a tight correlation given a fixed b-value, where again s is smaller for higher values of the anisotropy. This is true for the minor axis ratios at both $1\,R_{1/2,*}$ and $3\,R_{1/2,*}$. In addition to the trends with the minor axis ratio, the λ_R-parameter is also correlated with the triaxiality at $3\,R_{1/2,*}$: rotationally more supported galaxies tend to have triaxial to oblate shapes, whereas dispersion dominated galaxies tend to be triaxial to prolate. This is consistent with LTGs tending to be flat and being more rotationally supported. The much weaker trend at $1\,R_{1/2,*}$ is caused by the major axis ratio, $q(1\,R_{1/2,*})$, having a much larger variety of values than at $3\,R_{1/2,*}$. This is consistent with the previous finding that the galaxies' shapes are more oblate in the outer regions than in the inner ones (Section 4.1). Lastly, there are also weak correlations of the major axis ratio and triaxiality with the anisotropy, which do not have a tight relation at constant b-value, however: galaxies with higher anisotropies tend to have smaller values of q and be more prolate. These properties are likely related to the merger histories of such galaxies, where many accreted structures from different directions lead to more triaxial to prolate shapes with higher anisotropies. The fact that the tightest trends are found for the minor axis ratio, however, means that the edge-on ellipticity and the projected kinematic properties are a powerful combination in the investigation of galaxies.

For the DM halo shapes, similar trends to those found by Bett et al. (2007) for the DM-only Millenium simulation are recovered: DM halos tend to be flatter and more prolate at higher total masses. The median values and scatters of s and T are comparable to the findings

of Bett et al. (2007). This suggests that the additional baryonic component included in the simulations considered in this work does not strongly alter the shapes of the full DM halos. This is also consistent with the idea that these shapes are a result of halos forming through the collapse of matter along filament, leading to prolate shapes.

The mass-size relation of the stellar component of galaxies shows a clear trend with the triaxiality for ETGs, where larger galaxies at a given stellar mass have more prolate shapes and galaxies with smaller half-mass radii are more oblate. For the LTGs, which generally are larger at the same stellar mass, this relation cannot be found. This shows how both the shapes and the mass-size relation encode the mass distribution of galaxies, resulting in a slight correlation. The expected trend of more massive galaxies having more spherical shapes cannot be found, showing that not the stellar mass itself, but only the mass distribution is correlated with the shape of a galaxy.

The findings for the relation between the shape parameters and various properties of the formation history are overall consistent with the expectations: galaxies with ongoing star formation and younger stellar populations tend to be LTGs and are generally flatter. Interestingly, the galaxy sample also features a small number of star-forming ETGs and intermediate galaxies, which commonly also have younger stellar populations. These galaxies likely were hosts of starbursts through gas-rich mergers. Of course, such mergers are independent of the galaxies' morphologies in which they occur, and they appear to only occur in very few ETGs. A second interesting class of objects are quiescent and old LTGs, which seem to have more puffed-up shapes than the actively star-forming LTGs. These galaxies likely are located in a cluster environment, where their gas has been stripped away. This puffing-up would then occur over time through relaxation or other processes typical for cluster environments as introduced in Section 1.1.3. Neither the specific star formation rate, nor the mean central stellar age of galaxies correlates with the major axis ratio or the triaxiality. Finally, a fascinating trend with the in-situ fraction and the stellar mass can be found for all three shape parameters: at a given mass, galaxies with larger in-situ fractions tend to be more circular from a face-on perspective, flatter from an edge-on perspective, and therefore more oblate. As a parameter that is directly linked to the formation history, such a relation of the in-situ fraction with the shape shows how also the shape is connected to the past evolution of a galaxy. These tight relations further give observers a powerful way of constraining the in-situ fraction with easily obtainable properties.

As expected, the alignment between the stellar and DM angular momenta is also related to the morphologies and shapes: galaxies with well-aligned angular momenta tend to be LTGs and have flatter shapes. Above an alignment angle of approximately 45°, the median value of s and its scatter stay constant, showing that for strongly decoupled stellar and DM components, the shape is independent of the misalignment. The alignment angle does not correlate with the major axis ratio or the triaxiality, however.

6 Radial Profiles

Until now, only the behavior of the shape parameters at fixed inner to outer radii and their relations with other quantities at these radii have been investigated. In this chapter, the radial shape profiles and alignments are analyzed, where a particular focus is put on how these differ with respect to two kinematic classifications: first, the kinematic groups (introduced in Section 1.2.2) are based on the edge-on projected velocity maps, which carry information about the formation history by revealing a variety of different kinematic features on a larger (e.g. regular rotators or prolate rotators) or more local scale (e.g. KDCs). While regular rotators can be expected to feature overall flatter and more oblate shapes because of their rotational support, non-rotators will likely be more spherical and triaxial to prolate. The minor axis of the stellar shapes and the angular momenta of regular rotators should be well aligned, whereas the alignment for prolate rotators is expected to be close to 90° by definition. Non-rotators likely have random alignments.

The second kinematic classification are the radial λ_R-profile groups. As shown by Schulze et al. (2020), these classes also encode the formation history, having different amounts of matter that have been accreted through mergers, in particular through major mergers. As such, their relation with the shapes and the alignments has the potential of leading to new insights for the connection between the formation history and shapes. The radial profiles will also show if and how an increased amount of major mergers can affect the shapes and alignments of galaxies. Lastly, the decreasers have been found to have an inner in-situ dominated region, where the peak of the λ_R-profile indicates the transition to the outer ex-situ dominated region, such that differences in the inner and outer shapes of decreasers may be found.

The radial behavior of the shape parameters and alignment angles have the potential to reveal differences between the kinematic groups and radial λ_R-profile groups with respect to their inner and outer regions. These can provide further insights into their formation histories and enable improved interpretations of the radial ellipticity profiles in observations.

Finally, the possibility of directly comparing the stellar and DM shapes and their alignments in a radial manner for the different classes will show if and how closely the DM follows the stellar component. This aspect is vital for the understanding of the distribution of DM in galaxies, which is currently not directly detectable in observations. It further has the potential to allow a better understanding of the different evolution of the stellar and DM components.

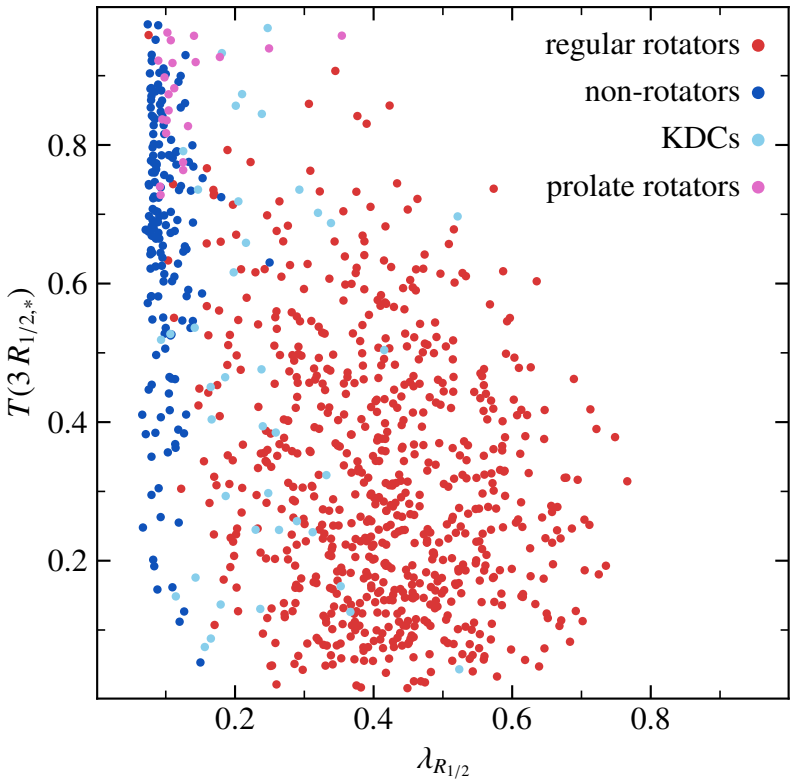

Figure 6.1: Location of the kinematic groups in the relation between $\lambda_{R_{1/2}}$ and the stellar triaxiality at $3\,R_{1/2,*}$.

6.1 Relations with the Kinematic Groups

λ_R-Parameter & Axis Ratios

Before turning to the radial profiles of the kinematic groups, we first look at the location of the different groups in two of the plots we have previously seen. As discussed by Schulze et al. (2018), the non-rotators usually have low values of $\lambda_{R_{1/2}} \lesssim 0.2$ (which is a result of the definition of non-rotators), as well as most of the prolate rotators (Figure 6.1). The regular rotators are mostly found with $\lambda_{R_{1/2}} \gtrsim 0.2$, and finally, the kinematically distinct cores span the lower range of $\lambda_{R_{1/2}}$ that the regular rotators occupy and can also reach slightly lower values. The shapes of the kinematic groups also show clear trends at $3\,R_{1/2,*}$: non-rotators tend to be more prolate, while regular rotators tend to be more oblate, in particular the ones with higher values of $\lambda_{R_{1/2}}$ (as shown in Section 5.1 for the full galaxy sample). KDCs do not appear to have a preferred triaxiality at $3\,R_{1/2,*}$, having any values between $T = 0$ and 1. Since our category of KDCs encompass galaxies with kinematically distinct cores without closer specifying in what way the cores are distinct or what the outer regions of the galaxies are like in a kinematic sense, their shapes can be anything as a result. Finally, we find the interesting behavior that prolate rotators have a very strong preference for prolate shapes, even at $3\,R_{1/2,*}$.

These trends with the triaxiality can also be found reflected in the individual axis ratios at $3\,R_{1/2,*}$, which were discussed for the full galaxy sample in Section 4.1: regular rotators tend to have large major axis ratios, q, i.e., they are the most circular from a face-on perspective

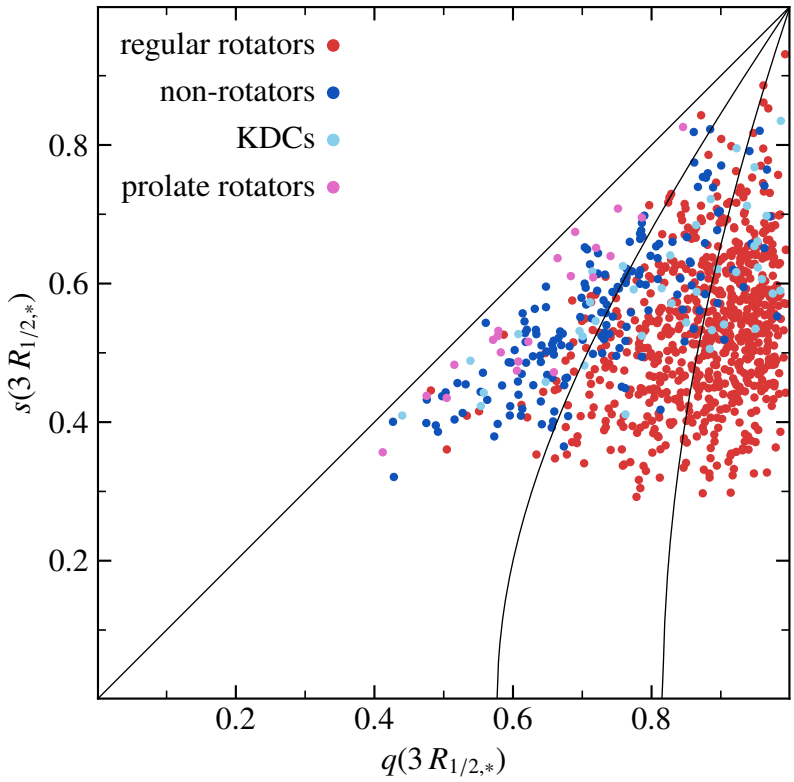

Figure 6.2: Axis ratios at $3\,R_{1/2,*}$ of the kinematic groups. The solid lines indicate the borders between prolate, triaxial, and oblate shapes, from left to right, respectively.

(Figure 6.2). They are the only kinematic group to feature flat oblate shapes with minor axis ratios of $s \lesssim 0.5$. In contrast, prolate and non-rotators tend to have lower values of q, leading to more elongated shapes. KDCs overall have similar combinations of q and s as the non-rotators, except that there are relatively more KDCs with oblate shapes. It is not immediately clear where this similarity of shapes comes from, since the kinematic behavior is overall expected to be very different. All kinematic groups can have somewhat spherical shapes, although very spherical shapes are rare at three half-mass radii in general.

Radial Shape Parameters

For the radial profiles, the stellar and DM shape parameters are computed at 100 equally-spaced radial distances from $0.05\,R_{1/2,*}$ to $5\,R_{1/2,*}$, but only at radial distances larger than the respective stellar or DM softening length, $R > \epsilon_{\rm soft}$. For the full galaxy sample, and for the individual kinematic groups, the median and scatter of the shape parameters are determined at all radial distances at which at least 25% of the galaxies or a number of 15 galaxies (whichever is larger) satisfy the condition $R > \epsilon_{\rm soft}$ to avoid statistical artifacts.

For the full galaxy sample, we observe an average increase of the major axis ratio, q, in the considered range until $5\,R_{1/2,*}$, which remarkably is almost identical for the stellar and DM components (top row of Figure 6.3). The slope of the profile is steepest in the inner regions and quickly drops towards the outside, reaching $q \approx 0.9$. Only the downward scatter is larger for the stellar component, which means that stellar shapes are more often less

circular from a face-on perspective than the DM. The minor axis ratio, s, however, shows a larger discrepancy between the stellar and DM components: while the stellar values of s increase linearly from $s \approx 0.4$ to $s \approx 0.55$, the values of s_{DM} behave more similarly to the q_* and q_{DM}-profiles by increasing strongly at low radii and flattening out in the outer regions, reaching $s_{\mathrm{DM}} \approx 0.7$. The DM component has noticeably larger median values of s for $R \gtrsim R_{1/2,*}$ by up to $\Delta s \approx 0.2$. This means that DM shapes are generally more spherical than stellar shapes (which is true for all kinematic groups as well, as seen in the bottom rows of Figure 6.3). Both components tend to have slightly more spherical shapes in the outer galaxy regions. It is unclear to what degree we observe a stellar halo here, since many of the considered galaxies are not well resolved in the outskirts. Future inspections of the radial shapes of galaxies in high-resolution cosmological simulations will help to gain a better understanding of this question. The deviations between the stellar and DM minor axis ratios lead to an increasing difference between their triaxialities. For both components, T decreases with increasing radius, which is mainly a result of q approaching 1, which would lead to $T = 0$, i.e., a perfectly oblate shape. The drop of T is strongest in the inner regions and the profile flattens out towards the outskirts, as for q and s. The median triaxialities indicate overall triaxial shapes, with the stellar shapes tending towards being more oblate than the DM, which is a result of the lower values of s for the stellar component. While the absolute difference between the stellar and DM triaxialities is smaller than for s, the scatter is larger since T is a function of q and s, for which galaxies can have different combinations, leading to the larger scatter.

All four kinematic groups feature overall distinct shape profiles, where especially the stellar and DM major axis ratios and triaxialities differ among the groups. Interestingly, the DM minor axis ratio, s_{DM}, is similar among all kinematic groups, which shows that the edge-on perspective of DM is only weakly dependent on the stellar kinematics.

The radial shapes of the regular rotators (second row of Figure 6.3) actually have very similar median profiles to that of the full sample, which is a result of this being the most common group (around 75% of the classified galaxies are regular rotators). The downward scatter of q is smaller than for the full sample, which means that regular rotators tend to have more circular stellar shapes from a face-on perspective. Also, the scatter of q_{DM} is smaller. The DM profile now matches the stellar q-profile even better than before and the median values are minimally higher than for the full sample. However, these differences are likely small enough to be statistically insignificant. There are also only small differences between the s-profiles of the regular rotators and of the full sample, with the most notable change being the smaller scatter for the regular rotators. These differences result in more oblate shapes of the regular rotators with a slightly smaller scatter of the triaxialities. The clearly distinct behavior of the inner region $R \lesssim 1.5\, R_{1/2,*}$ is mainly a result of increasing values of q and of the large slope of the s_{DM}-profile. Whether this is related to a bulge or bar, or if it is a resolution issue at the center due to softening, is not possible to conclude from these profiles alone. It will be necessary to follow up on this matter in the future by investigating the radial shape profiles of a subsample of larger galaxies that have well-resolved central regions and of

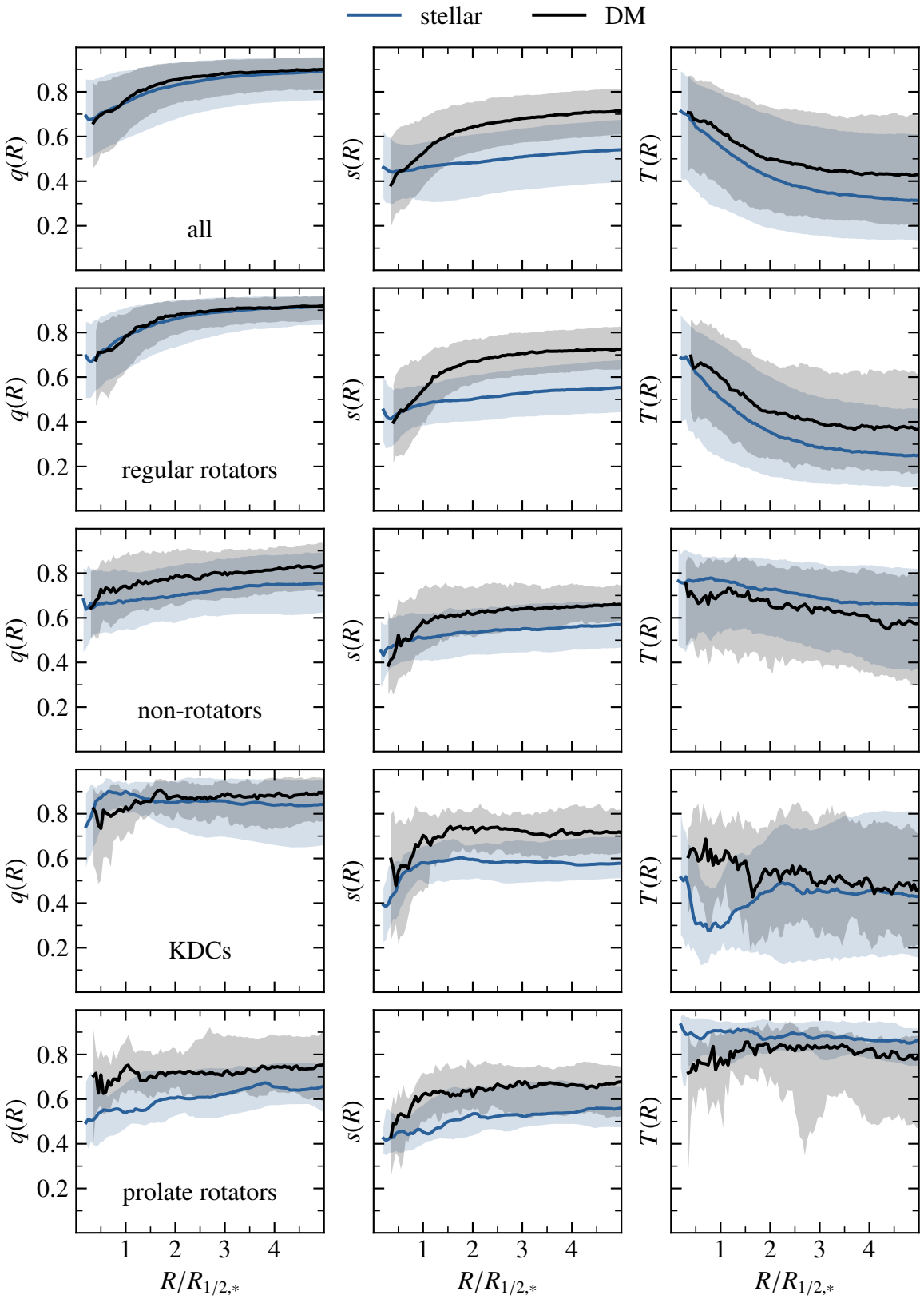

Figure 6.3: Radial shape profiles of the stellar (blue) and DM (black) components of the full galaxy sample (top row) and of the individual kinematic groups (bottom rows) from one to five stellar half-mass radii. The solid lines indicate the median at each radial distance of the galaxies for which that radial distance is larger than the softening length (1 kpc for the stellar component, 2 kpc for the DM component). Points at a given radial distance are plotted if $R > \epsilon_{\mathrm{soft}}$ for at least 25% or a number of 15 of the galaxies in the respective kinematic group to prevent statistical artifacts, whichever is larger. The shaded regions are the 1σ ranges containing 68% of the galaxies above and below the median.

galaxies in higher-resolution cosmological simulations. Additionally, splitting the galaxies according to fast- and slow-rotators and according to their morphology via the b-value could give us further insights into the characteristics and drivers of the radial shapes.

The shape profiles of the non-rotators feature lower values of q compared to the regular rotators, especially for the stellar component, which lies below the values of q_{DM} by $\Delta q \approx 0.1$. Both major axis ratios increase approximately linearly, as opposed to the regular rotators, but also have a larger scatter. In contrast to the more oblate shapes of the regular rotators, the large triaxialities of the non-rotators mean that they generally have triaxial to prolate stellar and DM shapes. Interestingly, the DM minor axis ratio is smaller than those of the regular rotators, which means that the DM shapes of non-rotators are flatter from an edge-on perspective. The opposite is true for the stellar component, such that the profiles of s_* and s_{DM} are more similar to each other than for regular rotators. Additionally, s_{DM}-profile flattens at smaller radii, leading to a smaller "core" region. Despite the larger difference between q_* and q_{DM}, the triaxialities are very similar, with the stellar triaxialities falling slightly from $T \approx 0.8$ to $T \approx 0.65$ and T_{DM} again tending towards more triaxial shapes by $\Delta T \approx 0.05$, except that compared to the regular rotators, T_{DM} is lower than T_* for the non-rotators. As before, the scatter of the triaxialities is larger than those of the axis ratios. It is unclear why the DM components of non-rotators tend to be less spherical than for the regular rotators. Possibly, this arises from differences in the contributions of kinematics and the stellar gravitational potential for the DM, depending on the kinematic behavior of the stellar component.

KDCs have the highest major axis ratios in the inner regions of all kinematic groups, in particular for the stellar component at $R \approx 0.75\, R_{1/2,*}$ with $q \approx 0.9$, indicating a distinct behavior in the core region. This shows that the core stellar region is almost circular from a face-on perspective. The stellar minor axis profile also behaves very differently compared to the regular and non-rotators: while it starts at $s \approx 0.4$, like for the regular rotators, it increases rapidly to its peak value and then stays nearly constant (except for the minor decrease after the peak) at almost $s \approx 0.6$, which is slightly higher than what we find for the non-rotators. Combining these axis ratio profiles results in two remarkable triaxiality profiles: while the outer median triaxialities are nearly identical between the stellar and DM components, which slightly decrease between $T \approx 0.55$ and $T \approx 0.45$, the stellar triaxiality shows an entirely different behavior in the central region of $R \lesssim 2\, R_{1/2,*}$. Here, the stellar triaxiality drops down to $T \approx 0.3$, while the DM component's triaxiality follows the same almost linear trend as in the outer regions. This large deviation is driven by the very high stellar value of q in the center, leading to a more oblate shape, whereas q_{DM} only reaches especially high values in the outer regions, where s_{DM} is also higher, such that T_{DM} never drops to such low values. As a result, the triaxiality magnifies the effect of the decoupled core that can be seen for q (and perhaps also for s through the mentioned slight peak feature). Note that the scatter of the triaxialities is much larger than for any other kinematic group in the outer regions, which is likely a result of the KDCs being classified by their core only, without consideration of the kinematics in the outskirts. The stellar value of q decreases towards the outer regions along with the downward scatter, which is very small in the inner regions. In contrast, q_{DM} rises

slowly towards the outer regions and has a smaller scatter than the stellar component beyond $R \approx 1.5\,R_{1/2,*}$. The DM component also does not feature a peak value of q in the inner part, as the stellar component does, which is likely the result of a decoupled stellar core, but could also be influenced by resolution issues due to the larger softening length of the DM. The behavior of the minor axis ratio profiles is also interesting, but subtle: Both the stellar and DM components reach a peak value (at $R \approx 1\,R_{1/2,*}$ and $R \approx 1.5\,R_{1/2,*}$, respectively) and then decline almost negligibly towards the outer regions. As already mentioned, the profile of $s_{\rm DM}$ is comparable to those of the other kinematic groups.

Finally, prolate rotators have the lowest values of q for both the stellar and the DM components. Both increase approximately linearly, where q_* goes from $q_* \approx 0.5$ to $q_* \approx 0.65$ and $q_{\rm DM}$ has a flatter slope, mostly staying in the range of $q_{\rm DM} \approx 0.7$–0.75. The deviation of q between the components is therefore the largest among the kinematic groups. Still, because both q_* and $q_{\rm DM}$ are the lowest of all groups, we find that the DM follows the stellar potential by being more elongated at all considered radii compared to the other kinematic groups. The minor axis ratio profiles are actually similar to those of the regular rotators. This is especially true for the stellar component, while $s_{\rm DM}$ increases faster at small radii, but then flattens earlier and remains slightly smaller than for the regular rotators, right below $s_{\rm DM} \approx 0.7$. It is not clear why the s-profiles are so similar for the prolate and regular rotators. An important future analysis will be to investigate the formation histories of the prolate rotators, which will shed light on a current topic and likely give further insights into what leads to these similarities in edge-on axis ratio profiles. As first found in Figure 6.1, prolate rotators also have prolate shapes. This is not only the case for the stellar component at $3\,R_{1/2,*}$, but even at all inspected radii for both the stellar and DM components. The stellar triaxiality has a very small scatter, which is likely related to all prolate rotators having similar values of q and s, while q is comparably low (the triaxiality becomes very sensitive to q as its value approaches 1). While the median triaxiality of the DM component is also remarkably high and in the prolate region, its downward scatter is much larger, showing that there are a number of cases in which the DM component does not trace the stellar shape that well. These galaxies could have a different formation pathway than the others, which will also be investigated in the future. It is also interesting how the median stellar triaxiality drops slowly towards the outer regions, whereas $T_{\rm DM}$ first increases to a peak at $R \approx 2.5\,R_{1/2,*}$ before dropping again. Because of the small number of galaxies classified as prolate rotators (21 in total), all of these results could be affected by low number statistics and should also be examined in larger cosmological simulations in the future. In particular, the strong dip of the DM triaxiality's scatter at $2.5\,R_{1/2,*}$ is an effect of the small number of prolate galaxies.

In conclusion, a strong correlation is found between most of the shape parameters and the kinematic groups. In particular, the radial profiles reveal a remarkable resemblance of the stellar and DM shapes, except in the core region of KDCs, where the stellar component appear to be decoupled from the DM.

Radial Alignment

Knowing that the DM shapes following those of the stellar component so closely for all kinematic groups, the question remains if the DM shapes are also oriented in the same direction as the stellar component. Additionally, the alignment between the minor axes of the shapes and the angular momentum within $3\,R_{1/2,*}$ can give more insights into the relation between kinematics and shapes. These alignment profiles can also reveal the average shape twists of the stellar and DM components. The alignment angles are computed at the same radii as the shape parameters, i.e., out to $5\,R_{1/2,*}$.

We consider the radial alignment angles between the stellar and DM shapes, and also compare the radial alignment of the shapes with the angular momentum vectors, $\boldsymbol{j}_*$ and $\boldsymbol{j}_{\rm DM}$, at a fixed radius of $3\,R_{1/2,*}$. As seen in Figure 6.4, the alignments of the full galaxy sample are dominated by the behavior of the regular rotators, where only the scatters are smaller when considering the regular rotators alone, just as seen for the shape parameters. For this reason, the alignment profiles of the regular rotators are directly discussed first. The stellar and DM shapes clearly become more aligned towards the outskirts (i.e., the angle between the minor axes of the shape ellipsoids becomes smaller). The median alignment angle falls from around $\theta(*, \mathrm{DM}) \approx 45°$ in the center to around $\theta(*, \mathrm{DM}) \approx 10°$ at $\sim 2\,R_{1/2,*}$, from where on it stays approximately constant. The scatter is largest in the inner region and decreases as the median angle approaches 10°, where the upward scatter is around three times larger than the downward scatter. Overall, there is therefore good alignment of the stellar and DM shapes. The alignment of the stellar shapes with their angular momentum at $3\,R_{1/2,*}$ (middle column) reveals that the median stellar shape is almost fully aligned with $\boldsymbol{j}_*(3\,R_{1/2,*})$ and has no twists beyond $0.5\,R_{1/2,*}$. Only the very inner part shows a slight upward trend, which is still minimal and likely related to the resolution, however. This shows that the stellar component is generally not responsible for the misalignment with the DM shapes in the inner region. In contrast, the median DM alignment with $\boldsymbol{j}_*$ shows a similar profile to the one between the stellar and DM shapes: the large angle in the center region decreases and reaches a value of slightly under $\theta(\mathrm{DM}, \boldsymbol{j}_*) \approx 15°$ at $\sim 2\,R_{1/2,*}$, from where on it stays constant. Clearly, the DM component's alignment in the center region generally has a twist, which also drives the misalignment with the stellar component. Further analysis will be needed in the future, however, to determine how large the contributions of resolution and more spherical shapes are. The latter point is related to the fact that small deviations in an almost spherical shape can lead to large twists of the ellipsoidal axes. It is remarkable how small the scatter of the stellar component's alignment with $\boldsymbol{j}_*$ is. Both the median and the scatter only increase slightly beyond $3\,R_{1/2,*}$, which is the radial distance at which $\boldsymbol{j}_*$ is computed. The scatter of the DM's alignment with $\boldsymbol{j}_*$ is larger and again is similar to the scatter of the alignment angle between the stellar and DM shapes. Finally, the alignment of the stellar and DM components with the DM angular momentum at $3\,R_{1/2,*}$ shows that both have a very similar alignment of $\theta(\mathrm{shape}, \boldsymbol{j}_{\rm DM}) \approx 15°$ in the outer regions, with the stellar component remarkably being slightly better aligned and having the smaller upward scatter. In the inner region, the stellar

component does not deviate from this angle due to the overall lack of twists. The DM component, however shows a similar profile as for the other alignment angles: it decreases from around $\theta(\mathrm{DM}, \boldsymbol{j}_{\mathrm{DM}}) \approx 45°$ in the inner regions to the limit angle, which is consistent with the conclusions from the other DM alignment profiles. Note that the median alignment angles of 45° in the center regions do not correspond to randomly oriented axes in space, but indicate preferentially aligned axes. For two randomly oriented axes, the median angle would be expected to be 60°, with the shaded region covering the range between 33° and 81° (see Appendix C for a derivation).

The non-rotators feature a very similar alignment profile between the stellar and DM shapes to that of the regular rotators, except for there being a larger misalignment in the very inner region and the alignment angle being slightly smaller at $5\,R_{1/2,*}$. Note that the non-rotators tend to be better resolved, leading to the plotted line starting at a slightly smaller radius than for the regular rotators. Still, the alignment angle in the center region approximately corresponds to a random orientation of the two shapes. As already mentioned, further analysis will be required to determine whether the increased misalignment towards the center is physical or not. It is interesting that the upward scatter at larger radii is smaller than for the regular rotators, which means that the components of non-rotators are better aligned than those of regular rotators. The origin of this behavior is still unclear, however. The alignment of the stellar and DM components with $\boldsymbol{j}_*$ is much higher than for the regular rotators and has a much larger scatter. The median stellar alignment again features no median twists and stays constant at around $\theta(*, \boldsymbol{j}_*) \approx 30°$, while the median DM alignment with $\boldsymbol{j}_*$ again decreases towards the outer regions and reaches a constant median value that is slightly above that of the stellar component. The upward and downward scatters of both angle profiles are approximately constant. The alignment profiles of the shapes with $\boldsymbol{j}_{\mathrm{DM}}$ are interestingly very similar to those with $\boldsymbol{j}_*$, except that the median angles are now approximately higher by $\Delta\theta \approx 5°$–$10°$. The DM alignment again drops to the constant stellar alignment angle with $\boldsymbol{j}_{\mathrm{DM}}$ in the inner region. This shows how the DM shape is oriented according to the stellar component and not to the DM angular momentum in the inner regions of a galaxy. In the future, the evolution of the orientations and their relation with the merger histories could further improve our understanding of this shape alignment.

The alignment angle profile between the stellar and DM shapes of the KDCs is similar to the ones found for the regular and non-rotators. Two differences are that there is more noise in the profile due to low number statistics, particularly in the central region, and that the threshold median alignment of ∼8° is reached further out, at around $3\,R_{1/2,*}$. The scatter is only a bit larger than that found for the non-rotators, but still smaller than for the regular rotators. It is unclear if the peak in the alignment angle profile in the inner part is a result of low number statistics or if this is a feature that can commonly be found in KDCs. While the former is likely the case, the profiles of individual well-resolved KDCs and also of a larger sample of KDCs should be analyzed in the future to especially further investigate the profiles of the shape alignment in the kinematically distinct region of the galaxies. The alignment between the stellar component and $\boldsymbol{j}_*$ is interesting: while the sudden drop at small radii is likely

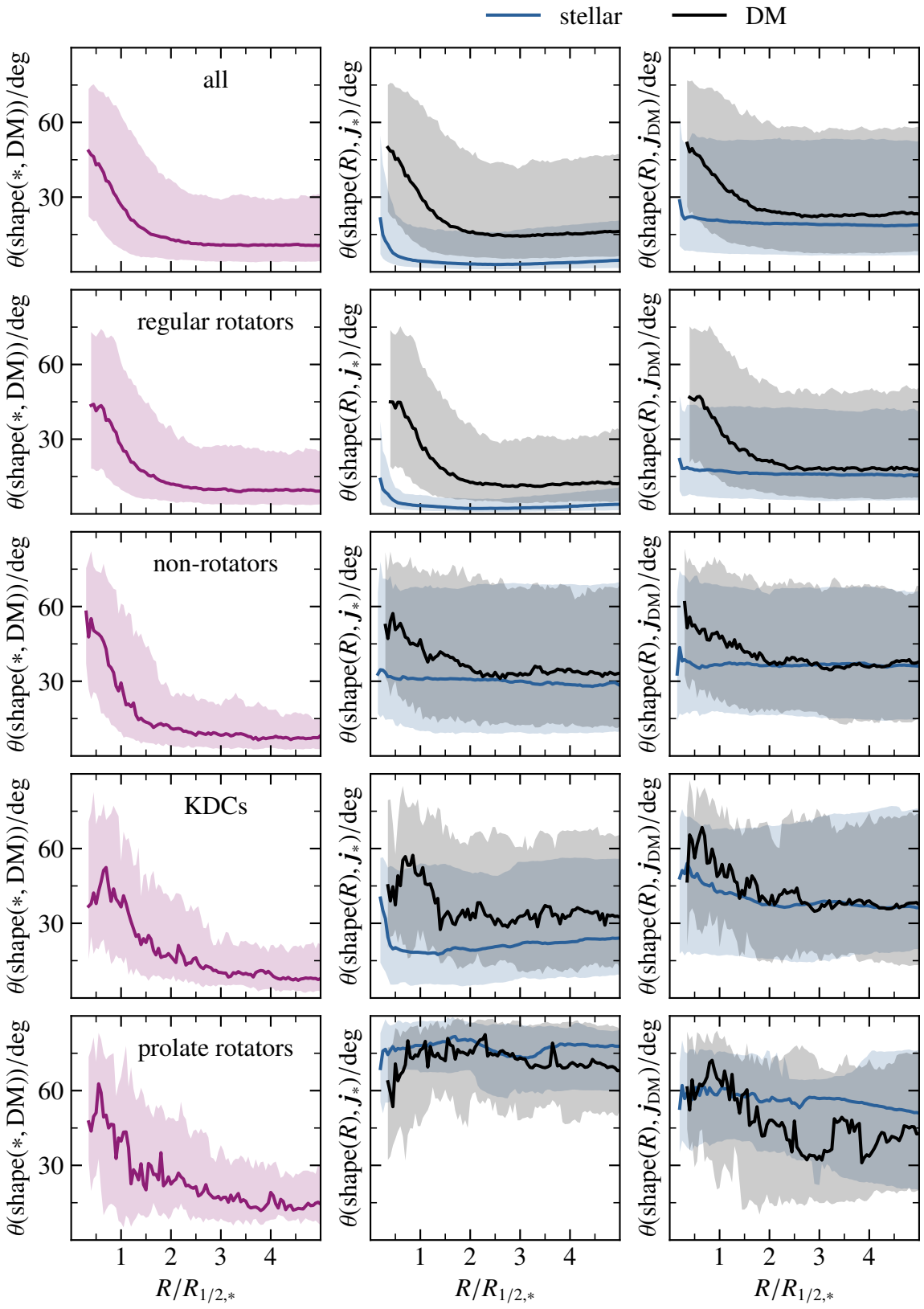

Figure 6.4: Radial alignment profiles of the stellar and DM components' shapes and angular momenta of the full galaxy sample (top row) and of the individual kinematic groups (bottom rows) from one to five stellar half-mass radii. The left column shows the angles between the minor axes of the stellar and DM shapes, the middle column the angles between the stellar angular momentum at 3 $R_{1/2,*}$ and the minor axis of the stellar and DM shapes, and the right column the angles between the DM angular momentum at 3 $R_{1/2,*}$ and the minor axis of the shapes. The solid lines and shaded regions have the same meaning and conditions for being plotted as in Figure 6.3.

related to resolution issues, the overall profile shows a slow, approximately linear increase of the alignment angle towards the outer regions with about constant upward and downward scatters. The better inner alignment could be related to the stellar angular momentum in the central region dominating the total stellar angular momentum within $3\,R_{1/2,*}$ for most KDCs. A quantitative determination of the stellar angular momentum contributions per radial distance will give more insight into this matter in the future. The DM shape is aligned worse with $\boldsymbol{j}_*$ and its profile shows the peak at $1\,R_{1/2,*}$ that leads to the higher misalignment between the stellar and DM shapes. The overall profile of the angle between the DM shape and $\boldsymbol{j}_*$ is similar to that of the non-rotators, however, unlike the stellar alignment. Finally, the alignment between the stellar and DM shapes and $\boldsymbol{j}_{\rm DM}$ are also similar to the profiles seen for the non-rotators, except for an increase of the stellar misalignment towards the center region, but less strong than what we observe for the DM.

The prolate rotators feature a similar alignment angle profile between the stellar and DM shapes as in the other kinematic classes. The angle is larger, however, and reaches a constant value of around 15° beyond $3\,R_{1/2,*}$. The scatter is comparable to that found for the KDCs. The angle between the stellar shape and $\boldsymbol{j}_{\rm DM}$ is almost constant, but decreases slightly. Interestingly, the median value starts at 60° in the center and has a scatter that is comparable to the values derived for two randomly oriented axes of 33° and 81° (Appendix C). Additionally, at least in the inner regions of prolate rotators, the stellar shape is approximately randomly oriented with respect to the DM angular momentum at $3\,R_{1/2,*}$. Unsurprisingly, we find an almost maximal misalignment between the stellar shape and $\boldsymbol{j}_*$ with an approximately constant median value above 75°, which is expected based on the kinematic classification of a prolate rotation about the major axis from an edge-on perspective. The scatter is larger than that found for regular rotators, but smaller than for non-rotators and KDCs. Interestingly, we also find a similar DM alignment profile with $\boldsymbol{j}_*$. Two differences are that the angle becomes smaller towards the outskirts and that the downward scatter is larger. It is also interesting that the alignment angle between the DM shape and $\boldsymbol{j}_{\rm DM}$ is similar to that found for the non-rotators and the KDCs. There increased noise of the profile is likely related to the small number of prolate galaxies, leading to low number statistic effects.

Overall, we have found that DM shapes are generally aligned according to the stellar component and not to the DM angular momentum at $3\,R_{1/2,*}$. While the orientation of the stellar component is constant across all radii, the DM shapes tend to have a different orientation in the central regions. This misalignment will be further analyzed in the future by only considering larger galaxies in a first step and then moving on to higher resolution simulations in a second step. The overall alignment profiles are similar between non-rotators and KDCs, which raises the question about the origin of the similarities. This may be further understood by analyzing and comparing the average kinematics of the outer regions of the KDCs to those of the non-rotators. The prolate rotators are finally found to have stellar alignments with the DM angular momentum that is consistent with a random alignment of two axes in 3D.

6.2 Relations with the Radial λ_R-Profiles

Having analyzed the shape and alignment relations of the individual kinematic groups, we now turn to the shape properties of the three different λ_R-profile types from Schulze et al. (2020), which encode the formation history in a different way than the kinematic groups. Because of this, the relations with the shapes and alignments have the potential to give further insights on the relation between the shapes and the formation history of galaxies. Note that the λ_R-profile types are only available for the 743 galaxies with stellar masses of $M_* \geq 3 \times 10^{10}\,\mathrm{M}_\odot$ (described in Section 2.2).

λ_R-Parameter & Axis Ratios

We start by inspecting the location of the different types in the $\lambda_{R_{1/2}}$-$T(3\,R_{1/2,*})$ plane (Figure 6.5). The galaxies with increasing and flat λ_R-profiles (which are referred to as increasers and flats in the following for brevity) show a similar range of $\lambda_{R_{1/2}}$ and triaxiality values: the types include galaxies with the lowest values of $\lambda_{R_{1/2}}$ and very prolate shapes, but also contain galaxies with $\lambda_{R_{1/2}} \approx 0.6$ and triaxial to prolate shapes. The increasers reach the higher values of $\lambda_{R_{1/2}}$ for $T < 0.2$ compared to the flats, though this may also be a result of them being the most common type of the classified galaxies (53%). The galaxies with decreasing λ_R-profiles (decreasers) finally show the tendency towards higher values of $\lambda_{R_{1/2}}$ ($\gtrsim 0.3$) and mostly have oblate or triaxial stellar shapes. The number of flats and decreasers is similar, at 22% and 24% of the classified galaxies, respectively. Note that all prolate rotators for which the λ_R-profile type was determined are increasers. Despite there being little difference between the distribution of increasers and flats in Figure 6.5, Schulze et al. (2020) found that the increasers include both fast and slow rotators with almost equal frequency, whereas the flats have a tendency of being slow rotators. They also found that the increasers have higher maximum values of λ_R within $5\,R_{1/2,*}$ compared to the other types. Finally, almost all decreasers are fast rotators, which is supported by their generally high values of $\lambda_{R_{1/2}}$.

The increasers and flats also occupy similar regions in the q-s plane at $3\,R_{1/2,*}$ (Figure 6.6). Both types include galaxies with a wide range of axis ratios with $q, s \gtrsim 0.4$. Some increasers have lower values of s that can reach values down to $s_{\mathrm{min}} \approx 0.3$, as well as the decreasers. In contrast, the flats are the only type that reach the highest values of s, meaning that the flats can have the most spherical shapes. However, due to the small number of near-spherical shapes, this may not be statistically significant. The decreasers span large major axis ratios of $q \gtrsim 0.6$, which is the main reason for their preferred triaxial and oblate shapes. The decreasers also have smaller minor axis ratios compared to the other two types, with most decreasers having $s \lesssim 0.7$, leading to less spherical shapes.

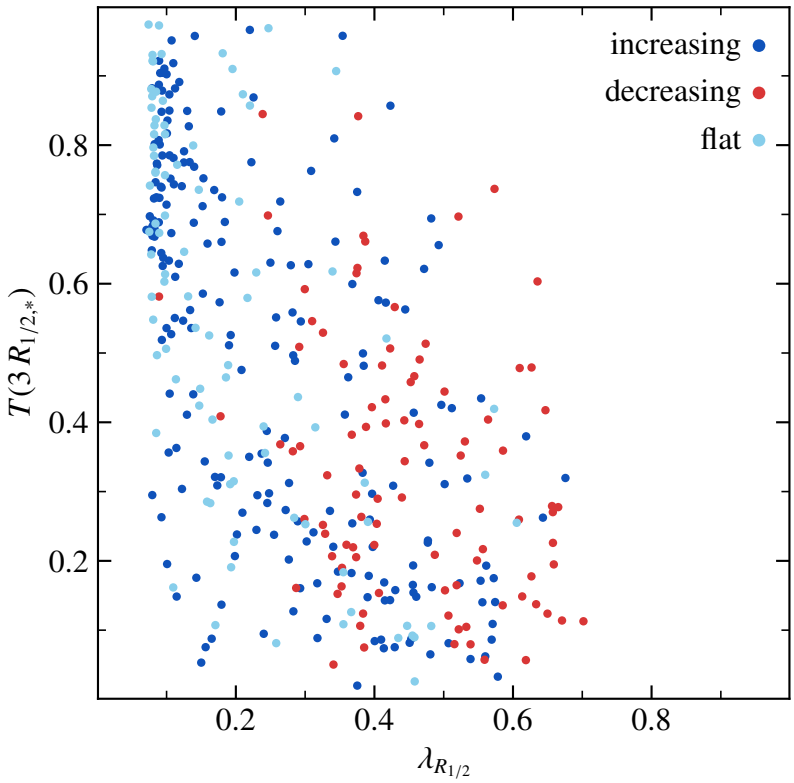

Figure 6.5: Location of the λ_R-profile types in the relation between $\lambda_{R_{1/2}}$ and the stellar triaxiality at $3\,R_{1/2,*}$.

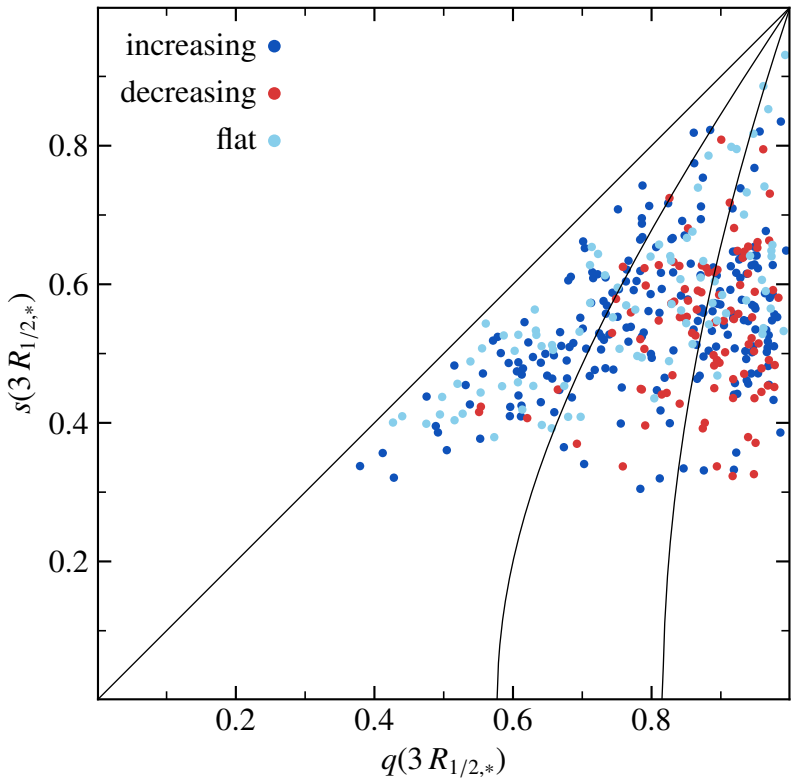

Figure 6.6: Axis ratios at $3\,R_{1/2,*}$ of the λ_R-profile types. The solid lines indicate the borders between prolate, triaxial, and oblate shapes, from left to right, respectively.

Radial Shape Parameters

The radial shape profiles of the λ_R-profile types can provide further insights into the relation between their different formation histories and the resulting shapes. For the increasers, the profile of the DM major axis ratio is similar to that found for the regular rotators, except for a larger downward scatter in the outer regions. This is due to 52% of the increasers being regular rotators and the DM q-profiles of the other kinematic groups not deviating strongly enough to sufficiently impact the profile. The median stellar profile of q, however, is lower than q_{DM} and rises approximately linearly. This shows how the increasers are not only regular rotators, but also includes galaxies of the other kinematic groups, where especially the non-rotators and prolate rotators lead to the lower median and a stronger downward scatter of q. The stellar and DM minor axis ratio profiles are both very similar to those of the regular rotators, except for being slightly flatter. In particular, the profile of s_{DM} increases with a larger slope in the inner region and is then nearly constant for $R \gtrsim 1.5\,R_{1/2,*}$. Both of the profiles' scatters are consistent with those for the kinematic groups. Finally, the triaxiality of the increasers features a large scatter around nearly linearly decreasing stellar and DM median values, which fall from $T \approx 0.7$ in the center to $T \approx 0.4$ at $5\,R_{1/2,*}$. Interestingly, the scatter of the stellar triaxiality is larger than that of the DM, which is only the case for KDCs in the outer regions. It is not clear where this large scatter originates from, but it is likely related to the diversity of kinematics found in the increasers. It is also remarkable how similar the triaxiality profiles of the stellar and DM components are to each other, which is not the case for any of the kinematic groups. Considering that the values of q and s differ from each other, this means that the relations between q and s, and between q_{DM} and s_{DM} happen to lead to the same triaxialities in terms of the median.

For the decreasers, we find a much smaller scatter of the major axis ratio profiles, which overall resemble those of the regular rotators. This is unsurprising since around 90% of the decreasers are regular rotators. One difference is that the profile of q_{DM} approaches its limit value of $q_{\mathrm{DM}} \approx 0.9$ at smaller radii and stays nearly constant at that value in the outer regions. This could be related to the higher mass of the galaxies that were classified with respect to their λ_R-profiles. The profiles of the minor axis ratios are intriguing: we find the largest deviation between s_* and s_{DM} compared to any of the kinematic groups for $R \gtrsim 1.5\,R_{1/2,*}$ while retaining the small scatters around the medians. It appears that the decreasers possibly comprise a specific group of galaxies that have relatively more spherical DM shapes compared to the stellar component, leading to such a deviation. This may be related to the typical mass accretion history of decreasers, which is dominated by mini and minor mergers, where accretion from random directions generally leads to more spherical shapes. Further analysis with a larger sample of galaxies will be able to investigate whether this is actually the case. Finally, the triaxiality profiles are also similar to those of the regular rotators, with a tendency towards being more triaxial in the outer regions. This could again be related to the overall more massive galaxies for which this profile is determined, but could also be influenced by the 10% of galaxies that belong to the other kinematic groups.

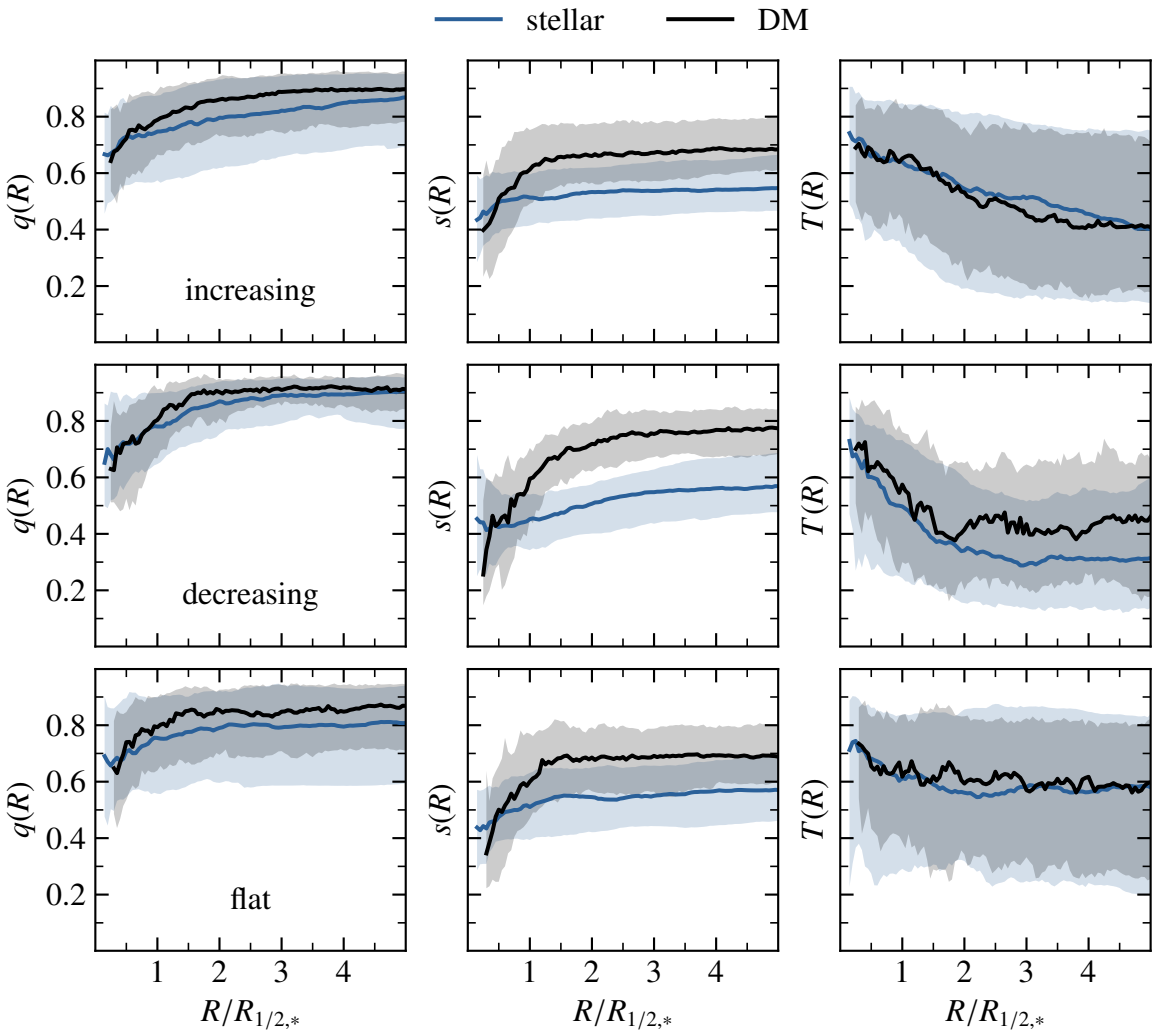

Figure 6.7: Radial shape profiles of the stellar (blue) and DM (black) components of the individual λ_R-profile types from one to five stellar half-mass radii. The solid lines indicate the median at each radial distance of the galaxies for which that radial distance is larger than the softening length (1 kpc for the stellar component, 2 kpc for the DM component). Points at a given radial distance are plotted if $R > \epsilon_{\text{soft}}$ for at least 25% or a number of 15 of the galaxies in the respective kinematic group to prevent statistical artifacts, whichever is larger. The shaded regions are the 1σ ranges containing 68% of the galaxies above and below the median.

Finally, the shape parameter profiles of the flats have similar properties to the ones of the increasers. This is not unsurprising, since the increasers and flats occupied similar regions in the q-s plane in Figure 6.6. There are some differences found in the profiles, however: the medians of the q-profiles are smaller, becoming constant around $q_* \approx 0.8$ and $q_{\rm DM} \approx 0.87$, and have larger upward and downward scatters. This shows that the flats cover a larger range of face-on axis ratios. In particular, the scatter of the stellar major axis ratios is interesting, since none of the kinematic groups features such a large scatter and only the prolate rotators have significantly smaller values of q_*, which are all increasers. Future work will include analyzing what type of galaxies or formation histories lead to the large scatter of q_*. While the profile of $s_{\rm DM}$ is very similar to that of the increasers, the profile of the stellar minor axis ratio shows overall larger values with a slightly increased scatter. This shows that the flats have overall less flat stellar shapes from an edge-on perspective compared to the increasers for similar DM shapes. The values of the triaxiality of the flats are the same as those of the increasers in the central region. However, the triaxialities only decrease to $\sim 2\, R_{1/2,*}$ and then stay constant at $T \approx 0.6$, larger than the triaxiality in the outer regions of the increasers by $\Delta T = 0.2$. The flats therefore have a tendency towards being triaxial to prolate in the outer regions, whereas the increasers tend towards being triaxial to oblate. The scatters are approximately the same, and again the stellar triaxiality has the slightly larger scatter. It is remarkable how we again find very similar stellar and DM triaxiality profiles, again highlighting how the stellar shapes influence the DM.

Radial Alignment

The profile of the alignment angle between the stellar and DM shapes for the increasers is very similar to those of the regular rotators, non-rotators, and KDCs, but has an even better median alignment in the outer regions. The scatter is small, like that of the non-rotators. The alignment angle profile between the stellar shapes and $\boldsymbol{j}_*$ shows similarities to that of the regular rotators, except that the angle is larger at around $\theta(*, \boldsymbol{j}_*) \approx 10°$ and the scatter is much larger, reaching up to almost 45°. This shows the influence of the other kinematic groups, which have worse alignments between the stellar shape and its angular momentum than the regular rotators. The same is true for the angle between the DM shape and $\boldsymbol{j}_*$, although the median and the scatter are only slightly larger for the increasers than for the regular rotators. The alignment angles between the shapes and $\boldsymbol{j}_{\rm DM}$ are overall the same as for the regular rotators, with the exception of slightly larger scatters. In general, all the previously discussed features, such as the median stellar shapes having no twists or the DM component being more misaligned in the inner regions and following the stellar component in the outer regions, are recovered in the increasers' alignment profiles.

For the decreasers, the alignment profile between the stellar and DM shapes features a larger median and scatter than the increasers. This may be related to the comparably large deviations of the minor axis ratios. It is possible that both the slightly larger misalignment between the components and the differences in the edge-on axis ratios are driven by the same

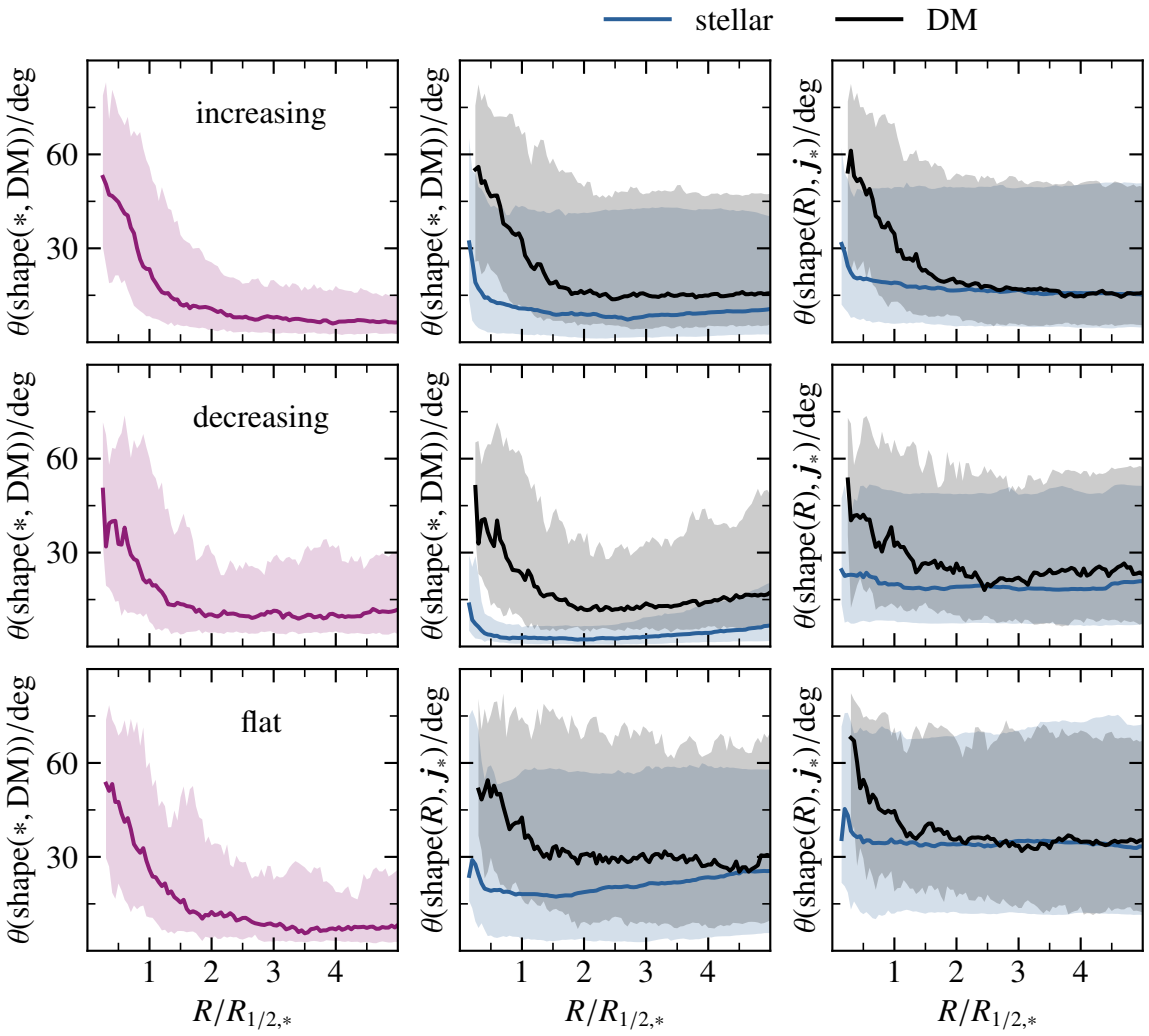

Figure 6.8: Radial alignment profiles of the stellar and DM components' shapes and angular momenta of the individual λ_R-profile types from one to five stellar half-mass radii. The left column shows the angles between the minor axes of the stellar and DM shapes, the middle column the angles between the stellar angular momentum at $3\,R_{1/2,*}$ and the minor axis of the stellar and DM shapes, and the right column the angles between the DM angular momentum at $3\,R_{1/2,*}$ and the minor axis of the shapes. The solid lines and shaded regions have the same meaning and conditions for being plotted as in Figure 6.7.

process. An analysis of what this process could be is beyond the scope of this work and will be the subject of future research. The alignment profiles of the stellar and DM shapes with $\boldsymbol{j}_*$ resembles those of the regular rotators, but with larger medians and scatters in the outer regions. The larger scatter could be a result of galaxies from other kinematic groups being classified as decreasers as well, or actually be a signal of the formation process typical for decreasers. The alignment profiles of the stellar and DM shapes with $\boldsymbol{j}_{\mathrm{DM}}$ is shifted towards slightly larger angles compared to the profiles of the regular rotators and also have larger scatters. In summary, we find the general trends of the regular rotators in all alignment profiles with larger scatters, which is consistent with 90% of the decreasers being regular rotators.

Finally, the flats also show an alignment profile between the stellar and DM shapes that is similar to those of the increasers and decreasers: while the median is small in the outskirts, as for the increasers, the scatter is approximately constant beyond $2\,R_{1/2,*}$, as for the decreasers (neglecting the noise due to low number statistics). Interestingly, the alignment angle profiles of the stellar and DM shapes with $\boldsymbol{j}_*$ are most similar to those of the KDCs with increased scatters and lower median angles for the DM component. This indicates the large variety of kinematics found for flats. It also reveals a main difference to the increasers: increasers tend to have better alignments of the stellar and DM shapes with $\boldsymbol{j}_*$, whereas flats have a larger median misalignment that additionally increases towards the outer regions for the stellar component to around 25°. Considering that all of the prolate rotators (which have very large angles between the shapes and $\boldsymbol{j}_*$) are increasers, it is surprising that the upward scatter is smaller for the flats than for the increasers. This suggests that the non-rotators and KDCs greatly impact the alignment profiles of the flats. It is unclear if the increase of the median stellar alignment angle with $\boldsymbol{j}_*$ is mainly driven by the KDCs (which show a similar increase) or if there are also other galaxies that have an increased misalignment in the outer regions. It will be helpful to analyze this in the future. We also find the largest misalignment of the shapes with $\boldsymbol{j}_{\mathrm{DM}}$ compared to the increasers and decreasers: the median angle between the stellar shape and $\boldsymbol{j}_{\mathrm{DM}}$ is approximately constant at $\theta(*, \boldsymbol{j}_{\mathrm{DM}}) \approx 35°$. As for the increasers and decreasers, the angle between the DM shapes and $\boldsymbol{j}_{\mathrm{DM}}$ is larger in the inner regions and drops to the same constant median angle as found for the stellar component at $\sim 2\,R_{1/2,*}$. The scatter is again very large, again likely due to the broad variety of kinematics found in the flats.

Overall, we have found less tight shape parameter and alignment profiles for the individual λ_R-profile types than for the kinematic groups. However, despite many profiles resembling those of some of the kinematic groups, we also find new features in the profiles, such as the larger difference of the stellar and DM s-profiles for the decreasers or the large increase of the stellar shape alignment angle with its angular momentum for the flats. While the increasers and flats have overall similar axis ratio profiles, the main differences lie in their alignments with the angular momenta. This is consistent with the differences found by Schulze et al. (2020) with respect to their maximum values of λ_R and to the fractions of slow and fast rotators found among them, since the flats are more likely to be slow rotators and have lower

values of $\lambda_{R,\mathrm{max}}$, for which more misalignment compared to fast rotators and higher values of $\lambda_{R,\mathrm{max}}$ would be expected. Lastly, the decreasers mostly reproduce the profiles found for the regular rotators with larger scatters due to the influence of galaxies of the other kinematic groups.

6.3 Summary & Conclusion

The relations between the kinematic groups and the shape parameters for the galaxy sample are mostly consistent with the expectations: regular rotators are the most rotationally supported and tend to have oblate shapes, whereas non-rotators are dispersion dominated and have more prolate shapes. The triaxiality overall becomes more oblate in the outer regions, which is consistent with the findings in Section 4.1. Interestingly, the prolate rotators have the most prolate shapes at all radii, which introduces the idea of prolate rotators being "rolling tubes". The KDCs feature a very oblate core region with a strong increase to more triaxial shapes in the outer regions beyond $2\,R_{1/2,*}$. The oblate shape at the center is the result of almost circular face-on shapes of the KDCs. Interestingly, the stellar minor axis ratio is very similar between the different kinematic groups, which shows a different behavior than the expectation that regular rotators would be flatter and non-rotators more spherical.

Remarkably, the DM radial shapes appear to behave similarly to the stellar shapes, suggesting that the DM generally follows the stellar component. Particularly the radial triaxiality profiles show how each kinematic group has a distinct profile which both the stellar and DM components follow. Only in the inner region of the KDCs the DM component does not show the same strongly oblate shape that the stellar component does, which indicates that the inner stellar component is not only decoupled from the outer regions, but also from the DM component in the inner regions. This is linked to the formation history and shows how the stellar and DM components can follow different evolution paths after merger events. Overall, the DM shapes are more spherical than those of the stellar component. A feature that is still unclear is why the DM shapes of regular rotators tend to be slightly more spherical than those of non-rotators.

The stellar and DM components show good alignment in their major axes throughout all kinematic groups, with stronger alignment outside of $2\,R_{1/2,*}$. In the inner regions, the orientation of the DM component becomes more misaligned, although it is unclear if this is due to physical reasons or to the limited resolution of the simulation. As expected, the minor axis of the stellar component is very well aligned with the stellar angular momentum at $3\,R_{1/2,*}$ for the regular rotators and is almost maximally misaligned for the prolate rotators (at an angle of almost 90°). Since the DM is aligned with the stellar component, this is also true for the minor axis of the DM. Both the non-rotators and the KDCs show medium alignments between the minor axis and the stellar angular momentum, with the KDCs showing slightly better alignment in the core region (around 20°) and having overall better alignment than the non-rotators (around 30° for the non-rotators). The alignment of the stellar and DM components with the DM angular momentum at $3\,R_{1/2,*}$ is worse by around 5°–15°

compared to the stellar angular momentum for all kinematic groups except for the prolate rotators. Interestingly, the alignment between the stellar minor axis and the DM angular momentum is consistent with two randomly oriented axes, which suggests that the stellar component in prolate rotators is mostly independent of the DM kinematics. The minor axis of the DM component has a slightly better alignment with $\boldsymbol{j}_{\mathrm{DM}}$ in the outer regions of prolate rotators. These results show in total that the stellar component features a tighter relation between its orientation and angular momentum than the DM component.

For the λ_R-profile groups, the increasers and flats largely have similar properties with respect to the λ_R-parameter at 1 $R_{1/2,*}$ and the shape parameters. The decreasers, in contrast, are more rotationally supported and have more oblate shapes, which is consistent with the idea of them having old disks because of mostly having experienced only mini and minor mergers. Mostly consisting of regular rotators, the general radial shape and alignment profiles of the decreasers are similar to those found for the regular rotators. An interesting deviation are the more spherical shapes of the decreasers compared to the regular rotators, especially for the DM component. This is likely related to their formation history typically dominated by mini and minor mergers, where many such mergers from random directions lead to more spherical shapes in the outskirts. The most evident difference between the flats and increasers is the more oblate shape of the increasers in the outer regions, although it is not entirely clear what the origin is for this. Just as for the kinematic groups, the DM shapes have similar profiles as the stellar component, which is particularly the case for the major axis ratio and triaxiality profiles. The DM components again have more spherical shapes compared to the stellar component.

The alignment of the stellar and DM minor axes is good for all λ_R-profile groups and again has larger misalignments in the inner regions due to the DM component being oriented differently. Interestingly, the alignment profiles of the stellar and DM components with their angular momenta are more similar between the increasers and decreasers, where both of those groups feature relatively good alignments. Only the flats show worse alignments by around 15°–25°, which is likely largely influenced by the non-rotators and KDCs found in this group, leading to an especially large scatter of the alignment angles.

In conclusion, the profiles show that the kinematic groups are the bigger influence on the shapes, though through the analysis of the λ_R-profiles it is potentially possible to further constrain the shape profiles. This result shows how the kinematic groups are more tightly connected to the details of the formation histories than the λ_R-profile groups, with the exception of the decreasers. The fact that the decreasers' profiles are distinct from the others shows that there is a signal for the formation history that can only be found in their shapes and not in those of the other classes. Further work will be necessary to investigate in what way the shape parameter profiles can be constrained when given a kinematic class combined with a λ_R-profile.

7 Shapes & Large Scale Properties

Having discussed the relations between the shapes and a number of global galaxy properties in Chapters 5 and 6, in this chapter the connection between the shapes and the large scale properties of galaxies is studied to investigate if the cosmic environment influences the shapes of galaxies at the centers of the large DM potentials or the shapes of the DM halos themselves. It has already been established that the inner kinematics of a galaxy are correlated with the shape (Section 5.1). Now, the kinematics of the full galaxy and of the individual components (DM, stars, and gas) will be considered through the global spin parameter within the virial radius to find how the large scale spin of a galaxy influences the inner kinematics and shapes of the galaxies. Based on the findings of Teklu et al. (2015) for the same cosmological simulation used in this work, that LTGs tend to have larger global spin parameters and that the formation history of the DM halo likely plays a significant role for the morphology of the galaxies, a trend between the shapes and the global spin parameters can be expected: galaxies with larger global spin parameters are likely flatter than galaxies with smaller global spin parameters.

The formation history of galaxies is strongly dependent on their cosmic environment, where certain processes can only occur in particular environments, such as galaxy clusters (some of which were presented in Section 1.1.3). Because of this, the shapes of galaxies and their DM halos are potentially also affected by the environment: denser environments could lead to more mergers from random directions, leading to more spherical and triaxial shapes, whereas LTGs, which are more common in less dense environments, could remain rather flat and oblate.

7.1 Relations with the Global Spin Parameter

Global Spin Parameter & λ_R-Parameter

The first large scale property that we consider is the global spin parameter, λ, within $R_{\rm vir}$ (introduced in Section 1.2.3). Before comparing the global spin parameters with the shapes, they are first related to a previously analyzed kinematic parameter, $\lambda_{R_{1/2}}$, and to the b-value as a morphological indicator (Figure 7.1). Out of the variations of λ, the one showing the strongest correlation with $\lambda_{R_{1/2}}$ is λ_* (top left plot). This is not unexpected, since $\lambda_{R_{1/2}}$ is computed based on the stellar component only and does not take gas or DM into account. Still, the fact that a correlation exists shows that the kinematics of the inner stellar half-mass radius are related to the global stellar spin of a galaxy. This is likely a result of most stars

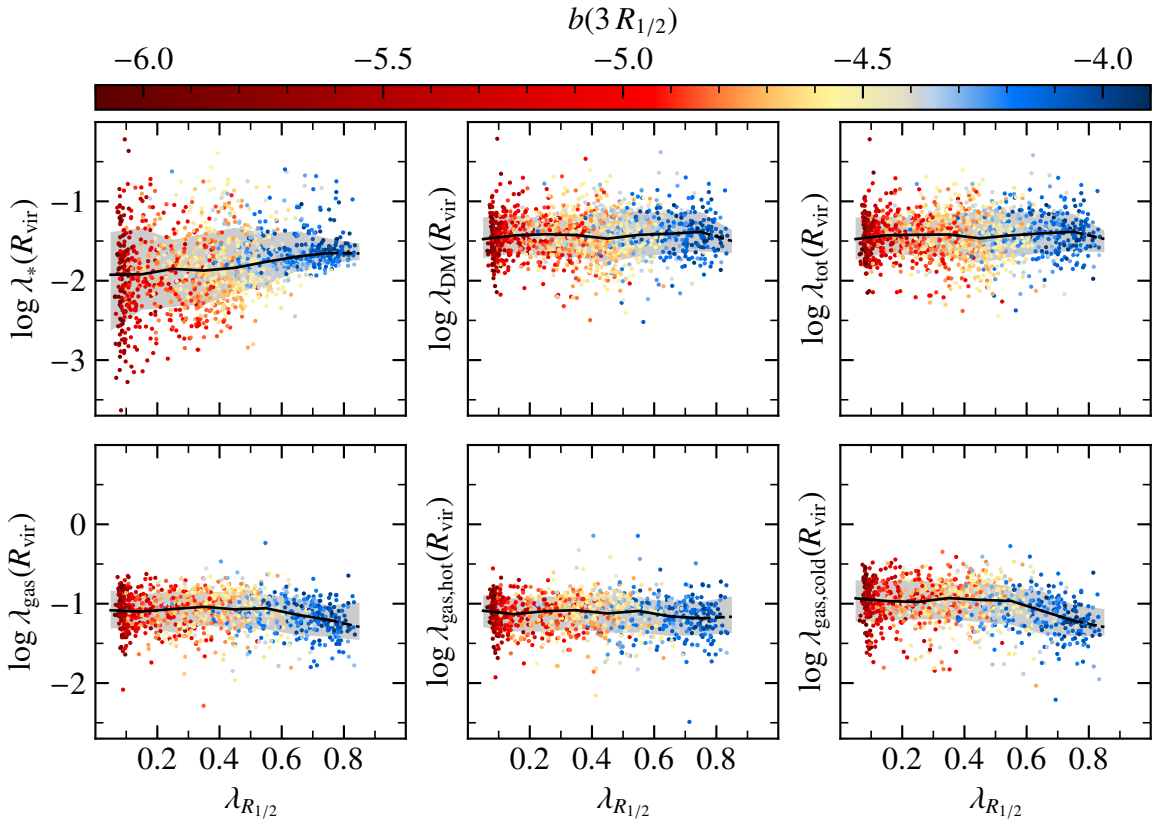

Figure 7.1: Relation between the global spin parameters of the galaxies within $R_{\rm vir}$ and the λ_R-parameter at one stellar half-mass radius, colored by the b-value. *Top*: Global spin parameters of only the stars, the DM, and of all particles (including the gas) within $R_{\rm vir}$. *Bottom*: Global spin parameters of the gas, only the hot gas, and only the cold gas. Only galaxies with $M_{\rm gas} \geq 10^{10}\,{\rm M}_\odot$ are plotted in the bottom row. Note the different range of the y-axis, but with the same scale as in the top row. The solid black lines indicate the median values in the respective $\lambda_{R_{1/2}}$ bins and the shaded regions the 1σ ranges (containing 68% of the galaxies above and below the median). The dashed part of the lines indicates where there may be effects caused by low number statistics.

being located in the inner regions of a galaxy, with half of the stellar mass being in $R_{1/2,*}$ by definition, such that the inner kinematics are able to strongly impact the global stellar spin in a galaxy. The most prominent feature is the lower bound of λ_* for a given value of $\lambda_{R_{1/2}}$, which increases with $\lambda_{R_{1/2}}$. In contrast, the upper bound seems to be approximately constant, although there are some outliers, including two ETGs at low $\lambda_{R_{1/2}}$ with the largest λ_*. Analyzing what causes these large stellar global spin parameters is beyond the scope of this work and will be further inspected in the future. The scatter of stellar global spin parameters is the largest at low values of $\lambda_{R_{1/2}}$, which mainly corresponds to ETGs, and decreases towards larger values of $\lambda_{R_{1/2}}$. These trends are consistent with the results found by Teklu et al. (2015) for the stellar global spin parameter within $0.1\,R_{\rm vir}$. Interestingly, the relation for the global stellar spin parameter of the LTGs is generally tight, but has a number of outliers towards higher values of λ_* by up to a full order of magnitude. It may be helpful to investigate the relation of the global spin parameters with the formation history and orbital configurations of the merging satellites in the future, which may reveal a connection to the galaxies with outlying values of λ_*.

The relations between $\lambda_{R_{1/2}}$ and the DM and total global spin parameters within $R_{\rm vir}$ are very similar, which is mainly a result of DM dominating the total mass of a galaxy, with there therefore being an almost linear relation between $\lambda_{\rm tot}$ and $\lambda_{\rm DM}$ (Appendix D). In contrast to λ_*, these global spin parameters show an approximately constant scatter with no clear trend for the upper and lower bounds of λ. The median increases very little from low to high $\lambda_{R_{1/2}}$, which is still consistent with the findings of Teklu et al. (2015): while the trends are investigated in logarithmic space in this work, they discussed an increase of the $\lambda_{\rm tot}$-distribution for larger b-values based on plots in linear space. The minor trend for the distribution of $\lambda_{\rm DM}$ with respect to ETGs and LTGs is also consistent with their findings in appendix C of Teklu et al. (2015). Overall, given the trends of the shape parameters with the b-value, it can be expected that there is at most a minor trend between $\lambda_{\rm DM/tot}$ and the inner shapes.

Finally, an interesting trend between the global spin parameter of the gas within $R_{\rm vir}$ and $\lambda_{R_{1/2}}$ is found (bottom left plot of Figure 7.1): while there is a minor increase of the median $\lambda_{\rm gas}$-value until $\lambda_{R_{1/2}} \approx 0.4$–$0.5$, it remarkably decreases for the LTGs for $\lambda_{R_{1/2}} \gtrsim 0.6$. Interestingly, even the outliers of the LTGs with large $\lambda_{\rm gas}$ are not as extreme as for the intermediate galaxies or the ETGs. Overall, the scatter indicated by the shaded region stays approximately constant for all values of $\lambda_{R_{1/2}}$. To further investigate the trend of more rotationally supported galaxies having lower gas spins, the global spin parameters of the hot and cold gas are considered separately: the same distinction as Teklu et al. (2015) is used, where gas particles with a temperature of $T < 10^5$ K or with a non-zero star formation rate are considered to be cold. The rest of the gas particles are defined as the hot gas. The finding is very clear: while there appears to be a very slight downward trend of $\lambda_{\rm gas,hot}$ for the LTGs, the global spin parameter of the cold gas features an even stronger decrease at high $\lambda_{R_{1/2}}$-values than found for all the gas. Therefore, the cold gas kinematics are responsible for the counter-intuitive trend. It is unclear what drives the relation of LTGs having smaller gas spins than intermediate galaxies and ETGs. This should be further analyzed in future studies by inspecting the kinematics of gas and the formation histories of the galaxies in more detail.

Global Spin Parameter & Shape Parameters

Having compared the central and global kinematic parameters, $\lambda_{R_{1/2}}$ and the global spin parameter, we now turn to the relations of the global spin parameter with the shapes. We first consider the stellar shape parameters at three stellar half-mass radii (Figure 7.2): while there is no clear correlation between λ_* and the major axis ratio, q, we find a downward trend of s with λ_*. This is consistent with the trend of λ_* being larger for the LTGs, which generally have smaller values of s. We find an approximate lower bound for the minor axis ratio for a given stellar global spin parameter that decreases with larger λ_*. Interestingly, the median increases again for $\lambda_* \gtrsim -1.5$, where the galaxies with especially high values of λ_* have an almost uniform distribution of minor axis ratios between $s \approx 0.2$ and $s \approx 0.8$. There is no clear correlation between λ_* and the triaxiality, where low number statistics at the low and

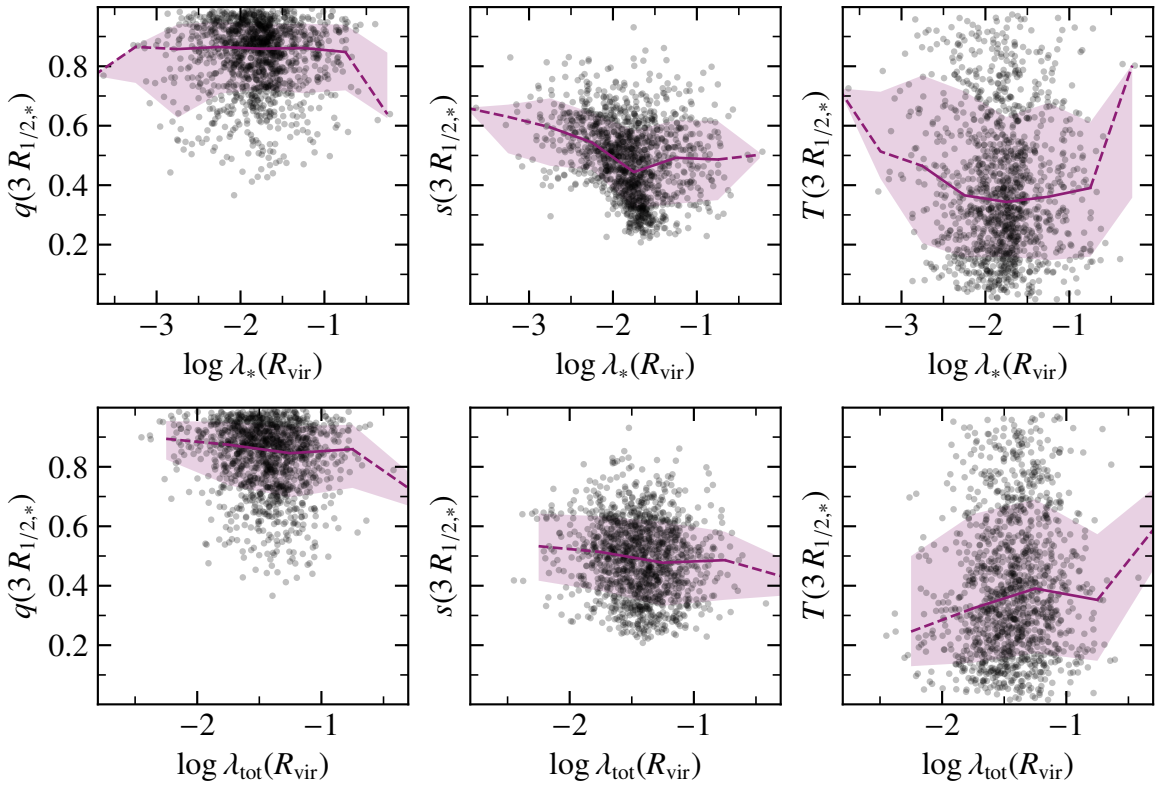

Figure 7.2: Relation between the stellar and total global spin parameters within $R_{\rm vir}$ and the stellar shape parameters at 3 $R_{1/2,*}$, q, s, and T. Note the different ranges of the x-axis in the top and bottom row. The solid blackberry lines indicate the median values in the respective global spin parameter bins and the shaded regions the 1σ ranges (containing 68% of the galaxies above and below the median). The dashed part of the lines indicates where there may be effects caused by low number statistics.

high ends of λ_* make it difficult to assess whether there is a slight correlation or not. There may be a downward trend towards oblate shapes where the median of s is the lowest, since the galaxies with the smallest minor axis ratios tend to be LTGs with more oblate shapes.

For the total global spin parameter, we find no clear correlations with any of the stellar shape parameters. This is not surprising, since the relations found between $\lambda_{\rm tot}$ and $\lambda_{R_{1/2}}$, and also with the b-value, are only weak. Combining this with the general trends of $\lambda_{R_{1/2}}$ and the b-value with the shape parameters, which are not very tight, results in very weak relations, if any at all. As a result, the correlation is lost between the total global spin parameter and the stellar shapes.

Given that $\lambda_{\rm tot}$ is measured from all particles within the virial radius, whose mass is dominated by the DM component, the relation between the total global spin parameter and the DM shapes is investigated (Figure 7.3). For the DM shapes at one DM half-mass radius, there is a very slight downward trend of q with increasing $\lambda_{\rm tot}$. There clearly is a larger downward scatter of q at large values of $\lambda_{\rm tot}$, however. The same appears to apply to s, resulting in slightly more prolate shapes at high values of $\lambda_{\rm tot}$. While it is possible that these trends are a result of low number statistics, it will still be insightful to analyze the kinematics of the galaxies with the lowest values of q and s in the future to understand what causes these extremely low values and if that is correlated to the formation history of the galaxies.

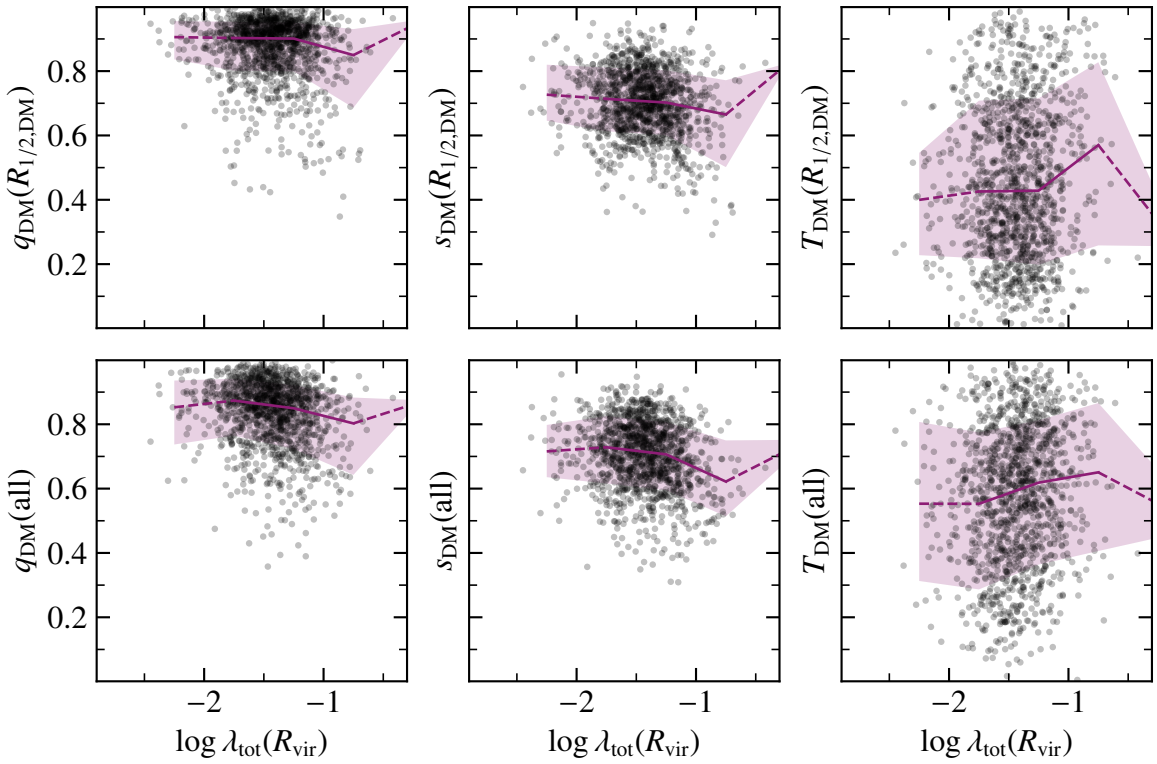

Figure 7.3: Relation between the total global spin parameter within R_{vir} and the DM shape parameters at 1 $R_{1/2,\mathrm{DM}}$ and of all DM particles, q, s, and T. The solid blackberry lines indicate the median values in the respective global spin parameter bins and the shaded regions the 1σ ranges (containing 68% of the galaxies above and below the median). The dashed part of the lines indicates where there may be effects caused by low number statistics.

Interestingly, similar trends can also be found for the shapes of the full DM halo (i.e., the shapes of all DM particles assigned to the galaxy by `SUBFIND`), except for overall lower values of q and higher values of T. There is only a very weak correlation between the DM shape parameters at 1 $R_{1/2,\mathrm{DM}}$ and of the full halo (Figure 4.3), which is the most noticeable for galaxies with the lowest values of q and s. This could be the reason for the same slight trends of the full halo shape parameters, i.e., $q_{\mathrm{DM}}(\mathrm{all})$, $s_{\mathrm{DM}}(\mathrm{all})$, and $T_{\mathrm{DM}}(\mathrm{all})$, with λ_{tot} as for those at 1 $R_{1/2,\mathrm{DM}}$. However, in both cases, the overall relations between the DM shapes and the total global spin parameter reveal no clear correlation and show that the DM shapes of galaxies on any scale are for the large part independent of the large scale spin properties. Even for the stellar component, only a trend between the minor axis ratios at 3 $R_{1/2,*}$ and the stellar global spin parameter can be found. Besides that, no correlation is found between the stellar shapes and λ_*, either. Therefore, it can be concluded that the global spin is not a primary driver of the stellar or DM shapes.

7.2 Relations with the Cosmic Environment

Cosmic Environment & Global Spin Parameter

Another possible influence on the shapes of galaxies is the local cosmic environment. As an indicator for the environment, the average density within a sphere of radius $r = 5\,\mathrm{Mpc}$ around each main galaxy's center, $\rho_{\mathrm{env}}(5\,\mathrm{Mpc})$, is used. This is similar to the quantification used by Teklu et al. (2017), who used the average number density of galaxies with $M_* > 10^8\,\mathrm{M}_\odot$ within a sphere of radius $r = 5\,\mathrm{Mpc}$ to trace the environmental density, where they chose the size of the sphere by following Treu et al. (2003). We first take a look at the relation between the local density and the total global spin parameter (Figure 7.4): there is a slight trend of λ_{tot} being larger in denser environments, which is an indicator that more accretion also leads to larger spins, assuming that galaxies accrete more on average in denser environments. This trend is consistent with the one found by Hellwing et al. (2021), who used the NEXUS+ algorithm (Cautun et al., 2013) for identifying the cosmic web environments, i.e., clusters, filaments, walls, and voids. This method computes density fields at multiple scale levels and can therefore associate cluster, filament, and wall environments to the densities in a scale-free way, depending on the local "environment response" at the different scales. The remaining space is classified as void environment. For virial masses of $M_{\mathrm{vir}} \gtrsim 10^{10}\,\mathrm{M}_\odot$, they found the lowest spins in voids, whereas galaxies in the other environments have larger median spins, and for virial masses of $M_{\mathrm{vir}} \gtrsim 10^{11.5}\,\mathrm{M}_\odot$, the median spin in the walls drops, too (although they noted that the statistics are too poor to confirm that trend robustly). Interestingly, the largest increase of the median global spin parameter in our galaxy sample is between the lowest and middle local densities, which should correspond to the void to wall galaxies. Similar to Hellwing et al. (2021), we find an approximately constant median spin for the denser regions. Overall, it can be concluded that the kinematics of galaxies are linked to the cosmic environment, but only up to a certain local density.

For a more in-depth analysis, different indicators of the cosmic environment should be tested in the future, since a simple average density measure may not be the best quantification of the environment, or the sphere's size could be suboptimal. Other possibilities include using different radii of the sphere, such as $r = 3\,\mathrm{Mpc}$ or $r = 7\,\mathrm{Mpc}$, using the average density within a radius given by the nth-closest galaxy neighbor, applying the galaxy number density measure by Teklu et al. (2017), instead, or actually using a cosmic web algorithm for determining the environment of each galaxy.

Cosmic Environment & Shape Parameters

The relation between the cosmic environment and the shape parameters is analyzed next. For this, we first consider the stellar shapes at $3\,R_{1/2,*}$ (top row of Figure 7.5): there are no trends with any of the shape parameters. On could argue that there is an increase of the median triaxiality, however the large scatter and the small slope of the trend show that the statistics are too poor to make any firm statements on this matter. The relation between the cosmic

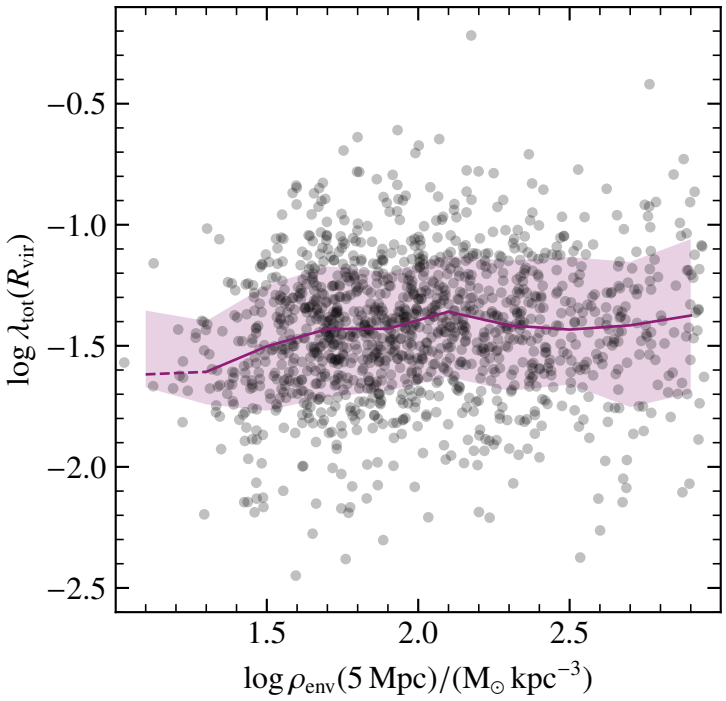

Figure 7.4: Relation between the average local density within a 5 Mpc radius and the total global spin parameter within $R_{\rm vir}$. The solid blackberry line indicates the median value in the respective density bins and the shaded region the 1σ range (containing 68% of the galaxies above and below the median). The dashed part of the line indicates where there may be effects caused by low number statistics.

environment and the shape parameters of the full DM halos is also investigated: again, we find no clear correlations with any of the parameters, although there could be a slight increase of the minor axis ratio and with the local density. This would mean that DM halos in clusters tend to be slightly more spherical than in voids, which could be a result of more accretion that takes place in a cluster environment. Still, the trend is too weak to make any definite statements. Interestingly, Hellwing et al. (2021) find that cluster halos at lower masses have larger triaxialities (these consist of a small number of galaxies, however), and wall and void halos with $M_{\rm vir} \gtrsim 10^{11}\,{\rm M}_\odot$ also have larger triaxialities. It should be noted that they only compute the shape for the particles within $R_{\rm vir}$ and use the non-iterative unweighted shape determination method, which has a bias towards more spherical shapes. It is unclear how the triaxiality is affected by it, however. In conclusion, no evidence is found that the environment quantified by the local density in a sphere of radius $r = 5\,{\rm Mpc}$ has any impact on the stellar or DM shapes of a galaxy (see Appendix E for two of the few quantities investigated for this work that are correlated with the local environment).

7.3 Summary & Conclusion

There is a clear trend for galaxies with larger stellar global spin parameters to be more rotationally supported in the inner regions, which is likely a result of the stellar component generally being concentrated in the center of the DM halo, such that the stellar global spin parameter is dominated by the inner kinematics. The correlation of the DM and total global

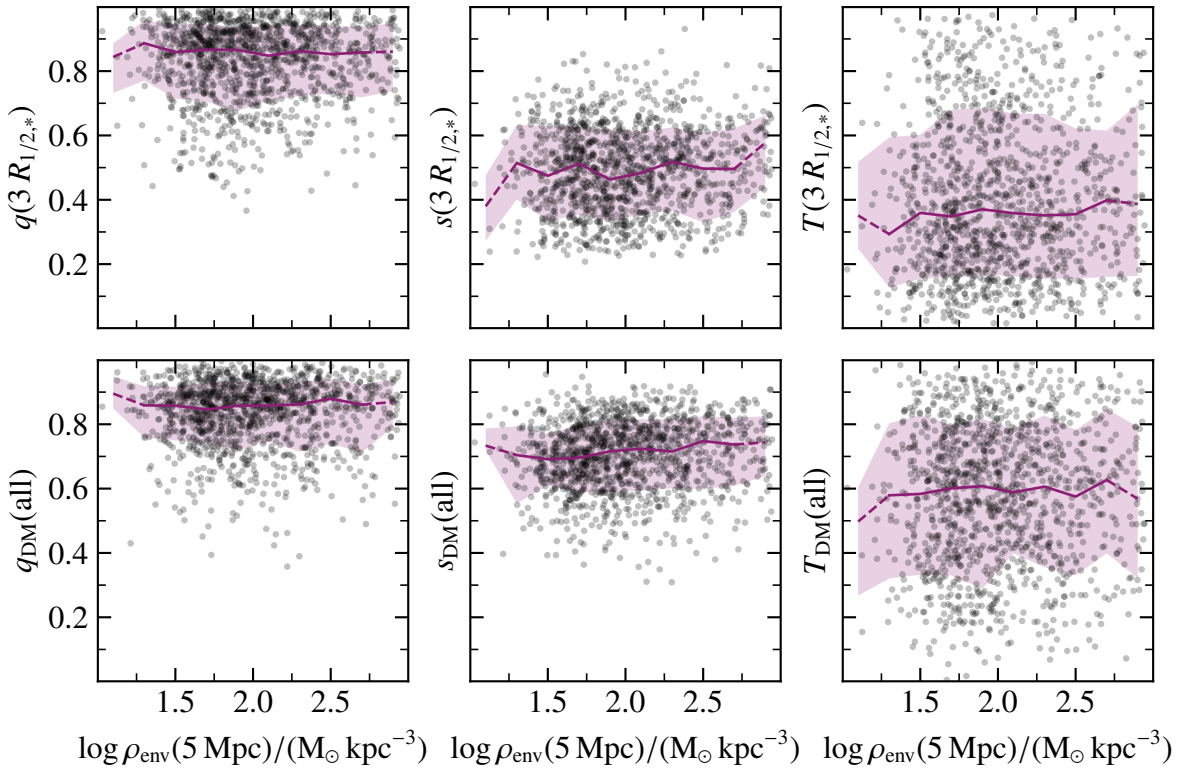

Figure 7.5: *Top*: Relation between the average local density within a 5 Mpc radius and the stellar shape parameters at 3 $R_{1/2,*}$, q, s, and T. *Bottom*: Relation between the average local density within a 5 Mpc radius and the DM shape parameters of the full DM halo, q, s, and T. The solid blackberry lines indicate the median values in the respective density bins and the shaded regions the 1σ ranges (containing 68% of the galaxies above and below the median). The dashed part of the lines indicates where there may be effects caused by low number statistics.

spin parameters, which are very similar to each other (Figure D.1), with the λ_R-parameter within 1 $R_{1/2,*}$ show a slight trend consistent with the findings of Teklu et al. (2015): LTGs, which have the highest rotational support, tend to have larger DM and total global spin parameters. This shows how the inner kinematics of a galaxy do not develop entirely independently of the global kinematics. A very surprising trend is found with the global spin parameter of the cold gas: galaxies with large values of λ_R, i.e., large rotational support in the inner regions, have lower values of the cold gas global spin parameter, for which the origin is still unclear and will have to be investigated in the future.

The minor axis ratio of the stellar component is found to have a lower bound for a given stellar global spin parameter, where the flatter galaxies all have larger values of $\lambda_*(R_{\rm vir})$. Through this lower bound, there is also a slight correlation between $\lambda_*(R_{\rm vir})$ and $s(3\,R_{1/2,*})$. This small trend is lost in the relation with the total global spin parameter, however. Also, the major axis ratio and the triaxiality show no correlation with the stellar shapes at 3 $R_{1/2,*}$. Similarly, the DM shapes at 1 $R_{1/2,\rm DM}$ show no trends with the total global spin parameter, and only the minor axis ratio of the full DM halo, $s_{\rm DM}(\rm all)$, shows a very small trend of DM halos being flatter with larger values of $\lambda_{\rm tot}(R_{\rm vir})$. In total, the global spin parameter is found to not be a primary driver of the stellar or DM shapes.

The environment, which is quantified as the average density within a radius of 5 Mpc of a galaxy in this work, shows a trend with the total global spin parameter: galaxies in denser environments tend to have larger spins, whereas galaxies in less dense environments have smaller spins. In the denser regions, the total global spin parameter is approximately constant, which is consistent with the findings of Hellwing et al. (2021). Just like $\lambda_{\mathrm{tot}}(R_{\mathrm{vir}})$, this quantification of the environment shows no evidence of a correlation with the stellar or DM shape parameters. In total, these results indicate that the large scales do not drive the stellar and DM shapes of galaxies and their halos.

8 Geometrical Symmetry

It has previously been mentioned that not all galaxies are appropriate for being described by an ellipsoid, including the galaxy seen in Figure 3.4, for example. This is especially the case for galaxies in the process of a merger. Not only the shapes can suffer from a reduced physical meaning, but also other properties like the half-mass radius, as seen for the two "largest" LTGs in Figure 5.5. Clearly, these kinds of outliers should be filtered out in these studies. Another application for the symmetry parameters may be to identify ongoing mergers, which could shed light on the question whether ETGs with ongoing star formation or relatively young stellar populations are in the process of merging, since this could be the reason for a recent starburst. A simple and reasonable approach to assessing which galaxies may be unsuitable for considering their shapes or half-mass radii is to filter out galaxies that are too unsymmetrical. For this, two different methods for measuring the symmetry of a galaxy are introduced.

8.1 Symmetry Quantification

Half-Space Symmetry

The first method for quantifying the symmetry of a galaxy's particle distribution is based on the assumption that two halves of the determined shape ellipsoid should contain the same amount of matter. The halves are given by the three planes that the ellipsoidal axes span, such that there are three pairs of halves in total. By counting the number of particles within each of the six halves, the symmetry is quantified by the ratio of the smallest and largest number of particles, therefore obtaining a value between 0 and 1. The half-space method measures the approximate mass ratio for the two halves with the largest asymmetry. Note that this simple implementation assumes a constant mass for all particles, which should not differ greatly from the results obtained by using the actual mass ratio.

Octant Symmetry

The second method instead splits the particles into eight groups according to the octants spanned by the ellipsoidal axes. The symmetry is then quantified by the ratio of the smallest and largest numbers of particles in the octants, again resulting in a value between 0 and 1.

8.2 Comparison Between the Symmetry Methods

We first compare the two measures of symmetry for the stellar component of the galaxies. Note that the ratios given by the octant symmetry, $\mathrm{Sym}_{\mathrm{oct}}$, and the half-space symmetry, $\mathrm{Sym}_{\mathrm{half}}$, are related by

$$\mathrm{Sym}_{\mathrm{oct}} \leq \mathrm{Sym}_{\mathrm{half}}. \tag{8.1}$$

This can be derived as follows: given the number of particles in eight octants, N_i for $i \in \{1, \ldots, 8\}$, we obtain

$$\mathrm{Sym}_{\mathrm{oct}} = \frac{\min_i(N_i)}{\max_i(N_i)}. \tag{8.2}$$

The total number of particles in any four of the octants is then constrained by

$$4\min_i(N_i) \leq N(4\,\mathrm{octants}) \leq 4\max_i(N_i). \tag{8.3}$$

Since this is also true for the four octants of any of the six halves of an ellipsoid, each having $N(\mathrm{half}_j)$ particles for $j \in \{1, \ldots, 6\}$, we finally obtain:

$$\mathrm{Sym}_{\mathrm{half}} = \frac{\min_j(N(\mathrm{half}_j))}{\max_j(N(\mathrm{half}_j))} \geq \frac{4\min_i(N_i)}{4\max_i(N_i)} = \mathrm{Sym}_{\mathrm{oct}}. \tag{8.4}$$

Plotting the stellar symmetry values against each other at one and three stellar half-mass radii, we find that the methods generally agree with each other with the octant method being more sensitive to asymmetry than the half-space method (top row of Figure 8.1). The majority of galaxies have large symmetry values, which is a good sign considering that galaxies are overall expected to be symmetrical (apart from galaxies in ongoing mergers, of course). The galaxies are more symmetrical at $1\,R_{1/2,*}$ than at $3\,R_{1/2,*}$, which mirrors the fact that more substructures are located further out, of which not all are identified as subhalos by `SUBFIND`. To confirm this, future tests will be necessary to relate the symmetry values to mergers, substructures, and other features. Work with respect to the classification by morphological features is in progress. There also appears to be a typical lower bound of the octant symmetry for a given half-space symmetry that is approximately equal for the shapes at both $1\,R_{1/2,*}$ and $3\,R_{1/2,*}$. Further analysis of the galaxies and their particle distributions will be necessary to determine what types of features lead to an especially low value of $\mathrm{Sym}_{\mathrm{oct}}$ in comparison to $\mathrm{Sym}_{\mathrm{half}}$. In the following sections, the values from the octant method will be used to quantify the symmetry of galaxies because of $\mathrm{Sym}_{\mathrm{oct}}$ being smaller than or equal to $\mathrm{Sym}_{\mathrm{half}}$ by definition, therefore suggesting a larger sensitivity of the octant method to asymmetries.

Considering the change of the symmetry values from $1\,R_{1/2,*}$ to $3\,R_{1/2,*}$, we find a close trend for most galaxies of having similar symmetry values at both radial distances (bottom row of Figure 8.1). As expected from the relations seen between the half-space and octant methods (top row of Figure 8.1), there are a number of galaxies that have much lower symmetry values at $3\,R_{1/2,*}$, especially for the octant method. These galaxies likely host substructure between one and three stellar half-mass radii that is not detected or not entirely

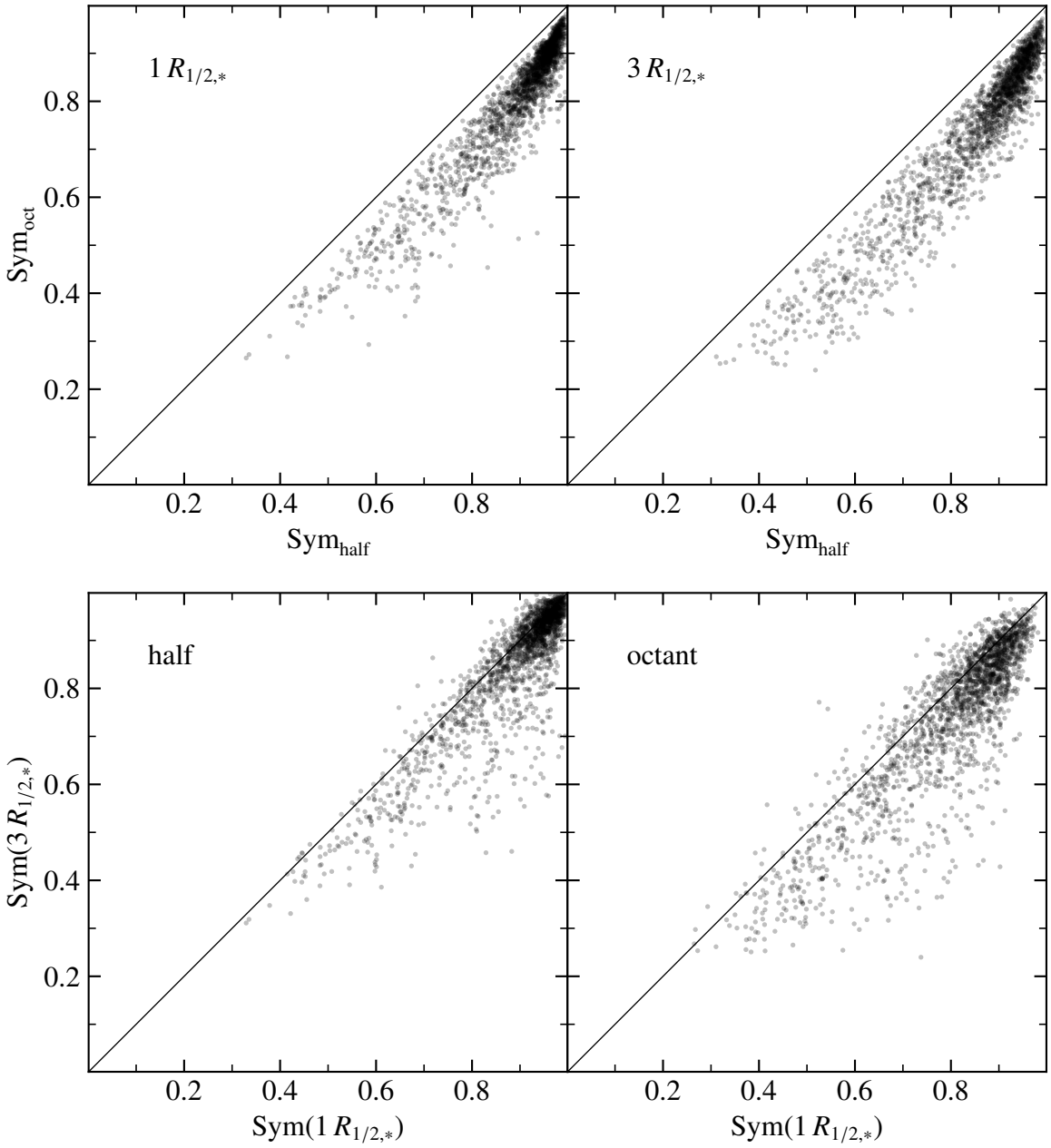

Figure 8.1: *Top*: Relation between the stellar symmetry parameters using the half-space and octant methods at one and three stellar half-mass radii. *Bottom*: Comparison between the stellar symmetry parameters at one and three stellar half-mass radii for the half-space and octant methods.

removed by SUBFIND, leading to larger asymmetries at larger radii. The latter possibility includes tidal arms and other asymmetric structures typically found in the outer regions of galaxies that are not attributed to the substructure by SUBFIND. These suppositions will have to be tested in the future, however.

8.3 Relations with the Symmetry

We now turn to the relations between the symmetry and the shape parameters for the stellar component (Figure 8.2). While there appears to only be a slight trend with q at both one and three half-mass radii, where q is lower for more asymmetric galaxies, there is a clear relation for the minor axis ratio: galaxies with a larger symmetry tend to have larger values of s, i.e., they tend to be more spherical. The most asymmetric galaxies, on the other hand, have the lowest values of s, which means that they are the flattest from an edge-on perspective. This is true at both considered radii, but is more pronounced at 1 $R_{1/2,*}$. The trends are mostly lost for the triaxialities, however. We also find a clear trend with the b-value, which is discussed in the following section.

Since one could argue that the meaningfulness of a shape is not affected by asymmetry in octants, but only by asymmetry in the halves of the shape ellipsoid, the same set of plots for the half-space symmetry values is shown in Appendix F. There, the same trends are found with the shape parameters and the b-value, as expected from the correlation between $\mathrm{Sym}_{\mathrm{half}}$ and $\mathrm{Sym}_{\mathrm{oct}}$ (Figure 8.1).

8.4 Symmetry & Global Galaxy Properties

Finally, the relations between the octant symmetry values and some global properties of the galaxies are investigated to gain a better understanding of where asymmetry tends to occur.

b-Value

As seen in Figure 8.2, LTGs can be the most asymmetric, whereas ETGs tend to be more symmetric. Since this involves many disk galaxies, an interesting question that still remains unclear is whether the asymmetries are usually caused by features in the disk plane or outside of it; future work will be required to further investigate this. Unfortunately, this also raises the question how meaningful the shapes determined for the LTGs in particular are, where the asymmetry is the highest.

We now consider the b-value explicitly (Figure 8.3). We have already seen the overall trend in Figure 8.2 that LTGs are more likely to have low symmetry values, whereas intermediate galaxies and ETGs are more symmetric. Interestingly, among the LTGs and ETGs, increased asymmetry generally corresponds to a higher b-value, while there the opposite appears to be true for the intermediate galaxies: large asymmetries tend to occur at b-values of $b \gtrsim -4.35$ (the limit between LTGs and intermediate galaxies) and at $b \approx -4.73$ (the limit between the

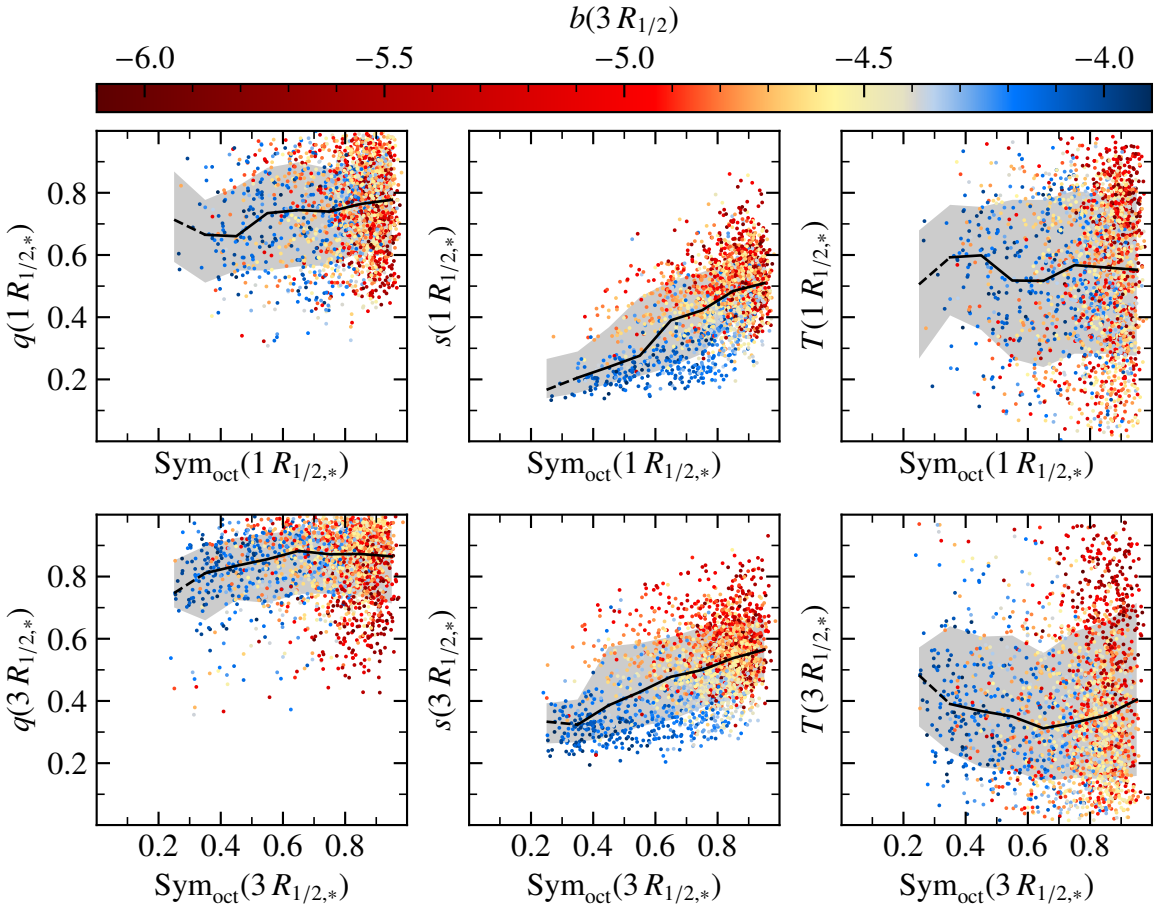

Figure 8.2: Relation of the octant symmetry at $1\,R_{1/2,*}$ (top row) and $3\,R_{1/2,*}$ (bottom row) with the shape parameters at the respective radial distances, q, s, and T, for the stellar component, colored by the b-value. The solid black lines indicate the median values in the respective symmetry bins and the shaded regions the 1σ ranges (containing 68% of the galaxies above and below the median). The dashed part of the lines indicates where there may be effects caused by low number statistics.

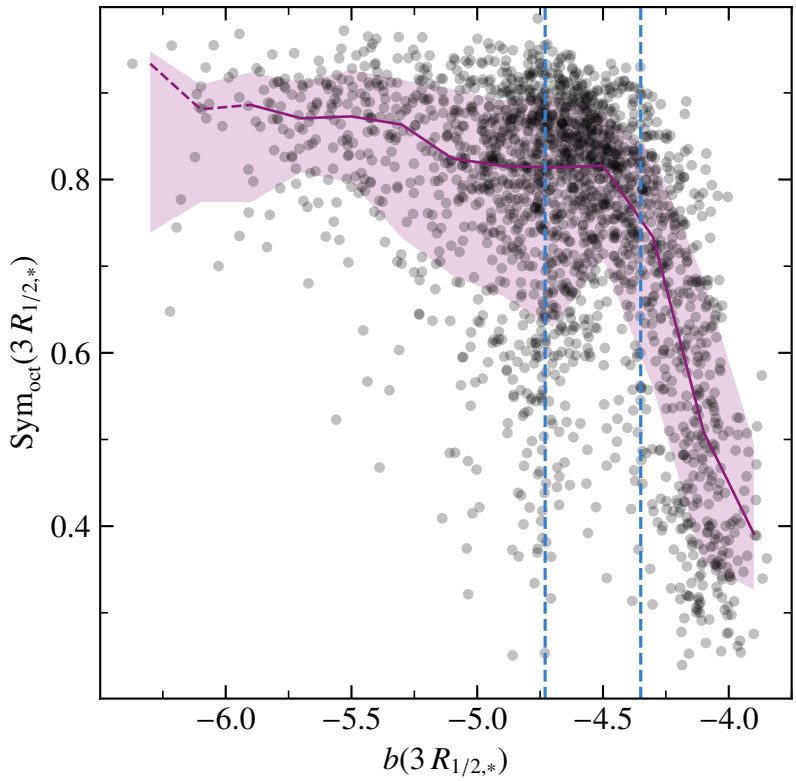

Figure 8.3: Relation between the octant symmetry of the stellar component and the b-value at $3\,R_{1/2,*}$. The dashed blue lines separate the ETGs (left) from the intermediate galaxies (middle) and LTGs (right) by b-value. The solid blackberry line indicates the median value in the respective symmetry bins and the shaded region the 1σ range (containing 68% of the galaxies above and below the median). The dashed part of the line indicates where there may be effects caused by low number statistics.

intermediate galaxies and ETGs), but overall less in between, seen by the small downward scatter between the two dashed lines. While it is possible that this is only a result of low number statistics, it is remarkable that the split occurs exactly in the region of the intermediate galaxies. A possible interpretation of this relation is that intermediate galaxies tend to be symmetric, whereas LTGs are the most asymmetric, and ETGs feature larger asymmetries the higher their b-value is. In the future, when the most common origins of asymmetry are determined, it will be easier to interpret the found relation with the b-value and possibly relate it to the formation histories of the galaxies, since the morphology is linked to the a galaxy's merger history. One simple step in this direction will be to analyze the cause of the asymmetries for the most asymmetric galaxies with b-values at the border between ETGs and intermediate galaxies and of the most asymmetric LTGs. Understanding their similarities and differences may be insightful. Possible causes for the asymmetric LTGs include substructure not identified by `SUBFIND`, shifted cores in the center, i.e., galaxies that have the dense core off-center in the disk, and asymmetric spiral structures, which can also be found in observations.

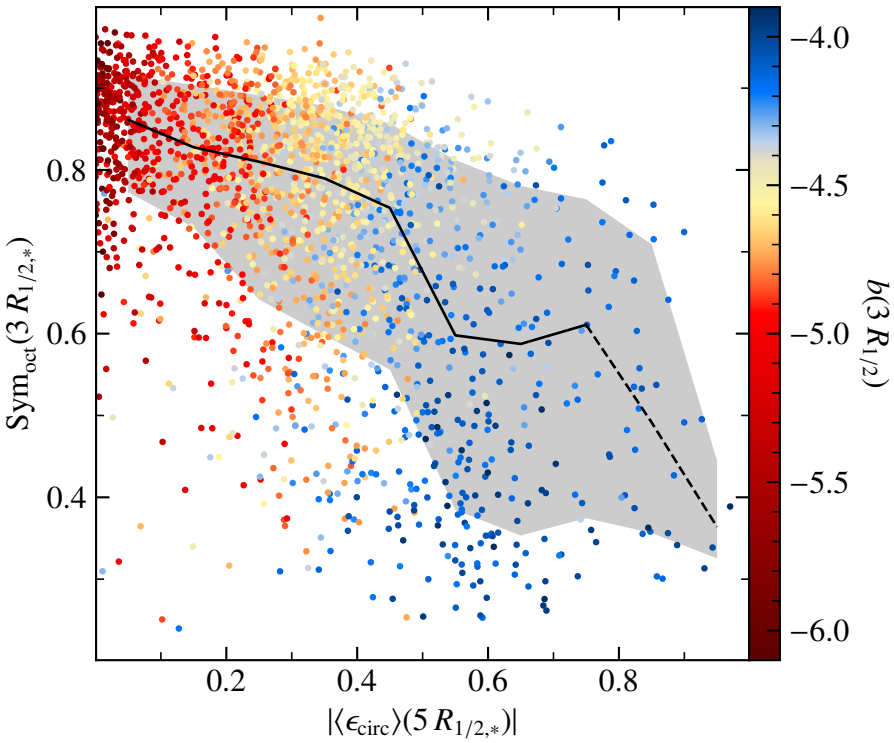

Figure 8.4: Relation between the octant symmetry of the stellar component at $3\,R_{1/2,*}$ and the absolute value of the average circularity, $|\langle\epsilon_{\mathrm{circ}}\rangle|$, of the stellar particles within $5\,R_{1/2,*}$, colored by the b-value. The solid black line indicates the median value in the respective symmetry bins and the shaded region the 1σ range (containing 68% of the galaxies above and below the median). The dashed part of the line indicates where there may be effects caused by low number statistics.

Circularity

As a quantity that has a strong correlation with the b-value, it is not surprising that we also find a trend with the symmetries for the circularity, ϵ_{circ}, which was introduced in Section 1.2.2. In Figure 8.4, the symmetry is plotted against the absolute average circularity of the stellar particles within $5\,R_{1/2,*}$. Since the circularity of particles in a perfect disk is $\epsilon_{\mathrm{circ}} = \pm 1$, LTGs are expected to have larger absolute average circularities than intermediate galaxies and ETGs. This is precisely what we observe in Figure 8.4, which also results in a trend between the symmetry and the absolute circularity: galaxies with larger absolute circularities tend to be more asymmetric. The scatter of the symmetry value also increases with the absolute circularity, recovering the trend that LTGs are found to span a large range of symmetry values. Interestingly, two of the galaxies with the largest asymmetries have very low absolute circularities of $|\langle\epsilon_{\mathrm{circ}}\rangle| \approx 0.1$. Investigating these galaxies may prove to be insightful with respect to kinematics and symmetries in the future.

Stellar Mass

The last galaxy property the symmetry is related to is the stellar mass. This is a quantity that has a weak correlation with the b-value, where most LTGs are low-mass galaxies and the high-mass galaxies tend to be ETGs. With that in mind, it is not surprising that we find a trend

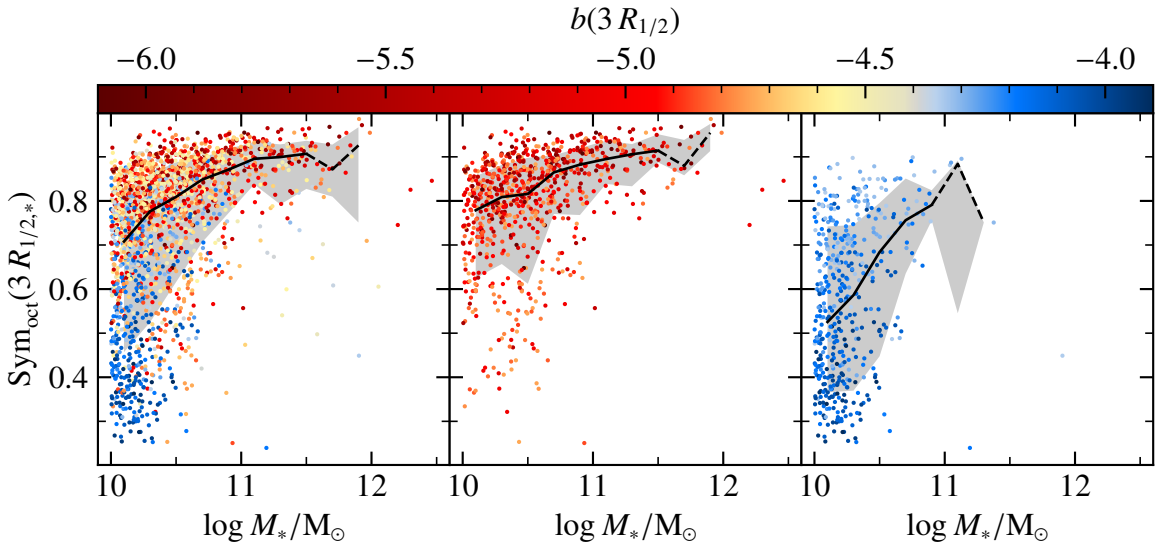

Figure 8.5: Relation between the octant symmetry of the stellar component at $3\,R_{1/2,*}$ and the stellar mass for the full galaxy sample (left), only the ETGs (middle), and only the LTGs (right), colored by the b-value. The solid black lines indicate the median value in the respective mass bins and the shaded regions the 1σ ranges (containing 68% of the galaxies above and below the median). The dashed part of the lines indicates where there may be effects caused by low number statistics.

with the octant symmetry value (left plot of Figure 8.5): galaxies with higher stellar masses tend to be more symmetric, whereas lower mass galaxies span a larger range of symmetry values, which is particularly the case for stellar masses of $M_* \approx 10^{10}\,\mathrm{M}_\odot$–$10^{10.5}\,\mathrm{M}_\odot$. There, the median symmetry is the lowest and the downward scatter the largest. To address the question whether this trend is driven by the b-value or the stellar mass, the ETGs and LTGs are considered separately in the middle and right plot of Figure 8.5. In both cases, we find an upward trend of the symmetry value with stellar mass. While the median symmetry of the ETGs increases slowly towards larger stellar masses, the median symmetry of the LTGs differs greatly between stellar masses, showing a median of $\mathrm{Sym}_{\mathrm{oct}} \approx 0.55$ for $M_* \approx 10^{10}\,\mathrm{M}_\odot$ and a much larger median of $\mathrm{Sym}_{\mathrm{oct}} \approx 0.8$ for $M_* \approx 10^{11}\,\mathrm{M}_\odot$. It therefore follows that the symmetry is primarily related to the morphology, i.e., the b-value, but also depends on the stellar mass for a given morphology. In the future, the dependence on mass will need to be further analyzed with respect to the origins of asymmetry in galaxies: it is possible that small substructures not identified by `SUBFIND` lead to asymmetries in low-mass galaxies, whereas in more massive galaxies, such small substructures are negligible compared to the total mass and size of a galaxy and larger substructures are generally identified as subhalos by `SUBFIND`, leading to remaining particle distributions that are more symmetric.

Formation History

In Section 5.4, it was found that there are a small number of ETGs that have ongoing star formation or relatively young stellar populations. Under the assumption that some of these galaxies experienced or are experiencing starbursts through a gas-rich merger, it is possible that such mergers would be visible through larger asymmetries of the galaxies. However,

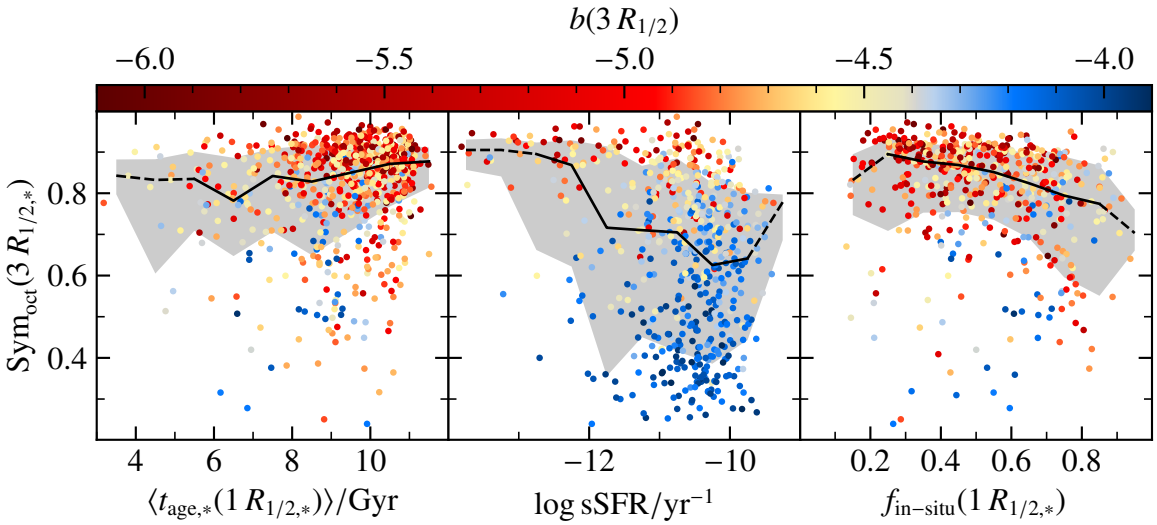

Figure 8.6: Relation of the octant symmetry of the stellar component at 3 $R_{1/2,*}$ with the mean stellar age within 1 $R_{1/2,*}$, the sSFR of the full galaxy, and the in-situ fraction within 1 $R_{1/2,*}$, colored by the b-value. The solid black lines indicate the median value in the respective bins and the shaded regions the 1σ ranges (containing 68% of the galaxies above and below the median). The dashed part of the lines indicates where there may be effects caused by low number statistics.

when determining the octant symmetry parameter of the galaxies without substructure, there is no trend of the symmetry with the central stellar age or the sSFR at constant b-value (left two plots of Figure 8.6). In contrast, the galaxies are found to be more asymmetrical the smaller the in-situ fraction is (right plot of Figure 8.6). The lack of a correlation with the star formation and stellar ages and the existing trend with the in-situ fraction shows that the symmetry is not driven by the star formation properties of the galaxies, but is more closely related to the mass accretion history. A dependence on the details of how `SUBFIND` determines the substructures cannot be excluded and will have to be investigated in the future.

8.5 Summary & Conclusion

Two different simple methods for quantifying the symmetry, the half-space and the octant methods, take the ratio of the numbers of particles in the half-space regions of the shape ellipsoid and in the octants obtained by the ellipsoid into account. This quantification shows how well the underlying particle distribution is actually described by the shape ellipsoid and can potentially be used in the future to filter out galaxies whose shapes cannot be appropriately described by ellipsoids. By definition, the octant method is more sensitive to asymmetry than the half-space method, such that the usage of the octant method should be preferred. Galaxies generally have similar symmetry values at 1 $R_{1/2,*}$ and 3 $R_{1/2,*}$. There are a number of galaxies, however, that are considerably more asymmetric at 3 $R_{1/2,*}$, which may result from substructure, tidal arms or other structures found further out.

The symmetry values are correlated with the flatness of galaxies, where flatter galaxies tend to be more asymmetric than more spherical galaxies. There is no trend found for the major axis ratio or the triaxiality. Because of the morphology's correlation with the minor

axis ratio, LTGs are also found to be more asymmetric than ETGs. Interestingly, it appears that intermediate galaxies may tend to be more symmetric than ETGs with high b-values, although this feature may be a result of low number statistics. The exact reason for the trend of the symmetry value with the morphology is still unclear, although possible drivers for the asymmetry include substructures not being identified by `SUBFIND` due to the generally lower masses of LTGs, off-center cores in the disk plane, and asymmetric spiral arms, which are also found in some observed LTGs.

Because of the trend with the b-value, the symmetry values also have a trend with another property correlated with the b-value: galaxies with large absolute values of the circularity tend to be more asymmetric. Even the stellar mass, where more massive galaxies tend to be ETGs, shows a clear correlation with the octant symmetry parameter: less massive galaxies tend to be more asymmetric. This trend is even true for a given morphology, where the differences between the symmetries of low-mass and high-mass LTGs are even larger than for ETGs. This shows that both the morphology and the stellar mass of galaxies influence their symmetries.

Finally, the mean central stellar age and the sSFR are found to not be drivers of the symmetry, since there is no trend with the symmetry values at a given morphology. In contrast, the in-situ fraction, which is strongly correlated with the formation history of a galaxy (Remus & Forbes, 2021), has a correlation with the symmetry: galaxies with smaller in-situ fractions tend to be more symmetric. Since the in-situ fraction is correlated with the stellar mass of the galaxies (Figure 5.8), this result is expected. It can be concluded that not the stellar age or the star formation rate drive the symmetry, but the formation history.

These first findings for the symmetries of galaxies should pave the way towards a more accurate treatment of galaxy shapes and a better understanding of the drivers of asymmetries. The next important step will be to compare the symmetry values with a classification of galaxies by the presence of mergers, tidal arms, streams, and shells. This will lead to an improved interpretation of the symmetry values themselves.

9 Summary & Conclusion

In this work, the shapes of a sample of galaxies from the cosmological hydrodynamical simulation suite *Magneticum Pathfinder* were investigated and related to a variety of galaxy properties, with a focus on kinematics and formation histories. The galaxies were taken from the medium-sized Box4 (uhr) of Magneticum Pathfinder, which combines a sufficiently large cosmological volume for the purposes of this work with high resolution. The galaxies were selected by a stellar and DM mass cut of $M_{*/\mathrm{DM}} \geq 10^{10}\,\mathrm{M}_{\odot}$ to ensure a particle number per galaxy that is sufficient for obtaining accurate results for the shapes. The DM mass cut prevents satellite galaxies from being considered to which only a very small number of DM particles were assigned by the halo finder, `SUBFIND`. Additionally, a threshold of at least twice the stellar softening length for the stellar half-mass radii was adopted.

The shapes of halos and galaxies are typically described by ellipsoids in the literature. Because of the large number of methods used to determine these ellipsoids, the theoretical background of the shape determination methods and a thorough comparison of these were first presented. For the sample of galaxies used, the method of choice for the local shape of a galaxy is the iterative unweighted method, where the volume of the deforming ellipsoid is kept constant. This is the method applied throughout this work. For the global shape of a galaxy, the preferred approach is the iterative reduced ellipsoidal method. The shapes are quantified by three parameters, where q is the major axis ratio of the ellipsoid, corresponding to one minus the face-on ellipticity, s is the minor axis ratio, corresponding to one minus the edge-on ellipticity, and T is the triaxiality, a quantity which solely depends on the two axis ratios and quantifies how prolate or oblate the shape ellipsoid is.

As expected from an intuitive understanding that disk galaxies are flat from an edge-on perspective and have oblate shapes, while elliptical galaxies have more spherical shapes, the relations between the shape parameters and the morphological parameter used in this work, the b-value, show clear trends: LTGs, which have large b-values and are typically disk galaxies, have the flattest shapes (i.e., low values of s) and are the most oblate. ETGs, which have small b-values and are typically elliptical galaxies, have the most spherical shapes (i.e., large values of s). While the shape parameters are generally similar at one and three stellar half-mass radii, the major axis ratio tends to be larger at $3\,R_{1/2,*}$ than at $1\,R_{1/2,*}$, which leads to a shift towards more triaxial to oblate shapes at $3\,R_{1/2,*}$.

Because of the strong correlation between the b-value and the minor axis ratio, s, any properties having a sufficiently tight relation with the b-value are found to also be correlated with s. This includes the λ_R-parameter, which quantifies the rotational support of a galaxy, where galaxies with more rotational support tend to be flatter. This relation can be identified

with the λ_R-ϵ plane for the edge-on ellipticity $\epsilon = 1 - s$, in which the fast rotators are typically distinguished from the slow rotators (e.g. Schulze et al., 2018). Since the anisotropy has a tight relation within this plane, the anisotropy is also found to correlate with the minor axis ratio. In fact, the minor axis ratio together with the b-value can be used to constrain the anisotropy well. Since the b-value is a measure of the morphology, which in turn is generally understood to be a result of the merger history of a galaxy, a number of quantities related to the formation history correlate with the b-value and therefore with the minor axis ratio: galaxies with higher sSFR tend to be flatter, as do galaxies with younger stellar populations within one half-mass radius. Even for a given b-value, galaxies with younger central stellar populations tend to be flatter, where only few ETGs have especially young average stellar ages, which are linked to ongoing star formation, likely caused by starbursts in mergers. While these ETGs with young stellar populations or ongoing star formation could be linked to galaxies in the process of merging and therefore have more asymmetric shapes, this could not be found in the analysis of the galaxies when ignoring substructure.

There are remarkable trends of the shapes with the in-situ fraction, however: at a given stellar mass, all three shape parameters have a tight correlation with the in-situ fraction. This will allow observers to further constrain the in-situ fractions (which is difficult to determine from observations) through the projected shape and the stellar mass. In contrast, the stellar mass itself shows no trends with the shapes. Only the mass distribution, described by the mass-size relation, is related to the shapes.

The alignment of the stellar and DM angular momenta are also related to the b-value: LTGs are typically found to have better alignment angles, such that flat galaxies generally have well aligned stellar and DM angular momenta. The trend breaks down at large misalignments, where the shapes of the galaxies (mostly ETGs) become independent of the angular momenta alignment.

An important finding is that DM follows the stellar component's radial profiles of shape and its alignment, which was investigated out to $5\,R_{1/2,*}$. The DM only has a different orientation in the core region, which may be linked to resolution issues. This is true across the different kinematic groups, all of which feature distinct shape profiles. Regular rotators are typically more oblate and have a good alignment between the stellar minor axis and the stellar angular momentum, non-rotators are triaxial to prolate and have poor alignment between the stellar minor axis and $\boldsymbol{j}_*$, KDCs feature a decoupled stellar shape from the DM in the core region, and prolate rotators have remarkably prolate shapes, even at large radii, and a maximum misalignment between the stellar minor axis and $\boldsymbol{j}_*$. For all groups except the prolate rotators, the alignment of the DM's minor axis and its angular momentum is worse than for the stellar component. Overall, a clear link between the inner kinematics of galaxies and their shapes is found.

For the radial λ_R-profile groups, the shape profiles are similar between the increasers and the flats, and only the decreasers distinguish themselves through more rotational support and more oblate shapes, very similar to the regular rotators. This is related to their different formation history that is dominated by mini and minor mergers at late times, where the peak

λ_R-value indicates the location of the transition from the in-situ dominated inner region to the ex-situ dominated outer region (Schulze et al., 2020). Interestingly, the alignment profiles of the increasers and decreasers are similar, whereas the flats feature worse alignments between the minor axes and angular momenta of the stellar and DM components. Clearly, the kinematic groups are found to have the stronger correlation with the shapes, which shows how they are more tightly connected to the formation histories than the λ_R-profile groups.

Despite there being a correlation between the stellar global spin parameter and $\lambda_{R_{1/2}}$, there is only a minor trend between the stellar minor axis ratio and the stellar global spin parameter through the existence of a lower bound of s. Aside from that relation, there are no clear trends between the shape parameters and the global spin parameters, neither for the inner stellar or DM shapes, nor for the shape of the full DM halo. This indicates that the global spin parameter is not a driver of the stellar or DM shapes.

In this work, the local cosmic environment is quantified using the average density within 5 Mpc of a galaxy. This value is correlated with the total global spin parameter, where galaxies with higher global spin parameters tend to be found in more dense environments. Just as for the global spin parameters, using this quantification for the cosmic environment, there is no evidence of the environment affecting the shapes of galaxies or their halos.

To assess how well the shape ellipsoids describe the underlying particle distributions, two methods to describe the symmetry of galaxies (with the substructure removed) were introduced. The half-space symmetry value is equal to the smallest ratio of the number of particles per half of the shape ellipsoids, and the octant symmetry value is equal to the smallest ratio of the number of particles per octant of the ellipsoids. Both symmetry values show overall agreement in distinguishing symmetric from more asymmetric galaxies. The octant symmetry method is preferred in usage because of its greater sensitivity to asymmetries in galaxies.

There is a clear trend of the symmetry with the minor axis ratio and the b-value: flat galaxies and LTGs tend to be more asymmetric. While the origin of this is still unclear, possible reasons include substructure not being identified by `SUBFIND` because of LTGs mostly having low stellar masses, and thus the satellites may have masses below the identification threshold, off-center cores in the disk, asymmetric spiral arms, and merger remnants like streams and shells. As the circularity is strongly related to the b-value, there is also a correlation between the symmetry and the circularity. In addition to the morphology, there is also a trend with the stellar mass and the in-situ fraction at constant b-value: more massive galaxies and galaxies with smaller in-situ fractions tend to be more symmetric. In contrast, the symmetry values are independent of the mean stellar age and the specific star formation rate. The symmetry is therefore influenced more by the formation history and not by the internal processes of star formation driven by gas.

In summary, this work has shown that the stellar shape parameters are correlated with a broad range of galaxy properties, from morphology and formation history to kinematics. It was also demonstrated that the minor axis ratio, i.e., the edge-on ellipticity, is the shape parameter that is most correlated with other properties. This is an important point for

observations, where the edge-on ellipticity can be obtained through the projected view and an estimation of the inclination of the galaxy. There is almost no evidence for correlations of the stellar and DM shapes with the investigated large scale galaxy properties, the global spin parameters and the cosmic environment, suggesting that the details of the shapes are mainly driven by the exact formation history and the resulting inner kinematics. In contrast, the inner kinematic groups feature distinct radial stellar and DM shape and alignment profiles. For the λ_R-profile groups, this is mostly only the case for the decreasers due to their particular formation histories compared to the increasers and flats. Finally, an important finding is that the DM overall follows the stellar component in shape and alignment, independent of the kinematics, with the exception of the core region of KDCs. This is an especially important result for the modeling of DM in galaxies, which is necessary for Jeans modeling, lensing models, and many other applications in astrophysics that try to connect the DM to the baryonic components to shed further light on the nature of DM.

A Shapes

A.1 Reduced Ellipsoidal Method Applied to a Merger

Applying the iterative reduced ellipsoidal method, keeping the volume of the deforming ellipsoid constant, to the merging galaxy shown in Figure 3.4 (for the unweighted method) at three half-mass radii results in the shape contour seen in Figure A.1. The shape is almost identical to the result found for the iterative unweighted method (dotted line for comparison), which shows that even the reduced ellipsoidal method, which is generally supposed to be less influenced by substructures, reaches its limits for such major mergers. The large number of particles in the merging structure appears to dominate the sum for the shape tensor even with the squared radial weighting applied by the reduced methods. Clearly, such ongoing mergers lead to shapes with questionable meaningfulness, further supporting the approach taken in Chapter 8 to provide the means to filtering out those objects by quantifying the asymmetry of a galaxy.

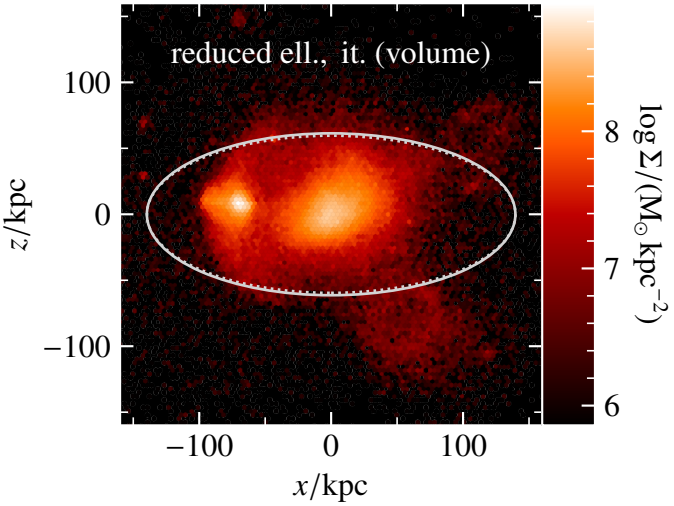

Figure A.1: Surface density map of the example galaxy seen in Figure 3.4 with the overplotted ellipsoid contour at three half-mass radii for the iterative reduced ellipsoidal shape determination method with constant volume (solid ellipse). The galaxy is viewed edge-on in the eigenvector coordinate system of the shape tensor. The dotted ellipse is the same ellipse as shown for the iterative unweighted method in Figure 3.4 for comparison.

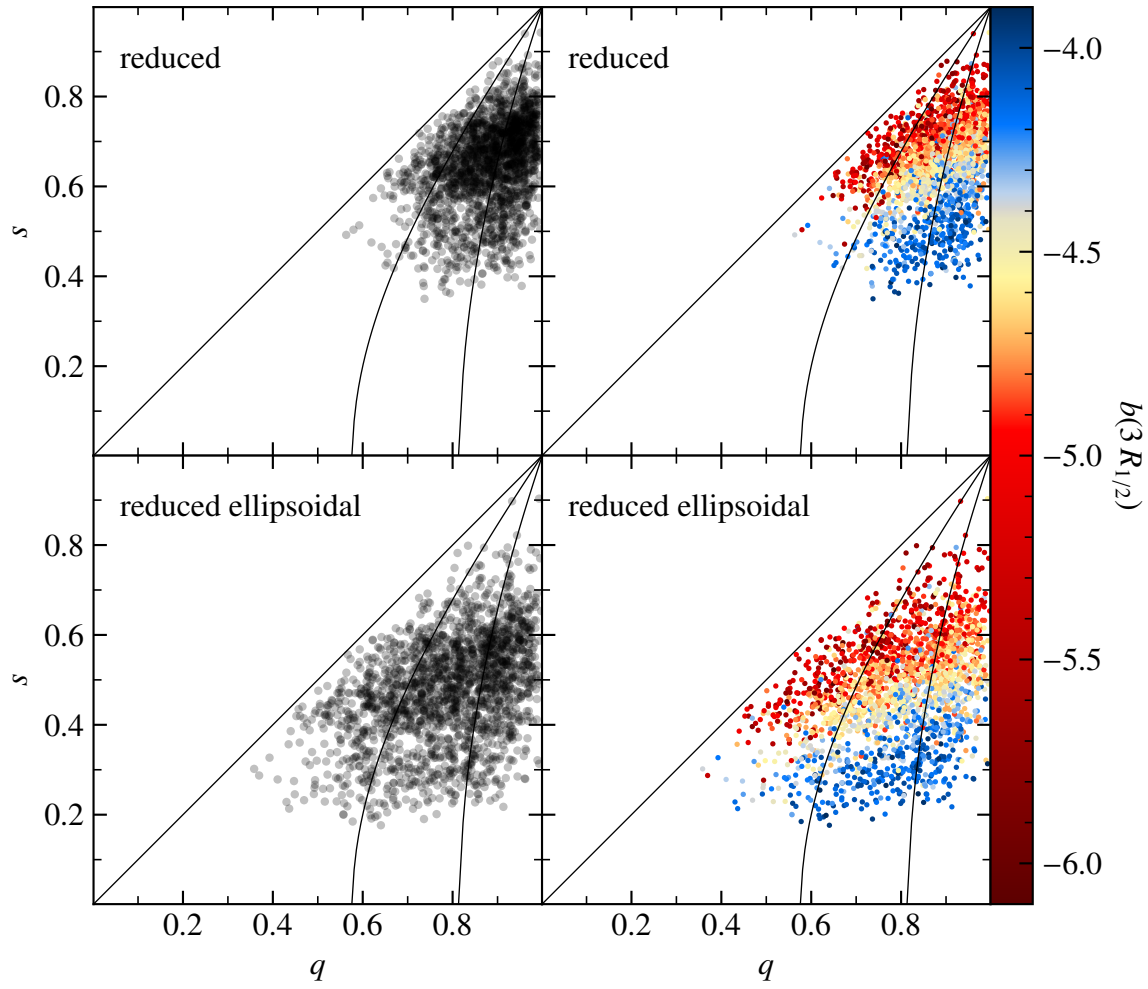

Figure A.2: Axis ratios q and s of the dark matter component of the galaxy sample at three half-mass radii for the iterative reduced and reduced ellipsoidal methods at constant ellipsoid volume. On the left, the points are plotted semi-transparently to better show their distribution, while the same points are colored by b-value on the right. The solid lines indicate the borders between prolate, triaxial, and oblate shapes, from left to right, respectively.

A.2 Axis Ratios of the Reduced Methods

The axis ratios q and s of the galaxy sample are dependent on the shape determination method used (Section 3.3.1). As discussed in that section, the reduced method has a bias towards more spherical shapes. Precisely this behavior is observed for the axis ratios at $3\,R_{1/2,*}$ in Figure A.2, with both q and s shifting up towards larger values compared to what is observed for the iterative unweighted method in Figure 4.1. For the reduced ellipsoidal method (bottom of Figure A.2), we find a distribution of points which lies approximately between what was observed for one and three half-mass radii for the unweighted method in Figure 4.1. This is consistent with the conclusion drawn in Section 3.3.1, that the reduced ellipsoidal method describes the average shape within the determined ellipsoid.

Neither of the two methods affects the correlation with the b-value observed for the unweighted method at $3\,R_{1/2,*}$, however. This shows that the reduced and reduced ellipsoidal

methods affect all galaxies similarly, distorting the absolute values of the axis ratios in a systematic rather than completely random way.

B Radial Profiles of Individual Galaxies

To give an idea of what the individual stellar and DM shape and alignment profiles look like that make up the median lines and scatter regions of Figure 6.3 and Figure 6.4 for the four kinematic groups, the profiles of selected galaxies from each group are presented here. For the radial shape parameters, the profiles of the 20 most massive galaxies in each group (Figure B.1) and those for the single most massive galaxy in each group (Figure B.2) are plotted. For the radial alignments, only the profiles of the single most massive galaxy in each group (Figure B.3) are plotted. The plots with the respective 20 most massive galaxies in each kinematic group give an impression of what the scatter region shown in Figure 6.3 represents and how much the individual profiles in the same kinematic group can deviate from each other. For the single most massive galaxies, it becomes very clear how similar the stellar and DM shape and alignment profiles can be to each other, emphasizing how the DM follows the stellar component. An interesting feature is found for the most massive KDC, where the shape of the DM component clearly has a large twist between 2 $R_{1/2,*}$ and 3 $R_{1/2,*}$ (seen for the black line in the second and third column of the KDC row in Figure B.3). Note, however, that the DM shape is also rather spherical for that KDC (seen for the s_{DM}-profile of the KDC in Figure B.2), such that twists can easily occur because small changes of the shape can lead to large changes of the principal axes.

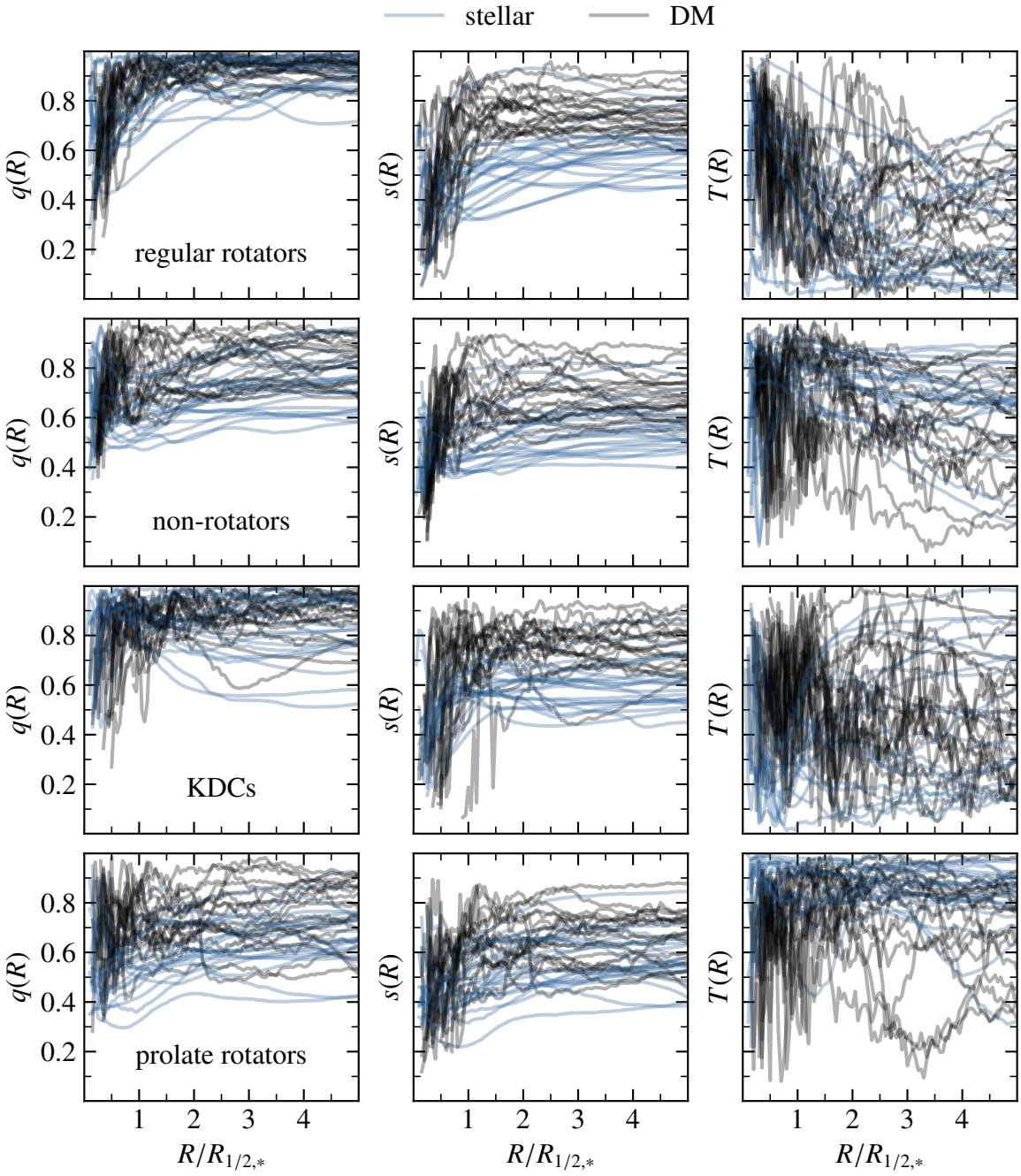

Figure B.1: Radial shape profiles of the stellar (blue) and DM (black) components of the 20 most massive galaxies in each of the kinematic groups from one to five stellar half-mass radii. The lines are only plotted for the radial distances that are larger than the softening length (1 kpc for the stellar component, 2 kpc for the DM component).

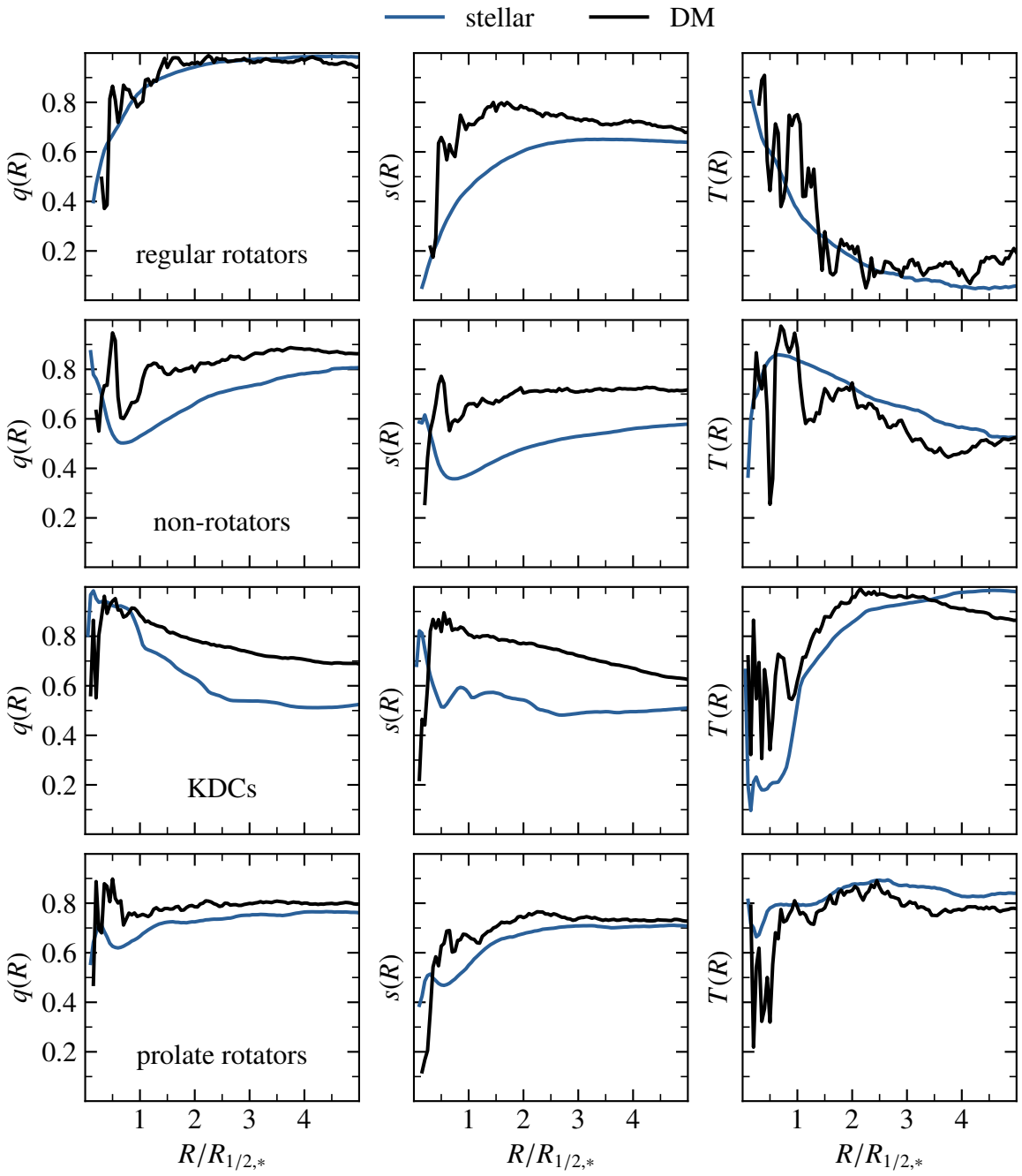

Figure B.2: Radial shape profiles of the stellar (blue) and DM (black) components of the single most massive galaxy in each of the kinematic groups from one to five stellar half-mass radii. The lines are only plotted for the radial distances that are larger than the softening length (1 kpc for the stellar component, 2 kpc for the DM component).

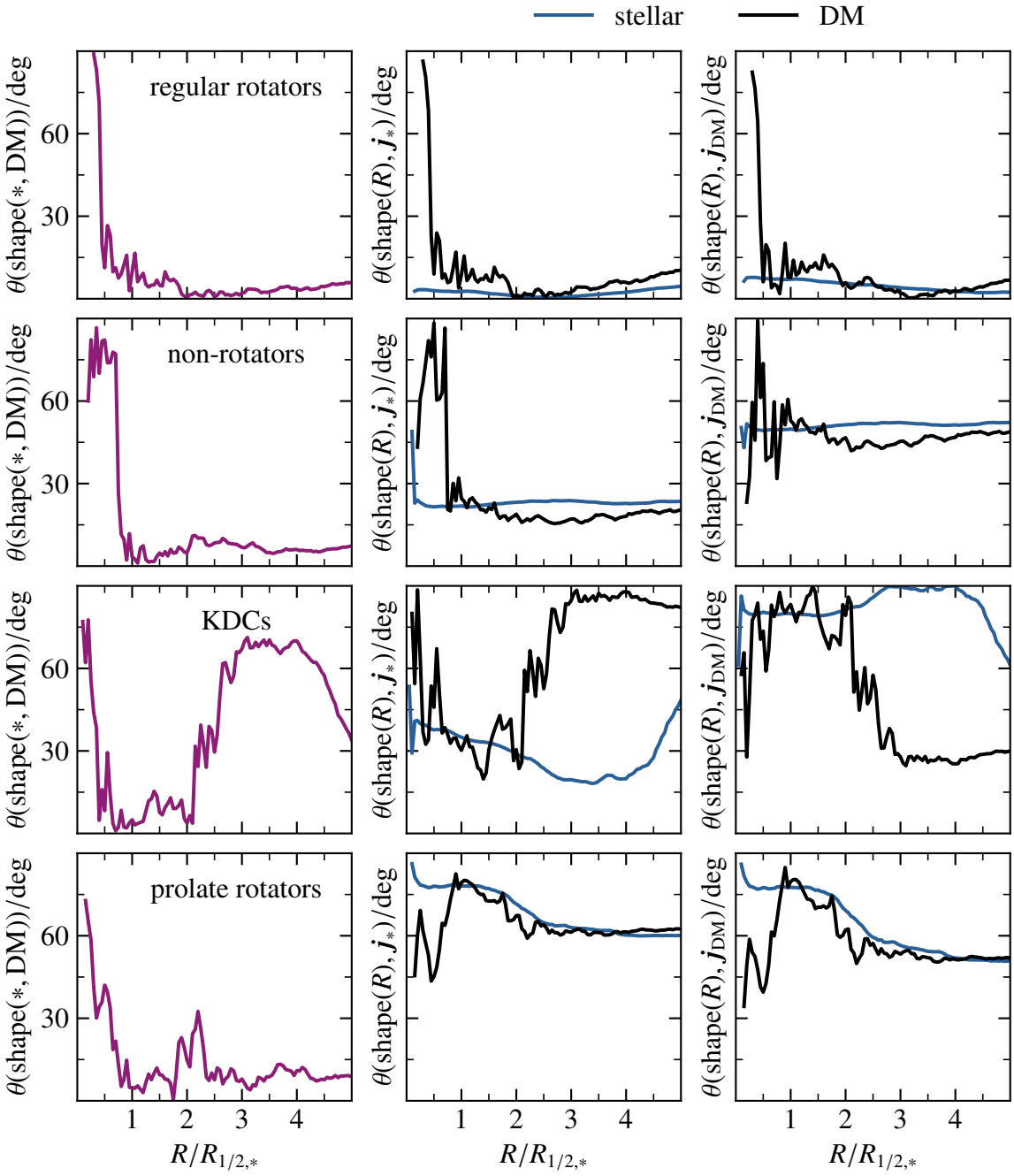

Figure B.3: Radial alignment profiles of the stellar (blue) and DM (black) components of the single most massive galaxy in each of the kinematic groups from one to five stellar half-mass radii. The left column shows the angles between the minor axes of the stellar and DM shapes, the middle column the angles between the stellar angular momentum at 3 $R_{1/2,*}$ and the minor axis of the stellar and DM shapes, and the right column the angles between the DM angular momentum at 3 $R_{1/2,*}$ and the minor axis of the shapes. The lines are only plotted for the radial distances that are larger than the softening length (1 kpc for the stellar component, 2 kpc for the DM component).

C Randomly Oriented Axes

For two randomly oriented axes, we find the probability distribution function (pdf) of the angle between them (in the range 0°–90°) to be proportional to the circumference of a circle on a sphere given by the polar angle, θ (which corresponds to the alignment angle). Such a polar angle is shown in Figure C.1 between the two red lines, for which the circle on the sphere is also highlighted in red. The circumference of a circle at a given polar angle, θ, is $2\pi \sin\theta$, such that we obtain the pdf $p(\theta) \propto \sin\theta$. It turns out that the proportionality factor is 1 since the pdf is already normalized:

$$\int_0^{\frac{\pi}{2}} d\theta \sin\theta = 1, \tag{C.1}$$

which means that the wanted pdf is (Ho & Turner, 2011):

$$p(\theta) = \sin\theta. \tag{C.2}$$

From this, we can derive the angle, θ_q, corresponding to a given quantile, q:

$$q \stackrel{!}{=} \int_0^{\theta} d\theta' \sin\theta' = 1 - \cos\theta \tag{C.3}$$

$$\Rightarrow \quad \theta = \arccos(1 - q). \tag{C.4}$$

For the median at $q = 0.5$, this gives us $\theta_{\text{median}} = 60°$, for the upper bound containing 68% of the data above the median, $q = 0.5 - 0.5 \cdot 0.68 = 0.16$, giving us 33°, and for the lower bound containing 68% of the data below the median, $q = 0.5 + 0.5 \cdot 0.68 = 0.84$, giving us 81°.

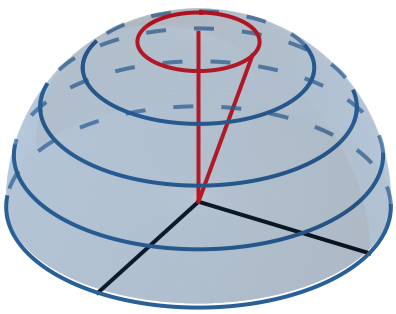

Figure C.1: Visualization of the derivation of the probability distribution function for randomly aligned axes, which is proportional to the circumference of a circle given by a polar angle, θ. The angle between the two red lines is an example for such a polar angle.

D Total & DM Global Spin Parameters

The total and DM global spin parameters are generally very similar to each other (Figure D.1). This mainly results from the DM dominating the total mass of galaxies, as can be seen by the coloring of the data points, where the outliers are satellite galaxies with small amounts of DM that were associated with the subhalos by `SUBFIND`. Also note that while the gas component can lose spin via redistribution of its angular momentum or through feedback leading to expulsion of gas, the DM only interacts gravitationally, preventing it from losing spin over time. As a result, the DM's spin can be expected to remain close to the total spin.

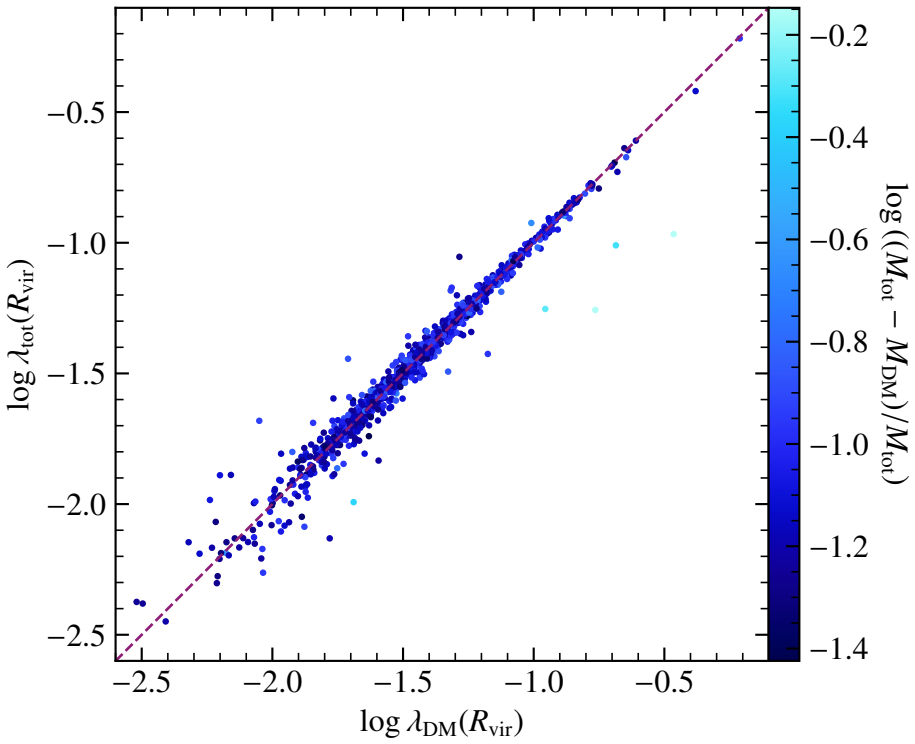

Figure D.1: Comparison between the total and the DM global spin parameters within $R_{\rm vir}$, colored by the relative difference between the total and DM mass. The dashed line indicates the one-to-one relation between the global spin parameters

E Cosmic Environment Correlations

As seen in Section 7.2, the quantification of the cosmic environment used in this work – the average density within a 5 Mpc radius of each galaxy – shows no trend with the stellar or DM shape parameters (Figure 7.5) and only a weak relation with the total global spin parameter (Figure 7.4). In the course of this work, a large number of possible correlations with other galaxy properties were analyzed for the cosmic environment. Surprisingly, one of the properties that correlates best with it is the index of each galaxy in the output list of SUBFIND, which is referred to as the SUBFIND ID in the following (left panel of Figure E.1): the galaxies with the smallest IDs are found in the densest environments, whereas galaxies with larger IDs are typically found in less dense regions. The origin of this relation is found through a second galaxy property that is correlated with the average local density: the stellar mass (right panel of Figure E.1). The most massive galaxies, which are the main galaxies in cluster and group environments, are located in the densest regions, whereas less massive galaxies are found in all types of environments, such that the median local density is much lower for low-mass galaxies. Since SUBFIND lists the the galaxy groups approximately sorted by their total mass and the main subhalos are found in the same order as their corresponding groups (with the satellites listed after their respective main subhalo), the correlation found for M_* with the environment gives rise to the one found for the SUBFIND ID.

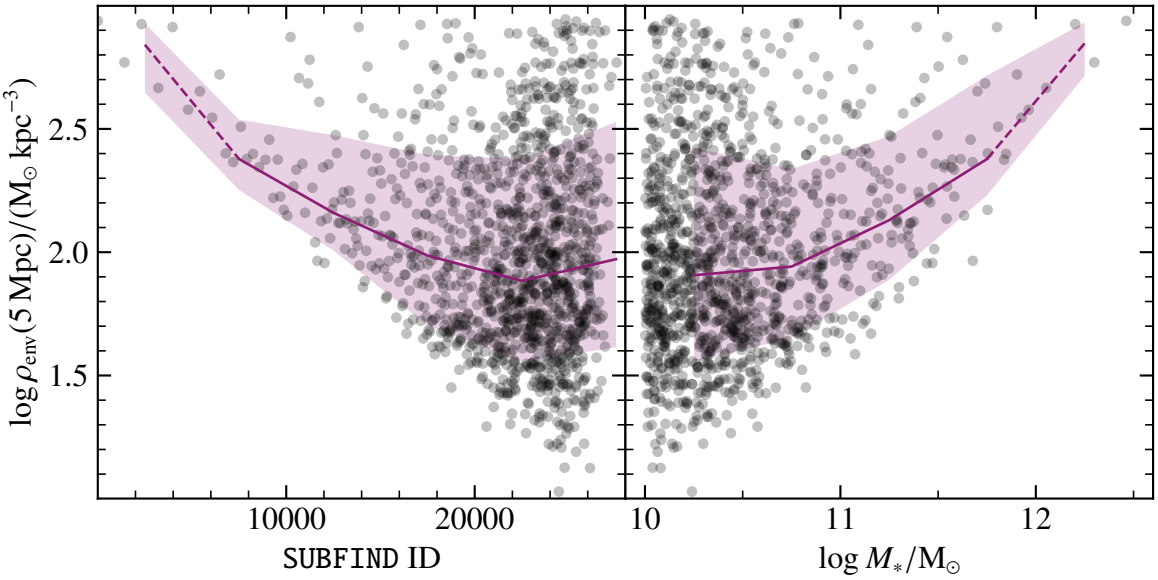

Figure E.1: Relations of the average local density within a 5 Mpc radius with the subhalo ID from SUBFIND (left) and with the stellar mass (right). The solid blackberry lines indicate the median values in the respective ID bins and the shaded regions the 1σ range (containing 68% of the galaxies above and below the median). The dashed part of the lines indicates where there may be effects caused by low number statistics.

F Shapes & Half-Space Symmetry

In Figure 8.2, a clear trend between the octant symmetry, the minor axis ratio, s, and the b-value is found at 1 $R_{1/2,*}$ and 3 $R_{1/2,*}$. To investigate whether this relation is only linked to the octant method or if it also is a trend found for the second discussed quantification of symmetry, the half-space method, the relation between the half-space symmetry values and the shape parameters at 1 $R_{1/2,*}$ and 3 $R_{1/2,*}$ are shown in Figure F.1. The relation is very similar to the one found for the octant symmetry method in Figure 8.2. The major difference is that $\mathrm{Sym}_{\mathrm{half}}$ spans a smaller range of values and is larger or equal to $\mathrm{Sym}_{\mathrm{oct}}$ (which is necessarily the case, see Section 8.1). As for the octant symmetry, we here find a slight trend at both considered radii for the major axis ratio, q, which tends to be lower for larger asymmetries. Interestingly, the downward scatter of q appears to be smaller for the largest asymmetries at 1 $R_{1/2,*}$, although this may be due to the small number of galaxies with the largest asymmetries. We again find the clear trend of the minor axis ratio being smaller for larger asymmetries, and finally, the trend is lost for the most part for the triaxiality. We also find the trend between the symmetry values and the b-value: galaxies with small values of $\mathrm{Sym}_{\mathrm{half}}$ tend to be LTGs, while ETGs tend to be more symmetric.

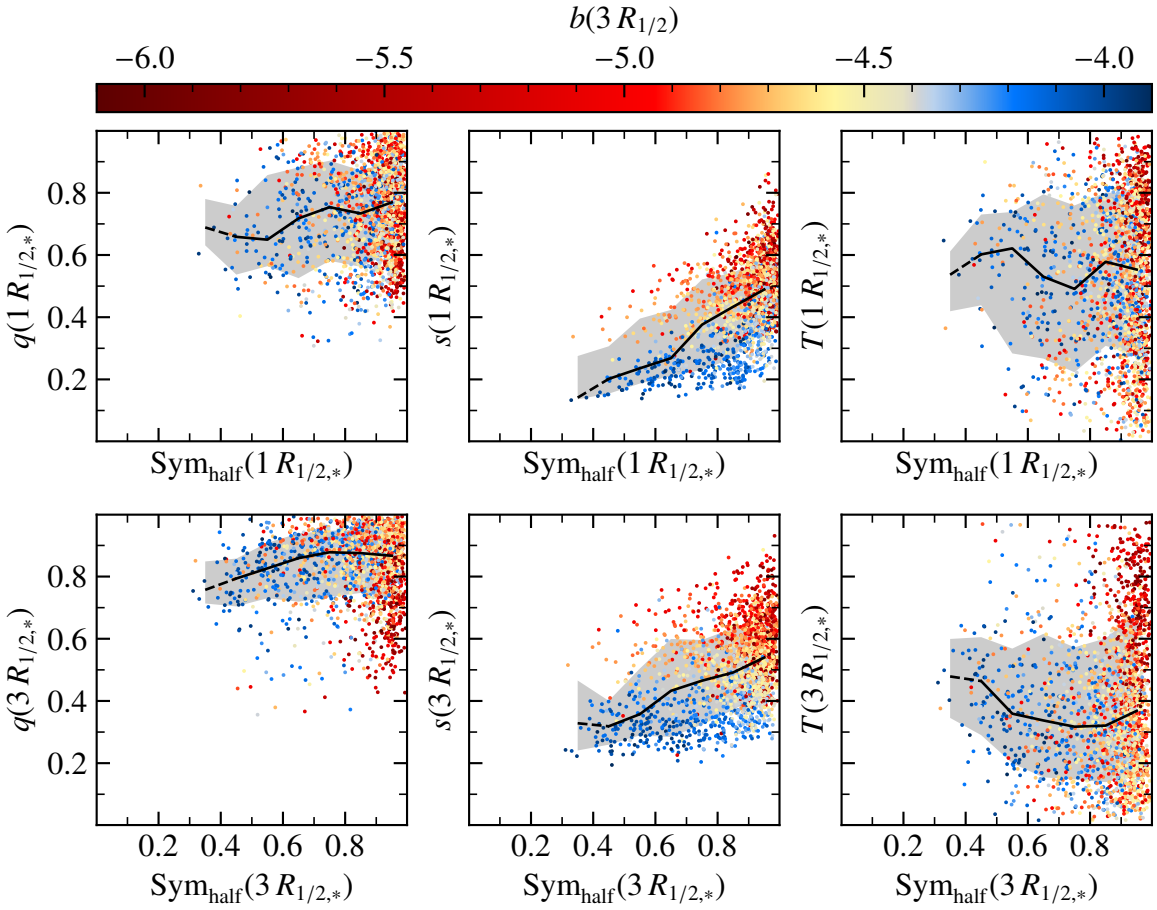

Figure F.1: Relation of the half-space symmetry at $1\,R_{1/2,*}$ (top row) and $3\,R_{1/2,*}$ (bottom row) with the shape parameters at the respective radial distances, q, s, and T, for the stellar component. The solid black lines indicate the median values in the respective symmetry bins and the shaded regions the 1σ ranges (containing 68% of the galaxies above and below the median). The dashed part of the lines indicates where there may be effects caused by low number statistics.

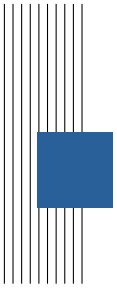

References

Abadi, M. G., Moore, B., & Bower, R. G. (1999). Ram pressure stripping of spiral galaxies in clusters. *MNRAS*, *308*(4), 947–954.

Abadi, M. G., Navarro, J. F., Steinmetz, M., & Eke, V. R. (2003). Simulations of Galaxy Formation in a Λ Cold Dark Matter Universe. II. The Fine Structure of Simulated Galactic Disks. *ApJ*, *597*(1), 21–34.

Allen, R. J., Kacprzak, G. G., Glazebrook, K., Labbé, I., Tran, K.-V. H., Spitler, L. R., Cowley, M., Nanayakkara, T., Papovich, C., Quadri, R., Straatman, C. M. S., Tilvi, V., & van Dokkum, P. (2017). The Size Evolution of Star-forming Galaxies since z ∼ 7 Using ZFOURGE. *ApJ*, *834*(2), L11.

Allgood, B., Flores, R. A., Primack, J. R., Kravtsov, A. V., Wechsler, R. H., Faltenbacher, A., & Bullock, J. S. (2006). The shape of dark matter haloes: dependence on mass, redshift, radius and formation. *MNRAS*, *367*(4), 1781–1796.

Arnold, J. A., Romanowsky, A. J., Brodie, J. P., Forbes, D. A., Strader, J., Spitler, L. R., Foster, C., Blom, C., Kartha, S. S., Pastorello, N., Pota, V., Usher, C., & Woodley, K. A. (2014). The SLUGGS Survey: Wide-field Stellar Kinematics of Early-type Galaxies. *ApJ*, *791*(2), 80.

Bacon, R., Copin, Y., Monnet, G., Miller, B. W., Allington-Smith, J. R., Bureau, M., Carollo, C. M., Davies, R. L., Emsellem, E., Kuntschner, H., Peletier, R. F., Verolme, E. K., & de Zeeuw, P. T. (2001). The SAURON project - I. The panoramic integral-field spectrograph. *MNRAS*, *326*(1), 23–35.

Balcells, M., & Quinn, P. J. (1990). The Formation of Counterrotating Cores in Elliptical Galaxies. *ApJ*, *361*, 381.

Beck, A. M., Murante, G., Arth, A., Remus, R. S., Teklu, A. F., Donnert, J. M. F., Planelles, S., Beck, M. C., Förster, P., Imgrund, M., Dolag, K., & Borgani, S. (2016). An improved SPH scheme for cosmological simulations. *MNRAS*, *455*(2), 2110–2130.

Beckwith, S. V. W., Stiavelli, M., Koekemoer, A. M., Caldwell, J. A. R., Ferguson, H. C., Hook, R., Lucas, R. A., Bergeron, L. E., Corbin, M., Jogee, S., Panagia, N., Robberto, M., Royle, P., Somerville, R. S., & Sosey, M. (2006). The Hubble Ultra Deep Field. *AJ*, *132*(5), 1729–1755.

Bender, R. (1988). Rotating and counter-rotating cores in elliptical galaxies. *A&A*, *202*, L5–L8.

Bender, R., Saglia, R. P., & Gerhard, O. E. (1994). Line-of-sight velocity distributions of elliptical galaxies. *MNRAS*, *269*, 785–813.

Bendo, G. J., & Barnes, J. E. (2000). The line-of-sight velocity distributions of simulated merger remnants. *MNRAS*, *316*(2), 315–325.

Bershady, M. A., Verheijen, M. A. W., Swaters, R. A., Andersen, D. R., Westfall, K. B., & Martinsson, T. (2010). The DiskMass Survey. I. Overview. *ApJ*, *716*(1), 198–233.

Bertola, F., Corsini, E. M., Beltrán, J. C. V., Pizzella, A., Sarzi, M., Cappellari, M., & Funes, J. G., S. J. (1999). The Bulge-Disk Orthogonal Decoupling in Galaxies: NGC 4698. *ApJ*, *519*(2), L127–L130.

Bett, P. (2012). Halo shapes from weak lensing: the impact of galaxy-halo misalignment. *MNRAS*, *420*(4), 3303–3323.

Bett, P., Eke, V., Frenk, C. S., Jenkins, A., Helly, J., & Navarro, J. (2007). The spin and shape of dark matter haloes in the Millennium simulation of a Λ cold dark matter universe. *MNRAS*, *376*(1), 215–232.

Beygu, B., Kreckel, K., van der Hulst, J. M., Jarrett, T. H., Peletier, R., van de Weygaert, R., van Gorkom, J. H., & Aragon-Calvo, M. A. (2016). The void galaxy survey: Star formation properties. *MNRAS*, *458*(1), 394–409.

Binney, J. (1978). On the rotation of elliptical galaxies. *MNRAS*, *183*, 501–514.

Binney, J. (2005). Rotation and anisotropy of galaxies revisited. *MNRAS*, *363*(3), 937–942.

Bois, M., Bournaud, F., Emsellem, E., Alatalo, K., Blitz, L., Bureau, M., Cappellari, M., Davies, R. L., Davis, T. A., de Zeeuw, P. T., Duc, P. A., Khochfar, S., Krajnović, D., Kuntschner, H., Lablanche, P. Y., McDermid, R. M., Morganti, R., Naab, T., Oosterloo, T., Sarzi, M., Scott, N., Serra, P., Weijmans, A., & Young, L. M. (2010). Formation of slowly rotating early-type galaxies via major mergers: a resolution study. *MNRAS*, *406*(4), 2405–2420.

Bois, M., Emsellem, E., Bournaud, F., Alatalo, K., Blitz, L., Bureau, M., Cappellari, M., Davies, R. L., Davis, T. A., de Zeeuw, P. T., Duc, P.-A., Khochfar, S., Krajnović, D., Kuntschner, H., Lablanche, P.-Y., McDermid, R. M., Morganti, R., Naab, T., Oosterloo, T., Sarzi, M., Scott, N., Serra, P., Weijmans, A.-M., & Young, L. M. (2011). The ATLAS^{3D} project - VI. Simulations of binary galaxy mergers and the link with fast rotators, slow rotators and kinematically distinct cores. *MNRAS*, *416*(3), 1654–1679.

Brammer, G. B., Whitaker, K. E., van Dokkum, P. G., Marchesini, D., Franx, M., Kriek, M., Labbé, I., Lee, K. S., Muzzin, A., Quadri, R. F., Rudnick, G., & Williams, R. (2011). The Number Density and Mass Density of Star-forming and Quiescent Galaxies at 0.4 <= z <= 2.2. *ApJ*, *739*(1), 24.

Bullock, J. S., Dekel, A., Kolatt, T. S., Kravtsov, A. V., Klypin, A. A., Porciani, C., & Primack, J. R. (2001). A Universal Angular Momentum Profile for Galactic Halos. *ApJ*, *555*(1), 240–257.

Bundy, K., Bershady, M. A., Law, D. R., Yan, R., Drory, N., MacDonald, N., Wake, D. A., Cherinka, B., Sánchez-Gallego, J. R., Weijmans, A.-M., Thomas, D., Tremonti, C., Masters, K., Coccato, L., Diamond-Stanic, A. M., Aragón-Salamanca, A., Avila-Reese, V., Badenes, C., Falcón-Barroso, J., Belfiore, F., Bizyaev, D., Blanc, G. A., Bland-Hawthorn, J., Blanton, M. R., Brownstein, J. R., Byler, N., Cappellari, M., Conroy, C., Dutton, A. A., Emsellem, E., Etherington, J., Frinchaboy, P. M., Fu, H., Gunn, J. E., Harding, P., Johnston, E. J., Kauffmann, G., Kinemuchi, K., Klaene, M. A., Knapen, J. H., Leauthaud, A., Li, C., Lin, L., Maiolino, R., Malanushenko, V., Malanushenko, E., Mao, S., Maraston, C., McDermid, R. M., Merrifield, M. R., Nichol, R. C., Oravetz, D., Pan, K., Parejko, J. K., Sanchez, S. F., Schlegel, D., Simmons, A., Steele, O., Steinmetz, M., Thanjavur, K., Thompson, B. A., Tinker, J. L., van den Bosch, R. C. E., Westfall, K. B., Wilkinson, D., Wright, S., Xiao, T., & Zhang, K. (2015). Overview of the SDSS-IV MaNGA Survey: Mapping nearby Galaxies at Apache Point Observatory. *ApJ*, *798*(1), 7.

Burkert, A., & Naab, T. (2003). Major Mergers and the Origin of Elliptical Galaxies. In G. Contopoulos, & N. Voglis (Eds.) *Galaxies and Chaos*, vol. 626, (pp. 327–339). Springer, Berlin, Heidelberg.

Butcher, H., & Oemler, J., A. (1978). The evolution of galaxies in clusters. I. ISIT photometry of Cl 0024+1654 and 3C 295. *ApJ*, *219*, 18–30.

Butcher, H., & Oemler, J., A. (1984). The evolution of galaxies in clusters. V. A study of populations since Z 0.5. *ApJ*, *285*, 426–438.

Cappellari, M. (2009). Voronoi binning: Optimal adaptive tessellations of multi-dimensional data. *arXiv e-prints*, (p. arXiv:0912.1303).

Cappellari, M. (2016). Structure and Kinematics of Early-Type Galaxies from Integral Field Spectroscopy. *ARA&A*, *54*, 597–665.

Cappellari, M., & Copin, Y. (2003). Adaptive spatial binning of integral-field spectroscopic data using Voronoi tessellations. *MNRAS*, *342*(2), 345–354.

Cappellari, M., Emsellem, E., Bacon, R., Bureau, M., Davies, R. L., de Zeeuw, P. T., Falcón-Barroso, J., Krajnović, D., Kuntschner, H., McDermid, R. M., Peletier, R. F., Sarzi, M., van den Bosch, R. C. E., & van de Ven, G. (2007). The SAURON project - X. The

orbital anisotropy of elliptical and lenticular galaxies: revisiting the (V/σ, ε) diagram with integral-field stellar kinematics. *MNRAS*, *379*(2), 418–444.

Cappellari, M., Emsellem, E., Krajnović, D., McDermid, R. M., Scott, N., Verdoes Kleijn, G. A., Young, L. M., Alatalo, K., Bacon, R., Blitz, L., Bois, M., Bournaud, F., Bureau, M., Davies, R. L., Davis, T. A., de Zeeuw, P. T., Duc, P.-A., Khochfar, S., Kuntschner, H., Lablanche, P.-Y., Morganti, R., Naab, T., Oosterloo, T., Sarzi, M., Serra, P., & Weijmans, A.-M. (2011). The ATLAS^{3D} project - I. A volume-limited sample of 260 nearby early-type galaxies: science goals and selection criteria. *MNRAS*, *413*(2), 813–836.

Cataldi, P., Pedrosa, S. E., Tissera, P. B., & Artale, M. C. (2021). Baryons shaping dark matter haloes. *MNRAS*, *501*(4), 5679–5691.

Cautun, M., van de Weygaert, R., & Jones, B. J. T. (2013). NEXUS: tracing the cosmic web connection. *MNRAS*, *429*(2), 1286–1308.

Chua, K. T. E., Pillepich, A., Vogelsberger, M., & Hernquist, L. (2019). Shape of dark matter haloes in the Illustris simulation: effects of baryons. *MNRAS*, *484*(1), 476–493.

Conselice, C. J., Wilkinson, A., Duncan, K., & Mortlock, A. (2016). The Evolution of Galaxy Number Density at z < 8 and Its Implications. *ApJ*, *830*(2), 83.

Cortese, L., Fogarty, L. M. R., Bekki, K., van de Sande, J., Couch, W., Catinella, B., Colless, M., Obreschkow, D., Taranu, D., Tescari, E., Barat, D., Bland-Hawthorn, J., Bloom, J., Bryant, J. J., Cluver, M., Croom, S. M., Drinkwater, M. J., d'Eugenio, F., Konstantopoulos, I. S., Lopez-Sanchez, A., Mahajan, S., Scott, N., Tonini, C., Wong, O. I., Allen, J. T., Brough, S., Goodwin, M., Green, A. W., Ho, I. T., Kelvin, L. S., Lawrence, J. S., Lorente, N. P. F., Medling, A. M., Owers, M. S., Richards, S., Sharp, R., & Sweet, S. M. (2016). The SAMI Galaxy Survey: the link between angular momentum and optical morphology. *MNRAS*, *463*(1), 170–184.

Croom, S. M., Lawrence, J. S., Bland-Hawthorn, J., Bryant, J. J., Fogarty, L., Richards, S., Goodwin, M., Farrell, T., Miziarski, S., Heald, R., Jones, D. H., Lee, S., Colless, M., Brough, S., Hopkins, A. M., Bauer, A. E., Birchall, M. N., Ellis, S., Horton, A., Leon-Saval, S., Lewis, G., López-Sánchez, Á. R., Min, S.-S., Trinh, C., & Trowland, H. (2012). The Sydney-AAO Multi-object Integral field spectrograph. *MNRAS*, *421*(1), 872–893.

Croom, S. M., Owers, M. S., Scott, N., Poetrodjojo, H., Groves, B., van de Sande, J., Barone, T. M., Cortese, L., D'Eugenio, F., Bland-Hawthorn, J., Bryant, J., Oh, S., Brough, S., Agostino, J., Casura, S., Catinella, B., Colless, M., Cecil, G., Davies, R. L., Drinkwater, M. J., Driver, S. P., Ferreras, I., Foster, C., Fraser-McKelvie, A., Lawrence, J., Leslie, S. K., Liske, J., López-Sánchez, Á. R., Lorente, N. P. F., McElroy, R., Medling, A. M., Obreschkow, D., Richards, S. N., Sharp, R., Sweet, S. M., Taranu, D. S., Taylor, E. N., Tescari, E., Thomas, A. D., Tocknell, J., & Vaughan, S. P. (2021). The SAMI Galaxy Survey: the third and final data release. *MNRAS*, *505*(1), 991–1016.

Danovich, M., Dekel, A., Hahn, O., Ceverino, D., & Primack, J. (2015). Four phases of angular-momentum buildup in high-z galaxies: from cosmic-web streams through an extended ring to disc and bulge. *MNRAS*, *449*(2), 2087–2111.

Davis, M., Efstathiou, G., Frenk, C. S., & White, S. D. M. (1985). The evolution of large-scale structure in a universe dominated by cold dark matter. *ApJ*, *292*, 371–394.

de Vaucouleurs, G. (1959). Classification and Morphology of External Galaxies. *Handbuch der Physik*, *53*, 275.

de Zeeuw, P. T., Bureau, M., Emsellem, E., Bacon, R., Carollo, C. M., Copin, Y., Davies, R. L., Kuntschner, H., Miller, B. W., Monnet, G., Peletier, R. F., & Verolme, E. K. (2002). The SAURON project - II. Sample and early results. *MNRAS*, *329*(3), 513–530.

de Zeeuw, T. (1985). Elliptical galaxies with separable potentials. *MNRAS*, *216*, 273–334.

Dekel, A., & Birnboim, Y. (2006). Galaxy bimodality due to cold flows and shock heating. *MNRAS*, *368*(1), 2–20.

Dekel, A., Birnboim, Y., Engel, G., Freundlich, J., Goerdt, T., Mumcuoglu, M., Neistein, E., Pichon, C., Teyssier, R., & Zinger, E. (2009). Cold streams in early massive hot haloes as the main mode of galaxy formation. *Nature*, *457*(7228), 451–454.

Di Matteo, T., Springel, V., & Hernquist, L. (2005). Energy input from quasars regulates the growth and activity of black holes and their host galaxies. *Nature*, *433*(7026), 604–607.

Dolag, K., Borgani, S., Murante, G., & Springel, V. (2009). Substructures in hydrodynamical cluster simulations. *MNRAS*, *399*(2), 497–514.

Dolag, K., Vazza, F., Brunetti, G., & Tormen, G. (2005). Turbulent gas motions in galaxy cluster simulations: the role of smoothed particle hydrodynamics viscosity. *MNRAS*, *364*(3), 753–772.

Dubois, Y., Pichon, C., Welker, C., Le Borgne, D., Devriendt, J., Laigle, C., Codis, S., Pogosyan, D., Arnouts, S., Benabed, K., Bertin, E., Blaizot, J., Bouchet, F., Cardoso, J. F., Colombi, S., de Lapparent, V., Desjacques, V., Gavazzi, R., Kassin, S., Kimm, T., McCracken, H., Milliard, B., Peirani, S., Prunet, S., Rouberol, S., Silk, J., Slyz, A., Sousbie, T., Teyssier, R., Tresse, L., Treyer, M., Vibert, D., & Volonteri, M. (2014). Dancing in the dark: galactic properties trace spin swings along the cosmic web. *MNRAS*, *444*(2), 1453–1468.

Ebrová, I., & Łokas, E. L. (2015). The Origin of Prolate Rotation in Dwarf Spheroidal Galaxies Formed by Mergers of Disky Dwarfs. *ApJ*, *813*(1), 10.

Ebrová, I., & Łokas, E. L. (2017). Galaxies with Prolate Rotation in Illustris. *ApJ*, *850*(2), 144.

Ebrová, I., Łokas, E. L., & Eliášek, J. (2021). Galaxies with kinematically distinct cores in Illustris. *A&A*, *647*, A103.

Efstathiou, G., Ellis, R. S., & Carter, D. (1982). Further observations of the elliptical galaxy NGC 5813. *MNRAS*, *201*, 975–990.

Einstein, A. (1916). Die Grundlage der allgemeinen Relativitätstheorie. *Annalen der Physik*, *354*(7), 769–822.

Eke, V. R., Cole, S., & Frenk, C. S. (1996). Cluster evolution as a diagnostic for Omega. *MNRAS*, *282*, 263–280.

Emami, R., Hernquist, L., Alcock, C., Genel, S., Bose, S., Weinberger, R., Vogelsberger, M., Shen, X., Speagle, J. S., Marinacci, F., Forbes, J. C., & Torrey, P. (2021). Inferring the Morphology of Stellar Distribution in TNG50: Twisted and Twisted-stretched Shapes. *ApJ*, *918*(1), 7.

Emsellem, E., Cappellari, M., Krajnović, D., Alatalo, K., Blitz, L., Bois, M., Bournaud, F., Bureau, M., Davies, R. L., Davis, T. A., de Zeeuw, P. T., Khochfar, S., Kuntschner, H., Lablanche, P.-Y., McDermid, R. M., Morganti, R., Naab, T., Oosterloo, T., Sarzi, M., Scott, N., Serra, P., van de Ven, G., Weijmans, A.-M., & Young, L. M. (2011). The ATLAS^{3D} project - III. A census of the stellar angular momentum within the effective radius of early-type galaxies: unveiling the distribution of fast and slow rotators. *MNRAS*, *414*(2), 888–912.

Emsellem, E., Cappellari, M., Krajnović, D., van de Ven, G., Bacon, R., Bureau, M., Davies, R. L., de Zeeuw, P. T., Falcón-Barroso, J., Kuntschner, H., McDermid, R., Peletier, R. F., & Sarzi, M. (2007). The SAURON project - IX. A kinematic classification for early-type galaxies. *MNRAS*, *379*(2), 401–417.

Fabjan, D., Borgani, S., Tornatore, L., Saro, A., Murante, G., & Dolag, K. (2010). Simulating the effect of active galactic nuclei feedback on the metal enrichment of galaxy clusters. *MNRAS*, *401*(3), 1670–1690.

Fall, S. M. (1983). Galaxy formation - Some comparisons between theory and observation. In E. Athanassoula (Ed.) *Internal Kinematics and Dynamics of Galaxies*, vol. 100, (pp. 391–398).

Fall, S. M., & Romanowsky, A. J. (2013). Angular Momentum and Galaxy Formation Revisited: Effects of Variable Mass-to-light Ratios. *ApJ*, *769*(2), L26.

Faltenbacher, A., Allgood, B., Gottlöber, S., Yepes, G., & Hoffman, Y. (2005). Imprints of mass accretion on properties of galaxy clusters. *MNRAS*, *362*(3), 1099–1108.

Fernández Lorenzo, M., Cepa, J., Bongiovanni, A., Pérez García, A. M., Ederoclite, A., Lara-López, M. A., Pović, M., & Sánchez-Portal, M. (2011). Evolution of the fundamental plane of 0.2 < z < 1.2 early-type galaxies in the EGS. *A&A*, *526*, A72.

Forbes, D. A., & Ponman, T. J. (1999). On the relationship between age and dynamics in elliptical galaxies. *MNRAS*, *309*(3), 623–628.

Förster Schreiber, N. M., Renzini, A., Mancini, C., Genzel, R., Bouché, N., Cresci, G., Hicks, E. K. S., Lilly, S. J., Peng, Y., Burkert, A., Carollo, C. M., Cimatti, A., Daddi, E., Davies, R. I., Genel, S., Kurk, J. D., Lang, P., Lutz, D., Mainieri, V., McCracken, H. J., Mignoli, M., Naab, T., Oesch, P., Pozzetti, L., Scodeggio, M., Shapiro Griffin, K., Shapley, A. E., Sternberg, A., Tacchella, S., Tacconi, L. J., Wuyts, S., & Zamorani, G. (2018). The SINS/zC-SINF Survey of z ∼ 2 Galaxy Kinematics: SINFONI Adaptive Optics-assisted Data and Kiloparsec-scale Emission-line Properties. *ApJS*, *238*(2), 21.

Foster, C., Mendel, J. T., Lagos, C. D. P., Wisnioski, E., Yuan, T., D'Eugenio, F., Barone, T. M., Harborne, K. E., Vaughan, S. P., Schulze, F., Remus, R. S., Gupta, A., Collacchioni, F., Khim, D. J., Taylor, P., Bassett, R., Croom, S. M., McDermid, R. M., Poci, A., Battisti, A. J., Bland-Hawthorn, J., Bellstedt, S., Colless, M., Davies, L. J. M., Derkenne, C., Driver, S., Ferré-Mateu, A., Fisher, D. B., Gjergo, E., Johnston, E. J., Khalid, A., Kobayashi, C., Oh, S., Peng, Y., Robotham, A. S. G., Sharda, P., Sweet, S. M., Taylor, E. N., Tran, K. V. H., Trayford, J. W., van de Sande, J., Yi, S. K., & Zanisi, L. (2021). The MAGPI survey: Science goals, design, observing strategy, early results and theoretical framework. *PASA*, *38*, e031.

Foster, C., van de Sande, J., Cortese, L., Croom, S. M., Bland-Hawthorn, J., Brough, S., Bryant, J. J., Goodwin, M., Lawrence, J. S., Lorente, N., Medling, A. M., Owers, M., Richards, S. N., & Scott, N. (2018). The SAMI Galaxy Survey: embedded discs and radial trends in outer dynamical support across the Hubble sequence. *MNRAS*, *480*(3), 3105–3116.

Foster, C., van de Sande, J., D'Eugenio, F., Cortese, L., McDermid, R. M., Bland-Hawthorn, J., Brough, S., Bryant, J., Croom, S. M., Goodwin, M., Konstantopoulos, I. S., Lawrence, J., López-Sánchez, Á. R., Medling, A. M., Owers, M. S., Richards, S. N., Scott, N., Taranu, D. S., Tonini, C., & Zafar, T. (2017). The SAMI Galaxy Survey: the intrinsic shape of kinematically selected galaxies. *MNRAS*, *472*(1), 966–978.

Franx, M., Illingworth, G., & de Zeeuw, T. (1991). The Ordered Nature of Elliptical Galaxies: Implications for Their Intrinsic Angular Momenta and Shapes. *ApJ*, *383*, 112.

Friedmann, A. (1922). Über die Krümmung des Raumes. *Zeitschrift fur Physik*, *10*, 377–386.

Friedmann, A. (1924). Über die Möglichkeit einer Welt mit konstanter negativer Krümmung des Raumes. *Zeitschrift fur Physik*, *21*(1), 326–332.

Fujita, Y. (2004). Pre-Processing of Galaxies before Entering a Cluster. *PASJ*, *56*, 29–43.

Genel, S., Nelson, D., Pillepich, A., Springel, V., Pakmor, R., Weinberger, R., Hernquist, L., Naiman, J., Vogelsberger, M., Marinacci, F., & Torrey, P. (2018). The size evolution

of star-forming and quenched galaxies in the IllustrisTNG simulation. *MNRAS*, *474*(3), 3976–3996.

Gerhard, O. E. (1981). N-body simulations of disc-halo galaxies - Isolated systems, tidal interactions and merging. *MNRAS*, *197*, 179–208.

Gerhard, O. E. (1983). A quasi-stable stellar system with prolate inner and oblate outer parts. *MNRAS*, *202*, 1159–1167.

Goto, T., Yamauchi, C., Fujita, Y., Okamura, S., Sekiguchi, M., Smail, I., Bernardi, M., & Gomez, P. L. (2003). The morphology-density relation in the Sloan Digital Sky Survey. *MNRAS*, *346*(2), 601–614.

Gott, I., J. Richard, Jurić, M., Schlegel, D., Hoyle, F., Vogeley, M., Tegmark, M., Bahcall, N., & Brinkmann, J. (2005). A Map of the Universe. *ApJ*, *624*(2), 463–484.

Gunn, J. E., & Gott, I., J. Richard (1972). On the Infall of Matter Into Clusters of Galaxies and Some Effects on Their Evolution. *ApJ*, *176*, 1.

Guo, R., Hao, C.-N., Xia, X., Shi, Y., Chen, Y., Li, S., & Gu, Q. (2020). Toward an Understanding of the Massive Red Spiral Galaxy Formation. *ApJ*, *897*(2), 162.

Hahn, O., Teyssier, R., & Carollo, C. M. (2010). The large-scale orientations of disc galaxies. *MNRAS*, *405*(1), 274–290.

Hau, G. K. T., Carter, D., & Balcells, M. (1999). The shell elliptical galaxy NGC 2865: evolutionary population synthesis of a kinematically distinct core. *MNRAS*, *306*(2), 437–460.

Hellwing, W. A., Cautun, M., van de Weygaert, R., & Jones, B. T. (2021). Caught in the cosmic web: Environmental effect on halo concentrations, shape, and spin. *Phys. Rev. D*, *103*(6), 063517.

Hernquist, L. (1990). An Analytical Model for Spherical Galaxies and Bulges. *ApJ*, *356*, 359.

Hilz, M., Naab, T., & Ostriker, J. P. (2013). How do minor mergers promote inside-out growth of ellipticals, transforming the size, density profile and dark matter fraction? *MNRAS*, *429*(4), 2924–2933.

Hirschmann, M., Dolag, K., Saro, A., Bachmann, L., Borgani, S., & Burkert, A. (2014). Cosmological simulations of black hole growth: AGN luminosities and downsizing. *MNRAS*, *442*(3), 2304–2324.

Ho, S., & Turner, E. L. (2011). The Posterior Distribution of sin(i) Values for Exoplanets with M_T sin(i) Determined from Radial Velocity Data. *ApJ*, *739*(1), 26.

Hoffman, L., Cox, T. J., Dutta, S., & Hernquist, L. (2010). Orbital Structure of Merger Remnants. I. Effect of Gas Fraction in Pure Disk Mergers. *ApJ*, *723*(1), 818–844.

Hopkins, P. F., Quataert, E., & Murray, N. (2012). Stellar feedback in galaxies and the origin of galaxy-scale winds. *MNRAS*, *421*(4), 3522–3537.

Hubble, E. P. (1925). Cepheids in Spiral Nebulae. *Popular Astronomy*, *33*, 252–255.

Hubble, E. P. (1926). Extragalactic nebulae. *ApJ*, *64*, 321–369.

Hubble, E. P. (1936). *Realm of the Nebulae*. Yale University Press.

Illingworth, G. (1977). Rotation (?) in 13 elliptical galaxies. *ApJ*, *218*, L43–L47.

Jesseit, R., Cappellari, M., Naab, T., Emsellem, E., & Burkert, A. (2009). Specific angular momentum of disc merger remnants and the λ_R-parameter. *MNRAS*, *397*(3), 1202–1214.

Jesseit, R., Naab, T., Peletier, R. F., & Burkert, A. (2007). 2D kinematics of simulated disc merger remnants. *MNRAS*, *376*(3), 997–1020.

Kaisin, S. S., Karachentsev, I. D., Hernandez-Toledo, H., Gutierrez, L., & Karachentseva, V. E. (2020). Ha Images of Ultra-Flat Edge-On Spiral Galaxies. *Astrophysical Bulletin*, *75*(1), 1–11.

Karademir, G. S., Remus, R.-S., Burkert, A., Dolag, K., Hoffmann, T. L., Moster, B. P., Steinwandel, U. P., & Zhang, J. (2019). The outer stellar halos of galaxies: how radial merger mass deposition, shells, and streams depend on infall-orbit configurations. *MNRAS*, *487*(1), 318–332.

Kasun, S. F., & Evrard, A. E. (2005). Shapes and Alignments of Galaxy Cluster Halos. *ApJ*, *629*(2), 781–790.

Katz, N. (1991). Dissipationless Collapse in an Expanding Universe. *ApJ*, *368*, 325.

Knebe, A., Gill, S. P. D., Gibson, B. K., Lewis, G. F., Ibata, R. A., & Dopita, M. A. (2004). Anisotropy in the Distribution of Satellite Galaxy Orbits. *ApJ*, *603*(1), 7–11.

Komatsu, E., Smith, K. M., Dunkley, J., Bennett, C. L., Gold, B., Hinshaw, G., Jarosik, N., Larson, D., Nolta, M. R., Page, L., Spergel, D. N., Halpern, M., Hill, R. S., Kogut, A., Limon, M., Meyer, S. S., Odegard, N., Tucker, G. S., Weiland, J. L., Wollack, E., & Wright, E. L. (2011). Seven-year Wilkinson Microwave Anisotropy Probe (WMAP) Observations: Cosmological Interpretation. *ApJS*, *192*(2), 18.

Kormendy, J., & Bender, R. (1996). A Proposed Revision of the Hubble Sequence for Elliptical Galaxies. *ApJ*, *464*, L119.

Krajnović, D., Cappellari, M., de Zeeuw, P. T., & Copin, Y. (2006). Kinemetry: a generalization of photometry to the higher moments of the line-of-sight velocity distribution. *MNRAS*, *366*(3), 787–802.

Krajnović, D., Cappellari, M., Emsellem, E., McDermid, R. M., & de Zeeuw, P. T. (2005). Dynamical modelling of stars and gas in NGC 2974: determination of mass-to-light ratio, inclination and orbital structure using the Schwarzschild method. *MNRAS*, *357*(4), 1113–1133.

Krajnović, D., Emsellem, E., Cappellari, M., Alatalo, K., Blitz, L., Bois, M., Bournaud, F., Bureau, M., Davies, R. L., Davis, T. A., de Zeeuw, P. T., Khochfar, S., Kuntschner, H., Lablanche, P.-Y., McDermid, R. M., Morganti, R., Naab, T., Oosterloo, T., Sarzi, M., Scott, N., Serra, P., Weijmans, A.-M., & Young, L. M. (2011). The ATLAS^{3D} project - II. Morphologies, kinemetric features and alignment between photometric and kinematic axes of early-type galaxies. *MNRAS*, *414*(4), 2923–2949.

Krajnović, D., Emsellem, E., den Brok, M., Marino, R. A., Schmidt, K. B., Steinmetz, M., & Weilbacher, P. M. (2018). Climbing to the top of the galactic mass ladder: evidence for frequent prolate-like rotation among the most massive galaxies. *MNRAS*, *477*(4), 5327–5337.

Kreckel, K., Platen, E., Aragón-Calvo, M. A., van Gorkom, J. H., van de Weygaert, R., van der Hulst, J. M., & Beygu, B. (2012). The Void Galaxy Survey: Optical Properties and H I Morphology and Kinematics. *AJ*, *144*(1), 16.

Kwasnik, B. (1999). The role of classification in knowledge representation and discovery. *Library Trends*, *48*.

Lagos, C. d. P., Theuns, T., Stevens, A. R. H., Cortese, L., Padilla, N. D., Davis, T. A., Contreras, S., & Croton, D. (2017). Angular momentum evolution of galaxies in EAGLE. *MNRAS*, *464*(4), 3850–3870.

Lange, R., Driver, S. P., Robotham, A. S. G., Kelvin, L. S., Graham, A. W., Alpaslan, M., Andrews, S. K., Baldry, I. K., Bamford, S., Bland-Hawthorn, J., Brough, S., Cluver, M. E., Conselice, C. J., Davies, L. J. M., Haeussler, B., Konstantopoulos, I. S., Loveday, J., Moffett, A. J., Norberg, P., Phillipps, S., Taylor, E. N., López-Sánchez, Á. R., & Wilkins, S. M. (2015). Galaxy And Mass Assembly (GAMA): mass-size relations of z < 0.1 galaxies subdivided by Sérsic index, colour and morphology. *MNRAS*, *447*(3), 2603–2630.

Lemaître, G. (1927). Un Univers homogène de masse constante et de rayon croissant rendant compte de la vitesse radiale des nébuleuses extra-galactiques. *Annales de la Société Scientifique de Bruxelles*, *47*, 49–59.

Liller, M. H. (1966). The Distribution of Intensity in Elliptical Galaxies of the Virgo Cluster. II. *ApJ*, *146*, 28.

Madau, P., & Dickinson, M. (2014). Cosmic Star-Formation History. *ARA&A*, *52*, 415–486.

Mo, H. J., Mao, S., & White, S. D. M. (1998). The formation of galactic discs. *MNRAS*, *295*(2), 319–336.

Moore, B., Katz, N., Lake, G., Dressler, A., & Oemler, A. (1996). Galaxy harassment and the evolution of clusters of galaxies. *Nature*, *379*(6566), 613–616.

Naab, T., Johansson, P. H., & Ostriker, J. P. (2009). Minor Mergers and the Size Evolution of Elliptical Galaxies. *ApJ*, *699*(2), L178–L182.

Naab, T., Oser, L., Emsellem, E., Cappellari, M., Krajnović, D., McDermid, R. M., Alatalo, K., Bayet, E., Blitz, L., Bois, M., Bournaud, F., Bureau, M., Crocker, A., Davies, R. L., Davis, T. A., de Zeeuw, P. T., Duc, P. A., Hirschmann, M., Johansson, P. H., Khochfar, S., Kuntschner, H., Morganti, R., Oosterloo, T., Sarzi, M., Scott, N., Serra, P., van de Ven, G., Weijmans, A., & Young, L. M. (2014). The ATLAS^{3D} project - XXV. Two-dimensional kinematic analysis of simulated galaxies and the cosmological origin of fast and slow rotators. *MNRAS*, *444*(4), 3357–3387.

Navarro, J. F., Frenk, C. S., & White, S. D. M. (1997). A Universal Density Profile from Hierarchical Clustering. *ApJ*, *490*(2), 493–508.

Oesch, P. A., Bouwens, R. J., Carollo, C. M., Illingworth, G. D., Trenti, M., Stiavelli, M., Magee, D., Labbé, I., & Franx, M. (2010). Structure and Morphologies of z ∼7-8 Galaxies from Ultra-deep WFC3/IR Imaging of the Hubble Ultra-deep Field. *ApJ*, *709*(1), L21–L25.

Oser, L., Ostriker, J. P., Naab, T., Johansson, P. H., & Burkert, A. (2010). The Two Phases of Galaxy Formation. *ApJ*, *725*(2), 2312–2323.

Ostriker, J. P., & Hausman, M. A. (1977). Cannibalism among the galaxies: dynamically produced evolution of cluster luminosity functions. *ApJ*, *217*, L125–L129.

Peebles, P. J. E. (1969). Origin of the Angular Momentum of Galaxies. *ApJ*, *155*, 393.

Peebles, P. J. E. (1971). Rotation of Galaxies and the Gravitational Instability Picture. *A&A*, *11*, 377.

Penzias, A. A., & Wilson, R. W. (1965). A Measurement of Excess Antenna Temperature at 4080 Mc/s. *ApJ*, *142*, 419–421.

Pereira, M. J., Bryan, G. L., & Gill, S. P. D. (2008). Radial Alignment in Simulated Clusters. *ApJ*, *672*(2), 825–833.

Pillepich, A., Nelson, D., Springel, V., Pakmor, R., Torrey, P., Weinberger, R., Vogelsberger, M., Marinacci, F., Genel, S., van der Wel, A., & Hernquist, L. (2019). First results from the TNG50 simulation: the evolution of stellar and gaseous discs across cosmic time. *MNRAS*, *490*(3), 3196–3233.

Pillepich, A., Springel, V., Nelson, D., Genel, S., Naiman, J., Pakmor, R., Hernquist, L., Torrey, P., Vogelsberger, M., Weinberger, R., & Marinacci, F. (2018). Simulating galaxy formation with the IllustrisTNG model. *MNRAS*, *473*(3), 4077–4106.

Planck Collaboration (2016). Planck 2015 results. I. Overview of products and scientific results. *A&A*, *594*, A1.

Planck Collaboration (2020). Planck 2018 results. VI. Cosmological parameters. *A&A*, *641*, A6.

Power, C., Navarro, J. F., Jenkins, A., Frenk, C. S., White, S. D. M., Springel, V., Stadel, J., & Quinn, T. (2003). The inner structure of ΛCDM haloes - I. A numerical convergence study. *MNRAS*, *338*(1), 14–34.

Pulsoni, C., Gerhard, O., Arnaboldi, M., Pillepich, A., Nelson, D., Hernquist, L., & Springel, V. (2020). The stellar halos of ETGs in the IllustrisTNG simulations: The photometric and kinematic diversity of galaxies at large radii. *A&A*, *641*, A60.

Pulsoni, C., Gerhard, O., Arnaboldi, M., Pillepich, A., Rodriguez-Gomez, V., Nelson, D., Hernquist, L., & Springel, V. (2021). The stellar halos of ETGs in the IllustrisTNG simulations. II. Accretion, merger history, and dark halo connection. *A&A*, *647*, A95.

Remus, R.-S., & Forbes, D. A. (2021). Accreted or Not Accreted? The Fraction of Accreted Mass in Galaxies from Simulations and Observations. *arXiv e-prints*, (p. arXiv:2101.12216).

Robaina, A. R., Hoyle, B., Gallazzi, A., Jiménez, R., van der Wel, A., & Verde, L. (2012). The similar stellar populations of quiescent spiral and elliptical galaxies. *MNRAS*, *427*(4), 3006–3015.

Robertson, H. P. (1935). Kinematics and World-Structure. *ApJ*, *82*, 284.

Robertson, H. P. (1936a). Kinematics and World-Structure II. *ApJ*, *83*, 187.

Robertson, H. P. (1936b). Kinematics and World-Structure III. *ApJ*, *83*, 257.

Rodríguez, S., & Padilla, N. D. (2013). The intrinsic shape of galaxies in SDSS/Galaxy Zoo. *MNRAS*, *434*(3), 2153–2166.

Romanowsky, A. J., & Fall, S. M. (2012). Angular Momentum and Galaxy Formation Revisited. *ApJS*, *203*(2), 17.

Sánchez, S. F., Kennicutt, R. C., Gil de Paz, A., van de Ven, G., Vílchez, J. M., Wisotzki, L., Walcher, C. J., Mast, D., Aguerri, J. A. L., Albiol-Pérez, S., Alonso-Herrero, A., Alves, J., Bakos, J., Bartáková, T., Bland-Hawthorn, J., Boselli, A., Bomans, D. J., Castillo-Morales, A., Cortijo-Ferrero, C., de Lorenzo-Cáceres, A., Del Olmo, A., Dettmar, R. J., Díaz, A., Ellis, S., Falcón-Barroso, J., Flores, H., Gallazzi, A., García-Lorenzo, B., González Delgado, R., Gruel, N., Haines, T., Hao, C., Husemann, B., Iglésias-Páramo, J., Jahnke, K., Johnson, B., Jungwiert, B., Kalinova, V., Kehrig, C., Kupko, D., López-Sánchez, Á. R., Lyubenova, M., Marino, R. A., Mármol-Queraltó, E., Márquez, I., Masegosa, J., Meidt,

S., Mendez-Abreu, J., Monreal-Ibero, A., Montijo, C., Mourão, A. M., Palacios-Navarro, G., Papaderos, P., Pasquali, A., Peletier, R., Pérez, E., Pérez, I., Quirrenbach, A., Relaño, M., Rosales-Ortega, F. F., Roth, M. M., Ruiz-Lara, T., Sánchez-Blázquez, P., Sengupta, C., Singh, R., Stanishev, V., Trager, S. C., Vazdekis, A., Viironen, K., Wild, V., Zibetti, S., & Ziegler, B. (2012). CALIFA, the Calar Alto Legacy Integral Field Area survey. I. Survey presentation. *A&A*, *538*, A8.

Sandage, A. (1961). *The Hubble Atlas of Galaxies*. Carnegie Institution.

Scannapieco, C., Tissera, P. B., White, S. D. M., & Springel, V. (2008). Effects of supernova feedback on the formation of galaxy discs. *MNRAS*, *389*(3), 1137–1149.

Schawinski, K., Urry, C. M., Simmons, B. D., Fortson, L., Kaviraj, S., Keel, W. C., Lintott, C. J., Masters, K. L., Nichol, R. C., Sarzi, M., Skibba, R., Treister, E., Willett, K. W., Wong, O. I., & Yi, S. K. (2014). The green valley is a red herring: Galaxy Zoo reveals two evolutionary pathways towards quenching of star formation in early- and late-type galaxies. *MNRAS*, *440*(1), 889–907.

Schaye, J., Crain, R. A., Bower, R. G., Furlong, M., Schaller, M., Theuns, T., Dalla Vecchia, C., Frenk, C. S., McCarthy, I. G., Helly, J. C., Jenkins, A., Rosas-Guevara, Y. M., White, S. D. M., Baes, M., Booth, C. M., Camps, P., Navarro, J. F., Qu, Y., Rahmati, A., Sawala, T., Thomas, P. A., & Trayford, J. (2015). The EAGLE project: simulating the evolution and assembly of galaxies and their environments. *MNRAS*, *446*(1), 521–554.

Schulze, F., Remus, R.-S., & Dolag, K. (2017). On the Kinematics, Stability and Lifetime of Kinematically Distinct Cores: A Case Study. *Galaxies*, *5*(3), 41.

Schulze, F., Remus, R.-S., Dolag, K., Bellstedt, S., Burkert, A., & Forbes, D. A. (2020). Kinematics of simulated galaxies II: Probing the stellar kinematics of galaxies out to large radii. *MNRAS*, *493*(3), 3778–3799.

Schulze, F., Remus, R.-S., Dolag, K., Burkert, A., Emsellem, E., & van de Ven, G. (2018). Kinematics of simulated galaxies - I. Connecting dynamical and morphological properties of early-type galaxies at different redshifts. *MNRAS*, *480*(4), 4636–4658.

Schwarzschild, M. (1979). A numerical model for a triaxial stellar system in dynamical equilibrium. *ApJ*, *232*, 236–247.

Schwarzschild, M. (1982). Triaxial equilibrium models for elliptical galaxies with slow figure rotation. *ApJ*, *263*, 599–610.

Sharma, S., & Steinmetz, M. (2005). The Angular Momentum Distribution of Gas and Dark Matter in Galactic Halos. *ApJ*, *628*(1), 21–44.

Sharma, S., Steinmetz, M., & Bland-Hawthorn, J. (2012). On the Origin of the Angular Momentum Properties of Gas and Dark Matter in Galactic Halos and Its Implications. *ApJ*, *750*(2), 107.

Shibuya, T., Ouchi, M., & Harikane, Y. (2015). Morphologies of ∼190,000 Galaxies at z = 0-10 Revealed with HST Legacy Data. I. Size Evolution. *ApJS*, *219*(2), 15.

Smoot, G. F., Bennett, C. L., Kogut, A., Wright, E. L., Aymon, J., Boggess, N. W., Cheng, E. S., de Amici, G., Gulkis, S., Hauser, M. G., Hinshaw, G., Jackson, P. D., Janssen, M., Kaita, E., Kelsall, T., Keegstra, P., Lineweaver, C., Loewenstein, K., Lubin, P., Mather, J., Meyer, S. S., Moseley, S. H., Murdock, T., Rokke, L., Silverberg, R. F., Tenorio, L., Weiss, R., & Wilkinson, D. T. (1992). Structure in the COBE Differential Microwave Radiometer First-Year Maps. *ApJ*, *396*, L1.

Springel, V. (2005). The cosmological simulation code GADGET-2. *MNRAS*, *364*(4), 1105–1134.

Springel, V., Di Matteo, T., & Hernquist, L. (2005a). Modelling feedback from stars and black holes in galaxy mergers. *MNRAS*, *361*(3), 776–794.

Springel, V., & Hernquist, L. (2003). Cosmological smoothed particle hydrodynamics simulations: a hybrid multiphase model for star formation. *MNRAS*, *339*(2), 289–311.

Springel, V., White, S. D. M., & Hernquist, L. (2004). The shapes of simulated dark matter halos. In S. Ryder, D. Pisano, M. Walker, & K. Freeman (Eds.) *Dark Matter in Galaxies*, vol. 220, (p. 421).

Springel, V., White, S. D. M., Jenkins, A., Frenk, C. S., Yoshida, N., Gao, L., Navarro, J., Thacker, R., Croton, D., Helly, J., Peacock, J. A., Cole, S., Thomas, P., Couchman, H., Evrard, A., Colberg, J., & Pearce, F. (2005b). Simulations of the formation, evolution and clustering of galaxies and quasars. *Nature*, *435*(7042), 629–636.

Springel, V., White, S. D. M., Tormen, G., & Kauffmann, G. (2001a). Populating a cluster of galaxies - I. Results at z=0. *MNRAS*, *328*(3), 726–750.

Springel, V., Yoshida, N., & White, S. D. M. (2001b). GADGET: a code for collisionless and gasdynamical cosmological simulations. *New A*, *6*(2), 79–117.

Steinborn, L. K., Dolag, K., Hirschmann, M., Prieto, M. A., & Remus, R.-S. (2015). A refined sub-grid model for black hole accretion and AGN feedback in large cosmological simulations. *MNRAS*, *448*(2), 1504–1525.

Szomoru, A., van Gorkom, J. H., Gregg, M. D., & Strauss, M. A. (1996). An HI Survey of the Bootes Void. II. The Analysis. *AJ*, *111*, 2150.

Teklu, A. F., Remus, R.-S., Dolag, K., Beck, A. M., Burkert, A., Schmidt, A. S., Schulze, F., & Steinborn, L. K. (2015). Connecting Angular Momentum and Galactic Dynamics: The Complex Interplay between Spin, Mass, and Morphology. *ApJ*, *812*(1), 29.

Teklu, A. F., Remus, R.-S., Dolag, K., & Burkert, A. (2017). The morphology-density relation: impact on the satellite fraction. *MNRAS*, *472*(4), 4769–4785.

Tornatore, L., Borgani, S., Dolag, K., & Matteucci, F. (2007). Chemical enrichment of galaxy clusters from hydrodynamical simulations. *MNRAS*, *382*(3), 1050–1072.

Treu, T., Ellis, R. S., Kneib, J.-P., Dressler, A., Smail, I., Czoske, O., Oemler, A., & Natarajan, P. (2003). A Wide-Field Hubble Space Telescope Study of the Cluster Cl 0024+16 at z = 0.4. I. Morphological Distributions to 5 Mpc Radius. *ApJ*, *591*(1), 53–78.

Tsatsi, A., Lyubenova, M., van de Ven, G., Chang, J., Aguerri, J. A. L., Falcón-Barroso, J., & Macciò, A. V. (2017). CALIFA reveals prolate rotation in massive early-type galaxies: A polar galaxy merger origin? *A&A*, *606*, A62.

Tsatsi, A., Macciò, A. V., van de Ven, G., & Moster, B. P. (2015). A New Channel for the Formation of Kinematically Decoupled Cores in Early-type Galaxies. *ApJ*, *802*(1), L3.

van de Sande, J., Bland-Hawthorn, J., Brough, S., Croom, S. M., Cortese, L., Foster, C., Scott, N., Bryant, J. J., d'Eugenio, F., Tonini, C., Goodwin, M., Konstantopoulos, I. S., Lawrence, J. S., Medling, A. M., Owers, M. S., Richards, S. N., Schaefer, A. L., & Yi, S. K. (2017a). The SAMI Galaxy Survey: revising the fraction of slow rotators in IFS galaxy surveys. *MNRAS*, *472*(2), 1272–1285.

van de Sande, J., Bland-Hawthorn, J., Fogarty, L. M. R., Cortese, L., d'Eugenio, F., Croom, S. M., Scott, N., Allen, J. T., Brough, S., Bryant, J. J., Cecil, G., Colless, M., Couch, W. J., Davies, R., Elahi, P. J., Foster, C., Goldstein, G., Goodwin, M., Groves, B., Ho, I. T., Jeong, H., Jones, D. H., Konstantopoulos, I. S., Lawrence, J. S., Leslie, S. K., López-Sánchez, Á. R., McDermid, R. M., McElroy, R., Medling, A. M., Oh, S., Owers, M. S., Richards, S. N., Schaefer, A. L., Sharp, R., Sweet, S. M., Taranu, D., Tonini, C., Walcher, C. J., & Yi, S. K. (2017b). The SAMI Galaxy Survey: Revisiting Galaxy Classification through High-order Stellar Kinematics. *ApJ*, *835*(1), 104.

van den Bergh, S. (1976). A new classification system for galaxies. *ApJ*, *206*, 883–887.

van den Bosch, F. C., Abel, T., Croft, R. A. C., Hernquist, L., & White, S. D. M. (2002). The Angular Momentum of Gas in Protogalaxies. I. Implications for the Formation of Disk Galaxies. *ApJ*, *576*(1), 21–35.

van der Wel, A., Franx, M., van Dokkum, P. G., Skelton, R. E., Momcheva, I. G., Whitaker, K. E., Brammer, G. B., Bell, E. F., Rix, H. W., Wuyts, S., Ferguson, H. C., Holden, B. P., Barro, G., Koekemoer, A. M., Chang, Y.-Y., McGrath, E. J., Häussler, B., Dekel, A., Behroozi, P., Fumagalli, M., Leja, J., Lundgren, B. F., Maseda, M. V., Nelson, E. J., Wake, D. A., Patel, S. G., Labbé, I., Faber, S. M., Grogin, N. A., & Kocevski, D. D. (2014). 3D-HST+CANDELS: The Evolution of the Galaxy Size-Mass Distribution since z = 3. *ApJ*, *788*(1), 28.

Vogelsberger, M., Genel, S., Springel, V., Torrey, P., Sijacki, D., Xu, D., Snyder, G., Nelson, D., & Hernquist, L. (2014). Introducing the Illustris Project: simulating the coevolution of dark and visible matter in the Universe. *MNRAS*, *444*(2), 1518–1547.

Walker, A. G. (1937). On Milne's Theory of World-Structure. *Proceedings of the London Mathematical Society*, *42*, 90–127.

Warnick, K., Knebe, A., & Power, C. (2008). The tidal streams of disrupting subhaloes in cosmological dark matter haloes. *MNRAS*, *385*(4), 1859–1883.

Wiersma, R. P. C., Schaye, J., & Smith, B. D. (2009). The effect of photoionization on the cooling rates of enriched, astrophysical plasmas. *MNRAS*, *393*(1), 99–107.

Zemp, M., Gnedin, O. Y., Gnedin, N. Y., & Kravtsov, A. V. (2011). On Determining the Shape of Matter Distributions. *ApJS*, *197*(2), 30.

Zhu, L., van den Bosch, R., van de Ven, G., Lyubenova, M., Falcón-Barroso, J., Meidt, S. E., Martig, M., Shen, J., Li, Z.-Y., Yildirim, A., Walcher, C. J., & Sanchez, S. F. (2018). Orbital decomposition of CALIFA spiral galaxies. *MNRAS*, *473*(3), 3000–3018.

Acknowledgments

This work would not have been possible without the support of numerous people. First of all, I am thankful to Klaus Dolag for inviting me to write this thesis in his group and for supporting me and my work during the last year. I especially appreciate the many digital meetings that were held in times of home office, such that I was able to quickly get to know the group. I would also like to thank Andreas Burkert for his continuous interest and support throughout my work on this thesis and also concerning additional side projects, and for his numerous suggestions that helped improve the work at hand.

Thanks are also due to Rhea-Silvia Remus and Felix Schulze for welcoming me so kindly into the Galaxies@CAST group and for offering me such a current topic to work on. Their availability for discussing the scientific results with me anytime and answering all of my questions is much appreciated. I am also very thankful for all the discussions with Lucas Kimmig, for the assistance in all things `Julia`[1] from Ludwig Böss, for the always great technical support from Tadziu Hoffmann, and for the many interesting questions and discussions in the Galaxies@CAST, Hydrosims, and CAST meetings.

And last but not least, I am grateful to all my friends and family who have always been supportive of me and my studies, and for their ever encouraging and motivating words for me. I would definitely not be where I am now without them!

[1] `www.julialang.org`

Selbstständigkeitserklärung

Hiermit erkläre ich, die vorliegende Arbeit selbstständig verfasst zu haben und keine anderen als die in der Arbeit angegebenen Quellen und Hilfsmittel benutzt zu haben.

München, 14. September 2021

_____

Lucas Valenzuela